Dª. MARÍA ZORAIDA SOSA FERRERA, SECRETARIA DEL DEPARTAMENTO DE QUÍMICA DE LA UNIVERSIDAD DE LAS PALMAS DE GRAN CANARIA,

CERTIFICA,

Que el Consejo de Doctores del Departamento en sesión extraordinaria tomó el acuerdo de dar el consentimiento para su tramitación, a la tesis doctoral titulada "High-resolution modelling of the Canary Basin oceanic circulation" presentada por el doctorando Dº. Evan Mason y dirigida por los Doctores Dº. Pablo Sangrà Inciarte y Dº. Francois Colas.

Y para que así conste, y a efectos de lo previsto en el Artº 73.2 del Reglamento de Estudios de Doctorado de esta Universidad, firmo la presente en Las Palmas de Gran Canaria, a 22 de Octubre de 2009.

UNIVERSIDAD DE LAS PALMAS DE GRAN CANARIA
Departamento de Química

PROGRAMA DE DOCTORADO EN OCEANOGRAFÍA

BIENIO 2006 - 2008

Título de la Tesis:

High-resolution modelling of the Canary Basin oceanic circulation

(Modelaje de alta resolución de la circulación oceánica en la Cuenca Canaria)

Tesis doctoral presentada por Dº. Evan Mason para obtener el grado de Doctor por la Universidad de Las Palmas de Gran Canaria. Dirigida por los Doctores Dº. Pablo Sangrà Inciarte y Dr. Dº. Francois Colas

Dr. Dº. Pablo Sangrà Inciarte Dr. Dº. Francois Colas Dº. Evan Mason

LAS PALMAS DE GRAN CANARIA, A 22 DE OCTUBRE DE 2009

Acknowledgments

First and foremost I wish to thank my supervisor, Pablo Sangrà, for his unfailing support, encouragement, help, and advice during these last four years. Pablo has been the facilitator behind all the work that has been done, giving me the opportunity to maximise my time at UCLA where I have learned so much about working with the ROMS ocean model.

I am very grateful also to Francois Colas, my supervisor during my visits to UCLA. He patiently took me through the long process of learning to use ROMS, taught me the philosophy behind the climatological approach to ocean modelling (over many a coffee break), and was always approachable and ready to share his knowledge.

Jeroen Molemaker too was a key person for me at UCLA, often putting aside his own work in order to spend time on problems and issues concerning my work. His contribution to this thesis has been substantial.

Alexander (Sasha) Shchepetkin has been an invaluable help, both with ROMS and with the myriad of problems one can face when dealing with the hardware and software related to working with an ocean model.

I thank Jim McWilliams for hosting me at UCLA during the three visits I made to Los Angeles between 2007 and 2009.

At ULPGC, I am grateful to Francis Machín, for his time and help from my first days at the university through to the present.

I thank Gheorghe Pop for his help with the computers, and eternal good humour.

I appreciate the work put in by Charles Troupin towards providing the northeast Atlantic climatology for the model forcing. It has been good also to have a fellow ROMS user at ULPGC.

Many others at ULPGC, UCLA and elsewhere have provided help and support at various times, in particular I'd like to mention: Marta, Laura, Ángeles, Charles, Timothée, Xavier, Florian, Mimi, Isora, Iván, Verónica, Ricardo and Belén (who in a sense made this all happen).

Outside of science, there are many people also to be mentioned. In particular, Dolors and Pep, Arminda, and Joana and José Ignacio. As well as being great friends, I am so grateful to you for the help that you have given to me during these years. You all made a difference.

Also Patricia, Nuni, Julia in LA, Antonio (Xevi) in Las Palmas.

All my LA/US friends, in particular Jenny and family.

Lastly, of course, my parents and family, for always being there.

Agradacimientos

En primer lugar deseo agradecer a mi supervisor, Pablo Sangrà, por su inquebrantable apoyo, estímulo, ayuda y asesoramiento durante estos últimos cuatro años. Pablo ha sido el que me ha facilitado todo el trabajo y ha estado detrás de todo lo que he hecho. Me ha dado la oportunidad de maximizar el tiempo en la UCLA, donde he aprendido mucho sobre cómo trabajar con el modelo oceánico ROMS.

También quiero dar las gracias a François Colas, mi supervisor durante mis visitas a la UCLA. Con paciencia me llevó a través del largo proceso de aprender a usar ROMS, me enseñó la filosofía que hay detrás del enfoque climatológico en la modelización oceánica (muchas veces durante la pausa para el café), y estuvo siempre accesible y dispuesto a compartir su conocimiento.

Jeroen Molemaker también fue una persona clave para mí en la UCLA, a menudo dejando de lado su propio trabajo con el fin de dedicar más tiempo a los problemas y las cuestiones relativas a mi investigación. Su contribución a esta tesis ha sido sustancial.

Alexander (Sasha) Shchepetkin ha sido una valiosa ayuda, tanto con ROMS como con la miríada de problemas a la que uno se puede enfrentar cuando se trata con el *hardware* y el *software* relacionados con el trabajo con un modelo sobre el océano.

Doy las gracias a Jim McWilliams por acogerme en UCLA durante las tres visitas que hice a Los Ángeles entre 2007 y 2009.

En la ULPGC, estoy agradecido a Francis Machín, por su tiempo y ayuda en mis primeros días en la universidad hasta el presente.

Doy las gracias a Gheorghe Pop por su ayuda con las computadoras, y su perpetuo buen humor.

Agradezco el trabajo realizado por Charles Troupin por dotar a la climatología del Atlántico Nordeste por el forzamiento del modelo. Ha sido muy agradable tener un compañero en la ULPGC que es también usuario de ROMS.

Muchos otros en la ULPGC, UCLA, y otros países han ofrecido ayuda y apoyo en diversas ocasiones, en particular, me gustaría mencionar: Marta, Laura, Ángeles, Charles, Timothée, Xavier, Florian, Mimi, Isora, Iván, Verónica, Ricardo y Belén (que en cierto sentido ha ayudado para que todo esto llegue a buen puerto).

Fuera de la ciencia, hay muchas personas que también merecen ser mencionadas. En particular, Dolors y Pep, Arminda, y Joana y José Ignacio. Además de ser grandes amigos, estoy muy agradecido por la ayuda que me han ofrecido durante estos años. Todos vosotros habéis marcado la diferencia.

También Patricia, Nuni, Julia en Los Ángeles, Antonio (Xevi) en Las Palmas.

Todos mis amigos de LA/Estados Unidos, en particular Jenny y la familia.

Por último, por supuesto, mis padres y el resto de mi familia, por estar siempre ahí.

Abstract

This research thesis presents novel results from a nested regional ocean model configuration of the Canary Basin. The solutions are climatologically forced, and are unique for the Canary region at this time owing to their high horizontal and vertical resolutions, and for the large number of model years simulated (50 years). The thesis work includes the development of new model boundary procedures that enable the generation of highly-realistic results at scales down to the submesocale.

Analysis of the model results, aside from an extensive validation, is largely restricted to aspects of the Canary Current and the Canary Island archipelago. In recent years there has been a shift in the view of the Canary Current, from being a broad weak eastern boundary current, to a well-defined flow with clear seasonal variability. This contemporary view of the Canary Current opens up new questions: Does the current have a discernible seasonal cycle? What are the characteristics of that cycle and how is it driven? The model solution suggests that, between the latitudes of the Canary Islands and Madeira, the path of the Canary Current is mediated by the westward passage of annually-excited planetary (*Rossby*) waves that are generated at the northwest African coast. Strong support is given to this result through comparison with altimetry, and also with *in situ* observations.

At the Canary Islands, the model reproduces observed levels of variance in surface fields that are brought about by the perturbation of the Canary Current as it passes the islands, and by frontal instabilities associated with the northwest African upwelling. Altimeter observations have recently revealed a zonal "eddy corridor" (Canary Eddy Corridor, CEC) that is populated by long-lived eddies whose source region is the lee of the archipelago. An eddy tracker is applied to the model results to test for preferred generation sites for CEC eddies: in the model, long-lived eddies are predominantly generated at the African coast, except in summer when they originate at the islands. A significant proportion are generated offshore, possibly through frontal instability.

Finally, a range of submesoscale phenomena emerge in the 1-km solution. Horizontal shear at island capes and headlands is a significant source of vorticity. Transient fronts with strong vertical velocities are widespread. In winter there are recurrent outbreaks of mixed layer instabilities. As yet, no submesoscale observations have been undertaken at the Canary Islands. Given the region's importance in terms of biological productivity, and the clear impact that submesoscale processes may have on production, as evidenced by the model results, there is a strong argument for discussion about how to approach this new challenge.

Resumen

Esta tesis presenta resultados novedosos obtenidos a partir de un modelo regional océanico de la Cuenca de Canarias, en una configuración anidada. Las soluciones están climatológicamente forzados, y en este momento son únicos para la región de Canarias debido a su alta resolución espacial, tanto horizontal como vertical, así como por el gran número de años simulados (50 años). El trabajo de tesis incluye el desarrollo de procedimientos con contornos nuevos en el modelo que permitan la generación de resultados muy realistas hasta llegar a resoluciones espaciales de submesoescala.

El análisis de los resultados del modelo, además de una validación extensa, está en gran medida restringido a los aspectos de la Corriente de Canarias y las condiciones dinámicas del archipiélago Canario. En los últimos años ha habido un cambio en la opinión de la Corriente de Canarias, de ser una extensa y débil corriente de frontera este, ha pasado a ser considadera como un flujo bien definido con la variabilidad estacional clara. Este punto de vista contemporáneo de la Corriente de Canarias, abre nuevos interrogantes: ¿La corriente tiene un ciclo estacional discernible? ¿Cuáles son las características de este ciclo y cómo es conducido? La solución del modelo sugiere que entre las latitudes de las Islas Canarias y Madeira, la Corriente de Canarias es atravesada por un pasillo de ondas planetarias (*Rossby*) anualmente excitadas, que son generadas en la costa noroeste de África, y se propagan hacia el oeste. Estos resultados están fuertemente apoyados por resultados obtenidos con la altimetría, y también con las observaciones *in situ*.

En las Islas Canarias, el modelo reproduce los niveles de varianza observados en los campos superficiales que son producidos por la perturbación de la Corriente de Canarias a su paso por las Islas Canarias y por la inestabilidad frontal asociada con el afloramiento del noroeste africano. Observaciones del altímetro recientemente han revelado un "corredor de remolinos" (*Canary Eddy Corridor*, CEC) zonal, que está poblado por remolinos de larga duración, cuya fuente es la región de sotavento del archipiélago. Al aplicar un programa de seguimiento de remolinos a los resultados del modelo se obtienen los lugares en los que se generan el mayor número de remolinos de la CEC: en el modelo, los remolinos de larga duranción se generan predominantemente en la costa africana, excepto en verano, cuando son originados en las islas. Una proporción significativa se generan en alta mar, posiblemente a través de la inestabilidad frontal.

Por último, una serie de fenómenos submesoescalares aparecen en la solución de 1 km. La cizalla horizontal en los contornos de las islas son una fuente importante de vorticidad. Frentes transitorios con fuertes velocidades verticales están muy extendidas. En invierno hay episodios recurrentes de inestabilidad en la capa de mezcla. Hasta el momento, no se han realizado observaciones submesoescalares en las Islas Canarias. Dada la importancia de la región en términos de productividad biológica, y el claro impacto que los procesos de submesoescala puede tener sobre la producción, como lo demuestran los resultados del modelo, hay un fuerte argumento para la discusión sobre cómo abordar este nuevo reto.

Thesis preview

This thesis, entitled *High-resolution modelling of the Canary Basin oceanic circulation*, is a compilation of three distinct studies that are based on ocean numerical modelling work carried out between the Universities of California, Los Angeles (UCLA) and Las Palmas de Gran Canaria (ULPGC), between the years 2007 and 2009. The work has primarily been supported by the Spanish-government-funded research project *Remolinos Oceánicos, Deposición Oceánica* (RODA, 2004 - 2007) (CTM2004-06842-C03-03), through which Evan Mason received a Spanish government FPI grant.

Dr. Pablo Sangrà, together with Dr. Francois Colas of UCLA, have been the supervisors of this thesis work. Dr. Sangrà of ULPGC was a co-Principal Investigator on the RODA project.

The structure of the thesis is as follows. A brief introductory chapter outlines the approach and rationale adopted in order to achieve the aims of the thesis. This is followed by a longer chapter which gives an in-depth description of the physical oceanography of the studied region, i.e., the Canary Basin in the northeast Atlantic Ocean. The three subsequent chapters form the core of the thesis, each of which is presented in article format. Of these, at the time of writing, only the first article (Chapter 3) has been submitted for publication. The status of the second (Chapter 4) and third (Chapter 5) articles is, respectively, close to submission and in preparation. The thesis concludes with a summary and discussion of the main findings and results from this work, as well as some comments on future work (Chapter 6). An appendix is found at the end of the thesis.

A requirement of the ULPGC (Ph.D. Thesis Regulations, BOULPGC. Art. 2, Chap. 1, 5 November 2008) is that a summary written in Spanish be included at the end of the thesis. This section is duly included in the final chapter (Chapter 7).

Presentación de la tesis

Esta tesis, titulado *Modelaje de alta resolución de la circulación oceánica en la Cuenca Canaria*, es una compilación de tres estudios diferentes que se basan en el trabajo de elaboración de modelos numéricos del océano llevado a cabo entre las Universidades de California, Los Angeles (UCLA) y Las Palmas de Gran Canaria (ULPGC), a lo largo de los años 2007 a 2009. El trabajo se ha desarrollado en el contexto del proyecto de investigación *Remolinos Oceánicos, Deposición Oceánica* (RODA) (CTM2004-06842-C03-03), a través del cual Evan Mason recibió una beca FPI del Ministerio de Educación y Ciencia.

El Dr. Pablo Sangrà, junto con el Dr. Francois Colas de UCLA, han sido los supervisores de este trabajo de tesis. Asimismo, el Dr. Sangrà de la ULPGC fue co-Investigador Principal en RODA.

La estructura de la tesis es la siguiente. Un breve capítulo de introducción describe el enfoque y los principios adoptados para alcanzar los objetivos de la tesis. Éste es seguido por un largo capítulo que da una descripción en profundidad de la oceanografía física de la región estudiada, es decir, la Cuenca de Canarias en el noreste del océano Atlántico. Los tres capítulos siguientes constituyen el núcleo de la tesis, cada uno de los cuales se presenta en formato de artículo. De estos, en el momento de la escritura de esta tesis, sólo se ha remitido el primer artículo (capítulo 3). El estado del segundo (capítulo 4) y tercero (capítulo 5) artículos es, respectivamente, listo para ser enviado y en preparación. La tesis concluye con un resumen y discusión de los principales resultados y conclusiones de este trabajo, así como algunos comentarios sobre futuras lineas de trabajo (capítulo 6). Al final de la tesis se encuentra un apéndice.

Un requisito de la ULPGC (Reglamento para la elaboración, tribunal, defensa y evaluación de tesis doctorales, BOULPGC. Art. 2, cap. 1, 5 noviembre de 2008) es que se incluya un resumen en español al fínal de la tesis. Esta sección está debidamente incluida en el capítulo final (capítulo 7).

Contents

List of Figures

List of Tables

1. Introduction

1.1. Introduction

The overarching aim of this study is to investigate the circulation and variability at the mesoscale and submesoscale in the Canary Basin, through the use of a numerical regional ocean model. Given the vast area of the basin, the study is focused towards the Canary Islands off northwest Africa. Few numerical studies exist for the islands, and none at the horizontal and vertical resolutions described herein. The Canary Islands lie across the transition zone between the open ocean and the wind-driven northwest African upwelling, which is known as the Canary Upwelling Ecosystem (CUE). The CUE is one of four major eastern boundary upwelling systems, which have a combined total area of just 0.1% of the world ocean yet account for 30% of the total global fish catch (Durand et al., 1998). Owing to the importance of the ecosystem that is sustained within the CUE, there has been intensive study in recent years of the mesoscale dynamics associated with the upwelling and its interaction with the island wake. It is important to understand these dynamics because biological production is dependent upon them: put simply, vertical and horizontal exchange of mass, mediated chiefly by the wind stress but also by topography, makes nutrients available by raising them into the photic zone. Relative to the other eastern boundary upwellings, the dynamics of the CUE are particularly complex because of the presence of the Canary Islands; at present we have only an elementary understanding of the island eddy field, and of the role of the upwelling front and related instabilities in mediating cross-shelf exchanges (Barton et al., 2004). Several review articles provide an overview of these aspects of the CUE (Barton, 1998; Arístegui et al., 2006, 2009).

With these perspectives in mind, a suite of *nested*[1] model configurations, with successively higher resolutions and smaller areas, has been developed (Figure 1.1). At the large scale (i.e., the Canary Basin), the questions relevant to this thesis concern the character of the geostrophic flows that impact the Canary Islands. The Canary Current is the incident flow at the archipelago; hence its strength, direction and timing are expected to determine much of the complex mesoscale variability that is associated with the islands. The importance of these factors is highlighted by recent studies that suggest the Canary Current does not conform to the eastern-boundary-current paradigm of a broad, weak, equatorward flow. Instead, it is a well-defined current with marked seasonality (Pelegrí et al., 2005a; Machín et al., 2006a). However, there remain many open questions concerning both its kinematics and dynamics.

It has also been shown that mesoscale variability at the Canary Islands has non-local effects: long-lived eddies are observed in altimetry propagating far into the open ocean from the Canary Island region. This "eddy corridor" has been named the Canary Eddy Corridor (CEC; Sangrà et al., 2009). Early estimates suggest the flux of mass associated with the CEC may be as much as a quarter the transport of the Canary Current, with corresponding implications for biogeochemical transports. It is speculated that the eddies are island-generated,

[1] Chapter 3 provides a full explanation of the concept and meaning of *nesting* in the context of numerical modelling.

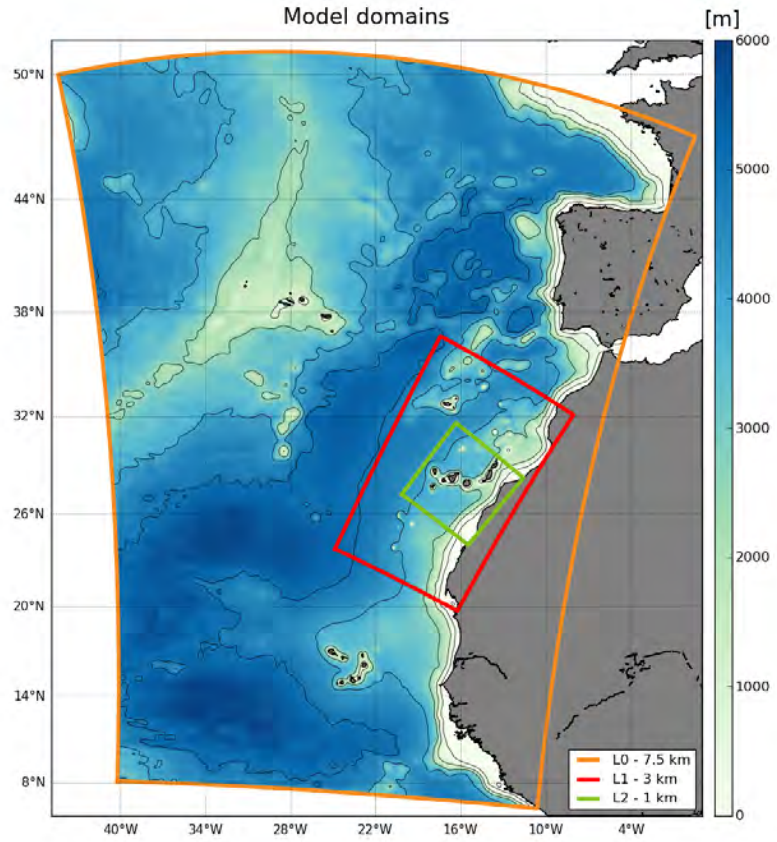

Figure 1.1.: The nested model domains: L0, L1 and L2. The topography for each grid is shown. Isobaths from L0 are plotted at 200, 1000, 2500, 4000 and 5000 m.

but altimetry does not have the resolution to provide definitive answers. The validated model solutions developed here are ideally-suited to answering questions about the eddy corridor: Where and when are the eddies generated? Is there any seasonal dependence for their generation and subsequent trajectories?

A small number of studies have aimed at quantifying the transports between the various island passages. The Lanzarote Passage, that separates the Canary Islands from the African continent, has received the most attention (Hernández-Guerra et al., 2003). The upwelling-associated equatorward-flowing Canary Upwelling Current is present all year, but there is a consistent reversal of the mean flow in the passage in autumn. It is speculated that this reversal is related to the relaxation of the upwelling-favourable Trade winds, which occurs in autumn. The model can provide insight into the processes that may be related to the autumn flow-reversal, and also can give an initial quantification of transports in the lesser-studied island passages.

Besides the long-lived eddies, there are many relatively-transient small-scale phenomena that contribute to the variability of the Canary Island region. Regional ocean modelling is presently undergoing a transition towards the resolution of submesoscale processes. Observational methods are also being developed and implemented. Recent submesoscale studies

reveal a multitude of hitherto unseen features, that have significant implications for biogeochemical processes (Capet et al., 2008a; Thomas et al., 2008). Intense fronts and eddies form and dissipate over short timescales. The vertical velocities associated with these features may exceed those of the mesoscale by an order of magnitude, enhancing greatly the pumping of nutrients to the surface where they become available for production.

The innermost domain of the nested configuration has a horizontal resolution of 1 km (Figure 1.1), putting it at the threshold of the mesoscale-submesoscale transition (Capet et al., 2008c). This solution displays an abundance of near-surface submesoscale eddies, fronts and filaments not seen in the two lower-resolution solutions. A first step towards detailed study of this new environment involves identifying and characterising the observed phenomena. How are known mesoscale features, such as island-generated eddies, different when viewed through the submesoscale lense? Are there "new" features, that simply don't exist in the mesoscale regime? What are the characteristics of the seasonal cycle under the submesoscale regime?

Clearly, a broad range of questions are posed in this introduction. Attempting to provide answers requires a high-quality model solution, that has undergone an extensive process of validation. In the next section, an outline of the methodology related to the model configuration is presented. In later chapters, the methodology will be expanded upon (Chapter 3) and appropriate validation exercises undertaken (Chapter 4).

1.2. Methodology

The modelling approach adopted is a *climatological* approach, where the equilibrium dynamics of the region are simulated. Our interest is the mean circulation, the seasonal cycle, and variability at the mesoscale and near-submesoscale. Forced interannual variability is not considered. Mesoscale variability has been shown to be largely intrinsic, particularly within upwelling systems (Marchesiello et al., 2003), suggesting that it is chaotic and difficult to predict. Its generation is linked to instabilities within larger-scale structures, such as currents and upwelling fronts. The large-scale structure itself is determined by (1) low-frequency, large-scale atmospheric forcing (which may be local or remote) and, (2) by the mean currents that flow into and out of any defined domain of interest.

In this study, in order to ensure the realism of the mean circulation at the Canary Islands, a model domain that extends well beyond the limits of the islands is required. In deciding where to put the domain boundaries, careful consideration is made of what features of the basin scale circulation it is desirable to include: The Canary Islands are embedded within the path of the equatorward-flowing Canary Current. The current is supplied in the north by a southward branching of the Azores Current, which flows zonally across the northeast Atlantic Ocean towards the Gulf of Cadiz. The Strait of Gibraltar, at the eastern limit of the Gulf of Cadiz, is an important singularity (in addition to the Canary Island archipelago) of the eastern boundary of the northeast Atlantic Ocean. Here, dense Mediterranean Water flows into the northeast Atlantic Ocean at a rate of $\sim$1 Sv (1 Sv = 10^6 m^3 s^{-1}). The

dynamics of the Azores Current[2] have been disputed, but there is increasing evidence that the downward entrainment of surface waters into the descending Mediterranean Water plume is a key process (Peliz et al., 2007; Kida et al., 2008). Therefore, given the apparent links between the Azores Current, the Canary Current, and the Canary Islands, it seems prudent to include within the model domain the Azores Current, and also an open Strait of Gibraltar thereby including processes related to the Mediterranean outflow. Through a process of experimentation with different domains and model grids, it was eventually decided to place the model boundaries well beyond both the Canary Islands and the Gulf of Cadiz. This leads to the rather large domain depicted in Figure 1.1, that encompasses the entire Canary Basin.

In choosing a scale for the horizontal resolution of this large domain (hereinafter L0), we note that the fine-scale resolution required at the Canary Islands ($\mathcal{O}1$ km) is prohibitively expensive in terms of computation if applied to L0. An acceptable compromise in terms of computing time for a grid of these physical dimensions is a resolution of 7.5 km. This, however, necessitates the adoption of the so-called nesting approach, in order to arrive at the desired 1 km at the Canary archipelago. Hence, the creation of two child domains, L1 and L2. L2 is the target 1-km solution. L1, at 3 km, is an intermediate solution, which is useful for a high-resolution mesoscale analysis. The solutions are run independently, the results from each outer domain are *downscaled* to supply boundary information to each respective child domain. In this way, the large-scale structure generated within L0 is passed to L1, and subsequently to L2.

Prior to the downscaling exercise, results from L0 are validated by comparison with a wide range of available observations. The validation is an essential part of the development of the configuration, not least because of the coupling to L1 and L2.

All seven of the Canary Islands that make up the archipelago are resolved in each of the nested domains, as well as the nearby African coast and the lee region where mesoscale island-generated eddies and upwelling-related coastal filaments typically interact (Figure 1.1). The full extent of the northwest African upwelling region is omitted from L2, but is present in L1 and L0. L0 is a multi-decadal L0 solution that totals 50 years, permitting the calculation of robust statistics for the purposes of both analysis and validation. For the most part, the analysis of L0 is limited to seasonal timescales. The L1 intermediate domain is significantly more costly in computional time than L0, but nevertheless a solution of 11 years is sufficient for reliable statistics to be calculated, at seasonal and monthly timescales. The L2 solution is just 3 years long, precluding a statistical analysis.

Three short additional simulations were run for the L2 domain using wind stresses obtained from an atmospheric numerical model (MM5) solution at the Canary Islands. The MM5 solution covers the period July - September 2006[3]. Results from these runs are included with the L2 results of Chapter 5.

[2]The Azores Current is historically a difficult current to model (Spall, 1990; Stammer and Böning, 1996; Hecht and Smith, 2008).

[3]The MM5 winds correspond to the period of an oceanographic cruise, where eddies at the Canary Islands were sampled as part of the Spanish government funded research project RODA.

The model code used in this thesis is the UCLA variant of the Regional Ocean Modelling System (ROMS; Shchepetkin and McWilliams, 2005, 2009b). Physical processes only are simulated. Modules exist for the simultaneous computation of biogeochemical processes using ROMS, but these have not been implemented in the present work.

1.3. Thesis outline

The thesis is organised as follows. Chapter 2 describes the physical oceanography of the northeast Atlantic Ocean, with a section covering the Canary Island region. The numerical model and the methodologies developed in the course of this study are presented in Chapter 3. Chapter 4 introduces the large-domain (L0) solution which covers the Canary Basin. We present a novel description of the seasonal migratory path of the Canary Current between the latitudes of Madeira and the Canary Islands. Further sections cover various aspects of the Azores Current and Canary Current; in particular we ask what might happen to the Canary Current if the Azores Current stopped? In a final section using the L0 solution, eddy tracking experiments shed light on the origins of the long-lived eddies that populate the Canary Eddy Corridor observed by Sangrà et al. (2009). The extensive validation of the L0 Canary Basin solution carried out in Chapter 4 provides a starting point for an analysis of the high-resolution child solutions (L1, L2), which is presented in Chapter 5. The focus is towards mesoscale/submesoscale variability at the Canary Islands. The mesoscale circulation at the archipelago introduces variability in the transports between the island passages. Most notably, in the Lanzarote Passage between the eastern islands and the African coast, the observed autumn reversal of the flow is reproduced by the model. However, the structure of the flow in the passage at this time suggests that relaxation of the upwelling winds may not be the cause of the reversal, as has been speculated. In the submesoscale regime, eddies are shown that do not fit the classic description of island-generated eddies observed at the Canary Islands. Finally, Chapter 6 brings together the main conclusions from the thesis work, and outlines ideas for the future exploitation of the model solutions. Chapter 7 contains a summary of the thesis which is written in Spanish.

2. Oceanography of the Canary Basin

2.1. Introduction

The Canary Basin region of the northeastern Atlantic Ocean has been well known to seafarers for many centuries. In the 1400s, Portuguese sailors followed the path of the Canary Current in their tours around Africa towards the Orient. In 1492, Christopher Columbus stopped at La Gomera in the Canary Islands on his way to discovering America. Columbus's interest in sailing westward stemmed from the lure of finding a short cut to the riches of Asia. He had spent several years becoming familiar with the Canary region. In September 1492, using lead and line, he made the first observations of the North Equatorial Current (Peterson et al., 1996). Columbus, plus a host of other European explorers, was later followed by traders, many of whom plied a triangular route, taking slaves from Africa to the Caribbean and the Americas, and sugar and cotton on the return leg to Europe. Throughout these circular trading journeys, sailing ships took advantage of the prevailing wind systems in the North Atlantic: the easterly Trade winds at lower latitudes for the outward leg, and the mid-latitude westerlies for the trip home. The Canary Islands therefore became an important marketplace, as well as a fountainhead for emigration to the Americas. Today, the economic and scientific importance of the Canary Island region is derived from its ecosystem. The fishery presently accounts for an annual catch of around 2 million tonnes, amid reports of a decline in landings which is possibly climate-driven (Arístegui et al., 2009).

2.2. Topography

The Canary Basin lies roughly within the limits of the western European and northwest African coasts and ∼40°W, and the meridians ∼10° - 40°N. It covers an area greater than 3 million km^2. The deepest part of the basin is the ∼4500-m Madeira Abyssal Plain (MAP), which lies about 1000 km west of the African margin. In contrast, the volcanic Canary and Madeira island archipelagos reach altitudes greater than 1800 m above sea level. The volcanic Teide massif on Tenerife (the largest of the Canary Islands), at 3718 m, is Spain's highest mountain.

The topology of the Canary Basin is illustrated in Figure 2.1. In the west, the basin is bounded by the Mid-Atlantic Ridge (MAR), which rises around 2000 m above the abyssal plain. The 2000-km long African continental coastline is generally orientated in a northeast-southwest direction. Average shelf width along the coast is ∼50 - 60 km, with a maximum of ∼100 - 120 km at ∼25°N, and a minimum of ∼20 - 30 km at ∼21°N (Mittelstaedt, 1991; Carr and Kearns, 2003). In the south between ∼7° - 13°N the shelf broadens to over 300 km. The shelf edge is well defined by the 200-m isobath. At the northern extent of the transect is the Gulf of Cadiz, where the Strait of Gibraltar facilitates exchange of water properties between the North Atlantic and the Mediterranean Sea. The coastline is marked by several large capes including Capes Ghir (30.6°N), Juby (28.0°N), Bojador (26.1°N), Blanc (20.8°N) and Verde (14.8°N). Along the western Iberian Peninsula (IP), the main capes are St. Vincent (37.0°N), Roca (38.8°N) and Finisterre (42.9°N).

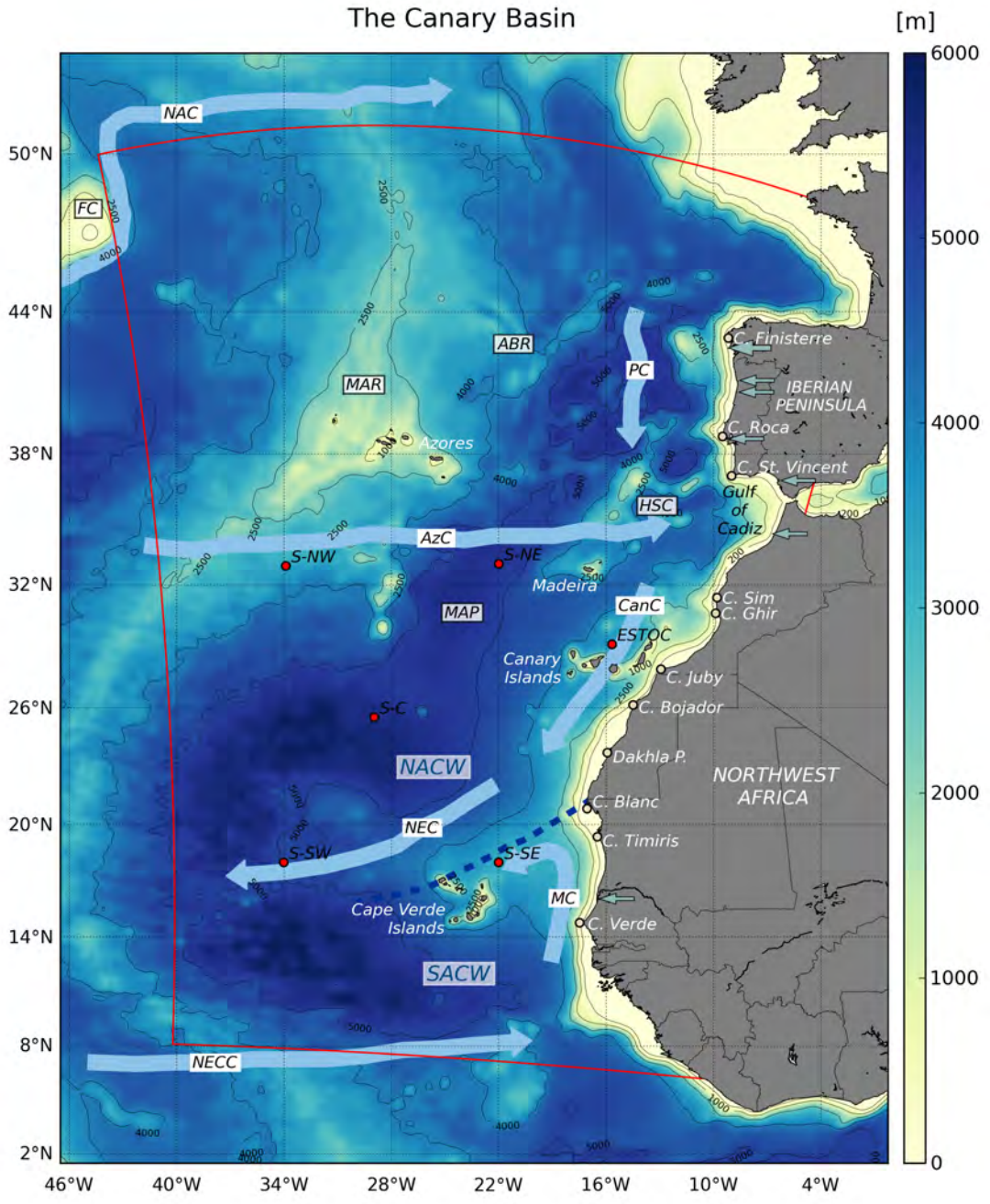

Figure 2.1.: Principal oceanographic features of the Canary Basin in the northeastern Atlantic Ocean. The Cape Verde Frontal Zone (CVFZ) separating North Atlantic Central Water (NACW) and South Atlantic Central Water (SACW) is marked by the dashed dark blue line. Red dots show the positions of the Subduction Experiment (SubExp) moorings. River outflow locations are shown by light blue horizontal arrows. Labels: AzC - Azores Current, CanC - Canary Current, MC - Mauritania Current, NEC - North Equatorial Current, NECC - North Equatorial Counter-Current; ABR - Azores-Biscay Rise, FC - Flemish Cap, HSC - Horseshoe Seamount Chain, MAP - Madeira Abyssal Plain, MAR - Mid-Atlantic Ridge. Contours in black mark isobaths at 200, 1000, 2500, 4000, 5000 m. The boundary of the L0 model domain (Chapter 4) is outlined in red. Topographic data from GEBCO (Hunter and Macnab, 2003).

The bottom topography in Figure 2.1 includes the typical morphological features of the eastern Atlantic continental margin: the continental shelf, slope and rise. The continental margin is indented along its length by several submarine canyons, particularly off western Iberia (Peliz and Fiúza, 1999). Canyons are associated with eddy generation, and are also sites of coastal sediment deposition (Fiúza et al., 1998; Peliz et al., 2002). The Portimão Canyon in the Gulf of Cadiz is a major topographic interruption across the path of the Mediterranean undercurrent, which is implicated in the formation of Mediterranean eddies *(Meddies)* (Serra and Ambar, 2002). At the Agadir Canyon, southwest of Cape Ghir, a subsurface anticyclonic eddy has been observed during two successive cruises (Pelegrí et al., 2005b). It is suggested that the eddy may be associated with interaction between the poleward undercurrent that flows along the slope and the canyon.

The island archipelagos of the Canary Basin have come to be collectively known as Macaronesia. The Canary Island archipelago is centrally located at about 28.5°N, 15°W. All seven of the islands that make up the archipelago lie upon a steep-sided zonally-orientated plateau that extends offshore from the continental boundary. The Madeira archipelago is found some 500 km north of the Canary Islands at ∼33°N, 16.5°W. The Cape Verde islands are located ∼700 km offshore of Cape Verde. The Azores archipelago is found east of the main MAR axis at ∼38°N, 28°W.

Seamounts of volcanic origin are common features of the offshore region between Cape Blanc and southwestern Iberia (Ye et al., 1999). West of the Gulf of Cadiz there is a cluster of seamounts named the Horseshoe Seamount Chain (Epp and Smoot, 1989). These seamounts, particularly Gorringe Bank, are thought to constrain the paths of *Meddies* generated near to Cape St. Vincent (Richardson et al., 2000; Serra and Ambar, 2002; Wang and Dewar, 2003).

The Mid-Atlantic Ridge is a major offshore topographic feature, which represents a significant barrier to inter-basin exchange. Results from a drifter analysis by Bower et al. (2002) suggest that, in order to cross the MAR, currents (i.e., the North Atlantic Current) flow preferentially over the deeper gaps, constrained by conservation of potential vorticity (f/H, where f is the *Coriolis* parameter and H is the fluid depth). These observations are supported through geostrophic current maps over the MAR, computed from altimetry (Bower and von Appen, 2008), and *in situ* measurements (Søiland et al., 2008).

At the far west of the domain, outside of the Canary Basin, the Flemish Cap 47°N, 45°W is a notable feature. This wide underwater plateau is just over 100 m deep, and has a strong topographic influence on the North Atlantic Current, which passes around it (Heywood et al., 1994; Rossby, 1996).

2.3. Surface forcing

The mid-latitude Canary Basin lies under the influence of the atmospheric high-pressure system known as the Azores High (AzH). Close to the northwest African landmass, over which lower pressure predominates, pressure gradients are steep resulting in intense northeasterly

alongshore winds, known as the Trade winds. At the low-pressure equatorial latitudes, the zone of convergence between the northern- and southern-hemisphere Trade winds is called the Inter-Tropical Convergence Zone (ITCZ; Molinari et al., 1986; Waliser and Gautier, 1993). The ITCZ is associated with rising air and high rainfall. Seasonal variations result from the latitudinal shifts of the AzH and of the ITCZ. During the boreal summer, both the Trade-wind belt and the ITCZ move northwards away from their wintertime positions. The seasonal cycle of the surface currents reflects the oceanic response to the seasonally-varying wind fields, which are related to the migrations of these atmospheric phenomena.

2.3.1. Wind stress

The northeasterly alongshore Trade wind regime drives an extensive upwelling system along the Iberian and northwest African coasts (Wooster et al., 1976; Mittelstaedt, 1991; Nykjær and Van Camp, 1994). Figure 2.2 shows fields of the seasonal mean wind stress curl over the subtropical northeast Atlantic, illustrating both large- and small-scale variability in the wind structure. Vectors show the magnitude and direction of the winds at 10 m above the surface. The data are taken from the 8-year SCOW wind speed and wind stress climatology of Risien and Chelton (2008), which is based on the 25-km resolution SeaWinds scatterometer carried aboard the QuikSCAT satellite (Chelton et al., 2004). Also shown are the 1016- and 1020-mbar isobars from the Comprehensive Ocean-Atmosphere Dataset (COADS, Release 2.1; Worley et al., 2005), which indicates the position of the AzH. Whilst monthly and longer-term averages of the wind vectors show a decrease in magnitude from southeast to northwest, scalar averages have been shown by Weller et al. (2004) to produce much lower variability, indicating greater directional variability in the northwest.

In winter and autumn, with the AzH located in its southerly position at around 33°N, the northeasterly Trade winds extend far to the south. In the north this permits the easterly passage of frequent cyclonic depressions. The northwestern part of the region is influenced by moderate anticyclonic wind stress curl and, as a result, the region is known to experience subduction of cold surface waters as *Ekman* convergence at the surface causes downwelling. Weller et al. (2004) found mean values of 50 m yr^{-1} near to mooring S-C (Figure 2.1).

Along the African and Iberian coasts, strong cyclonic curl tends to dominate, particularly downwind of the major capes. One example is Cape Ghir, where the curl is present all year but is strongest in summer. At Cape Sim just to the north, strong cyclonic curl occurs in summer, but is largely absent during the rest of the year. Off western Iberia, the upwelling season commences in spring and continues through the summer, consistent with the northward migration of the AzC. Cyclonic curl augments the coastal upwelling by inducing open-ocean upwelling away (>100 km) from the shore. In the south, the open-ocean upwelling extends offshore to beyond the Cape Verde islands. Weller et al. (2004) reported summer upwelling velocities of 60 m yr^{-1} at 15°N, 27°W.

It is noteworthy that QuikSCAT/SCOW succeeds in resolving the atmospheric wakes at the island archipelagos, i.e., Madeira, the Canary Islands and the Cape Verde islands,

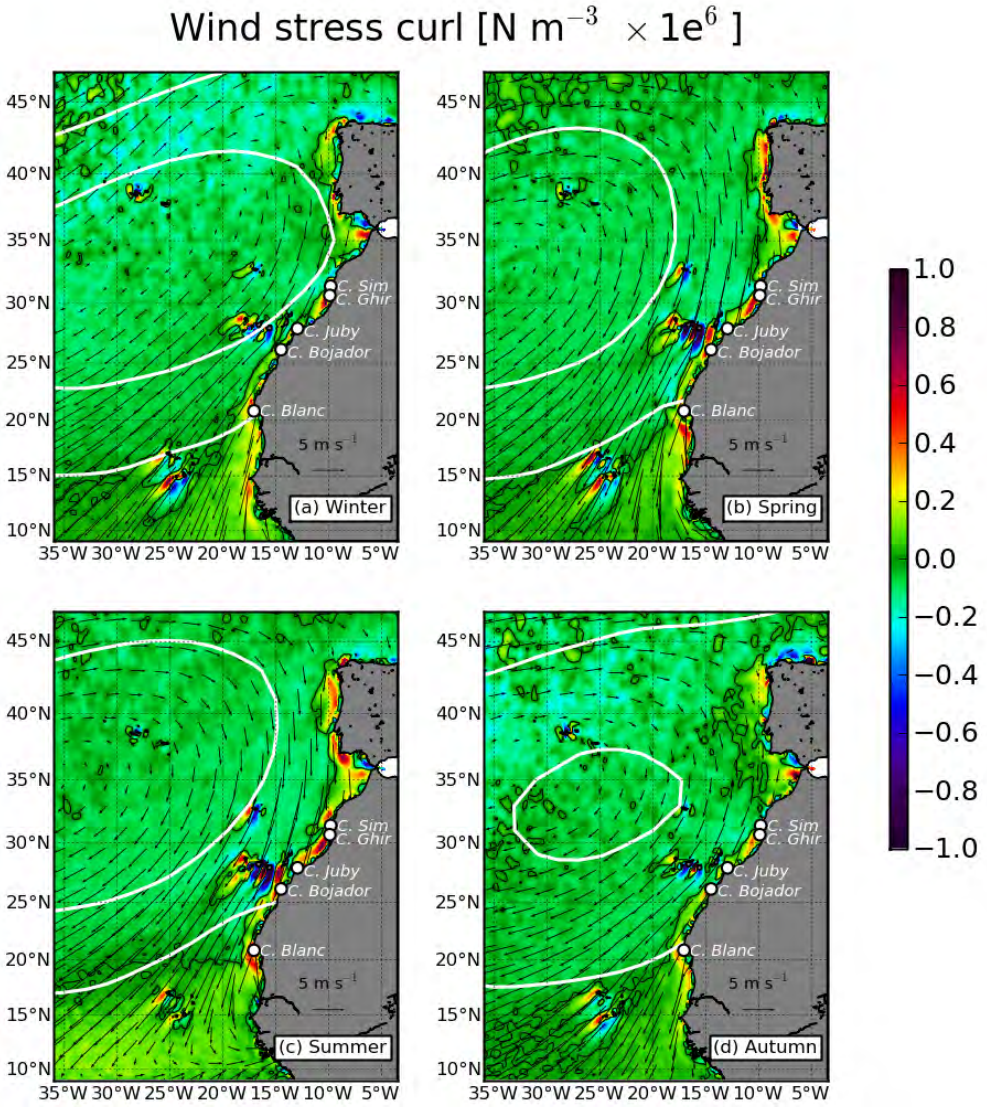

Figure 2.2.: Seasonal fields of the normalised wind stress curl from the QuikSCAT-derived SCOW wind stress climatology of Risien and Chelton (2008) over the subtropical northeast Atlantic. The zero curl contour is shown in black. White contours show the 1016- and 1020-mbar isobars from the COADS air-sea flux climatology. Vectors in black give the 10-m wind speed and direction.

all of which are under the influence of the Trades. Channeling of the winds as they pass through the inter-island gaps results in the formation of jets, which extend several hundred kilometres downstream. Comparing the Cape Verde and Canary Island wakes, one can see that the Cape Verde islands lead the Canaries by about a season in the development of the wake, corresponding to the AzH migration. Curl associated with the wind jet is a potential instigator of oceanic eddies (Barton, 2001; Chavanne et al., 2002; Jiménez et al., 2008).

2.3.2. Heat fluxes

Annual cycles in solar insolation and the strength and position of the AzH account for much of the spatial and temporal variability in the thermocline waters of the Canary Basin. Variability at annual scales of the surface forcing is high, and large-scale latitudinal gradients are steep. Latitudinal temperature gradients are a major source of zonal available potential energy.

Figure 2.3 shows seasonal fields of the mean net heat flux (NHF) from COADS. Positive (negative) values show ocean heat gain (loss). Spring and autumn are distinct from the other seasons in that, across the domains shown, there is almost total heat gain and loss, respectively. Coastal regions equatorward of about 38°N consistently gain heat, apart from in autumn. Weller et al. (2004) analysed three years of surface meteorological data from the five Subduction Experiment (SubExp) moorings, whose locations are shown in Figure 2.3. The moorings were positioned to straddle the zero line in the annual mean NHF, so as to sample both net heating to the south and net cooling to the north. At these sites in the COADS data however, annual averages of the NHF are all close to zero. Yet Weller et al. (2004) reported positive annual averages (in the range $\sim$20 - 40 W m^{-2}) from the moorings[1], which were in agreement with a study by Josey (2001). At all five sites, a net heat gain was recorded in the summertime, and a net heat loss in winter. In the Canary Island region, the NHF is positive from March to August, and negative from September to February (Pelegrí et al., 2005a).

2.3.3. Freshwater flux

Figure 2.4 shows seasonal means of evaporation minus precipitation (E-P) from COADS. Between about 15°N and 35°N, evaporation exceeds precipitation in all seasons. In summer, high rainfall associated with the ITCZ as it occupies its northernmost position is seen within a band of negative E-P along 10°N.

Schmitt et al. (1989) presented a compilation of evaporation and precipitation data for the North Atlantic. They showed that, in the Canary Basin, mean annual evaporation exceeds precipitation by between 50 cm year^{-1} in the north, and >100 cm year^{-1} in the south. In contrast to the rest of the North Atlantic, these differences remain constant.

[1] The model forcing in this thesis uses the COADS net heat flux climatology. Therefore, heat gain in the modelled Canary Basin (at least in the region of the SubExp moorings) may be assumed to have a negative bias.

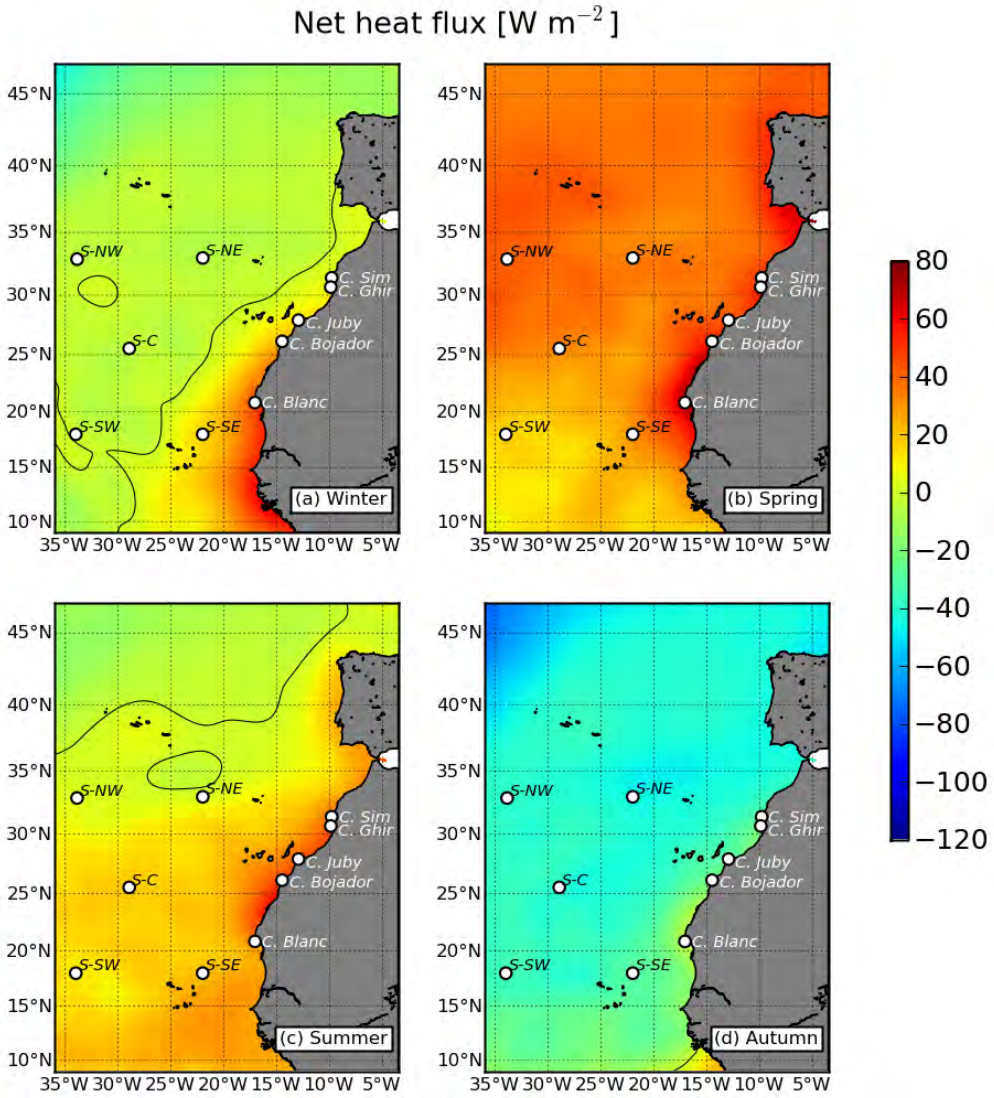

Figure 2.3.: Seasonal fields of the surface net heat flux (NHF) from the COADS air-sea flux climatology of Worley et al. (2005). Positive (negative) values show ocean heat gain (loss). The zero NHF contour is shown in black. The five Subduction Experiment (SubExp) mooring locations are marked in white.

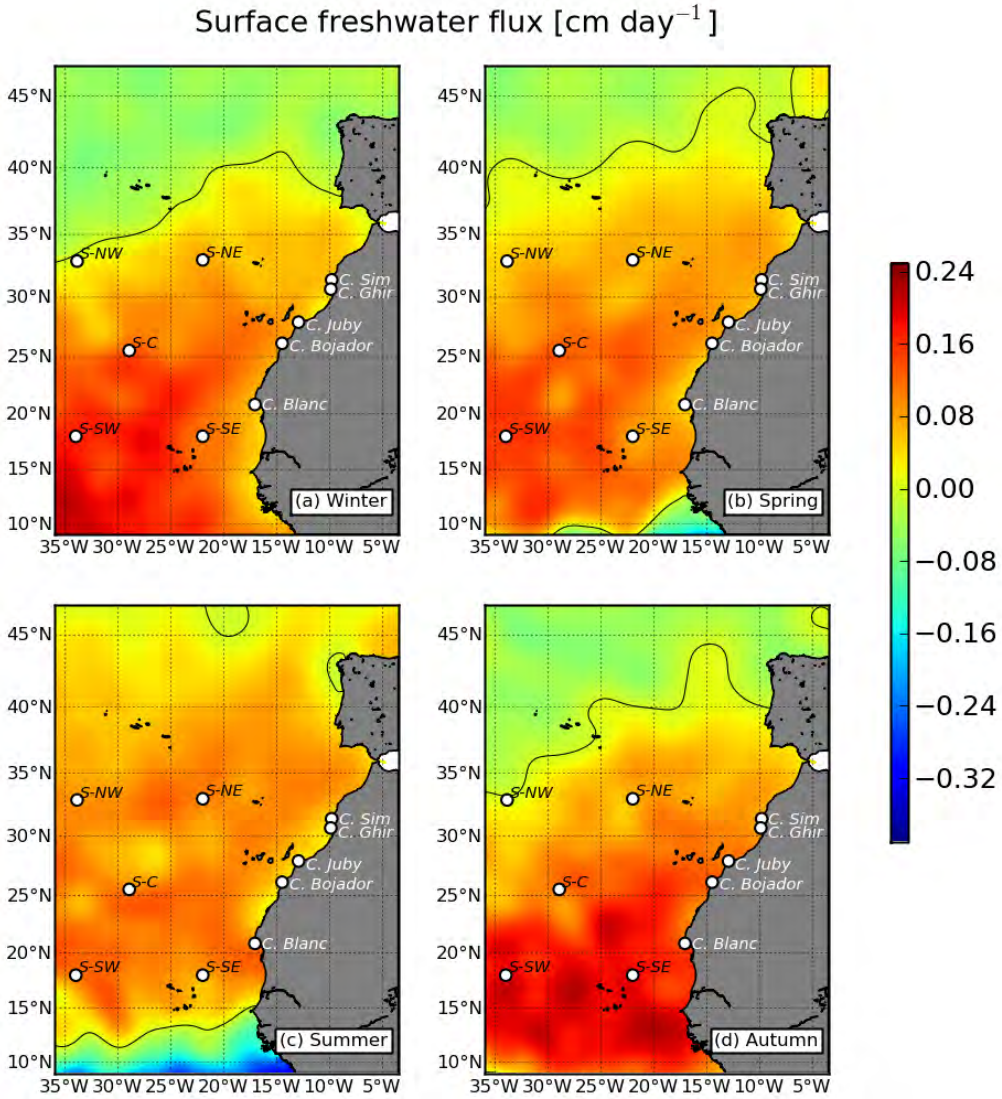

Figure 2.4.: Seasonal maps of evaporation minus precipitation (E-P) from the COADS air-sea flux climatology of Worley et al. (2005). The zero E-P contour is shown in black. The five Subduction Experiment (SubExp) mooring locations are marked in white.

Over the Canary Basin, Schmitt et al. (1989) showed that thermal density fluxes exceed haline density fluxes by between 2 and 20, with values increasing towards the coast. The relatively high evaporation is associated with the high and consistent NHF, and high sea surface temperatures (SST) (Pelegrí et al., 2005a).

In general, the Canary Basin region experiences only a minor contribution to the buoyancy forcing from precipitation. At the Canary Islands, rainfall is minimum in May (0.04 cm day^{-1} at Gran Canaria). In December and January, rainfall is maximum (0.06 cm day^{-1} at Gran Canaria) (Pelegrí et al., 2005a). At the sites of the Subduction Experiment moorings, Weller et al. (2004) observed small rain rates (up to ∼1 cm day^{-1}) from spring through summer. In autumn, increased precipitation was observed at the southern moorings, which decreased with the onset of winter. At the northwestern mooring (S-NW), passing synoptic weather events in autumn and winter contributed to increased rain rates (up to ∼3.8 cm day^{-1}).

Locations of significant riverine imput to the coastal ocean are indicated in Figure 2.1. River runoff is important off the northwest coasts of Portugal and Spain, with peak values in winter (Peliz et al., 2005). However, there are no major river discharges for much of the northwest African coast. Along the Moroccan coast at about 34°N there are a small number of flooding rivers, whose plumes are sometimes visible in colour satellite images after intensive flooding (Warrick and Fong, 2004). These plumes are typically advected polewards. High river discharges along the equatorial African coast affect water masses to as far north as 18°N. The fresh water has a warm anomaly, and can be seen spreading northwards in winter satellite SST images (Van Camp et al., 1991).

2.4. Water masses

The Canary Basin contains the three general classes of water-mass type found in the mid-latitude world oceans, which are the Central, Intermediate and Deep Waters. Their distribution has been summarised by Barton (1998) and Arístegui et al. (2006). Figure 2.5 summarises the vertical and horizontal distributions of these water masses for a hypothetical ocean. Central Waters occupy the layer below the surface water to the base of the main thermocline (which varies with latitude), typically ∼200 - 1000 m. The surface water in the Canary Basin tends to be salty owing to high insolation and low rainfall. Central Waters are formed largely as a result of wind action. The Intermediate Waters are found below the Central Waters, with maximum depths of ∼1500 m. The Deep Waters extend towards the bottom (∼4000 m), but are not in contact with the bottom. These are the most voluminous of all the water masses in the world ocean.

2.4.1. Central waters

In the subtropical North Atlantic, the Trade winds and the westerlies force the oceanic circulation that defines the basin-wide anticyclonic subtropical gyre. Within the gyre, instabilities, particularly in the winter months, lead to intense vertical mixing which homogenises

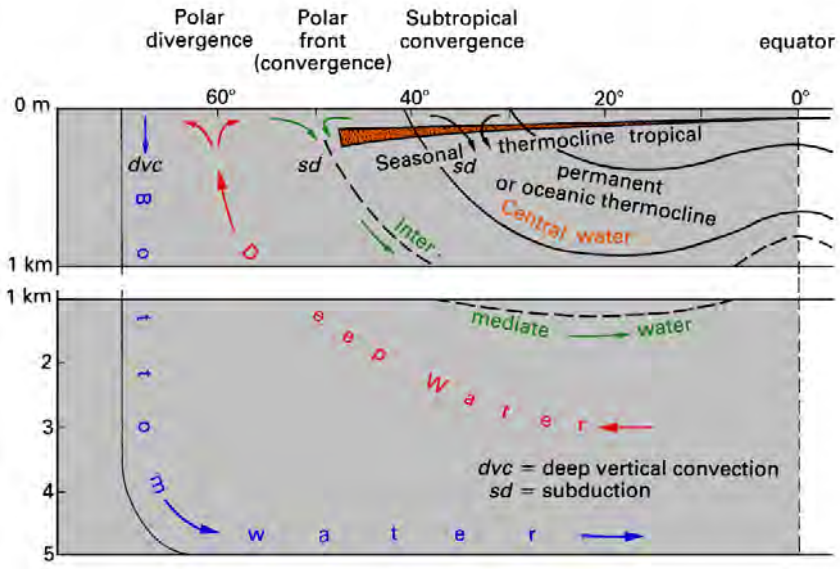

Figure 2.5.: Schematic diagram of the distribution of the major water masses. The position of the subtropical convergence zone is shown, as well as the depths of the permanent and seasonal thermoclines. Note the scale change below 1000 m. Reproduced from Tomczak and Godfrey (2003).

the upper layers, resulting in the Central Water mass known as North Atlantic Central Water (NACW). NACW is dominant above 600 m (Harvey, 1982), and is generally characterised by quasi-horizontal isotherms (10° - 12°C) and isohalines (35.405 - 35.650) (Arhan et al., 1994). There is some meridional variability in its composition, such that NACW may be further defined by its location of origin, either subtropical or subpolar.

The subtropical variety is subtropical Eastern North Atlantic Central Water ($ENACW_T$), whose temperature ranges between 13° and 15°C. $ENACW_T$ has been identified south of Iberia and is thought to originate at the frontal region near to the Azores (Fiúza and Halpern, 1982; Fiúza, 1984; Ríos, 1992), spreading with the general eastward flow towards Iberia. At the northern $ENACW_T$ limit, off Cape Finisterre (42.9°N), a sharp subsurface (∼200 m) water mass front separates the $ENACW_T$ from cooler, fresher, subpolar-originating $ENACW_P$ (11° - 13°C) to the north (Fraga et al., 1982). This front is sometimes referred to as the Galicia Front (Fiúza, 1984; Peliz and Fiúza, 1999). $ENACW_T$ and $ENACW_P$ are both transported northwards and southwards within the complex western Iberian system of coastal alongshore currents and counter-currents (Ríos, 1992; Álvarez-Salgado et al., 1993, 2003).

To the south of Cape Blanc (20.8°N), the major frontal region between NACW and South Central Atlantic Water (SACW) is known as the Cape Verde Frontal Zone (CVFZ) (Zenk et al., 1991; Arhan et al., 1994; Pastor et al., 2008), the front extends zonally across the Atlantic at ∼15°N (Lozier et al., 1995; Stramma and Schott, 1999). Between about 30°W and the African shelf, the front acquires a southwest-northeast orientation (Figure 2.1). SACW is cooler and fresher (10° - 16°C, 35.21 - 35.77) than NACW (Tomczak and Hughes, 1980), and is also richer in oxygen and nutrients. With SACW and NACW occupying the

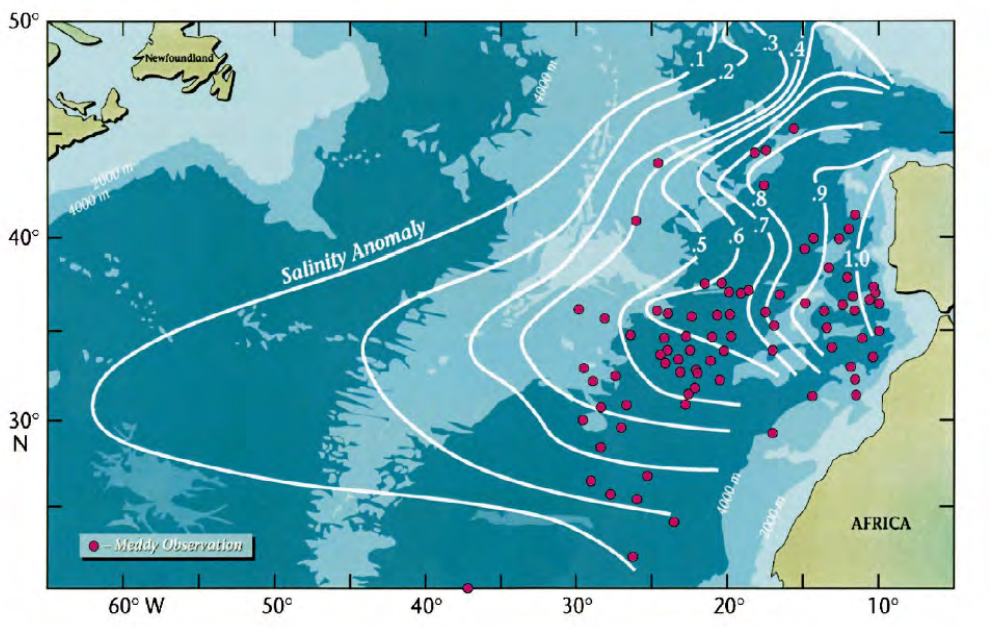

Figure 2.6.: Mediterranean Water salinity anomaly and summary of historical *Meddy* observations, reproduced from Richardson et al. (2000). Contours of the salinity anomaly are shown relative to 35.01 near a depth of 1100 m.

same density range, the CVFZ is density-compensated, resulting in a multitude of intrusions, filaments and lenses (Tomczak and Godfrey, 1994; Pastor et al., 2008).

2.4.2. Intermediate waters

Intermediate waters are generally formed at convergence zones at higher latitudes (Figure 2.5), and therefore tend to be cool and fresh. However the Canary Basin has an anomalous intermediate water mass which is the Mediterranean Water (MW). MW is formed in the Mediterranean Sea, where evaporation is high and freshwater input is low. Warm and salty MW leaves the Mediterranean Sea at the Strait of Gibraltar. As it descends the slope within the Gulf of Cadiz the turbulent plume entrains overlying NACW. At ∼1000 m the MW reaches a level of neutral density, whereupon it spreads out into the northeast Atlantic (Richardson et al., 2000). Figure 2.6 shows the extent of the resulting MW salinity anomaly.

Also shown in Figure 2.6 is a compilation of Mediterranean eddy (*Meddy*) observations. *Meddies* are coherent anticyclonic eddies which are generated along the Gulf of Cadiz and western Iberian slope at MW depths (i.e., 800 – 1400 m) (Bower et al., 1997), and hence contain MW. With diameters of 40 – 150 km and thicknesses of ∼600 m, *Meddies* spread out into the NEA where they make a significant contribution to the spreading of the MW salt tongue (Wang and Dewar, 2003).

Antarctic Intermediate Water (AAIW) is the more conventional intermediate water mass of the Canary Basin. After its formation in the Antarctica Polar Frontal Zone, AAIW enters the South Atlantic, and proceeds northward towards the North Atlantic at depths between

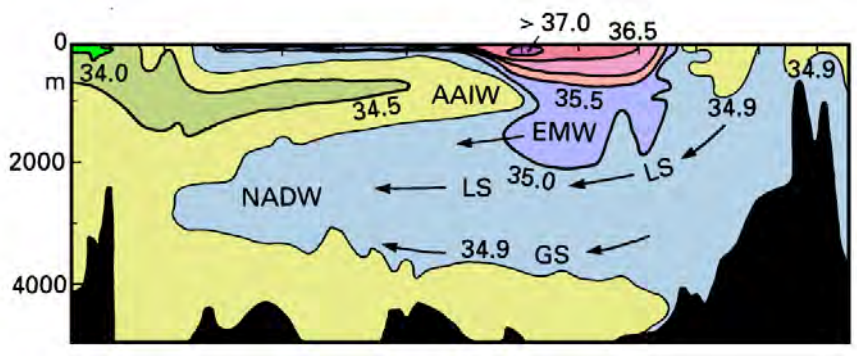

Figure 2.7.: Salinity along a meridional section (55°S - 65°N) in the western North Atlantic. EMW is Eurafrican Mediterranean Water. Reproduced from Tomczak and Godfrey (2003).

~600 - 1100 m (Suga and Talley, 1995). Figure 2.7 shows a vertical section of salinity in the western North Atlantic; the advancing AAIW tongue is visible at ~800 m, it encounters MW at ~20°N. There appear to be two pathways taken by AAIW into the Canary Basin, one is from the west via the Gulf Stream (see Section 2.5), the other is a northward penetration along the eastern boundary, i.e., northwest Africa (Machín and Pelegrí, 2009). The latter authors showed that the poleward extent of AAIW is maximum in autumn, when it may be observed north of Cape Ghir. AAIW is the most widespread intermediate water mass in the oceans.

2.4.3. Deep waters

North Atlantic Deep Water (NADW) is found below the MW and AAIW in the Canary Basin. NADW is formed by convective processes in the subpolar gyres in the Norwegian and Greenland Seas. It passes into the North Atlantic through deep channels in the submarine ridges that separate Scotland, Iceland, and Greenland. NADW is found throughout the Atlantic Ocean in the depth range ~2000 - 4500 m (McCartney, 1992; van Aken, 2000).

2.5. Principal currents

The Canary Basin is a complex region rich in dynamic activity over multiple scales (Arhan et al., 1994; Le Traon and De Mey, 1994; Reverdin et al., 2003; Weller et al., 2004; Machín et al., 2006a). The mean circulation is dominated by the components of the anticyclonic eastern subtropical gyre (ESG): The eastward-flowing Azores Current, its recirculation southward as the Canary Current, and a westward return flow as the North Equatorial Current (Figure 2.1) (Klein and Seidler, 1989; Mittelstaedt, 1991). The total transport of the ESG has been estimated to be ~12 Sv (Stramma, 1984; Siedler and Onken, 1996). Associated with the AzC is a convergent thermohaline frontal system, the Azores Front/Current system (AzFC; Juliano and Alves, 2007), that separates the ESG from the cyclonic subpolar gyre to the north (Figure 2.5). The inter-gyre region displays generally weak advection and is dominated by mesoscale activity. Off western Iberia, the Portugal Current system comprises

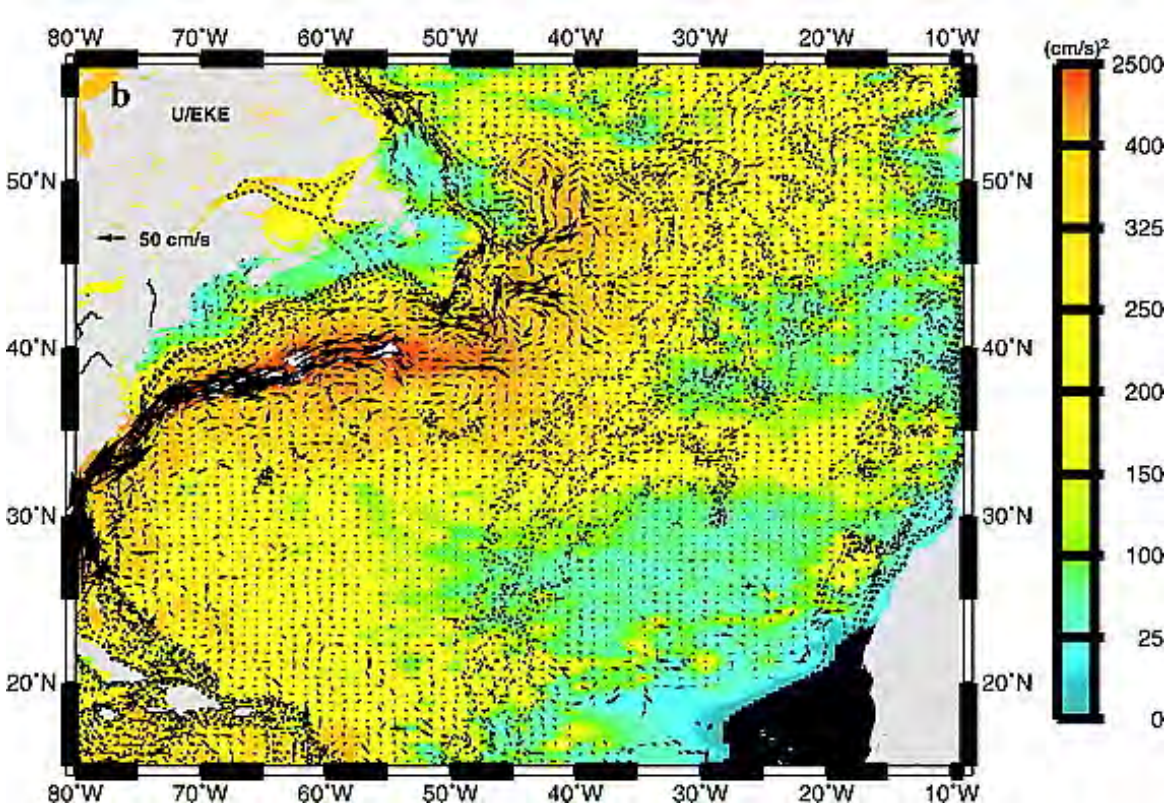

Figure 2.8.: Map of the mean surface currents and EKE in the North Atlantic, reproduced from the drifter study of Reverdin et al. (2003). Contours show the isobaths at 200, 1000, 2000, 3000, and 4000 m.

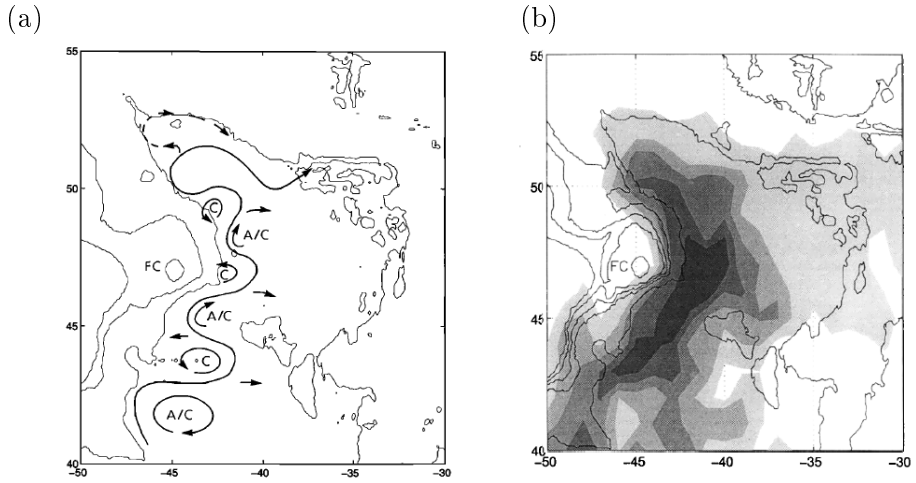

Figure 2.9.: (a) Schematic diagram illustrating the path of the North Atlantic Current and its associated meanders and recirculation cells. (b) Eddy kinetic energy from drifters at 50 - 100 m depth. Shading is in increments of 250 $cm^2\ s^{-2}$. The elevated EKE corresponds to the North Atlantic Current as it rounds the shallow Flemish Cap (FC). Bathymetry corresponds to the 200-, 2000-, and 4000-m isobaths. Reproduced from Rossby (1996).

a weak equatorward circulation that is bounded onshore by seasonal upwelling-related currents (Sena Martins et al., 2002; Peliz et al., 2005). Between its two zonal components (i.e., the AzC and NEC), the ESG has been characterised by an eastward shoaling of the thermocline and an equatorward broad, weak flow. At tropical latitudes below about 10°N, the characteristic feature is the eastward-flowing North Equatorial Counter-Current (NECC), the strength of which is highly seasonal (Stramma et al., 2003).

Figure 2.8 shows a map of the North Atlantic surface currents and of eddy kinetic energy (EKE), as determined from an analysis of a multi-year drifter dataset by Reverdin et al. (2003). Instabilities in the major currents are an important source of EKE. It is generally accepted that, away from the influence of topography, regions of high EKE correspond to the locations of energetic currents, such that EKE is considered to be a proxy for the paths of the major currents (Heywood et al., 1994; Reverdin et al., 2003). The ESG recirculation stands out in the EKE map: the meandering zonal AzC at ∼34°N, the eastern boundary CanC, with elevated EKE downstream of the Canary Islands, and the NEC extending westward between ∼20° - 25°N. The most striking feature in this figure is the energetic Gulf Stream (GS) in the west. At about 40°N, 55°W, the GS is known to bifurcate into two distinct systems, that of the North Atlantic Current to the north, and the AzC to the southeast. Although the bifurcation is not entirely clear in the drifter data of Figure 2.8, continuity towards the north and the southeast is evident. Both of these branches are thought to play a role in the structure and dynamics of the ESG (Schmitz and McCartney, 1993; Rossby, 1996).

2.5.1. The North Atlantic Current

The North Atlantic Current (NAC) is a well-defined western boundary current with a stable but meandering path (Rossby, 1996), which transports ∼42 Sv at 42°N (Kearns, 1996; Carr et al., 1997). Flowing north from about 40°N along the east side of the shallow Grand Banks and the Flemish Cap, it turns sharply to the east at ∼51°N and proceeds across the Atlantic. The current is well known for its crucial role in the transport of heat towards western Europe. The NAC is a baroclinic front, separating cold inshore waters from warmer (subtropical) offshore waters. During its passage northwards, the NAC exhibits a series of large but non-propagating meanders, indicating generation by prominent topographic features (i.e., the Grand Banks and the Flemish Cap) (Kearns and Paldor, 2000). This path is shown schematically in Figure 2.9a. As a result of instabilities of the meanders, or of their growth or decay, there is an exchange of mass between the current and the surrounding waters. Float trajectories have indicated that the bulk of this "loss" of fluid is eastward (Rossby, 1996). In Figure 2.9a, zonally orientated arrows indicate probable pathways of loss to the surrounding waters[2].

Figure 2.9b shows the EKE associated with the NAC as it passes northward around the Flemish Cap. The EKE in this region west of the MAR shows a sharp negative gradient towards the east, away from the NAC. Rossby (1996) explains this drop in the EKE to be a result of the loss of fluid from the NAC: the expelled water parcels decelerate rapidly as they move eastwards into more quiescent waters. These waters, as eddies, streamers, or pools of water, become part of a large-scale eastward drift of subtropical water, a portion of which is thought to diffuse into the ESG (Klein and Seidler, 1989; Krauss et al., 1990; Rossby, 1996), contributing to the formation of the shallow but well-defined AzFC.

2.5.2. The Azores Current

The zonal AzC, whose origin is a southeastward branching of the Gulf Stream, is a permanent feature located between ∼33° - 35°N that crosses the MAR and flows towards the Gulf of Cadiz. Juliano and Alves (2007) identify a quasi-permanent cyclonic meander at ∼35°N, 47.5°W as the link between the current and its GS source. The current's mean transport is estimated to be in the range ∼10 - 12 Sv (Gould, 1985; Stramma and Muller, 1989). The AzC is deep, up to 1000 m, typically ∼250 km wide, with a jet-like meandering character (Siedler et al., 1985; Le Traon and De Mey, 1994; Juliano and Alves, 2007). Mean speeds determined from a drifter analysis in the Canary Basin by Zhou et al. (2000) are ∼0.10 - 0.15 m s^{-1}. Along its length, the AzC has been reported to have a number of southward-turning branches, so that only ∼4.5 Sv reach the Gulf of Cadiz (Klein and Seidler, 1989; Paillet and Mercier, 1997). Pelegrí et al. (2005b) suggest that only the last of these branches, east of the Madeira plateau (∼17°W), should be considered to have a permanent position (see also Zhou et al., 2000). Observations of branching made further to the west are most likely

[2] The eastward flow pathways are an important component of the boundary forcing of the large model domain presented in Chapter 4, where the open western boundary at ∼42°N traverses the zonal pathways.

to be related to the unstable nature of the current. North and south of the AzC there is evidence for a westward-flowing Azores Counter-Current (AzCC) (Onken, 1993; Le Traon and De Mey, 1994; Cromwell et al., 1996; Alves and Colin de Verdière, 1999; Juliano and Alves, 2007).

Stramma and Siedler (1988) reported a ∼2° northward shift of the AzC zonal axis in summer (see Figure 2.10), however other authors have not found evidence for this seasonal variation in the position of the AzC (Le Traon and De Mey, 1994; Cromwell et al., 1996). Le Traon and De Mey (1994), analysing altimeter data, found the current to be more coherent and penetrate further eastward in summer than in winter.

The western part of the convergent AzFC frontal system that is associated with the AzC separates 18°C and 13°C subtropical Mode Waters (Pollard et al., 1996). Käse et al. (1985) reported temperature and salinity steps east of the Azores of order 2°C and 0.3, respectively, across the front. In the vertical, the front contains NACW overlying MW (Harvey and Arhan, 1988). The convoluted path of the front has been attributed to quasi-stationary *Rossby* waves originating at the eastern boundary of the Canary Basin (Le Traon and De Mey, 1994), and also to baroclinic instability of the jet (Alves and Colin de Verdière, 1999). Cyclonic (anticyclonic) meanders typically form to the north (south) of the current's main axis. Mesoscale eddies have been observed on both sides of the front with typical scales of 200 km. The eddies, and the meandering of the front, lead to high variability in the path of the current and, consequently, its high EKE signal as seen in Figure 2.8. Zhou et al. (2000) observed the EKE to be highest on the southern flank of the current.

The AzC was initially thought to be wind-forced (Käse and Krauss, 1996), but there is growing evidence that its dynamics are related to entrainment processes in the Gulf of Cadiz (Jia, 2000; Peliz et al., 2007; Kida et al., 2008). Model simulations with and without MW characteristics in the Gulf of Cadiz[3] show clearly that the AzC is weak or absent without MW. However, wind forcing does appear to play a complementary role as shown by Townsend et al. (2000). A series of numerical experiments in the North Atlantic (without MW), forced at the surface using different wind products, showed that AzC-like circulation may develop depending on the quality of the applied wind data.

2.5.3. The Canary Current

The Canary Current constitutes the eastern boundary current of the ESG, which flows towards the equator parallel to the northwest African coast. Its mean transport of pure NACW is about 3 Sv southward, with an additional ∼1 Sv associated with the coastal upwelling (Machín et al., 2006a). The current has been generally viewed as a broad weak flow, driven by the wind, which spans the transition zone between the open ocean and the coastal region, where wind-driven upwelling takes place for much of the year. The CanC is described as feeding the AzC, which branches southward as it passes north of Madeira at ∼17°W . After traversing the Canary Island archipelago, the main flow of the CanC

[3] MediterraneanWater can be introduced into a model domain by either opening the Strait of Gibraltar, or by restoring water over the Gulf of Cadiz slope towards climatological MW tracer values.

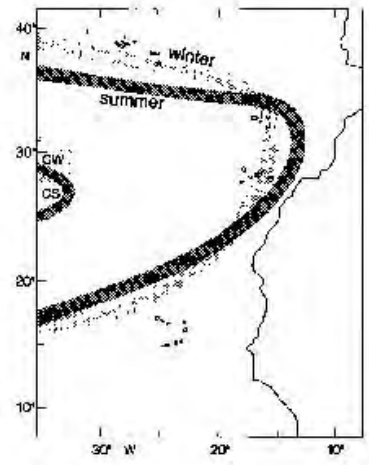

Figure 2.10.: Stramma and Siedler (1988)'s schematic representation of the eastern subtropical gyre (ESG) in summer and winter in the top 200 m of the ocean.

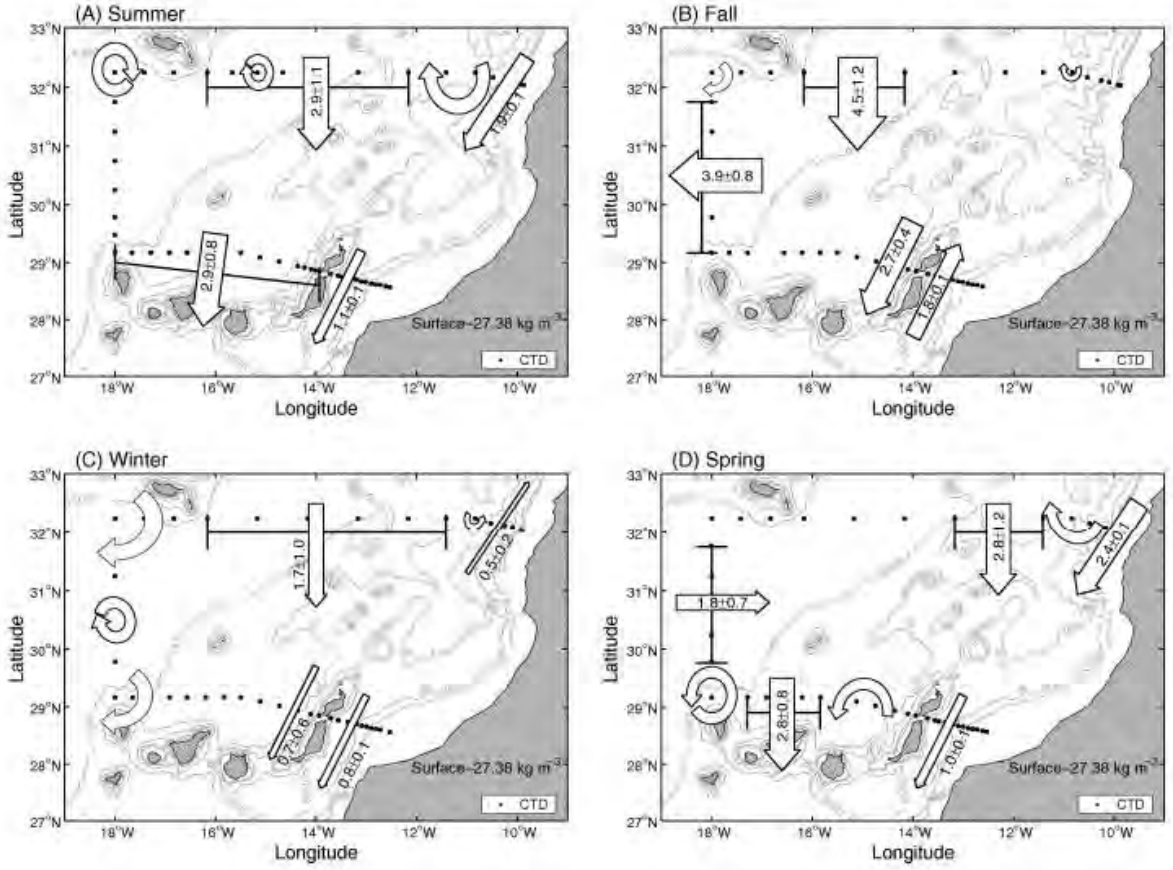

Figure 2.11.: Schematics of the seasonal Canary Current transport reproduced from Machín et al. (2006a). Arrow width is proportional to mass transport (Sv). Curved arrows (without transport figures) are suggestive of mesoscale structures.

continues southward until it separates away from coast near to Cape Blanc to join the North Equatorial Current (NEC) (Stramma, 1984).

Recent studies indicate that the above general description of the CanC omits considerable variability, even at seasonal timescales. Stramma and Siedler (1988), analysing the geostrophic flow field using historical data, related the seasonal displacement of the CanC to that of the ESG. Figure 2.10 shows that in winter they observed the CanC far offshore, near to Madeira, while in summer the CanC occupied a more central position between Madeira and the African coast. Zhou et al. (2000) found that drifters in the CanC tended to occupy a narrow band, rather than the broad swath predicted from climatological datasets. These depictions are in agreement with seasonal meridional geostrophic velocity sections presented by Machín et al. (2006a) where, for example, in summer 1998 the CanC was seen as an intense ∼800-m deep current centred at about 14°W (Figure 2.11).

The CanC, therefore, has a concentrated flow structure with a well-defined but seasonally-variable position. Furthermore, its behaviour appears to be strongly linked to the coastal upwelling: Pelegrí et al. (2005a) stress the close interconnectivity between the coastal upwelling region and the open ocean (to be discussed in Section 2.6 below). Yet, because observations of the region are still relatively sparse, a definitive description of the path and seasonal variability of the CanC remains elusive.

2.5.4. The North Equatorial Current and Counter-Current

The North Equatorial Current defines the southern dynamic boundary of the ESG, and is the northernmost current of the complex equatorial Atlantic current system (Stramma and Schott, 1999; Stramma et al., 2003). The NEC is a broad, wind-driven, surface current that flows westward across the North Atlantic, taking a path north of the Cape Verde Frontal Zone (Stramma and Muller, 1989; Section 2.4). Stramma et al. (2005) observed the NEC to be composed of several distinct bands rather than a single main flow (Figure 2.12), with the depth of each band increasing from south to north. Figure 2.13 shows accumulated mass transports associated with the NEC between 20° - 24°N along the western section of a box cruise (Hernández-Guerra et al., 2005). Banding of the current is evident. The average transport of the NEC is about 5 Sv (Fiekas et al., 1992; Hernández-Guerra et al., 2005). The NEC is supplied by the CanC, transporting a mixture of NACW and SACW, the latter being advected northward across the CVFZ (Arhan et al., 1994). Stramma and Siedler (1988) described seasonal variations in the position of the NEC. In autumn the current was found further to the north than in spring, likely a result of the northward shift of the ITCZ (Molinari et al., 1986; Waliser and Gautier, 1993).

The eastward-flowing North Equatorial Counter-Current is part of the equatorial current system that forms the southern part of a tropical cyclonic gyre (Figure 2.12). The NECC lies between ∼3° - 10°N, and has maximum velocities in autumn, when the ITCZ is located at its northernmost position. Stramma et al. (2005) reported a transport of 11.5 Sv in October/November 2002. The NECC weakens, or even reverses to westward flow in the

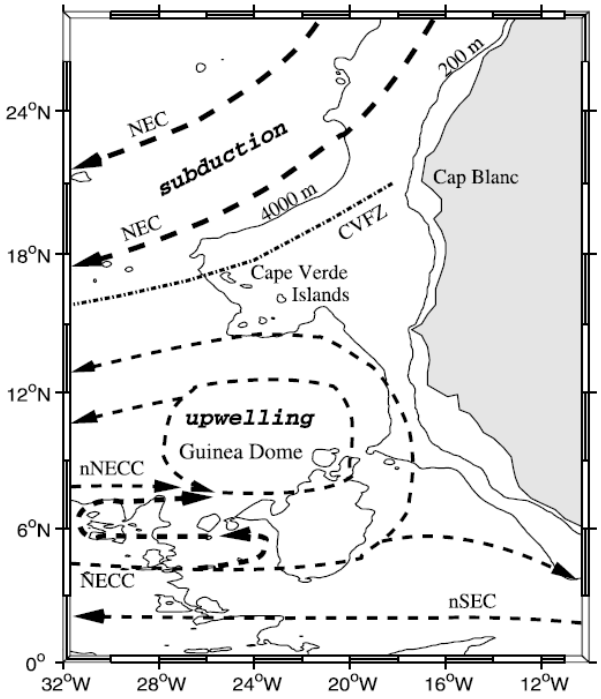

Figure 2.12.: Map of the North Equatorial Current (NEC) and North Equatorial Counter-Current (NECC) off west Africa. Also shown is the Guinea Dome south of the Cape Verde islands. Reproduced from Stramma et al. (2005).

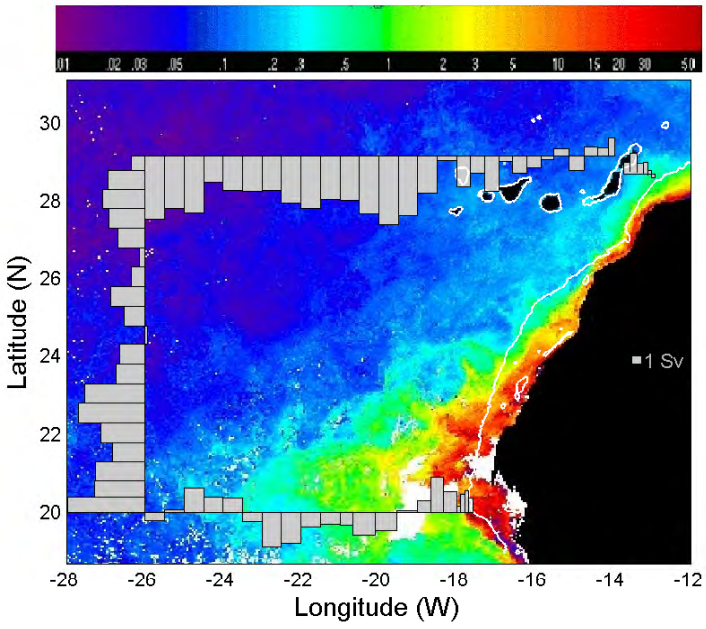

Figure 2.13.: Surface-layer accumulated mass transports south of the Canary Islands from the inverse model study of Hernández-Guerra et al. (2005). Also shown are mean phytoplankton pigment concentrations (mg m^{-3}) from the SeaWiFS ocean colour sensor (McClain et al., 1998) for September 2003. The white line demarks the 200-m isobath. Reproduced from Hernández-Guerra et al. (2005).

western tropical Atlantic, in spring (Lumpkin and Garzoli, 2005). As it approaches the African landmass, the NECC splits, with a portion turning northward along the coast as the Mauritania Current (MC) and the remainder continuing eastwards as the Guinea Current (Lázaro et al., 2005). The northward recirculation is a component of the Guinea Dome, a permanent quasi-stationary cyclonic feature that lies south of the Cape Verde islands, bordered by the NEC and NECC. The Guinea Dome is a region of strong upwelling, and shows some seasonal variability (Lázaro et al., 2005). The MC flows polewards towards the CVFZ, transporting SACW which mixes with the NACW of the NEC.

Stramma et al. (2005) noted the significant presence of eddy-like features in the NEC and NECC. These eddies are likely to enhance the exchange of water between the subtropical and tropical gyres.

2.6. The Canary Upwelling System

The Canary Upwelling System (CUS), which includes the Iberian upwelling to the north, is one of the four major eastern boundary upwelling systems (EBUS) of the world ocean (Carr and Kearns, 2003), and it supports an economically-important fishing industry (Arístegui et al., 2006). Sustained nutrient input to the surface waters by vertical circulation associated with *Ekman* dynamics, leads to the characteristically high primary production found in upwelling ecosystems. Carr (2002) defines the *active zone* of an upwelling system to be the area where chlorophyll concentrations exceed a threshold value equal to 1 mg m^{-3}. The CUS has the largest active zone of all the EBUS.

The Canary upwelling is maintained by the northeasterly Trade winds (Section 2.3.1). Between Cape Blanc and the Strait of Gibraltar the upwelling is active throughout the year, although it is less intense north of the Canary Island archipelago. In summer, the influence of the Trades extends northwards to the western Iberian Peninsula and, in winter, southwards to Cape Verde (Wooster et al., 1976; Mittelstaedt, 1991; Van Camp et al., 1991; Nykjær and Van Camp, 1994). Subsurface NACW is brought up along the coast into the photic zone, following Ekman (1905)'s classical exposition of the setting up of a vertical cell in response to alongshore winds, coupled with the development of an alongshore jet. In the CUS, Pelegrí et al. (2006) maintain that the coastal jet be considered as an eastern branch of the CanC, the Canary Upwelling Current (CanUC).

The CanUC displays marked seasonality along its length, which is a result of both spatial and temporal variability in the wind stress. The CanUC appears to originate between the Strait of Gibraltar and Cape Ghir, where several studies have shown the existence of an inflow of NACW (∼1 - 2 Sv) from the open ocean towards the coastal region (Stramma, 1984; Lozier et al., 1995; Pelegrí et al., 2005a; Machín et al., 2006b). This water flows equatorwards as the CanUC, as shown schematically in Figure 2.14. In winter, the inflow to the coastal region is nearly zonal and recirculates south within a narrow band along the coast. In summer, the flow intensifies but recirculates over a wider region (Machín et al., 2006b). Near to Cape Ghir, whilst in summer the CanUC continues its southward journey

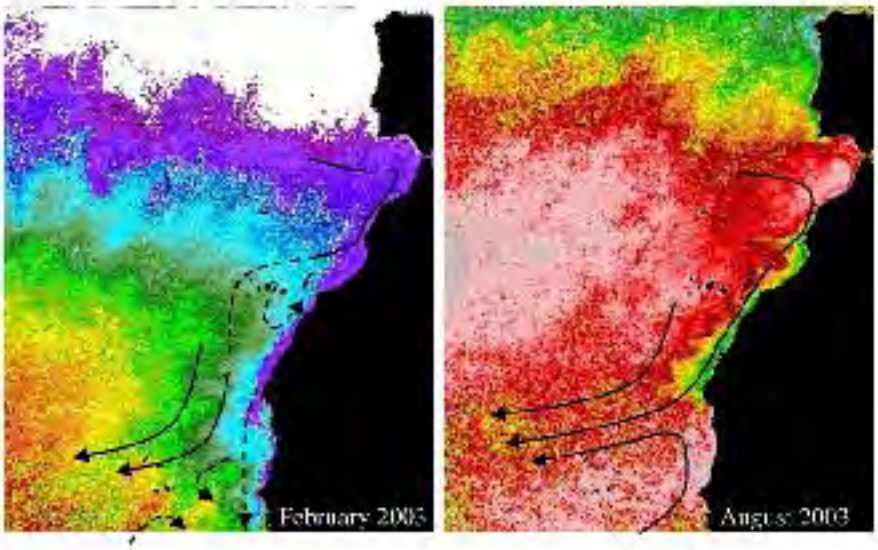

Figure 2.14.: Monthly mean SST for the eastern subtropical gyre in (left) winter and (right) summer 2003. Schematic flow patterns of the CanC and CanUC are superimposed. Solid lines indicate well-determined flow paths, while dashed lines suggest possible connections. Reproduced from Pelegrí et al. (2006) (colour-bar not available).

adjacent to the coastline, in winter it appears to make a large offshore detour at ∼30°N to merge with the CanC. A cyclonic recirculation develops that loops around the Canary Islands, its return path implying a reversal of the coastal flow inshore of the Canary Islands (Pelegrí et al., 2005a). Whilst autumn flow reversals are indeed a robust feature of the inner coastal flow at the latitude of the Canary Islands (Hernández-Guerra et al., 2002; Knoll et al., 2002; Machín et al., 2006a), that have been attributed to relaxation of the upwelling, details of the extent and structure of the winter cyclonic loop between the archipelago and Cape Ghir are unclear.

The CUS contains the typical mesoscale features that are associated with EBUS. Cool nutrient-rich upwelled waters at the coast interact with the CanC, producing highly-variable fronts, eddies and zonal filaments. The quasi-permanent filaments at Capes Ghir and Blanc (Pelegrí et al., 2005b), both of which extend hundreds of kilometres offshore, are the most notable examples. The Cape Ghir filament may be clearly seen in satellite SST images of the region (Figure 2.14) (Van Camp et al., 1991; Pelegrí et al., 2005b). Other major filaments include those frequently seen between Capes Bojador and Juby (Barton et al., 1998), which are associated with the transport of organic material to the eastern Canary Islands (Bécognee et al., 2006; Moyano et al., 2009). Indeed, the downstream lee region of the Canary Islands is where the greatest variability exists in the CUS (see the EKE in Figure 2.8). Complex interactions between island-generated eddies, upwelling fronts and filaments are frequently observed (Arístegui et al., 1994; Barton et al., 1998; Basterretxea et al., 2002; Barton et al., 2004; Sangrà et al., 2009).

At its southern limit, the CanUC converges with SACW in the region of the CVFZ. In summer and autumn, when the MC penetrates north to Cape Blanc, intense convergence

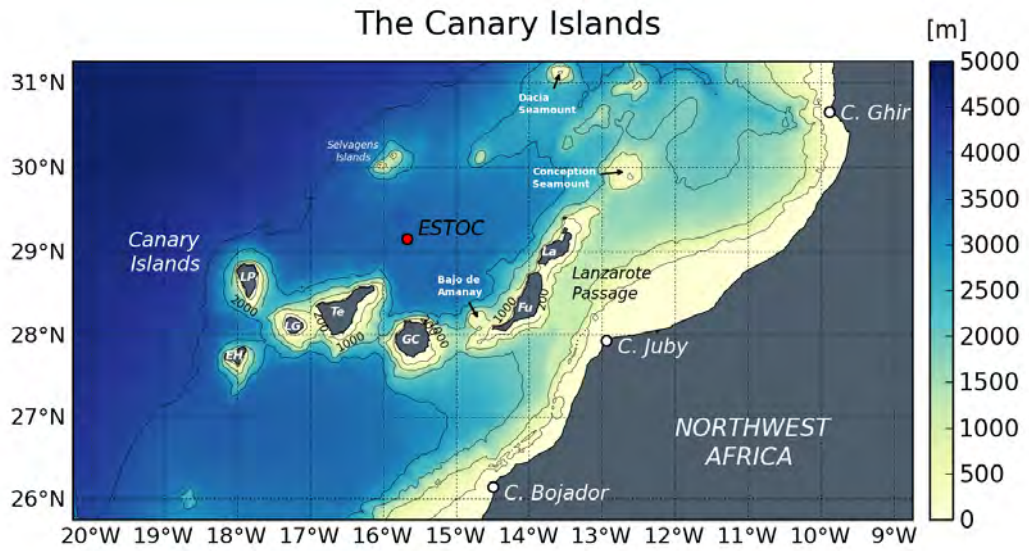

Figure 2.15.: The Canary Island archipelago. LP - La Palma; EH - El Hierro; LG - La Gomera; Te - Tenerife; GC - Gran Canaria; Fu - Fuerteventura; La - Lanzarote. The ESTOC mooring is shown north of Gran Canaria. Contours in black mark isobaths at 200, 1000, 2000, 3000, 4000 m. Topographic data from GEBCO (Hunter and Macnab, 2003).

(between NACW and SACW) and offshore export occurs. In winter and early spring, as upwelling reaches further south towards Cape Verde (Figure 2.14), convergence and offshore transport are reduced but still present (Pelegrí et al., 2006). The offshore export includes a high nutrient load, hence the elevated phytoplankton concentrations commonly seen offshore of Cape Blanc, such as in Figure 2.13. The filament-like structure associated with the convergence zone, known as the Cape Blanc giant filament, has a persistent low-temperature high-chlorophyll signature that extends several hundred kilometres offshore (Gabric et al., 1993).

Associated with the upwelling circulation is a poleward undercurrent that follows the northwest African shelf at a depth of about 300 m (Barton, 1989). The undercurrent transports SACW northwards, a portion of which penetrates beyond the CVFZ at Cape Blanc. An undercurrent is also observed off western Iberia, but the nature of any continuity between the northwest African and Iberian regimes is uncertain, owing to the outflowing MW at Gibraltar (Barton, 1998; Hagen, 2005).

2.7. The Canary Island archipelago

The Canary Island archipelago is a grouping of seven islands and several islets that form a zonal chain situated off northwest Africa (Figure 2.15). The islands lie between about 27.5° and 30°N, level with the southern portion of the large embayment that separates Cape Juby and Cape Ghir, and have an east-west extent of ∼500 km. Although just 95 km separates Fuerteventura from the African landmass, the channel reaches depths greater than 1000 m.

All of the islands, bar Lanzarote and Fuerteventura, are mountainous and have peaks that exceed 1000 m. The islands, which are thought to lie on oceanic crust (Roest et al., 1992), form part of a 3000-km long belt of islands and seamounts which have been volcanically active for >16 Ma, and extend from approximately 37°N (Madeira-Tore Rise) to as far south as 15°N (Cape Verde Islands). The highest density of islands and seamounts is found between latitudes 20° and 35°N, which include the Canary and Madeira archipelagos. The seven islands show a generally westward age progression, the oldest being Lanzarote and Fuerteventura (>35 Ma) and the youngest La Palma (2 Ma) and El Hierro (<1 Ma).

The Canary Island archipelago is a major topographic feature which lies directly in the path of the Canary Current and the Canary Upwelling Current, thereby straddling the transition zone between coastal and oceanic waters (Barton et al., 1998; Pelegrí et al., 2005a).

2.7.1. Topography

The Canary Island topography is shown in Figure 2.15. The islands lie upon a ∼2500-m-deep plateau which protrudes westward away from the continental boundary. The sides of the plateau are steep, and deeper waters of over 3500 m are quickly reached to the north, south and west. The islands, rising above the plateau to the surface, constitute an abrupt barrier to the oncoming CanC, which must pass through the deep channels that separate them.

There are four main passages that divide the islands. The so-called Lanzarote Passage is the easternmost, lying between the islands of Lanzarote and Fuerteventura and the African coast. Here the seafloor shoals gently towards the continent. Two secondary, relatively shallow, passages separate Tenerife and La Gomera, and Fuerteventura and Lanzarote, respectively. The islands are characterised by narrow shelves and steep topography.

Other regional bathymetric features of interest are the Selvagen Islands, and the presence of a number of offshore seamounts. The two small Selvagen Islands lie in deep water ∼200 km north of Tenerife, roughly midway between Madeira and the Canary Islands. They occupy a land area of just 2.73 km^2. Conception Seamount lies ∼120 km to the northeast of Lanzarote, and Dacia Seamount is found ∼130 km to the northwest of Conception. Both seamounts rise to within less than 100 m of the surface. Several smaller seamounts are found between the two. It should be noted that these features are located upstream of the Canary Islands, and thus they may be expected to perturb the CanC north of the archipelago. About 8 km to the northwest of the southern tip of Fuerteventura is a smaller seamount, Bajo de Amanay, which rises to within ∼25 m of the surface.

2.7.2. Atmospheric circulation and forcing

Tall oceanic islands modify not only the oceanic flow, but also the atmospheric flow. As the Trades impinge upon the Canary Islands in spring and summer, they are capped by a strong atmospheric temperature inversion between ∼400 and 1000 m above the surface of the ocean (Naya, 1984). Gran Canaria, Tenerife and La Palma are steep-sided and extend above the low-lying inversion. On the northern slopes of these islands, the ascending wind often forms

(a) (b)

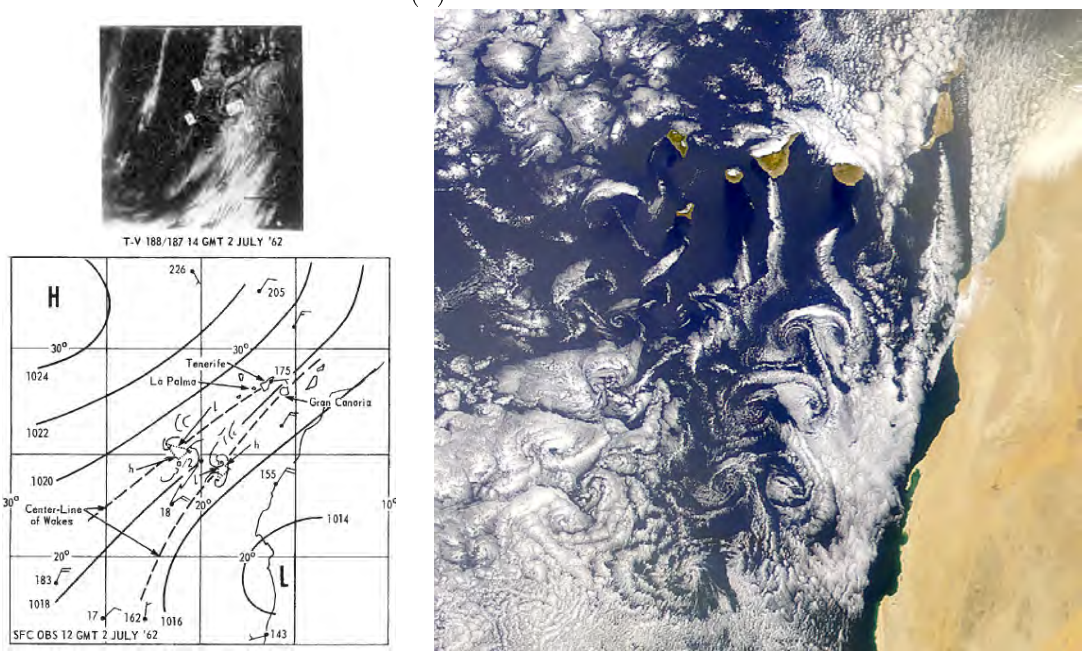

Figure 2.16.: Complex atmospheric eddy patterns downstream of the Canary Islands. (a) Schematic diagram and photo from the *Tiros-V* weather satellite on 2 July 1962, reproduced from Chopra and Hubert (1964). (b) Canary Island atmospheric vortex patterns observed from the MODIS sensor aboard the *Terra* satellite on 4 June 2000.

a layer of stratocumulus at the base of the inversion. This stable inversion layer forms a barrier to further convection, so that the air is forced around the island flanks. Extensive cloud rarely forms at the leeward coasts because of subsidence down the lee slopes.

Observations of a persistent atmospheric wake at Gran Canaria were reported long before those of the oceanic wake (Chopra and Hubert, 1964, 1965a,b; La Violette, 1974). Figure 2.16a shows a photograph presented by Chopra and Hubert (1964) from the *Tiros-V* weather satellite taken over the Canary Islands in July 1962: a trail of atmospheric vortices extends several hundred kilometres downstream from Gran Canaria. The eddies, whose characteristic properties were described by Hubert and Krueger (1962), are visible in the stratocumulus clouds lying beneath the temperature inversion. The authors remarked upon the resemblance between these vortices and the *Von Karman* vortex street pattern observed in laboratory experiments. A vortex trail downstream of the neighbouring island of Tenerife is also discussed. A more recent image showing the same phenomena is seen in Figure 2.16b. Von-Karman-type vortices originating at Gran Canaria are clearly seen. From Fuerteventura, a standing eddy extends southward towards Cape Bojador. Wake effects are also visible downstream of Tenerife and the western islands. Periodic fluctuations in atmospheric pressure observed at Tenerife have been shown to correspond to such eddy shedding events (Wilkins, 1968; Zimmerman, 1969). See Chopra (1973) for a comprehensive review of the above-mentioned articles.

Figure 2.17 shows the seasonal cycle of the wind stress curl and wind speed over the Ca-

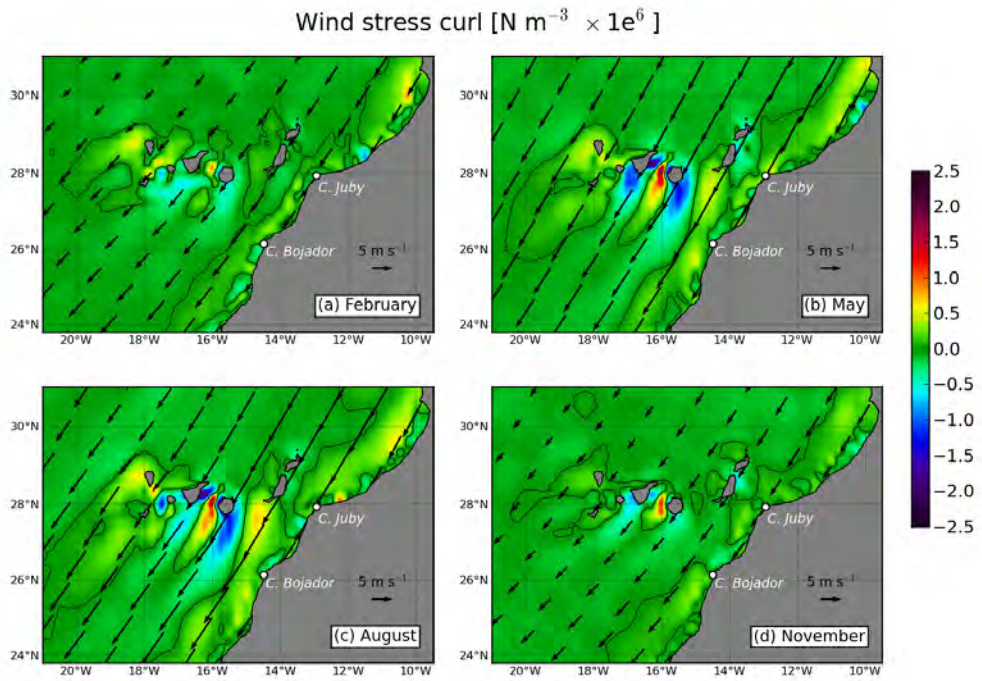

Figure 2.17.: Monthly averages of the normalised wind stress curl from the QuikSCAT-derived SCOW wind stress climatology of Risien and Chelton (2008) at the Canary Islands. The zero curl contour is shown in black. Vectors in black give the 10-m wind speed and direction.

nary Islands, the data are taken from the SCOW climatology of Risien and Chelton (2008). Averages for the months of February, May, August and November are shown[4]. The persistence of the upwelling-favourable Trades is evident. They reach their peak intensity between March and September, when the Azores High approaches its northernmost limits (Wooster et al., 1976; Nykjær and Van Camp, 1994). The maximum monthly mean windspeed in the SCOW data occurs in August (12.3 m s^{-1}), at a location to the east of Gran Canaria. This is higher than the 8.7 m s^{-1} mean given by Pelegrí et al. (2005a). The minimum windspeed is in February (1.4 m s^{-1}) at a location far offshore.

The curl fields of Figure 2.17 illustrate the constriction of the wind as it passes through the inter-island gaps at the Canary Islands. When the mean wind is sufficiently intense, jets are formed within the gaps. When viewing the flanks of these jets from upwind, the curl is alternately positive (right) and negative (left). Between the jets, in the lee of each island, is the island wind shadow zone where the winds are weak. The effect of the wind jets on the ocean is to induce rapid variations in *Ekman* transport, strong upwelling and downwelling, and the spin-up of mesoscale eddies (Basterretxea et al., 2002; Chavanne et al., 2002). Wind jet patterns and wind shadows are also seen at the Cape Verde islands and at Madeira.

[4] All of the model runs in this thesis are forced with monthly averages of the wind stress, bar the MM5 runs of Chapter 5.

2.7.3. Canary Island currents and variability

The seasonal variability of the Canary Current north of the Canary Islands was discussed in Section 2.5.3. The importance of recent work on the CanC, and also the Canary Upwelling Current, was emphasised. However, the theories expounded are incomplete and require extensive further investigation, not least because, at the Canary Islands, the path and variability of these currents has direct relevance, owing to their role as the incident flow at the archipelago (Sangrà, 1995).

Early views of the region hinted at a steady equatorward-flowing CanC impinging upon the the islands and continuing southwards (Stramma, 1984; Stramma and Siedler, 1988). These studies were hampered by low resolution, so that flow disturbance associated with the islands was unresolved. However, the seasonal picture as determined by Stramma and Siedler (1988) (see Figure 2.10), where the large-scale structure was associated with variability in the ESG, has been confirmed (Barton et al., 1998; Navarro-Pérez and Barton, 2001). Using sea level data from tide gauges located on the western islands (La Palma and Tenerife) and on the eastern islands (Tenerife and Lanzarote), Navarro-Pérez and Barton (2001) calculated meridional geostrophic velocities and found the strongest flow to be nearer to the African coast in summer, while in winter it is stronger further offshore, consistent with the advance and retreat of the ESG. The mean flow in the surface layers around the archipelago is weak ($\sim$0.02 m s^{-1}), so that the instantaneous flow is typically dominated by larger-amplitude mesoscale variability. Navarro-Pérez and Barton (2001) further showed that, in the west, there was a tendency for southward (northward) flow in winter (summer), while in the east, the mean flow was southward all year (note that this eastern flow is west of the Lanzarote Passage, where northward flow does occur in autumn).

Several authors have made mention of a meandering cyclonic flow *around* the archipelago (Mittelstaedt, 1991; Navarro-Pérez and Barton, 2001). Navarro-Pérez and Barton (2001) speculated that this flow could be topographically steered, as it appeared to follow the depth contours of the plateau upon which the islands lie. But they pointed out that the channels separating the islands are deep ($\sim$2000 m), and so should have little influence on the currents, which are weak below $\sim$500 m. There is evidence for variable flow between the islands, i.e., through the channels, although this has been better studied at the eastern channels (Hernández-Guerra et al., 2002; Knoll et al., 2002). Hernández-Guerra et al. (2002), from bimonthly XBT profiles obtained between November 1996 and September 1998, found almost identical southward geostrophic transports of $\sim$1 Sv between Gran Canaria and Fuerteventura, and Fuerteventura and Africa. At Fuerteventura - Africa, transport was southward apart from in November 1996 and 1997. Knoll et al. (2002) reported mean southward current speeds of $\sim$0.05 m s^{-1} from current meters in the upper 200 m of the Lanzarote Passage during 1997 and 1998, and also observed an autumn reversal to northward flow. Hernández-Guerra et al. (2002) suggested that the reversal was associated with the surfacing of the poleward undercurrent. In the Gran Canaria - Fuerteventura sections, anomalous northward transport occurred in May of both years.

At interannual timescales, whilst the mean flow across the archipelago as a whole has been found to be southward with speeds of up to 0.05 m s^{-1}, there can be substantial periods of flow reversal, i.e., against the sense of the gyre (Navarro-Pérez and Barton, 2001; Barton et al., 2004). Navarro-Pérez and Barton (2001) calculated geostrophic velocities from ∼20-year time-series of sea surface height obtained from tide gauge stations located at opposite extremes of the archipelago (La Palma and Lanzarote). They found several periods of northward flow, with magnitudes of up to 0.04 m s^{-1} and typical durations of a few months.

The studies cited in this section hint at considerable mesoscale variability occurring in and around the Canary Island archipelago. However, owing to the complexity of the circulation and topography, continuing sparseness of observations, and uncertainty about the character of the incoming CanC flow, relatively little is known about circulation in and around the Canary Islands.

2.7.4. Canary Island wake

The flow of the CanC through the Canary Island archipelago favours the generation of mesoscale eddies, a significant further contributor to the upwelling-induced variability of the region (Figure 2.18) (Barton et al., 2004). Eddies are mostly observed downstream of the islands (La Violette, 1974; Hernández-Guerra et al., 1993; Arístegui et al., 1994, 1997; Barton et al., 2004; Sangrà et al., 2005, 2007; Piedeleu et al., 2009), but have also been sampled within the channels (Molina et al., 1996; Knoll et al., 2002) and north of the islands (Hernández-Guerra et al., 2005).

The earlier studies cited above used remote sensing methods to detect SST anomalies associated with mesoscale eddies downstream of the Canary Islands. Arístegui et al. (1994) presented the first *in situ* measurements, using data collected southwest of Gran Canaria. One anticyclonic (warm core) and three cyclonic (cold core) eddies were sampled, using both AXBTs (Airborne Expendable Bathy-Thermograph) and CTDs (Conductivity-Temperature-Depth sensor). The eddies had diameters of 40 - 60 km, which scales with the 50-km diameter of Gran Canaria, and depths of up to 265 m. Arístegui et al. (1997) described interactions between the island-generated eddies and filaments extending offshore from the coast.

Navarro-Pérez and Barton (1998) gave an account of a large (100-km diameter) cyclonic eddy situated southwest of the sill between Fuerteventura and the African coast. They suggest that it is topographically generated, cyclonic vorticity being produced through vortex stretching as the mean flow encounters deeper water. SST imagery presented by La Violette (1974) and Barton et al. (1998) supports the suggestion that this eddy is a recurrent feature. Knoll et al. (2002) recorded large horizontal shears in the upper 300 m of the Lanzarote Passage, remarking that this is sometimes caused by eddies in this area. Molina et al. (1996) observed a cyclonic eddy between Tenerife and La Gomera, which they suggested had a permanent presence.

Gran Canaria eddies have been tracked using drogued buoys (Sangrà et al., 2005, 2007). The buoy trajectories indicate that both cyclones and anticyclones are long-lived coherent

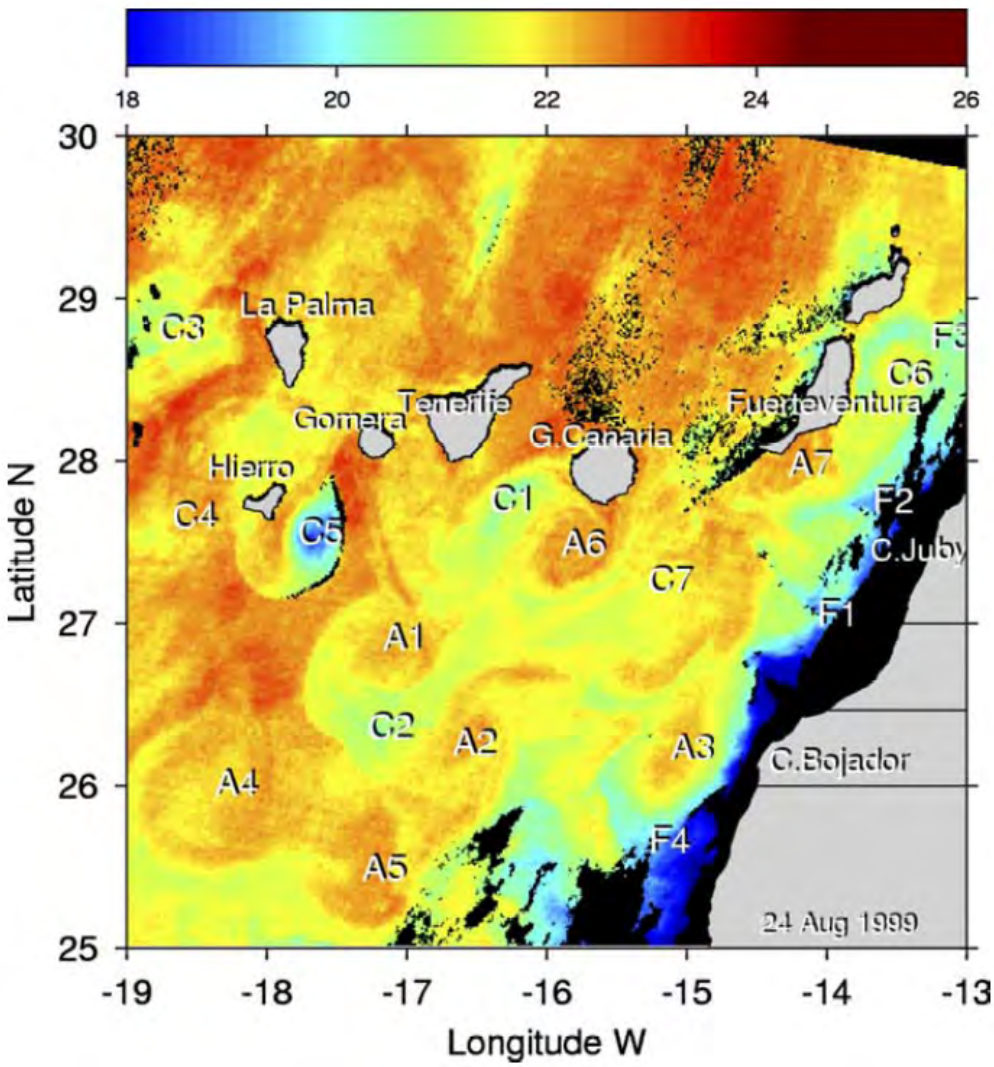

Figure 2.18.: AVHRR sea surface temperature (°C) image of the Canary Island wake on 24 August 1999, reproduced from Barton et al. (2004). Eddy (C - cyclonic, A - anticyclonic) and filament (F) locations are indicated. Colour-bar not available.

structures that may last for several months. Sangrà et al. (2009) describe how these eddies contribute to a zonal eddy corridor that extends towards the MAR at around 26°N. The Canary Eddy Corridor (CEC) conveys carbon and organic matter to the oligotrophic ocean interior.

2.8. Open questions

During the course of this review of the physical oceanography of the Canary Basin a number of open questions and issues have arisen, some that are in the literature, and some that have occurred to me. These are now summarised:

- The Azores Current is said to "feed" the Canary Current. Does this mean that there is a dynamic link between the two currents? In the context of developing a model configuration for the Canary Islands, this is an important question because, without this knowledge, inclusion of a realistic Azores Current within the domain is essential.

- Is a better description of the seasonal path and variability of the Canary Current attainable? What governs its dynamics? The Canary Current has been described as having a clear and well-defined path. However, the description is generally limited to a broad distinction between summer- and wintertime scenarios mediated by the advance and retreat of the subtropical gyre. It is known that the region of Cape Ghir plays a critical role in late summer.

- What is the nature of the incident flow (i.e., the Canary Current) at the Canary Islands? It is known that it reaches its peak intensity in the summer months, but what about its direction? Does it change? Is it systematic? The presence, direction and strength of the incident flow is expected to determine a large part of the character of mesoscale and submesoscale variability at the archipelago, which includes island-generated eddies. The potential importance of these eddies has been highlighted by the recent description of the Canary Eddy Corridor.

In the following chapters that describe the Canary Basin model development, analysis and results, these issues will be addressed. In some cases definitive answers are beyond the scope of the present work. Nevertheless, perspectives and ideas for future modelling and observational work are opened up.

3. Model and methodology

Procedures for offline grid nesting in regional ocean models[1]

Evan Mason[1], Jeroen Molemaker[2], Alexander Shchepetkin[2], Francois Colas[2],

James C. McWilliams[2] and Pablo Sangrà[1]

1. *Departamento de Física, Universidad de Las Palmas de Gran Canaria, 35017, Las Palmas de Gran Canaria, Spain*
2. *Institute of Geophysics and Planetary Physics, University of California Los Angeles, Los Angeles, California, USA*

Abstract

One-way offline nesting of a primitive-equation regional ocean numerical model (ROMS) is investigated, with special attention to the boundary forcing file creation process. The model has a modified open boundary condition which minimises false wave reflections, and is optimised to utilise high-frequency boundary updates. The model configuration features a previously computed solution which supplies boundary forcing data to an interior domain with an increased grid resolution. At the open boundaries of the interior grid (the child) the topography is matched to that of the outer grid (the parent), over a narrow transition region. A correction is applied to the normal baroclinic and barotropic velocities at the open boundaries of the child to ensure volume conservation. It is shown that these steps, together with a carefully constructed interpolation of the parent data, lead to a high-quality child solution, with minimal artifacts in the form of rim currents at the boundaries.

Sensitivity experiments provide information about the robustness of the model open boundary condition to perturbations in the surface wind stress forcing field, to the perturbation of the volume conservation enforcement in the boundary forcing and to perturbation of the vertical density structure in the boundary forcing. This knowledge is important when extending the nesting technique to include external data from alien sources, such as ocean models with physics and/or numerics different from ROMS, or from observed climatologies of temperature and salinity.

[1] At the time of submission of this thesis, the article presented in this chapter has been sent to the journal *Ocean Modelling* for publication.

3.1. Introduction

In numerical oceanic and atmospheric modelling, downscaling is a practical solution to the problem of resolving wide-ranging spatial and temporal scales of motion under the constraint of finite computing power and storage (Auclair et al., 2006; Penven et al., 2006; Cailleau et al., 2008). Downscaling involves the embedding, or nesting, of multiple model grids one within the other, each successive grid having a higher resolution than its parent. Such grid configurations may be run independently (offline nesting) or synchronously (online nesting). The important distinction between the two is the frequency of the boundary updates, which is higher for the online case. Higher frequencies are desirable but, in the offline case, judicious choice of the updating interval allows the resolution of the primary features of interest. Both approaches therefore yield realistic high-resolution solutions permitting study of local problems: the large-scale mean circulation and its associated variability (mostly mesoscale, plus seasonal and possibly inter-annual contributions) is provided by and passed down from the outermost parent, while the innermost child generates the high-resolution mesoscale and submesoscale data for the physical problem at hand.

Downscaling is a one-way process, in that information is passed solely downstream, from parent to child. Upscaling is the reverse process, where information is passed from a child solution back to the parent. Two-way nesting brings together downscaling and upscaling, so that there is a dual exchange of information: parent-to-child and child-to-parent. This technique is necessarily online, requiring additional software tools beyond the model code itself to facilitate the information exchange.

In regional oceanic modelling, the AGRIF Fortran (Adaptive Grid Refinement in Fortran; Debreu et al., 2008) package is one such tool in use. AGRIF has been incorporated into, amongst others, the ROMS (Regional Ocean Modelling System; Shchepetkin and McWilliams, 2005, 2009b) and NEMO-OPA (Madec et al., 1998; Madec, 2008) hydrodynamic models, permitting synchronous multi-level downscaled simulations. An evaluation of the system is presented by Penven et al. (2006), who conducted nested ROMS experiments for the U.S. West Coast. Cailleau et al. (2008), in a comparative study of different nesting techniques, report the use of two-way OPA nesting using AGRIF. These authors also introduce a more sophisticated coupling method, the *Schwarz* domain-decomposition method, which is shown to improve on the two-way solution, albeit at a high computational cost. A recent development is a ROMS-AGRIF two-way setup, described by Debreu et al. (2009). See also Debreu and Blayo (2008) for a review of the algorithms used in two-way embedding.

However, the purpose of this paper is to show how careful formulations of one-way offline nesting are still valuable in regional ocean modelling, despite the emergence of more advanced methods. Offline nesting permits great flexibility in terms of grid dimensions and orientation. Grids may be rotated, enabling boundaries to be aligned with coastlines to maximise the oceanic extent of the computational domain. Furthermore, timestep and grid-resolution ratios between each grid and its parent may be varied. Downscaling is often sufficient

to provide an adequate physical posing of a problem, so that two-way nesting becomes excessively laborious. In this respect, there is still no clear idea of when one approach or the other may be expected to make an important difference.

3.1.1. 2D versus 3D boundary forcing methods

ROMS permits the use of either 2D (Fennel et al., 2006) or 3D boundary forcing. For 3D boundary forcing, the parent 3D variables (i.e., baroclinic velocities and tracers) used at the child boundaries are stored in three-dimensional arrays on the child grid. 2D variables (barotropic velocities and sea surface height) are stored in 2D arrays. The bulk of these data, i.e., those within the interior of the domain, are redundant because only data at the boundary itself, plus a several-grid-cell-deep variable-strength relaxation (or *nudging*) layer, are used. Within the nudging layer, the model variables are restored towards the 3D boundary forcing values (Marchesiello et al., 2001). In practical terms, this has required modellers to restrict the size of child domains and, more importantly, the temporal frequency of the boundary forcing. Without these restrictions the storage size of 3D boundary forcing files becomes prohibitive, making it difficult to provide boundary information which resolves the mesoscale, let alone the submesoscale.

The use of 2D boundary forcing files, where only information at the boundaries is used (i.e., no interior nudging layer), is clearly more efficient in terms of disc storage than 3D. Hence, using the 2D approach together with adequate computing resources, long solutions (multiple model years, see Section 3.4 for example) on large grids (order of $1000 \times 1000 \times 80$ gridpoints, e.g., McWilliams et al., 2009) with high-resolution (in time, $<$1 day, and space, $<$100 m) boundary inputs, are feasible.

3.1.2. Rim currents

The volumetric nudging used in the 3D boundary forcing method is not possible with the 2D method; here we choose not to explore any sensitivity to the loss of this option. However, nudging is often credited with reducing so-called *rim currents*, which are a primary error mode that may occur in ocean model simulations. Figure 3.1 shows an example of a persistent rim current: In the v-component of the annual mean velocity from a 50-year UCLA-ROMS (Shchepetkin and McWilliams, 2009b) simulation of the northeast Atlantic Ocean at 7.5-km resolution (see Chapter 4 for details of this solution), a narrow strip of anomalous velocities (positive and negative) is seen along the western boundary.

Rim currents are a result of mismatches between the boundary forcing and the evolving child solution, and also the ability of the chosen OBC to ameliorate mismatches. Mismatches may occur in the stratification, particularly within the mixed layer; they may also arise if there are differences in the parent and child surface forcings, switching from one wind product to another for example; and also if volume conservation is not enforced in the boundary velocities. Rim currents, if present, show up most readily by viewing just the tangential component of the velocity along a boundary as in Figure 3.1. However, because we have

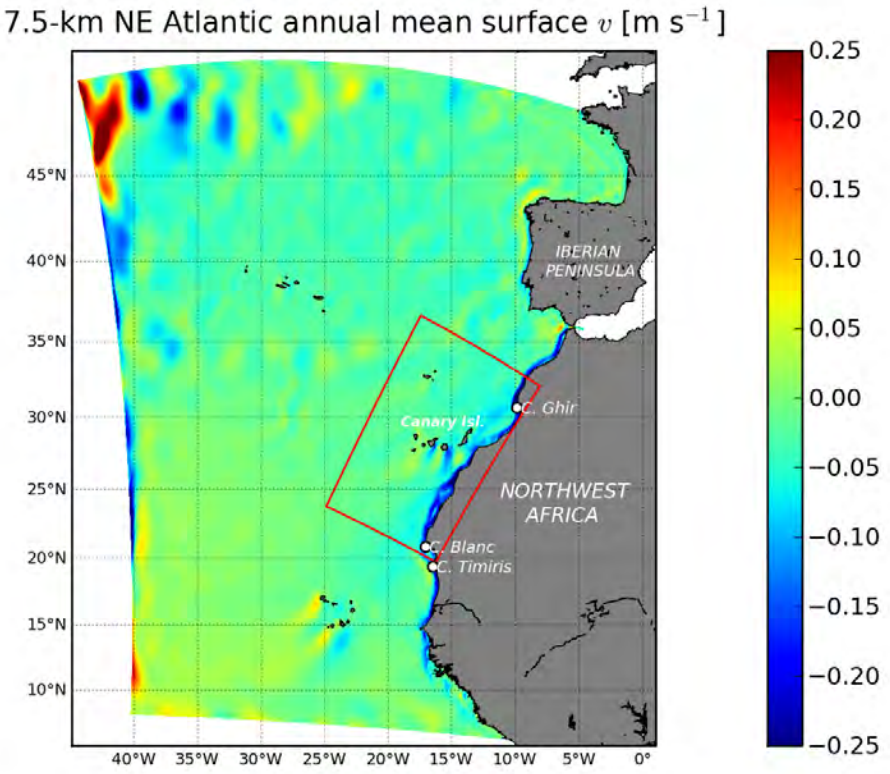

Figure 3.1.: Example of western boundary rim currents in the v-component of the mean annual model velocity of the 7.5-km parent (L0) solution, which covers the northeast Atlantic. Red lines demark the boundary of the child (L1) domain discussed throughout the present text. The locations of the Canary Islands and capes mentioned in the text are marked. Note that the strong positive velocity in the northwest corner is likely to be a realistic feature, see Section 2.5.1 on page 25.

largely minimised rim currents in our nested solutions, in the following sections we shall show them using relative vorticity, which is especially sensitive to velocity anomalies.

We have developed a methodology to facilitate downscaling within a ROMS framework. The need for such a methodology has come about because of recent developments in the UCLA-ROMS code that invite the use of high-frequency boundary forcing. In the following sections we present results from a ROMS configuration centred on the Canary Island archipelago in the northeast Atlantic, prepared using the new methodology. In Section 3.2 we briefly describe the ROMS model that provides the numerical framework for our experiments and the regional configuration that we have designed, and we also introduce the downscaling techniques that have been developed for the experiments. Results are presented in Section 3.3, which demonstrate the effectiveness of the procedures we use. In Section 3.4 we test the model's sensitivity to perturbations in the boundary and surface forcing data. Section 3.5 concludes with a discussion of the implications of our results.

3.2. Numerical methods and configuration

3.2.1. The ROMS model

ROMS is a primitive-equation, free-surface model which uses an orthogonal curvilinear coordinate system in the horizontal direction and a generalised terrain-following coordinate in the vertical. For the purposes of computational efficiency, the code utilises the natural time-scale separation of barotropic and baroclinic processes by employing a mode-splitting algorithm which solves the vertically-integrated barotropic momentum equations using a much smaller time step. A specially designed fast-time-averaging procedure prevents aliasing of processes unresolved by the longer baroclinic time step and, at the same time, maintains all necessary conservation properties (Shchepetkin and McWilliams, 2005). For this study we use the UCLA variant of the ROMS kernel (Shchepetkin and McWilliams, 2009b).

From the very beginning, ROMS was intended to be a regional model, which means that a numerical side-boundary forcing algorithm must be developed to supply external data at the open boundary of a limited-area domain. This algorithm must be mathematically compatible with the rest of the model, which leads to an overall design somewhat unique to the particular variant of the ROMS code we use.

3.2.1.1. Overview of numerical boundary condition algorithms

The task of the OBC is to supply the external information needed by the limited-area model domain at the boundaries, whilst, at the same time, allowing information generated within the model domain to exit through the boundaries with minimal artificial influence into the interior solution. The problem is mathematically non-trivial, because it is impossible to predict *a priori* which boundaries play the role of inflow or outflow and, furthermore, the same segment of open boundary may be both inflowing and outflowing for different physical processes. Also, because of the mode splitting used by the main time stepping algorithm

of ROMS, the boundary conditions must be formulated in terms of model variables, i.e., separately for the barotropic and baroclinic modes. In the approach we choose, the external data are provided along single rows at the open boundaries, i.e., there is no volumetric nudging over an interior boundary layer; for this approach to be successful, the performance of the OBC and the quality of the external data are critical. Lateral viscosity and diffusion are, however, allowed to decrease away from the boundary within a so-called *sponge* layer, in order to smooth minor inconsistencies between the evolving model solution and the external data. The values and profiles of viscosity and diffusivity within the sponge layers must be prescribed.

For the barotropic mode, the free surface and normal velocity components utilise a Flather-type condition (Flather, 1976), which is based on radiation and the prescription of *characteristic variables* (Riemann invariants; Blayo and Debreu, 2005). This new numerical implementation warrants a more detailed description which we provide below. For the tangential velocity, an upstream advection scheme is used for both outflow and inflow. This uses a fully 2D *corner algorithm* involving all nearest points. The local advection velocity is used for the phase speed. In the case of inflow, external data provided by a boundary file are used for the upstream donor-cell values. For outflow, the external data are ignored. There are no user-definable variable parameters (i.e., nudging time-scales) associated with the barotropic mode boundary condition.

The baroclinic mode utilises, for the normal velocity components of the momentum equations, an Orlanski-type (Orlanski, 1976) condition with adaptive strong (weak) nudging for inflow (outflow). Parameters for the nudging strength must be defined by the user. For the tangential velocity an upstream advection scheme with local advection velocity as phase speed is used. In the case of inflow, the external data are used for the upstream donor-cell value. For outflow, the external data are ignored. There are no tunable parameters to be defined. Tracers use an upstream advection scheme scheme similar to that for the tangential velocity above. Again, no tunable parameters are involved.

3.2.1.2. Flather boundary conditions for staggered grids

The original rationale for the Flather boundary condition comes from the assumption that the dominant physical processes are surface gravity waves and the desire to allow incoming surface gravity waves specified by the external data to enter the computational domain, while, at the same time, achieving unimpeded radiation for the outgoing waves (Chapman, 1985). In practice, this situation occurs only in purely tidal simulations in a small domain (hence it is physically acceptable to assume that the sea-surface field is controlled entirely by the lateral boundaries while neglecting the effect of the gravitational tidal potential). Furthermore, ROMS, as a split-explicit model, averages barotropic processes over one baroclinic time step, effectively filtering out unresolved barotropic time scales, while the slower barotropic processes (e.g., tides) behave as if the internal solution had adjusted itself instantaneously (from the point of view of the 3D mode, which resolves only time scales larger than the

baroclinic time step, Δt) to the externally imposed boundary conditions. Thus, the ultimate goal of the Flather condition is to achieve the best possible matching between the model field and the external data, for the free-surface elevation and barotropic (vertically-integrated) normal velocity components, in situations when straightforward clamping of both would result in over-specification, while if taken alone, neither primitive variable could be used to specify a well-posed boundary problem. In contrast with the purely wave and tidal cases, posing of the problem in a regional configuration requires specification of the large-scale flow across the open boundaries. Previously, in the case of rigid-lid models, the barotropic component was simply prescribed by imposing Dirichlet-type boundary condition on the barotropic streamfunction (Barnier et al., 1998; Marchesiello et al., 1998; de Miranda et al., 1999). This is possible because the free-surface wave motions are excluded completely, while the remaining barotropic dynamics are governed by elliptic-type equations, which need all-round specified boundary conditions for mathematical well-posedness. Physically, this means the specification of an external flow which is subject to the constraint of zero net flux for volume conservation.

In the case of long-term, limited area simulations using a free-surface model, the goal is essentially the same: to constrain the model solution to be close to the externally-defined flow at the boundaries. However, the method of achieving it is different: it is no longer possible to simply impose the normal velocities as a hard constraint. There are two reasons for why: (i) doing so would not guarantee the proper integral value of the net flux, resulting in drift of the horizontally-averaged free surface elevation and, (ii) the appearance of a barotropic non-damped wave field trapped inside the model domain (recall that the advective velocities are usually small in comparison with the external gravity wave speed, so the prescribed boundaries would effectively behave as perfectly reflective rigid walls. To address both of these issues, Marchesiello et al. (2001) proposed a combination of an Orlanski-type radiation boundary condition applied individually to each prognostic boundary with differential relaxation towards external data (at empirically chosen time scales; overall this can be classified as a soft constraint), and an integral flux constraint to avoid net volume gain or loss. A similar approach, except that a radiation boundary algorithm is applied to the difference between the model solution and external data, was explored by Perkins et al. (1997). Although both are viable approaches, in practice, success or failure depends on careful choice of user-defined parameters, often requiring elaborate empirical tuning to avoid artifacts associated with open boundaries. We are therefore motivated to explore an alternative approach which does not require such tuning.

The Flather-type characteristic boundary conditions are derived as follows:

$$\partial_t u = -g \cdot \partial_x \zeta, \qquad \partial_t \zeta = -h \cdot \partial_x u, \tag{3.1}$$

with the possibility to rewrite the above in terms of characteristic variables,

$$\Re^{\pm} = u \pm \sqrt{\frac{g}{h}} \cdot \zeta \qquad \text{hence} \begin{cases} \partial_t \Re^+ + c \cdot \partial_x \Re^+ = 0 \\ \partial_t \Re^- - c \cdot \partial_x \Re^- = 0 \end{cases} \qquad c = \sqrt{gh}, \tag{3.2}$$

so that $\Re^+$ and $\Re^-$ propagate to the right and to the left independently of each other with a known phase speed, c. This means that $\Re^- = \Re_0^- (x + ct) = const$ and $\Re^+ = \Re_0^+ (x - ct) = const$ along their respective characteristics, $x \pm ct = const$. The boundary conditions for $\Re^+$ and $\Re^-$, taken individually, are self-obvious: one must specify a value at the incoming side, while there is no need for a boundary condition at the outgoing side, hence,

Left-side:	Right-side:
$\Re^+ = u^{(ext)} + \sqrt{\frac{g}{h}} \cdot \zeta^{(ext)}$	$\Re^+$ from free radiation condition
$\Re^-$ from free radiation condition	$\Re^- = u^{(ext)} - \sqrt{\frac{g}{h}} \cdot \zeta^{(ext)}$

(3.3)

after which $\Re^+$ and $\Re^-$ are transformed back to the original variables u, ζ. In principle, Eq. (3.3) provides a method of solution for (3.1) not only near the boundaries, but also within the domain: one can discretise the latter using a non-staggered grid with u, ζ co-located; point-wise transform them into (3.2); and then solve as two independent advection problems for $\Re^+$, $\Re^-$. This approach is known as the Riemann solver for systems of equations such as, in the simplest cases, (3.1), and they are widely used for gas dynamical simulations, especially for shocks.

However, virtually all ocean models use horizontally-staggered grids, where cells for the free surface and velocity components are not co-located, and time step (3.1) directly using the original variables. This, however, cannot be applied to the boundaries, where the problem is well-posed only for $\Re^+$, $\Re^-$; but, at the same time, translation from u, ζ to $\Re^+$, $\Re^-$ is obscured because of the different locations of the variables. Nevertheless, the ocean modelling literature has numerous examples of the use of Flather boundary conditions, especially in the context of tidal simulations. In virtually all cases the dilemma of placing u, ζ at different locations has been addressed by applying an *ad hoc* interpolation scheme to translate each variable to the location of the other; see e.g., Chapman (1985) for a review. This procedure has several drawbacks, such as excessive reflections and the imposition of an additional restriction on timestep size relative to the stability limit of the main scheme. Below we describe a numerical algorithm for Flather boundary conditions, which is suitable for the staggered C-grid.

Assuming that the ghost-points of the free surface elevation, ζ, are located a half-grid-interval away from the normal velocity points, u, the purpose of the algorithm is to impose the normal velocity in such a way that Equation 3.3 is respected. This translates into the following four steps:

- Radiate out (details are below) u, ζ independently from each other to a common

location at each new time step:

$$\nearrow u^* = \tilde{u}^{n+1}_{j+1/2} \qquad\qquad \nearrow \zeta^* = \tilde{\zeta}^{n+1}_{j+1/2}$$

- Construct the outgoing characteristic variable, $\Re^+$ or $\Re^-$ depending on the side, using u^*, ζ^*. E.g., on the right-side boundary it is

$$\Re^+ = u^* + \sqrt{\frac{g}{h}} \cdot \zeta^*$$

where g is gravity and h is depth.

- Prescribe the incoming characteristic variable from external data, e.g., on the right-side

$$\Re^- = \left(\Re^-\right)^{(\mathrm{ext})} = u^{(\mathrm{ext})} - \sqrt{\frac{g}{h}} \cdot \zeta^{(\mathrm{ext})}$$

- Translate back

$$u^{n+1}_{j+1/2} = \frac{\Re^+ + \Re^-}{2} = \frac{u^* + u^{(\mathrm{ext})}}{2} + \sqrt{\frac{g}{h}} \cdot \frac{\zeta^* - \zeta^{(\mathrm{ext})}}{2}$$

The above differs from the original Flather condition, where $u = u^{(\mathrm{ext})} + \sqrt{\frac{g}{h}}\left(\zeta^* - \zeta^{(\mathrm{ext})}\right)$. Overall, apart from the *radiate out* step, the above algorithm follows the characteristic method of Blayo and Debreu (2005). Note that $\Re^+$ and $\Re^-$ never appear explicitly in the code. Boundary conditions for ζ (i.e., setting ζ at ghost points a half-grid point outside the boundary row of u-points) are needed only by the radiation scheme; they are not needed outside of the Flather OBC and are therefore auxiliary. Since the time step Δt for the barotropic mode is always expected to be limited by the stability criterion for the explicit time stepping, a simple explicit radiation scheme is sufficient to compute u^*,

$$u^* = u^{n+1}_{j+1/2} = (1 - \tilde{c})\, u^n_{j+1/2} + \tilde{c} u^n_{j-1/2}, \tag{3.4}$$

without causing any additional time step restriction. In the above, $\tilde{c}$ is the normalised phase speed, i.e., the *Courant* number, $\tilde{c} = \Delta t \cdot c/\Delta x = \Delta t\sqrt{gh}/\Delta x < 1$.

For the free surface, ζ, the situation is more complicated because it is located half-way between u-points, and an explicit scheme would be stable only until $\tilde{c} \leq 1/2$. One can devise a switched explicit-implicit scheme,

$$\zeta^* = \tilde{\zeta}^{n+1}_{j+1/2} = \begin{cases} \zeta^n_j \left(\dfrac{1}{2} + \tilde{c}\right) + \zeta^n_{j+1} \left(\dfrac{1}{2} - \tilde{c}\right), & \text{if} \quad \tilde{c} < \dfrac{1}{2}, \\ \dfrac{\zeta^n_j + \zeta^{n+1}_j \left(2\tilde{c} - 1\right)}{2\tilde{c}} & \text{if} \quad \tilde{c} > \dfrac{1}{2}, \end{cases} \tag{3.5}$$

which, in its turn, may need boundary values for the free surface at their natural locations,

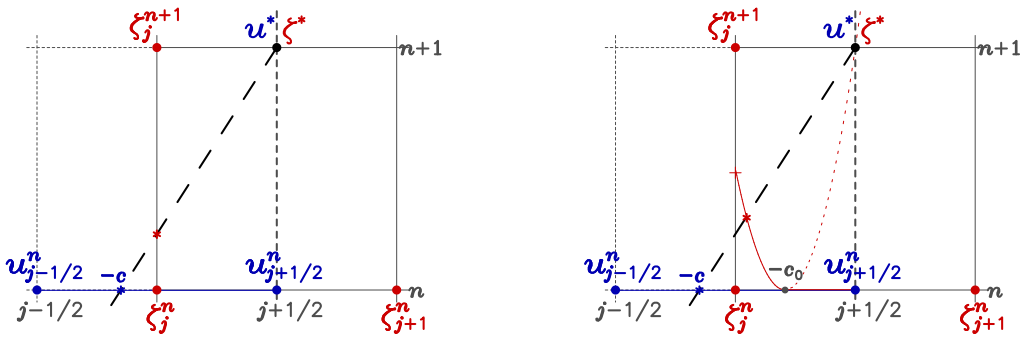

(a) (b)

Figure 3.2.: Geometric explanation of computing ζ^* and u^* in Eqs. (3.4), (3.5), and (3.7). The open boundary is represented by the vertical dashed line going through the normal velocity point $u_{j+1/2}$, so that the interior of the domain is to the left of it. The inclined line passing through ζ^* and u^* represents the characteristic for the outbound Riemann invariant $\Re^+$. Since the time step is expected to be limited by the stability criterion, $\tilde{c} < 1$, u^* can always be computed by an explicit scheme via (3.4). This is not the case for ζ^* because of its placement: Eq. (3.5) uses one of the two pairs of points, either ζ^n_j, ζ^n_{j+1} or ζ^n_j, ζ^{n+1}_j, depending on which segment is crossed by the characteristic (denoted by the red dot on the left panel). If $\tilde{c} = 1/2$, then $\zeta^*{=}\zeta^n_j$, which results in a slow-growing instability due to the non-dissipative nature of the interpolation in this case. The right panel illustrates how to avoid using a single point if $\tilde{c} = 1/2$, by taking the value of ζ^* from the point where the characteristic intersects the parabolic of the segment starting at $-c_*$.

ζ^n_{j+1}. These are computed using an auxiliary radiation boundary condition,

$$\zeta^{n+1}_j = (1 - \tilde{c})\, \zeta^n_{j+1} + \tilde{c}\zeta^n_j \,. \tag{3.6}$$

The sketch in Figure 3.2a illustrates the placement of all variables.

Unfortunately the above algorithm suffers from a numerical instability when $c \approx 1/2$. This instability is rather unusual because it occurs only within a narrow band of Courant numbers, and is associated with the fact that, if $\tilde{c} = 1/2$, the outcome of the algorithm above is $\zeta^* = \zeta^n_j$ without any interpolation, and therefore dissipation. This instability can be eliminated by

avoiding single-point values when $\tilde{c} = 1/2$. To do so, we modify the algorithm as follows:

$$\zeta^* = \begin{cases} \zeta_j^n \left(\frac{1}{2} + \tilde{c}\right) + \zeta_{j+1}^n \left(\frac{1}{2} - \tilde{c}\right), & \text{if} \quad \tilde{c} < \tilde{c}_0, \\ \zeta_j^n \left[\frac{1}{2} + \tilde{c}_0 \left(2 - \frac{\tilde{c}_0}{\tilde{c}}\right) - \left(1 - \frac{\tilde{c}_0}{\tilde{c}}\right)^2\right] & \\ \quad + \zeta_{j+1}^n \left[\frac{1}{2} - \frac{\tilde{c}_0}{\tilde{c}} \left(2 - \frac{\tilde{c}_0}{\tilde{c}}\right)\right], & \text{if} \quad \tilde{c} > \tilde{c}_0, \\ \quad + \zeta_j^{n+1} \left(1 - \frac{\tilde{c}_0}{\tilde{c}}\right)^2 & \end{cases} \tag{3.7}$$

where $\tilde{c}_0 = 1/\left(2 + \sqrt{2}\right)$. This scheme, shown in Figure 3.2b, is always stable[2]. The newly-modified Flather OBC has been shown to return a reflected wave with an amplitude of just 1% of that of the original signal reaching the boundary.

3.2.2. The ROMS configuration

The experiments are based on a regional model configuration of the Canary Basin in the subtropical northeast Atlantic Ocean. Figure 3.3a shows the child grid (hereafter L1) topography, embedded within that of the parent grid (hereafter L0). The L1 domain includes the Canary Island archipelago that lies within the path of the equatorward-flowing Canary Current (CanC). A large portion of the Canary upwelling region is captured, from Cape Blanc (20.80°N) to Cape Ghir (30.65°N). In general, it may be expected that the direction of flow at the open boundaries will correspond to the local characteristics of the subtropical gyre (Hernández-Guerra et al., 2005; Machín et al., 2006a). Hence, at the northern boundary inflow is expected to predominate and, at the south, outflow, both related to the CanC. At the western boundary, an inflow in the north is associated with the eastward-flowing Azores Current (AzC), while a weaker outflow to the south is due to an offshore branch of the CanC. Downstream of the Canary Islands, high mesoscale variability in the form of island-generated cyclonic and anticyclonic eddies is prevalent (Tejera et al., 2002; Sangrà et al., 2005). Filaments associated with the coastal upwelling interact with these eddies (Arístegui et al., 1994; Sandulescu et al., 2006).

The L1 grid has 332 × 534 grid points, making physical dimensions of 996 × 1602 km^2. The horizontal resolution is $\Delta x = 3$ km. The domain is rotated clockwise 28.5°, so that the closed eastern boundary is aligned with the African coast. The southern, western and northern boundaries are open.

The parent L0 is an extensive domain that includes the entire Canary Basin (Figure 3.1),

[2]The *hole* instability, $\sim 0.48 < c < \sim 0.52$, was first encountered by Xavier Capet in a problem with realistic topography. It manifests itself as a blow-up at the boundary, with the particular location dependent on the setting of the time step; no blow-up occurs for $\tilde{c} < 1/2$. Because $\tilde{c}$ depends on the topography, and topography varies from very shallow near the coast to deep offshore, once the time step is large enough, there is always a location at the boundary where $\tilde{c} \approx 1/2$, resulting in this instability. We are able now to reproduce it within an idealised wave problem.

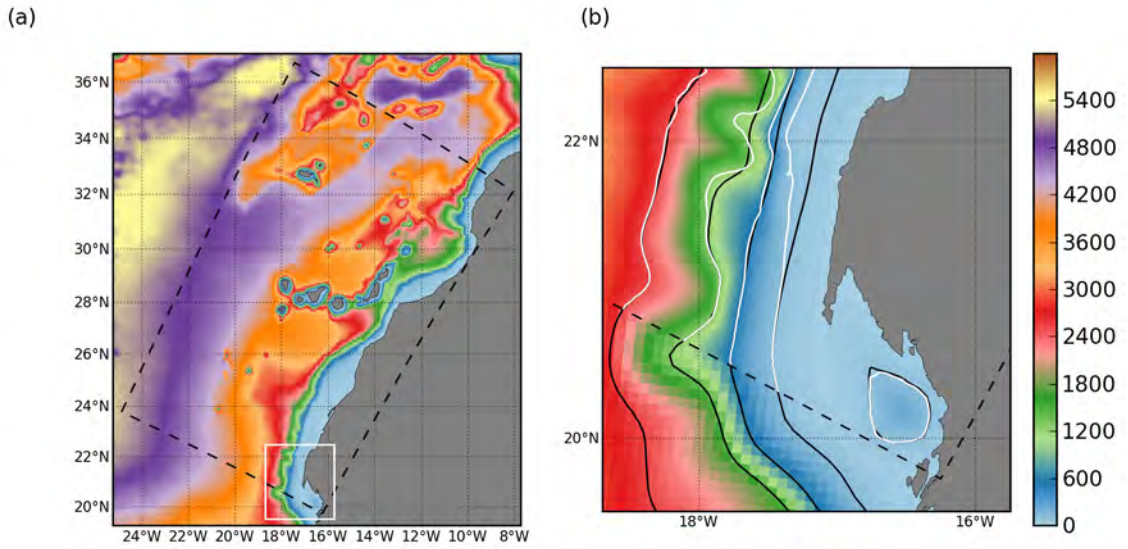

Figure 3.3.: (a) Child (L1) model domain (dashed black line) and topography of the Canary upwelling region, shown embedded within the parent (L0) domain (shown in Figure 3.1). (b) Zoom of the topography over the white box in (a), demonstrating the matching of L1 topography to that of L0 in the boundary region. Child (parent) isobaths are shown in white (black). Isobaths are at 100, 500, 1250 and 2500 m.

extending between ∼12° - 45°N and 5° - 40°W. L0 has horizontal resolution $\Delta x = 7.5$ km. This implies a relatively small grid refinement coefficient between L0 and L1 of 2.5 (Debreu and Blayo, 2008). More about the preparation of L0 may be found in Chapter 4.

L0 and L1 both contain 32 vertical sigma-levels, with $hc = 120$ m and a surface stretching factor of $\theta_s = 6$ maintaining high vertical resolution throughout the surface layers (i.e., boundary layers) of the domains. θ is a refinement parameter that determines the magnitude of *stretching* of the vertical grid in either the surface (θ_s) or bottom layers (θ_b). We use no refinement at the bottom ($\theta_b = 0$). hc is a depth above which the vertical grid spacing of the sigma layers becomes (a) nearly uniform and, (b) nearly independent of local depth, h, as long as $h \gg hc$. The model bathymetries are taken from (a) the ETOPO2 2-minute topography of Smith and Sandwell (1997) for L0 and, (b) the GEBCO 1-minute topography of Hunter and Macnab (2003) for L1. To prevent aliasing when interpolating to the model grids, the raw topographies are smoothed using a Gaussian filter of width twice the size of each raw data point. The interpolated topographies are then further smoothed by iteratively applying a filter to reduce the r-factor to below 0.2 ($r = \triangle h/2h$; Haidvogel and Beckmann, 1999). All depths shallower than 15 m (5 m) in L0 (L1) are reset to 15 m (5 m). See Section 3.2.3.1 for more on the preparation of the L1 grid.

The two grids both employ the same climatological forcing at the surface. Wind stress

is taken from the QuikSCAT-based Scatterometer Climatology of Ocean Winds (SCOW, Risien and Chelton, 2008). Heat fluxes and precipitation come from the Comprehensive Ocean-Atmosphere Dataset (COADS; da Silva et al., 1994; Woodruff et al., 1998), with a mild sea surface temperature (SST; 9-km Pathfinder, Kilpatrick et al., 2001) and sea surface salinity restoring (Barnier et al., 1995). The forcing files are created using the tools described by Penven et al. (2008). The L1 initial and lateral boundary forcing files are prepared following the procedures laid out in Section 3.2.3. See Chapter 4 for more on the preparation of the L0 initialisation and boundary files.

An L1 base case (BC) solution is run for 10 years, with averages of the outputs saved every 2 days. The baroclinic time-step is 540 seconds. At runtime there are two input parameters which influence boundary behaviour: the sponge and the baroclinic normal velocity nudging timescale, $M3$. We apply a weak sponge layer at the boundaries, with the viscosity coefficient, A_h, decaying from 10 m^2 s^{-1} at the boundary to zero at the inner part of the sponge. Such a low value was chosen because we are interested in velocity anomalies at the boundary, which a stronger sponge may smooth away. The eventual use of small sponge values was anticipated by Marchesiello et al. (2001): high-resolution absolute velocities at the boundaries may minimise differences between parent and evolving child solution to such an extent that the sponge is largely redundant. We set the velocity nudging coefficient $M3 = 0.1$, 10 days for the respective incoming and outgoing flows. These values were chosen considering a typical advective timescale: for our 3-km grid with maximum velocities of $\sim$0.4 m s^{-1}, we obtain $3000/0.4 = 7500$ seconds ≈ 0.1 days for the inflow. Given the upwind advection scheme used by ROMS, the outflow parameterisation is less critical than the inflow, and so we set it to 10 days.

3.2.3. Downscaling methodology

In this section we describe the interpolation of the model prognostic variables from a parent ROMS solution to child boundary and initial files.

3.2.3.1. Preparation of the child grid

Advance preparation of the child grid, beyond the description given in Section 3.2.2, is important to facilitate the interpolation. At higher resolutions steep slopes, such as at continental shelf edges, islands, ridges and seamounts, are better resolved than at lower resolutions. This means that depth mismatches between child and parent grids may be significant in these regions and become a problem when they lie along open boundaries, because volume conservation is difficult to enforce. Figure 3.3b illustrates the potential for such a problem. The child isobaths (white) in the interior of the L1 domain are seen to diverge from the parent isobaths (black). In order to prevent such a situation occurring near to the boundaries, topography mismatches are minimised by applying (Penven et al., 2006):

$$h^{child} = \alpha h^{child} + (1 - \alpha)\, h^{iparent}\,, \tag{3.8}$$

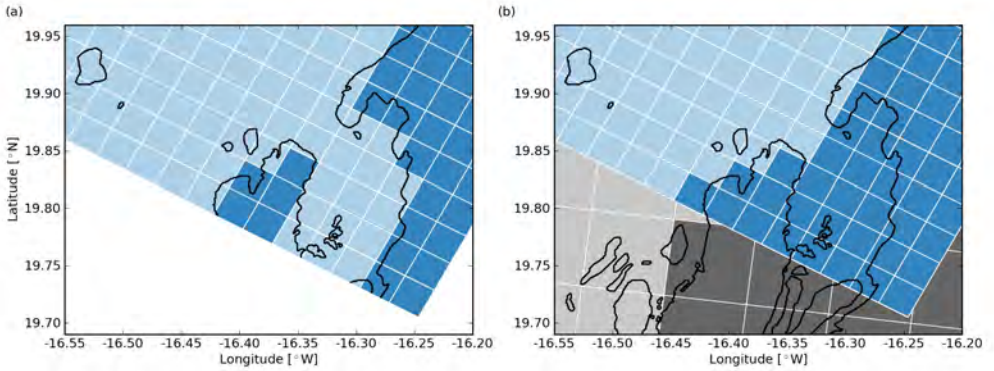

Figure 3.4.: Schematic diagrams showing the landmasking (darker blue) just north of Cape Timiris on the southeastern corner of the child (L1) domain. In (a) we show a grid where the landmasking is based only on the visible coastline (shown in black), so that an open channel is created. The L1 base case grid is shown in (b); here we include the parent mask (darker grey) to illustrate the need for correspondence between the parent and child masks near their boundary, hence leading to the omission of the open channel.

where h^{child} is the child-grid bottom topography, and $h^{iparent}$ is the parent topography interpolated to the child grid. α is a parameter that ranges from 0 at the lateral boundary to 1 over a distance d (typically 10% of the domain) inside the domain.

We also stress that, when defining the child landmask close to the open boundaries, it is important to pay attention to details of the parent landmask. In Figure 3.4a we show hypothetical landmasking at *rho*-points (ROMS uses the Arakawa-C grid; Arakawa, 1966) on the southeastern corner of the child grid. The coastline (in black) may lead us to naively assume Cape Timiris (on the southern boundary at ∼16.4°W) to be separated from land by a 9-km open channel, so that we would construct our landmask accordingly. The landmask that we in fact use in our experiments is shown in Figure 3.4b. The parent mask and full coastline are included, revealing the absence of a channel and, furthermore, that the parent is masked all along the child boundary to as far as one child grid cell to the west of the cape. We therefore choose to put a corresponding mask into our child grid. This procedure is followed at all open boundaries where landmasking is required.

These steps, that attempt to match child boundaries as closely as possible to those of the parent, work to minimise the need for extrapolation during the interpolation procedure.

3.2.3.2. Interpolation

The interpolation process is broken down into two stages. For a given time step there is, first, a horizontal stage where the parent variables (both 2D and 3D) are interpolated to the horizontal coordinates (longitude, latitude) of the child domain. In a second, vertical stage for each 3D variable, at each horizontal coordinate in the new matrix, a two-step vertical interpolation transforms the data from parent sigma-coordinates to z-coordinates, and then to child sigma-coordinates. At this point we have the full set of 2D and 3D prognostic variables on the child grid.

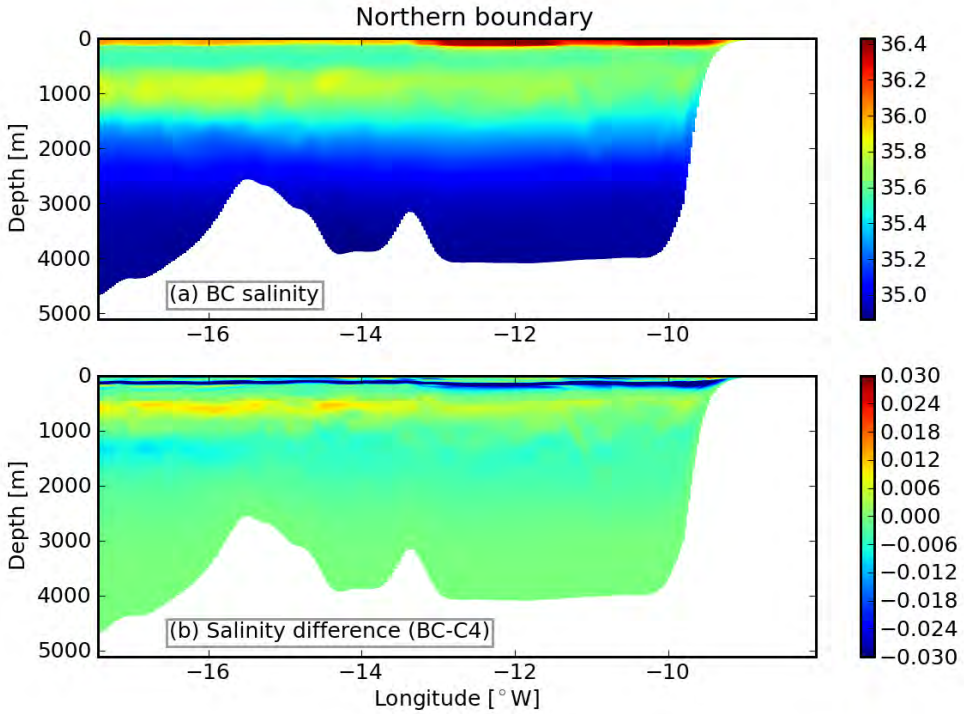

Figure 3.5.: (a) Salinity section at the northern boundary taken from the BC boundary forcing file at day 800 (year 2, month 6, day 20). (b) The difference between BC salinity in (a) and a transformed salinity section (C4). The transformation involves shifting the salinity values downwards by up to a maximum of 20 m at the depth of the thermocline.

To ensure volume conservation, a global barotropic velocity correction is applied to both the baroclinic and barotropic velocities at the open boundaries. The correction, $\bar{U}_{\perp corr}$, is calculated as

$$\bar{U}_{\perp corr} = -\int_{\Gamma} \bar{U}_{\perp} \cdot h / \int_{\Gamma} h \,, \tag{3.9}$$

where $\bar{U}_{\perp}$ is the barotropic normal velocity at the open boundaries, $\int_{\Gamma}$ is a line integral along the open boundaries, and h is the water depth.

Finally, slices are taken from the open boundary sides of each matrix and written to the boundary file. This procedure is applied for each successive time record within a specified time range that is available in the parent solution.

For the present experiments, the L0 solution provides 3-day averages of the prognostic variables. The resulting L1 boundary file contains data at the three open boundaries (north, south, west) of the L1 grid, at the 3-day frequency of L0. As an example, Figure 3.5 shows a summer salinity section at the northern boundary. The prominent features are a high salinity surface layer, typical of subtropical eastern North Atlantic Central Water and, centred at about 900 m, a second high salinity layer which corresponds to Mediterranean Water (MW).

3.2.3.3. Initialisation file extrapolation

An L1 initialisation file containing the full set (2D and 3D) of prognostic variables is built using the first time record extracted from the parent. Here, the essential steps described above are followed. However, in the interior where depth mismatches between parent and child topography do occur, an extrapolation step is sometimes required before the vertical interpolation: If, at a particular point in the respective grids, there is no parent variable at or deeper than the child depth, we search horizontally for the nearest suitable point where the required information is available. This information is then used for the vertical interpolation. This is a relatively simple extrapolation scheme. Recently, Auclair et al. (2006) have demonstrated that crude extrapolation techniques can lead to erroneous currents near steep topography. They propose an optimal scheme to avoid such errors. However, because we use extrapolation only when preparing the initialisation file, our solutions will suffer any such effects only in the very early stages of the model run.

3.3. Results

In this section we show a series of short-term and long-term averages from our base case (BC) solution of surface fields of SST and the vertical component of the relative vorticity, ω. These demonstrate the quality of the agreement between our L0 and L1 solutions using the methodology described above.

3.3.1. Instantaneous surface fields

The efficacy of the boundary condition and the boundary preparation procedure is demonstrated in Figure 3.6. Two-day average (i.e., quasi-instantaneous) surface fields in summer of the model (a) SST and (b) ω (normalised by the *Coriolis* parameter, f), are shown. The L1 solution is superimposed upon the temporally-coincident L0 solution (not shown in its entirety). The dashed-line box indicates the boundaries of the L1 grid.

Figure 3.6a shows a strong upwelling front punctuated by filaments that extend a few hundred kilometers offshore. The most marked of these filaments is that off Cape Ghir at 30.65°N (Pelegrí et al., 2005b). Further south, filaments are seen reaching the Canary Islands, where they facilitate exchange of nutrients and organic matter between the African coast and the archipelago (Bécognee et al., 2006; Sandulescu et al., 2006). The eddy-rich wake downstream of the islands peaks in late summer; an anticyclonic eddy is seen just south of the island of Gran Canaria at 28°N. In the offshore region the strongest SST gradients occur along the northern L1 boundary. These are likely related to the Azores front, which is associated with the zonal AzC located at about 34°N (Le Traon and De Mey, 1994). Along the open model boundaries there is little evidence in the SST of discontinuities between the L0 and L1 solutions.

A sterner test of the boundary behaviour is provided by considering the ω field in Figure 3.6b. L1 ω, owing to the increased grid resolution, has a noticeably greater amplitude

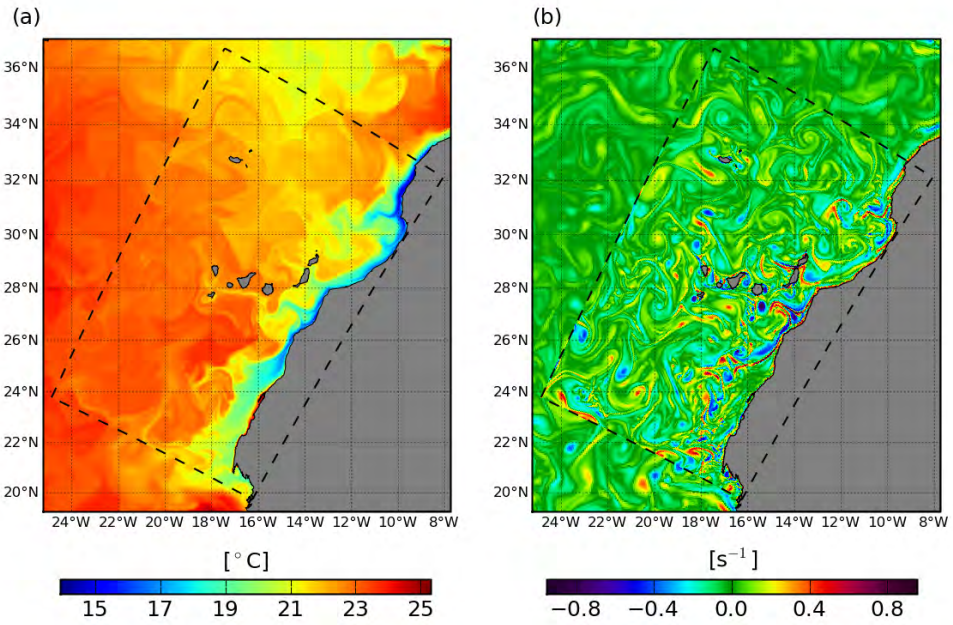

Figure 3.6.: 2-day child (L1) averages of (a) SST and (b) surface relative vorticity (ω) in the summer of model year 2, superimposed upon the parent (L0) field which is nearest in time (half a day). Dashed lines mark the L1 boundary.

than that of L0. Agreement between the two solutions is particularly close at the northern (inflow) boundary. Along the western and southern boundaries there are several instances of discontinuities, with elevated ω appearing to be trapped along the L1 boundary: for example, between 23.0° - 23.5°N there is a region of high cyclonic ω in L1 that is not seen in L0. It is noteworthy that the best agreement between L0 and L1 occurs at inflow regions along the open boundary.

Nevertheless, the correspondence between the solutions is remarkable given that we use one-way nesting where there is no feedback to the parent domain. Animations produced with time series of ω, plotted similarly to Figure 3.6b, show that the quality of agreement at the boundaries is persistent.

3.3.2. Mean surface fields

Figure 3.7 shows L1 7-year annual averages at the surface of SST and normalised ω, superimposed upon corresponding L0 mean fields. The SST field in Figure 3.7a is typical of eastern boundary upwelling regions, with a band of cooler upwelled surface waters along the coast. The coldest SSTs are found in the vicinity of Cape Ghir at 30.65°N. A frontal region associated with the AzC is seen at 34°N. The agreement between L0 and L1 mean SST all along the boundaries is good.

The annual mean surface ω comparison in Figure 3.7b is less clear than the SST. Averaging tends to minimise the signal, so that low values are found in both solutions, particularly in

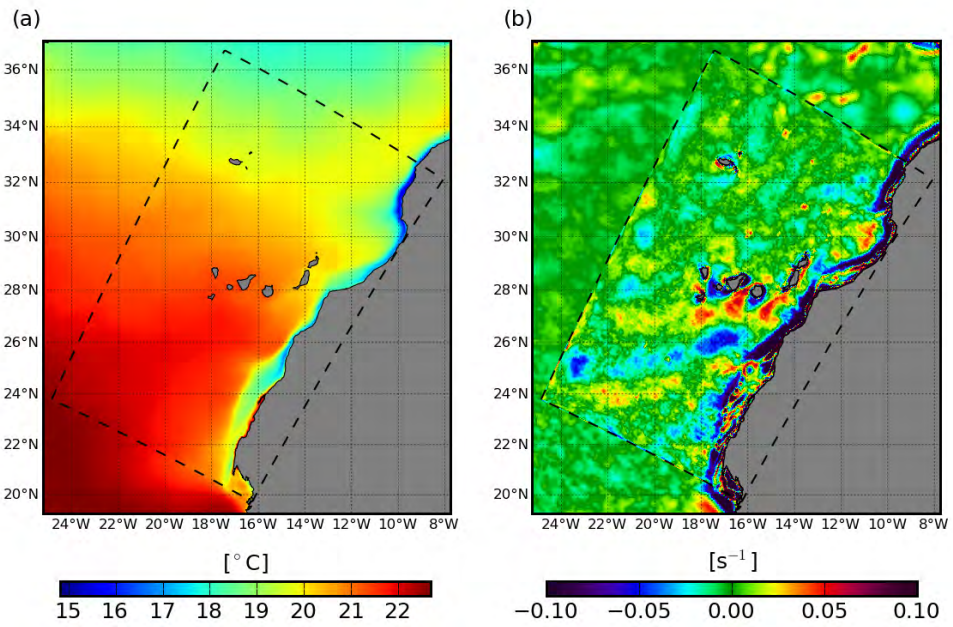

Figure 3.7.: Child (L1) 7-year annual averages of (a) SST and (b) vorticity (ω) for the base case experiments, superimposed upon the equivalent averages from the parent (L0). Dashed lines show the L1 boundary.

the offshore regions where there is less variability. Along the southern half of the western boundary there is a thin band of trapped cyclonic vorticity, indicative of transient normal-velocity mismatching; along the northern half, there is a wider band of anticyclonic activity. To the southwest of the Canary Islands zonal bands of alternating cyclonic and anticyclonic vorticity can be distinguished. These are associated with the Canary Island eddy field (Sangrà et al., 2009). The most intense band is anticyclonic with a width of ∼1°, centred at ∼25.5°N; its tail at ∼23.5°W appears to have a spuriously high magnitude. Close to the coast, however, there is good agreement between the L0 and L1 vorticity. Trapped against the coast is a strip of intense anticyclonic vorticity, which is bounded by a wider ribbon of cyclonic flow. A closeup of the annual mean coastal ω distribution in the southeast of the domain at the shallow Banc d'Arguin is seen in Figure 3.8: (a) shows just the L0 vorticity, (b) shows the L1 vorticity overlain onto L0. The distribution of vorticity is essentially the same in the parent and child solutions, including along the boundary.

3.4. Perturbation experiments

In this section we describe four sensitivity experiments where we attempt to *break* the BC solution described in Section 3.3. In the first two experiments (C1 and C2) we introduce a small modification to the surface wind forcing. In the third experiment (C3) we perturb the volume conservation imposed by our methodology. In the final experiment (C4) the depth

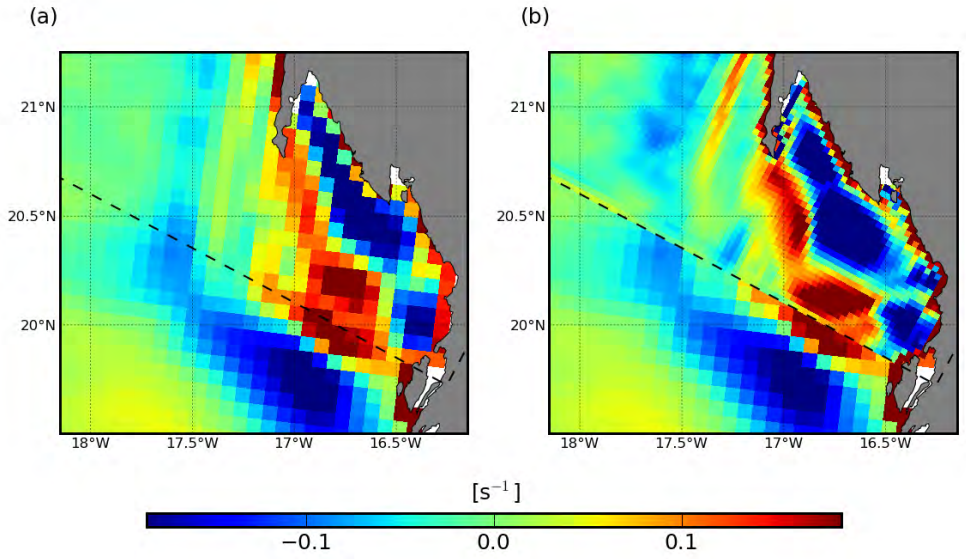

Figure 3.8.: 7-year annual-mean surface vorticity (ω) at the southeastern corner of the child (L1) domain. In (a) only the parent (L0) ω is shown, while in (b) L1 ω is superimposed upon L0. The dashed black line demarks the L1 boundary. The inshore region shown is the Banc d'Arguin where the water depth is shallow ($\sim$ 20 m).

of the thermocline in the boundary files is artificially lowered by up to 20 m. Table 3.1 provides a summary of the experiments. A comparison between BC and C1, C3 and C4 is given in Figure 3.9, which shows annual averages (26 years for BC, 7 years for C1, C3 and C4) of surface ω (normalised by f). The aim of the sensitivity experiments is to explore the robustness of the boundary condition under a variety of credible less-than-perfect forcing scenarios, such as may be encountered when downscaling from an Ocean General Circulation Model (OGCM) to ROMS.

Figure 3.9a shows the BC surface ω field embedded within that of L0. This is a long-term mean, 26 years, which contains less noise in comparison with the 7-year mean of Figure 3.7. The largest vorticity signals are found all along the coast, positive at the coastal boundary and negative just offshore. The Canary Island wake constitutes the other dominant signal, traces of which extend as far as the western boundary at $\sim$25°N.

3.4.1. Modified wind experiments (C1, C2)

Two experiments were run where the surface forcing wind stress field was modified with respect to BC. For C1 (C2), 0.02 N m^{-2} was subtracted from the u-component (v-component) of the wind stress for each month of the surface forcing climatology. Figure 3.9b shows the C1 surface ω. The patterns are generally similar to BC, with largest values associated with the coastal region and the Canary Island wake. The further reaches of the wake ($\sim$19°W), however, have considerably larger ω magnitudes than BC. At the boundaries, there are

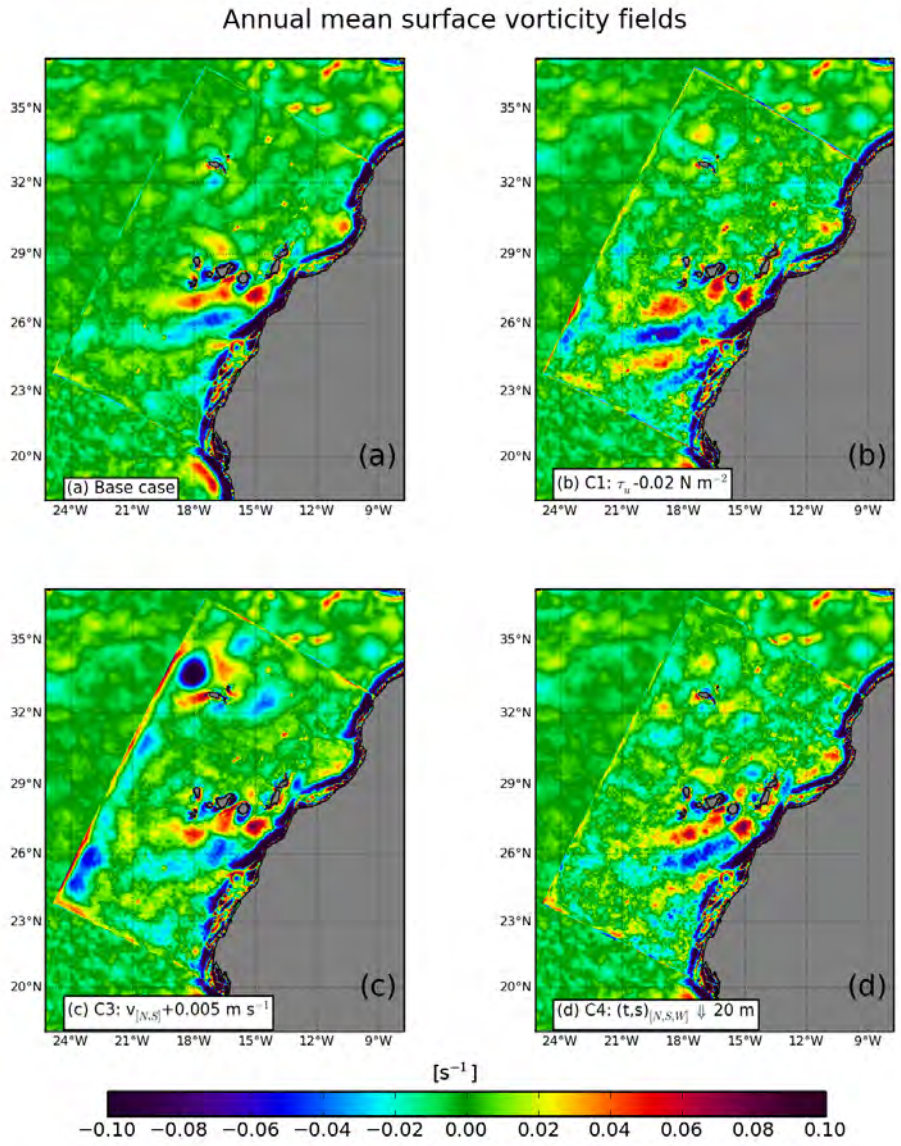

Figure 3.9.: Annual mean surface relative vorticity (ω) fields from (a) the base case experiment, (b) case 1, (c) case 3 and, (d) case 4. See Table 3.1 for a summary of the cases. The L1 boundary is intentionally not demarked.

Table 3.1.: Sensitivity experiments (C1 - C4) in relation to the base case, BC. QC is QuikCOW, the surface wind stress product described in Section 3.2.2. *ds* signifies L1 boundary data downscaled from L0.

	Wind stress	Volume conservation	Boundary thermocline
BC	QC	Yes	$(temp,\ salt)_{\,ds}$
C1	$\mathrm{QC}_u - 0.02$ N m^{-2}	Yes	$(temp,\ salt)_{\,ds}$
C2	$\mathrm{QC}_v - 0.02$ N m^{-2}	Yes	$(temp,\ salt)_{\,ds}$
C3	QC	$(v, \bar{v})_{[N,S]} + 0.5$ cm s^{-1}	$(temp,\ salt)_{\,ds}$
C4	QC	Yes	$(temp,\ salt)_{\,ds} \Downarrow 20$ m

conspicuous strips of anomalous positive ω, in particular at the western boundary. The C2 surface ω field is not shown as it is not markedly different in character from C1.

3.4.2. Barotropic flux perturbation experiment (C3)

In this experiment the baroclinic and barotropic normal velocities (v, $\bar{v}$) applied at the northern and southern boundaries are altered by adding a constant value of 0.5 cm s^{-1}, effectively removing the volume conservation imposed during boundary file creation. The effect of this perturbation is clearly seen in the mean surface ω field along the western boundary in Figure 3.9c, in the form of a large anticyclonic standing eddy. The latitudinal position of this eddy, which has a radius of $\sim$1.5°, is that of the incoming AzC. Along almost the entire western boundary, C3 surface ω is strongly positive, exceeding that of the wind cases. In addition, a wide strip of negative ω runs parallel to the positive boundary anomaly. The overall pattern of ω in the interior is similar to BC.

3.4.3. Mixed layer depth perturbation experiment (C4)

In the final perturbation experiment, temperature and salinity in the boundary forcing is lowered in depth, by up to a maximum of 20 m in the region of the thermocline. The depth change was done by setting $hc = 80$ (Section 3.2.2) during the boundary file creation process. Figure 3.5b illustrates the transformation by showing the difference between a BC and modified C4 salinity section at the northern boundary. The largest differences, positive and negative, correspond to the two high salinity layers seen in Figure 3.5a, the surface and the MW depth layer. Below about 2500 m differences tend to zero. The intention behind this modification is to introduce into the ROMS solution, a small but significant horizontal density gradient within the region of, and normal to, the open boundaries.

The C4 annual mean surface ω is shown in Figure 3.9d. The effect of the thermocline perturbation is most visible along the western boundary, in the form of a narrow intermittent strip of positive vorticity with a similar magnitude to that in C2. In the interior, the far-field island wake vorticity is somewhat greater than it is for BC.

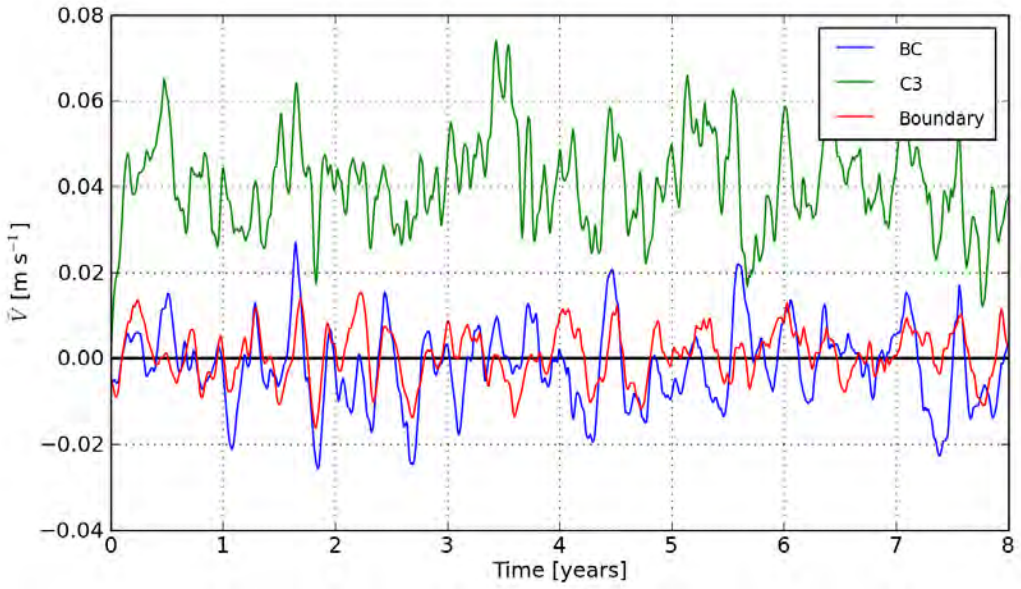

Figure 3.10.: 8-year time-series of monthly-mean western-boundary tangential barotropic velocities for BC (blue), C3 (green) and the boundary forcing file (red). For BC and C3 the average is taken over the first 3 columns of the grid.

3.4.4. Discussion

Our choice of perturbations was motivated by the ongoing need to go beyond a ROMS-to-ROMS downscaling (i.e., where the parent is a ROMS solution). We want to be able to downscale at will from model outputs other than ROMS, such as OGCMs like SODA (Carton and Giese, 2008), and also from climatologies. In these situations, all of the above perturbations may come into play: the OGCM is likely to employ a different vertical mixing scheme from ROMS, and to be forced with a different wind stress product. For this reason we chose perturbations (0.02 N m^{-2} and 20 m, respectively) comparable to the expected differences that may be found between typical OGCM and child ROMS values. We note, however, that our wind perturbations are constants, so that we are not considering wind stress curl differences (between ROMS and OGCM) which may be significant. Our results show that ROMS is relatively robust in response to the perturbations, although the mean solutions presented do show some degradation (Figures 3.9b, d).

Of the perturbations (C1 - C4), our methodology is only able to "fix" C3. We show in Figure 3.9c that, for C3 where the volume conservation is broken, the mean solution is significantly altered. The noise at the western boundary, in particular the standing eddy, is persistent in the instantaneous records (not shown). Figure 3.10 compares 8-year time-series from BC and C3 of the monthly mean tangential barotropic velocity ($\bar{v}$) over a three-point-

wide strip along the western boundary:

$$\bar{V} = \frac{1}{N_i \times N_j} \sum_{i=1}^{N_i} \sum_{j=1}^{N_j} \bar{v}_{ij}, \tag{3.10}$$

where $N_i = 3$ and $N_j = 534$. $\bar{V}$ is also computed from the boundary forcing file with $N_i = 1$. The figure shows that the effect of perturbation C3 is rapid: within a couple of months from the initialisation, C3 $\bar{V}$ is strongly positive and does not approach zero thereafter, indicative of a significant anomaly at the boundary (i.e., rim current). BC $\bar{V}$, however, oscillates around the zero mark, as does the boundary $\bar{V}$. The amplitude ranges for both cases are similar, that for the boundary is slightly smaller. Plots for C1, C2 and C4, not shown, lie roughly within the same range as BC.

A further finding of these experiments answers the question: does the quality of the boundary data matter? Modellers place boundaries far away from a region of interest in an attempt to minimise the effects of small boundary artifacts on the interior. Figure 3.11 shows comparisons of 7-year annual means from BC and C3 of surface fields in the vicinity of the Canary Islands, the centre of the L1 domain. Figures 3.11a, c, e show, respectively, u- and v-velocity components and SST from BC. Differences in these variables between BC and C3 are shown in Figures 3.11b, d, f. The figures show that velocity differences frequently exceed 0.05 m s^{-1} for both u and v, despite the distance from the boundary. Similarly for SST, the ΔSST field shows that BC SST offshore of the shelf edge is cooler than C3 by more than 0.25°C. These differences strongly suggest that remote forcing does have a global impact upon the model solution, such that the steps taken in our methodology (Section 3.2.3) are justified.

3.5. Summary

A new formulation of the barotropic open boundary condition is proposed that minimises wave reflection at the open boundaries of the regional domain. High quality ROMS solutions with minimal artifacts at the boundaries are achievable using one-way ROMS-to-ROMS offline-nesting techniques, provided that suitable care is taken in the boundary file creation process. The main components of our boundary forcing methodology are accurate interpolation to child grid-points of parent data, matching of the parent-child topography and land-mask, and a normal velocity correction at the child boundaries to ensure volume conservation (Section 3.2.3).

A major advantage of a boundary forcing that is strictly 2-dimensional as opposed to a 3-dimensional nudging region is the ability to provide high-frequency boundary information for the inner grid over an extended period of time. This allows the inner grid to be forced with an outer solution that contains meso- or even submesoscale variance in the tracer and velocity fields. Such a nesting strategy provides a unique and convenient approach to study phenomena such as frontal instabilities and submesoscale eddies (Capet et al., 2008a;

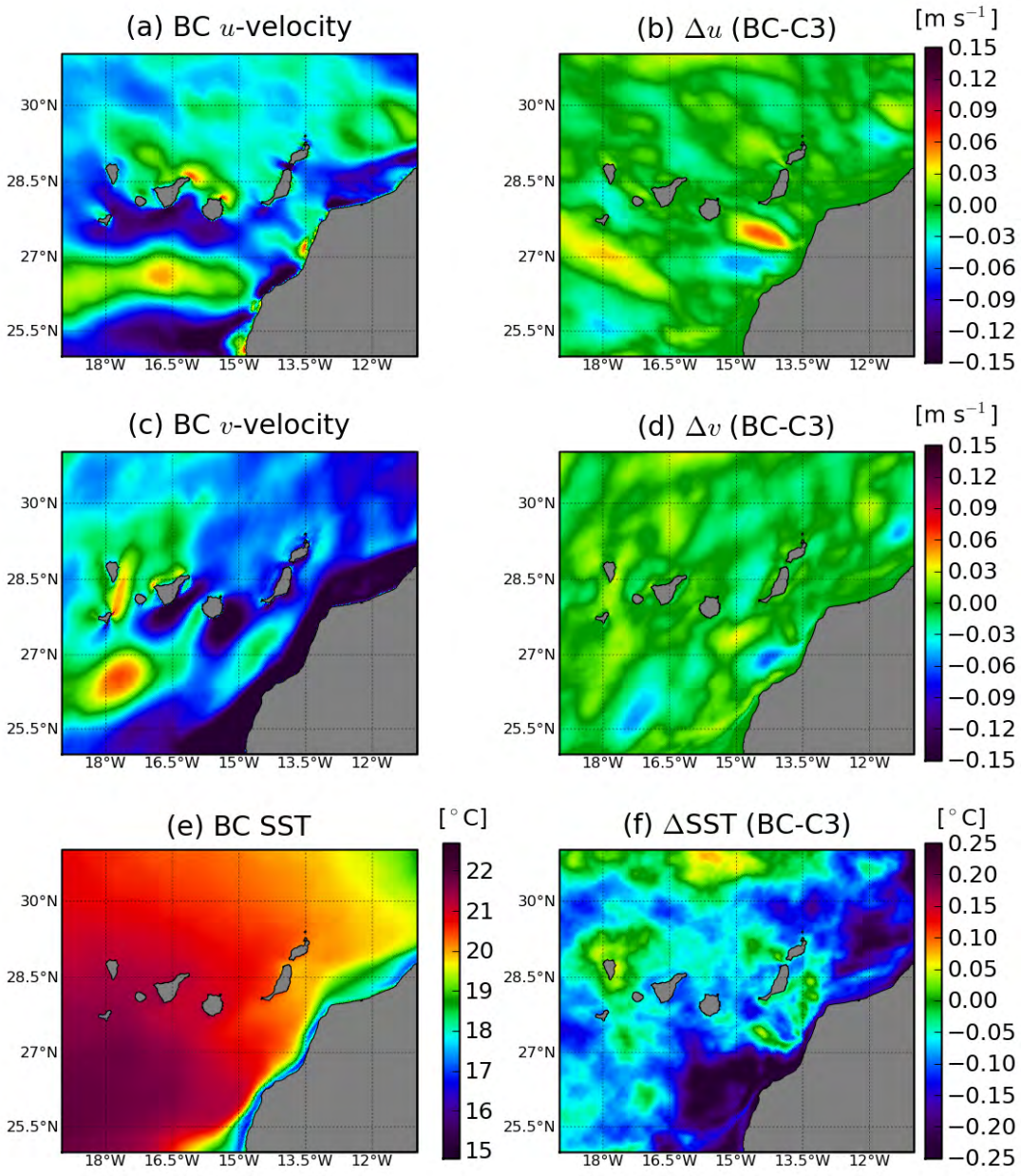

Figure 3.11.: Zoom near the Canary Islands of long-term annual mean surface fields of u-velocity, v-velocity and SST for BC (left panel) and their differences from C3 (i.e., BC - C3; right panel). The variables are (a, b): u, $\triangle u$; (c, d): v, $\triangle v$; (e, f): SST, $\triangle$SST.

Thomas and Ferrari, 2008) in a realistic environment in the higher-resolution inner grid (Capet et al., 2008c; McWilliams et al., 2009). When averaging the outer solution to, for instance, monthly means (Dong et al., 2009) one removes the mesoscale variability at the boundaries that is essential for the submesoscale variability to be generated correctly. When a computational domain is large enough, some of the mesoscale variability may be recovered by means of baroclinic instability within the domain. When one is nesting in multiple steps to increasingly higher-resolution (but also smaller in physical size) domains, it is essential to retain all variability of the parent grid solutions.

A limitation of the current paper is that we still have an incomplete understanding of which properties of the parent solutions are essential to transfer accurately to the child grid. To further our understanding we performed a number of perturbation experiments. From those experiments it appears that the consideration of volume conservation across the open boundaries of the child grid is important. A small correction to the velocities at the boundaries leads to significant tangential velocities at the domain boundaries (Figure 3.9). Other types of perturbations lead to responses in the solution of the inner grid that are less pronounced. However, our experience with similar experiments for different parent-child configurations are somewhat inconclusive. What this means is that we are currently able to obtain high quality solutions when downscaling a ROMS solution to ROMS configuration. Our ability to downscale arbitrary data such as observations or solutions computed by different models is currently not as advanced. In these latter cases, our methodology is not as capable as evidenced by our parent (L0) solution (see the rim currents in Figure 3.1 on page 46) which was forced with a monthly observation-based climatology.

Finally, we show that small changes in boundary forcing data may lead to differences in the solution throughout the numerical domain (see Figure 3.11). Even in cases where the region of interest is located away from the boundaries of the computational domain it remains therefore important to downscale the parent solution correctly.

Acknowledgments

Evan Mason is supported by the Spanish research project RODA (CTM2004-06842-C03-03). ROMS development at UCLA is supported by the Office of Naval Research (currently grant N00014-08-1-0597). This work was partially supported by the National Center for Supercomputing Applications under grant number OCE030007 and utilised the *abe* system. We thank Florian Lemarié for his revision and comments on the manuscript.

4. Seasonal study of the Canary Basin

Seasonal variability in the Canary Basin: a numerical study[1]

Evan Mason[1], Francois Colas[2], Jeroen Molemaker[2], Alexander Shchepetkin[2],

James C. McWilliams[2] and Pablo Sangrà[1]

1. *Departamento de Física, Universidad de Las Palmas de Gran Canaria, 35017, Las Palmas de Gran Canaria, Spain*
2. *Institute of Geophysics and Planetary Physics, University of California Los Angeles, Los Angeles, California, USA*

Abstract

A high-resolution numerical model study of the Canary Basin is presented. A long-term climatological solution reveals mesoscale variability along the Azores Front/Current system, and at the Canary Island archipelago off northwest Africa. The Azores Current transports ∼9 Sv, in line with observations. Experiments with the Strait of Gibraltar open and closed, permitting or blocking the entrance of Mediterranean Water into the northeast Atlantic domain, demonstrate the impact of entrainment processes in the Gulf of Cadiz on the generation of the Azores Current; further confirmation of the topographic β-plume hypothesis reported in recent model studies of the Azores Current. The Azores Current is thought to feed the Canary Current off the African coast at around 32.5°N. The Canary Current is a wind-driven eastern boundary current, which is perturbed by the Canary Islands as it flows south. In the model, the Canary Current has a well-defined path with pronounced seasonal variability. This variability is shown to be mediated by the westward passage of two large annually-excited rotating structures, that originate at the African coast. Because they have a sea surface expression, the anomalies can be detected in altimetry. The anomalies travel at the phase speed of baroclinic *Rossby* waves. In the model experiment where the Strait of Gibraltar was closed and the Azores Current was very weak, this behaviour of the Canary Current persisted, suggesting that the Canary Current is independent of the Azores Current.

At the Canary Islands, mesoscale variability arises through topography/current interaction, and baroclinic instability of the coastal upwelling that is driven by the northeasterly Trade winds. Eddies generated in the lee region of the archipelago have recently been shown to have a remote impact: eddies with lifetimes exceeding 6 months are observed to propagate westwards to as far as 32°W. Such eddies are present in the model solution. They are generated all year, with a preference for island-generation in summer and coastal generation in winter.

[1] This article requires a final round of review by the authors and is expected to be submitted for publication before the end of 2009.

4.1. Introduction

4.1.1. The Canary Basin

Motivated by interest in the seasonal variability of the dynamics and processes in the eastern boundary of the North Atlantic Subtropical Gyre (NASG), a climatology-forced high-resolution numerical model configuration has been developed for the Canary Basin. The Canary Basin is loosely defined by the limits 10° to 40°N, and 40°W to the eastern boundary (Spall, 1990; Arhan et al., 1994; Arístegui et al., 2006) (Figure 4.1). It contains the three major recirculating currents of the eastern portion of the NASG, which are the Azores Current (AzC), the Canary Current (CanC), and the North Equatorial Current (NEC). The total transport of this eastern portion of the NASG has been estimated at ∼12 Sv (1 Sv = 10^6 m^3 s^{-1}) (Stramma, 1984; Siedler and Onken, 1996). Two other important currents are the North Atlantic Current (NAC) and North Equatorial Counter Current (NECC). The NAC is a northern branch of the Gulf Stream, and is associated with high levels of mesoscale variability in the northwest of the Canary Basin between the shallow Flemish Cap and the Mid-Atlantic Ridge (MAR) (Rossby, 1996). The highly seasonal eastward-flowing NECC is found in the tropics below about 10°N (Lumpkin and Garzoli, 2005).

The topology of the Canary Basin is illustrated in Figure 4.1. The 2000-km long African continental coastline is generally orientated in a northeast-southwest direction. Average shelf width along the coast is 50 - 60 km, the shelf edge is well defined by the 200-m isobath. At the northern extent of the transect is the Gulf of Cadiz (36° - 37°N), where the Strait of Gibraltar facilitates exchange of water properties between the North Atlantic and the Mediterranean Sea. The coastline is marked by several large capes and corresponding embayments. The Canary Island archipelago, lying upon a steep-sided 2500-m deep plateau which protrudes westward away from the continental boundary, is located at about 28.5°N. Other island groupings are the Cape Verde islands ∼700 km offshore of Cape Verde, Madeira to the north of the Canaries at ∼33°N, and the Azores found east of the main MAR axis at ∼38°N, 28°W.

The zonal AzC, whose origin is a southward branching of the Gulf Stream, crosses the MAR and flows towards the Gulf of Cadiz along ∼34°N. Its mean transport is reported to be in the range 10 - 12 Sv (Gould, 1985; Stramma and Muller, 1989) although, along its length, the AzC has a number of southward-turning branches so that only ∼4.5 Sv reach the Gulf of Cadiz (Paillet and Mercier, 1997). The AzC is associated with a thermohaline front, the Azores Front/Current system (AzFC) which, in the west, separates 18°C and 13°C Subtropical Mode Waters (Pollard et al., 1996). The AzC was initially thought to be wind-forced (Käse and Krauss, 1996), but there is growing evidence that its dynamics are related to entrainment processes in the Gulf of Cadiz (Jia, 2000; Peliz et al., 2007; Kida et al., 2008).

The CanC is the eastern boundary current of the NASG, which transports about 3 Sv southwestward, parallel to the northwest African coast (Stramma, 1984; Stramma and Siedler, 1988; Navarro-Pérez and Barton, 2001). The CanC has been generally viewed as a broad weak flow, driven by the northeasterly Trade winds, which spans the transition zone between the open ocean and the coastal region. The current originates in the region

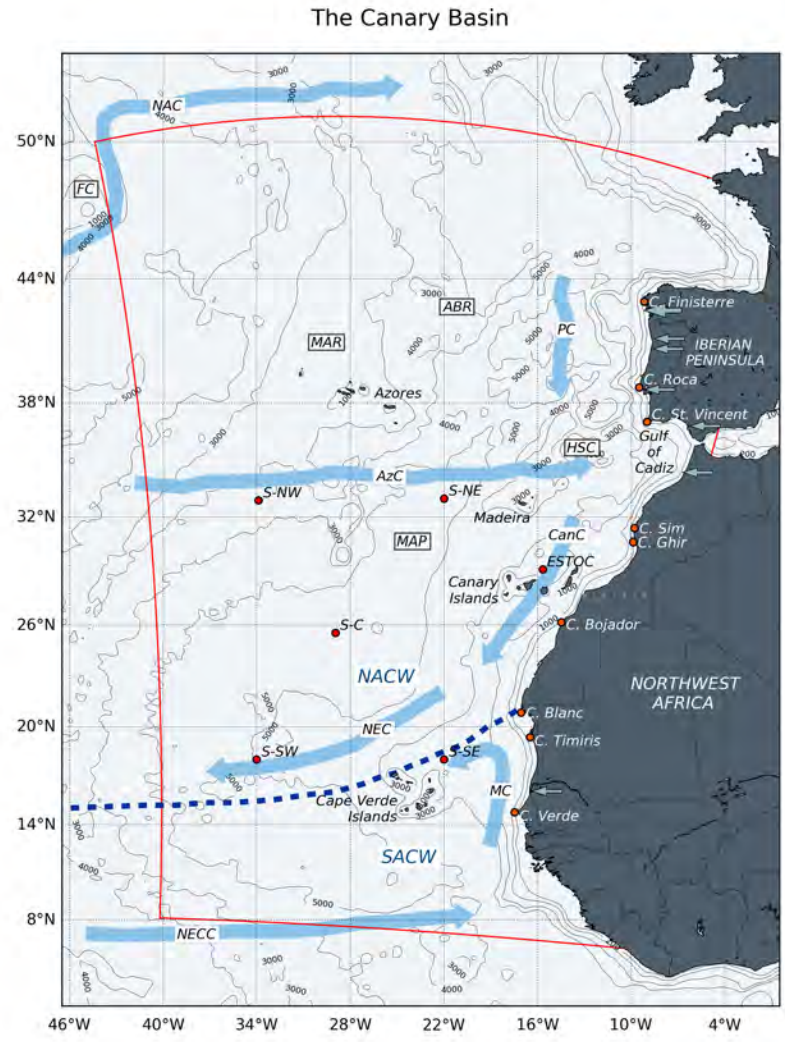

Figure 4.1.: Topology and large-scale circulation of the Canary Basin in the subtropical northeast Atlantic. The boundary of the L0 model domain is outlined in red. Red dots show the positions of moorings used in the text (see Table 4.2 on page 83). Labels: AzC - Azores Current, CanC - Canary Current, MC - Mauritania Current, NEC - North Equatorial Current, NECC - North Equatorial Counter-Current; ABR - Azores-Biscay Rise, FC - Flemish Cap, HSC - Horseshoe Seamount Chain, MAP - Madeira Abyssal Plain, MAR - Mid-Atlantic Ridge. Contours in black mark isobaths at 200, 1000, 3000, 4000, 5000 m. Topographic data from GEBCO (Hunter and Macnab, 2003). Blue arrows along the coast mark locations of significant river input.

between Madeira and the African coast, and is fed by the easternmost branch of the AzC. After passing the Canary Islands, the CanC feeds into the NEC near to the Cape Verde Frontal Zone (CVFZ), which separates NACW and South Atlantic Central Water (SACW) at ∼21°N (Barton, 1987; Zenk et al., 1991).

The alongshore wind regime drives a permanent upwelling of North Atlantic Central Water (NACW) between Cape Blanc and the Gulf of Cadiz. Seasonal variations in the position of the Azores high pressure cell, which is responsible for the Trades, mean that north of the Canaries the winds peak in summer but are weaker during the rest of the year (Wooster et al., 1976; Mittelstaedt, 1991). The Canary Islands are embedded within the path of the CanC, and also span the open ocean-coastal transition (Barton et al., 1998). Associated with the islands is a downstream wake region, where island-generated eddies interact with upwelling-related filaments that extend offshore from the coast (Arístegui et al., 1994).

However, recent studies indicate that the CanC north of the Canary Islands has a more well-defined position than is suggested in the above description (Stramma and Siedler, 1988; Zhou et al., 2000; Pelegrí et al., 2005a; Machín et al., 2006a). The CanC demonstrates seasonal dependence, Stramma and Siedler (1988) suggested that the current tends to be found far offshore near to Madeira in winter, while in summer it occupies a more central position between Madeira and the African coast. This depiction is partially confirmed in seasonal meridional geostrophic velocity sections of Machín et al. (2006a) where, in summer 1998, the CanC was seen as a relatively strong (>0.08 m s^{-1}) ∼800-m-deep current centred around 14°W. Pelegrí et al. (2005a) stress close inter-connectivity between the coastal upwelling region and the open ocean (i.e., the CanC): the equatorward surface jet associated with the upwelling, the Canary Upwelling Current (CanUC; Pelegrí et al., 2006), is present for most of the year over the northwest African shelf. In late autumn, the portion of the CanUC near to the Canary archipelago reverses and, in the vicinity of Cape Ghir, the current detaches from the coast and moves offshore. This leads to the formation of a large winter-time cyclonic circulation cell, which Pelegrí et al. (2005a) speculate extends around the archipelago. Despite these and other studies, owing to a lack of observations (Pelegrí et al., 2005a), a definitive description of the path and seasonal variability of the CanC remains elusive.

A newly observed phenomenon in the Canary Basin are several "eddy corridors" that originate at preferential locations along the northwest African coast (Sangrà et al., 2009). The most densely populated is the Canary Eddy Corridor (CEC) at ∼26°N (just south of the Canary Islands). Altimetry data show series of long-lived (>3 months), mesoscale, cyclones and anticyclones propagating westwards from the lee of the Canary Islands to as far west as ∼32°W. Transport in the corridor is estimated to be greater than a quarter (i.e., ∼1 Sv) that of the CanC, with implications for primary production and the offshore export of carbon and organic material to the oligotrophic ocean interior. It is speculated that the eddies are island generated but, given the observations of eddy corridors at other latitudes, other processes such as baroclinic instability of the upwelling front at the coast may also play a role.

A numerical model is an important tool to tackle the uncertainties about the Canary Current and the Canary Eddy Corridor outlined above. A model provides synopticity and

resolution, which cannot be achieved with current observational approaches.

4.1.2. Modelling studies

In the years since Spall (1990) presented the first eddy-resolving (0.4°) regional model solution for the Canary Basin, a significant number of Canary Basin modelling studies have emerged. At the basin scale, the work of Smith et al. (2000) stands out for being the first to capture the AzC. Theirs was a 0.1° simulation of the North Atlantic, which used realistic winds covering the period 1985 - 1996. Johnson and Stevens (2000) presented a 0.16° regional model solution which focused on the area between the Azores, the Canary Islands and the Strait of Gibraltar. The model was run for 8 years and achieved good representation of the regional features and circulation, especially variability associated with the AzC and CanC. Spreading of MW was consistent with observations as far as Madeira. In a second study, Stevens and Johnson (2003) used outputs from their 0.16° solution to force a nested 4-year simulation at 0.08°, in order to examine filament activity off the northwest African coast.

Comparative studies between the Canary and California upwelling systems have been done by Marchesiello et al. (2004) and Marchesiello and Estrade (2009). Whilst these papers are somewhat limited in scope, and detailed descriptions of the upwellings are not given, they suggest that lower mesoscale energy in the Canary upwelling results from differences in stratification between the two systems. Marchesiello and Estrade (2009) further argue that topography differences also play a role: upwelling intensity and frontal formation are affected by the topography of the shelf, which is distinct for the two regions.

Concerning the forcing and generation of the AzC, Kida et al. (2008) in an idealised study show that entrainment by the Mediterranean Outflow (MO) is a plausible mechanism to explain the dynamics of the AzC. Earlier work to establish the potential impact of the MO on the circulation in the upper layers of the northeast Atlantic was done by Jia (2000), who showed that the formation of the AzC in an Ocean General Circulation Model (OGCM) is affected by the presence or absence of MW characteristics in the Gulf of Cadiz. Peliz et al. (2007) present a high-resolution modelling study focusing on the circulation in the Gulf of Cadiz. They achieve an accurate representation of the AzC. In their solution, the geostrophic flow-field east of Madeira is associated with a large cyclonic recirculation cell, which is predicted by β-plume models. They remark that the wind is likely to play a complementary role in AzC forcing. Townsend et al. (2000) obtain credible AzC circulations in a suite of numerical experiments (without MW influence) to evaluate different wind products. Townsend et al. (2000) conclude that wind forcing through Sverdrup dynamics may explain up to $\sim$20% (i.e., 1 - 2 Sv) of the transport of the AzC.

In spite of the above modelling efforts there is still no evaluation of the mean seasonal cycle and variability of the Canary Basin using a high-resolution, quasi-equilibrium, long-term solution from a regional ocean numerical model. The goal of this paper is to address this issue using the Regional Ocean Modelling System (ROMS; Shchepetkin and McWilliams,

2005, 2009b). Our main focus is the question identified in Section 4.1.1, namely to determine the seasonal path of the CanC north of the Canary Islands. We investigate the importance of the AzC as a source for the CanC, by including (excluding) the AzC in simulations with an open (closed) Strait of Gibraltar. Finally, we track mesoscale eddies in the model outputs in order to detect the existence of the Canary Eddy Corridor in the solution. The tracks can provide information about the sites of origin of the eddies, and also any temporal dependence.

The paper is organised as follows: Section 4.2 gives a detailed description of the model configuration setup, and the methodologies we have developed in realising the present solution. In Section 4.3 an extensive validation of the model solution by means of comparison with a range of observations is performed. This solution is presently in use as a parent solution to force the boundaries of several higher-resolution regional configurations within the Canary Basin, the validation serves to underpin these studies, as well as the results presented in the subsequent sections of this paper. Sections 4.4 and 4.5 are concerned, respectively, with the AzC and the CanC. Each section commences with a short review of the work that has been done on these currents, followed by the model results and diagnostics. Section 4.6 presents results from the Canary Eddy Corridor tracking experiment. Finally, Section 4.7 presents some brief conclusions.

4.2. The numerical model configuration

Following the examples of the USWC and Peru upwelling model simulations of, respectively, Marchesiello et al. (2003) and Penven et al. (2005), we base our model on a monthly climatological forcing cycle. This approach, where synoptic and interannual forcing is excluded, reveals the intrinsic variability that occurs at smaller scales within a regional system, while capturing basin-scale structures that are determined by low-frequency atmospheric forcing at the surface, and also transmitted through the open model boundaries. We use high-resolution climatological data to force the model, including a 0.25° wind climatology and a custom-built temperature and salinity climatology of the northeast Atlantic.

4.2.1. The Regional Ocean Modelling System (ROMS)

ROMS is a free-surface, primitive-equation, curvilinear-coordinate ocean model, where the barotropic and baroclinic momentum equations are resolved separately. ROMS uses a terrain-following (or *sigma*) vertical coordinate system (Haidvogel and Beckmann, 1999). We use the UCLA version of the ROMS code (Shchepetkin and McWilliams, 2005, 2009b). Recent developments in UCLA ROMS include a modification to the commonly used Flather-type (Flather, 1976) barotropic open boundary condition (OBC) (Section 3.2.1.2 on page 48), and a new sigma-coordinate transformation (Shchepetkin and McWilliams, 2009a). Subgrid-scale vertical mixing processes are parameterised using the non-local K-profile planetary (KPP) boundary layer formulation of Large et al. (1994).

Table 4.1.: Grid and configuration parameters for the L0 model configuration.

	L0
Horizontal resolution [km]	7.5
Length [years]	50
Latitude [°N]	6° - 51°
Longitude [°W]	1° - 45°
Grid dimensions [km^2]	3315 × 4845
Grid size	442 × 646 × 32
Minimum depth [m]	15

4.2.2. Model domain

4.2.2.1. The grid

The ocean model experiments were conducted using a high resolution 7.5-km grid (hereinafter L0) covering the eastern North Atlantic, from ∼7°N at Monrovia (Liberia) to ∼48.5°N at Brest (northwest France). The area of the L0 domain, outlined in red in Figure 4.1, is 3315 × 4845 km^2. The model grid employs 32 levels in the vertical. Increased near-surface resolution is achieved over the domain using a surface stretching factor $\theta_s = 6$, while at the bottom $\theta_b = 0$ (Haidvogel and Beckmann, 1999). The sigma-coordinate system is a new formulation which is designed to ensure good resolution of the thermocline independently of the total depth, h (Shchepetkin and McWilliams, 2009b). Table 4.1 provides a summary of the characteristics and parameterisations relating to the L0 configuration.

We will demonstrate that this domain provides a good representation of the seasonal circulation and variability of the region. In particular, we have sought a solution that reproduces the high levels of mesoscale variability associated with the NAC in the northwest of the domain (Section 4.1), the meridional sea level and density gradients at the latitude of the AzFC (∼34°N) and, in the east, as realistic an exchange at the Strait of Gibraltar as the [relatively coarse (Serra et al., 2005)] resolution permits. For the latter objective we leave the Strait of Gibraltar open and parameterise the flux as will be detailed in Section 4.2.2.3. In order not to suppress NAC variability which is generated near to the open boundary in the northwestern part of the domain, we use a small sponge[2] set to 25 m^2 s^{-1}. Overall, L0 is intended to capture the anticyclonic circulation of the subtropical gyre: eastward flow in the north at around 34°N (AzC), southern return flow and upwelling parallel to the northwest African coast (CanC and CanUC) and, finally, a westward return flow out of the domain (NEC).

The horizontal resolution of L0 (7.5 km) is about a quarter the *Rossby* radius near to the AzC (Chelton et al., 1998). This is below the 0.1° threshold for model eddy-resolution

[2]Early experiments with a 15-km grid using sponge values of $\gtrsim$100 m^2 s^{-1} were unsatisfactory because high SSH variance related to the NAC west of the MAR was largely absent.

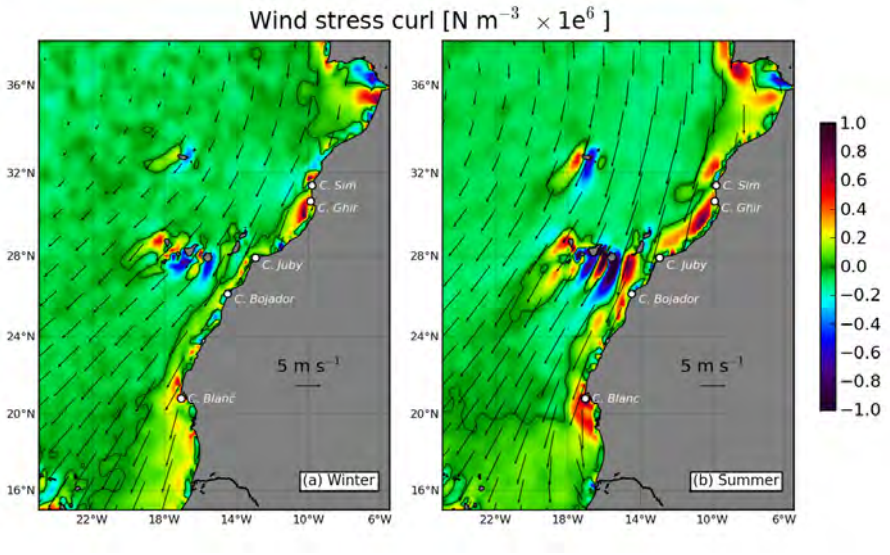

Figure 4.2.: Normalised wind stress curl from the QuikSCAT-derived SCOW wind stress climatology of Risien and Chelton (2008) over the northeast Atlantic in summer and winter. Vectors show the wind speed and direction. The zero wind stress curl is contoured in black.

described by Bryan and Smith (1998) and Smith et al. (2000). L0 is rotated to an angle of 004°T, permitting the eastern model boundary to generally follow the northwest African coastline. In the west the model boundary extends well beyond the MAR. The northwestern part of the domain is a region of high mesoscale variability associated with the inflowing NAC. All four model boundaries are open, although the eastern boundary contains only two non-land grid points at the Strait of Gibraltar, where exchange between the Mediterranean and North Atlantic occurs. The parameterisation of this exchange requires modification of the topography to ensure a minimum sill depth (300 m) at the strait. The model bathymetry is taken from the ETOPO2 2-minute topography of Smith and Sandwell (1997). The raw topography is coarsened to prevent aliasing errors before interpolation to the model grid, followed by several passes of a smoothing filter to reduce the r-factor to below 0.2 ($r = \triangle h/2h$; Haidvogel and Beckmann, 1999). Points where the model grid depth is shallower than 15 m are reset to 15 m.

4.2.2.2. Forcing and initial file preparation

Monthly climatological surface forcing files are created using the tools described by Penven et al. (2008), which include heat- and freshwater (E-P) fluxes provided by the 1° Comprehensive Ocean-Atmosphere Dataset climatology (COADS; da Silva et al., 1994; Woodruff et al., 1998; Worley et al., 2005). We use a high resolution (0.25°) surface wind stress product, the 8-year Scatterometer Climatology of Ocean Winds (SCOW, based on QuikSCAT) climatology by Risien and Chelton (2008) (see Table 4.2). Figure 4.2 shows fields of the mean SCOW summer and winter wind stress curl at the Canary Islands and along the northwest African coast. There is a general dominance of strong cyclonic curl along the coast, and

weak anticyclonic curl offshore (Bakun and Nelson, 1991; Mittelstaedt, 1991). Alternating bands of cyclonic and anticyclonic curl downstream of Madeira and the Canaries show that atmospheric island wakes are resolved in SCOW (Chelton et al., 2004). The figures illustrate the large differences in the curl that occur along the coast during the seasonal cycle. In summer, particularly strong cyclonic curl lies directly adjacent to Cape Sim at 31.4°N. This may be related to the influence of the Atlas mountain chain (northern Morocco) on the summer Trade winds (Hagen et al., 1996).

There is a mild restoration (360 days) of the sea surface temperature (SST, 9-km Pathfinder) and sea surface salinity (SSS) to climatological values (Barnier et al., 1995).

Lateral boundary forcing and initialisation files are prepared using temperature and salinity data from the monthly northeast Atlantic climatology (hereinafter NEAClim) of Troupin et al. (2009a). This climatology has a grid resolution of 0.1° and is based on a dataset compiled from multiple sources, from which duplicates and outliers are removed. The interpolation technique consists of solving a variational principle using a finite-element method which allows for a better resolution of the coastal area. Hence, use of NEAClim may be advantageous in the nearshore regions, and also to better resolve dynamically-important features such as the Azores front at the western model boundary. The data are linearly interpolated to the model grid. Geostrophic baroclinic velocity components are calculated through the thermal wind relation:

$$\mathbf{u}\,(z) = \mathbf{u}_\zeta + \frac{1}{f}\int_\zeta^z \left(-\frac{g}{\bar{\rho}} \times \nabla\rho\right) dz, \tag{4.1}$$

where $\mathbf{u}$ is the horizontal velocity, $\mathbf{u}_\zeta$ the horizontal velocity at the sea surface (ζ), f the *Coriolis* parameter, g the gravitational acceleration and, ρ the density corresponding to each month of NEAClim. The (reference level) sea surface geostrophic velocity, $\mathbf{u}_\zeta$, is calculated as:

$$u_\zeta = -\frac{g}{f}\frac{\partial\zeta}{\partial y}, \qquad v_\zeta = \frac{g}{f}\frac{\partial\zeta}{\partial x}, \tag{4.2}$$

where ζ is first interpolated to the model grid from a monthly sea surface height (SSH) climatology compiled from 15 years of AVISO absolute sea level data (see Table 4.2).

An *Ekman* velocity correction, shown in Figure 4.3, is applied to $\mathbf{u}$. Because of seasonal and spatial variability of the *Ekman* depth over the large L0 domain, we apply a variable *Ekman* layer as follows: we assume that the velocities (u, v) from a monthly mean of a multiple year ROMS solution will be in balance with the wind stress vector, i.e., the *Ekman* profile is close to that of an idealised *Ekman* profile, with differences likely arising from details of the ROMS vertical mixing scheme (KPP; Large et al., 1994). Hence, from a July monthly average of an early version of L0 (hereinafter $\mathrm{L0}_{early}$), we took a series of velocity profiles from within the interior of the domain (i.e., away from the sponge layer). Profiles that were shallow ($h < 2000$ m) or where the wind stress was weak ($\tau < 0.05$ N m^{-2}) were excluded. The profiles were normalised in the vertical by *hbl*, the mixed layer depth as

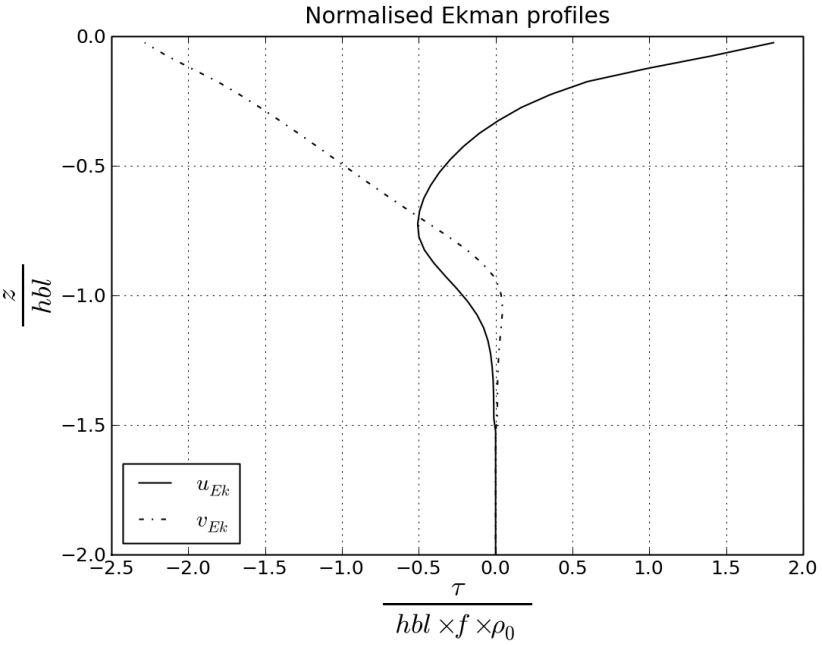

Figure 4.3.: Normalised *Ekman* layer velocity profiles (u_{Ek}, v_{Ek}) applied to the baroclinic velocities during preparation of the model boundary forcing file.

determined by KPP and, in the horizontal, the wind stress (τ_u, τ_v) was scaled by $hbl \times f \times \rho_0$ (ρ_0 = 1027.4 kg m^{-3}). The resulting averages of the non-dimensional profiles are used to compute the L0 *Ekman* profiles using τ, f, ρ_0 and the monthly ROMS mixed layer depth, hbl, from L0$_{early}$. This depth, which therefore defines the depth of the *Ekman* layer, is extrapolated from the interior of the sponge layer to the model boundaries. Once the *Ekman* correction is applied to **u**, barotropic velocities are calculated by integrating over h. Finally, a barotropic flux correction is calculated and applied to the velocities in order to enforce volume conservation (Section 3.2.3.2 on page 56). The eastern (Strait of Gibraltar) boundary is treated differently as detailed in the next section below. All of the variables located at the boundaries are saved to a monthly (2D) boundary forcing file.

The model is initialised using January values from NEAClim and AVISO, processed similarly to the boundary forcing file.

4.2.2.3. Parameterisation at the Strait of Gibraltar

The open boundary at the 300-m deep Strait of Gibraltar is a critical location that controls the exchange between surface (top 150 m) Atlantic-to-Mediterranean flow of NACW and, at depth (bottom 150 m), Mediterranean-to-Atlantic outflow of dense Mediterranean Water (MW). A parameterisation of the prognostic variables in the lateral boundary forcing file is required to enforce the required fluxes which are, approximately, 0.7 Sv (MW, bottom) and 0.8 Sv (NACW, surface) (Tsimplis and Bryden, 2000; Baschek et al., 2001; Harzallah, 2009). Following the methodology laid out by Peliz et al. (2007), we use monthly Strait

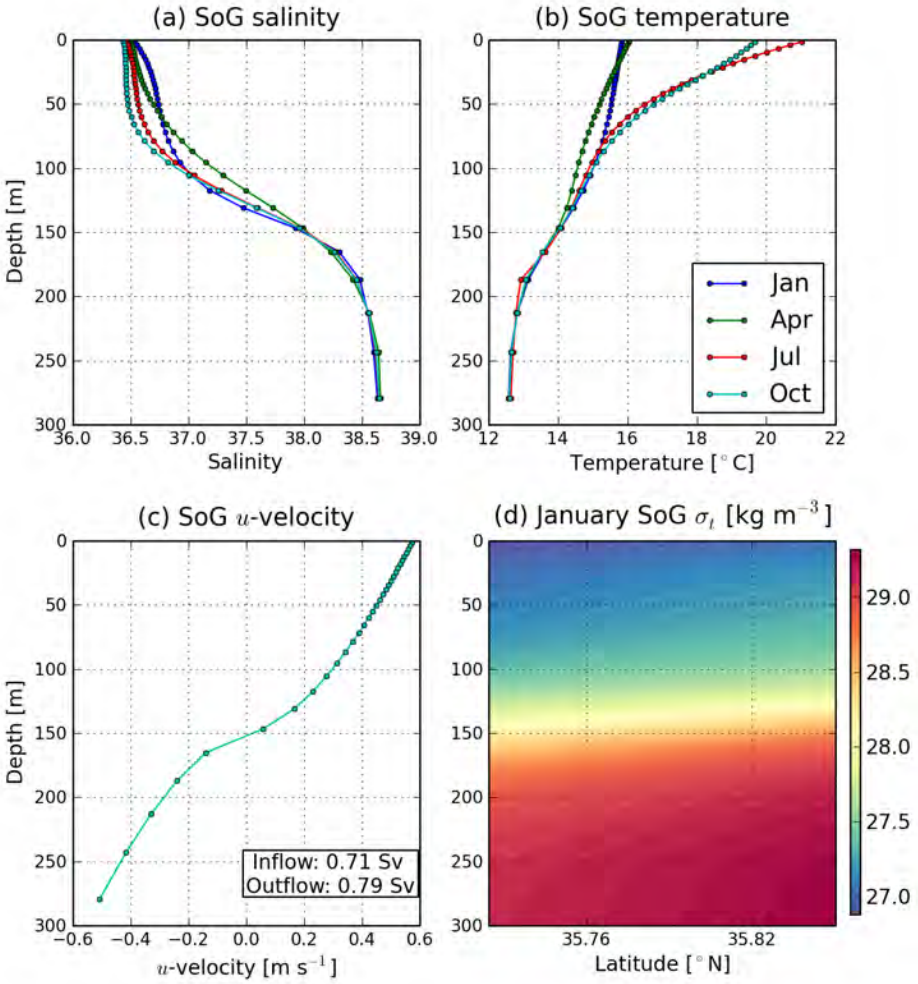

Figure 4.4.: Vertical profiles of (a) salinity, (b) temperature and (c) u-velocity imposed at the Strait of Gibraltar (SoG) open boundary in the L0 model domain. For salinity and temperature, the four profiles plotted correspond to January, April, July and October. The velocity profile defines respective transports into and out of the domain of 0.71 and 0.79 Sv. The open channel occupies two model grid cells, bold dots show the depths of the 32 vertical sigma levels at the 300-m deep strait. (d) Shows a geostrophically-balanced January density anomaly section across the strait that corresponds to the parameterised salinity and temperature.

of Gibraltar salinity and temperature profiles from NEAClim for the surface layers. In the bottom layers, salinity and temperature for all months are set as follows: 150+ m - 14.23°C, 38.35; 170+ m - 13.0°C, 38.5; 200+ m - 12.8°C, 38.51; 250+ m - 12.6°C, 38.65. A cubic spline fitted through the values provides continuous profiles at the model sigma depths. A simple algebraic curve gives a velocity profile appropriate to the required Strait of Gibraltar volume transports: fluxes are 0.79 Sv exiting the model domain (entering the Mediterranean) and 0.71 Sv entering at depth; these values ensure a net annual salt flux of ∼0 Sv (Baringer and Price, 1997). We do not attempt to introduce seasonality into the transport because we are not aware of any clear observations providing such information in the Strait of Gibraltar. Finally, to ensure geostrophic balance, a small correction is made to the salinity across the strait. The resulting profiles (S, T, u) are shown in Figures 4.4a-c. The cross-strait velocity, v, is set to 0 m s^{-1}. Figure 4.4d shows the cross-strait density anomaly, where the sloping isopycnals indicate the effect of the salinity correction.

Within the L0 domain, the eastern OBC applies only to the open Strait of Gibraltar. It is treated the same way as the other three boundaries, except for the barotropic component: the Flather-type, characteristic OBC (Section 3.2.1.2 on page 48) is replaced with a *Neumann* condition for the free surface elevation, ζ, and prescribed $\bar{u}$, $\bar{v}$. This change is needed to avoid interference with the other open ocean boundaries, which effectively act in such a way that the normal barotropic velocity component is always adjusted to minimise mismatches in ζ between the model solution and the external data; this adjustment happens in barotropic time, i.e., it is very stiff. As a result, imposing the Flather-type OBC at the Strait of Gibraltar results in the need to specify ζ in the Mediterranean and the appearance of a multiply-connected (double in this case) domain problem, and, correspondingly, flow sensitivity to the difference between external ζ specified at the Strait of Gibraltar OBC versus elsewhere on the other three sides of the domain.

From a physical point of view, sea surface height in the Mediterranean is entirely controlled by (in fact, slaved to) the Atlantic, and the integral water flux through the Strait of Gibraltar is controlled by integral precipitation/evaporation (and also riverine inflow) in the Mediterranean, in such a way that there is continuity in the free surface between the Mediterranean and the Atlantic. This is distinct, and somewhat opposite in a mathematical sense, to the Flather-type OBC: the prescribed $\bar{u}$ (a small net flow into the Mediterranean) serves to parameterise net evaporation in the Mediterranean, while ζ is free to adjust itself to the conditions inside the model domain.

4.3. Model/data comparison

A validation of the model solution is performed by considering the evolution of select model diagnostic variables, and by comparing mean and eddy variables with observations. Annual and seasonal means are computed, where the seasons are defined as successive 3-month periods, starting from winter as months 1 through 3. For L0 we use a 40-year mean (years 11 to 50). In Section 4.4.1 on page 92 we refer to an L0-MW mean; this is computed using

Table 4.2.: Description of observational data products used for forcing and/or in the validation of the L0 solution.

Product	Description
AVISO	Fifteen years (October 1992 to May 2007) of mean absolute dynamic topography, computed by Archiving, Validation and Interpretation of Satellite Oceanographic data using merged altimeter data and the Rio05 mean dynamic topography (Rio and Hernandez, 2004; Pascual et al., 2006).
SVP drifters	The Surface Velocity Program monthly drifter-derived climatology of surface currents at 1° resolution, described by Lumpkin and Garraffo (2005). The drifters are drogued at 15 m.
Pathfinder SST	Monthly climatology of 9.28-km global SST from the NOAA/NASA AVHRR Oceans Pathfinder Program (Version 4, Kilpatrick et al., 2001).
OSTIA SST	Global high resolution (6 km) SST from the Operational Sea Surface Temperature and Sea Ice Analysis (Stark et al., 2007). Records are daily, beginning in April 2006.
Subduction Experiment moorings	Five moorings measuring currents and temperature over the water column, deployed as part of the Subduction Experiment (Weller et al., 2004) in the northeastern Atlantic between June 1991 and June 1993. See Figure 4.1 on page 73 for locations.
ESTOC mooring	European Station for Time-Series in the Ocean, Canary Islands, a deep water mooring deployed 100 km to the north of the Gran Canaria (Canary Islands) since 1991 (Llinás et al., 1994). We use data for the period 1994 - 1997. See Figure 4.1 on page 73 for location.

years 5 to 15 of L0, and is used for comparison with a 15-year L0 simulation where the Strait of Gibraltar is closed (L0-NOMW).

The observational data sources and products used throughout the text are summarised in Table 4.2.

4.3.1. Equilibrium solutions

L0 is integrated over 50 years. Instantaneous values are saved at the end of every model month (30 days), whilst averages are saved every 3 days (10 records per month). Figure 4.5a details the evolution of the volume- (0 - 300 m) and surface-averaged kinetic energies (VKE, SKE). L0 requires a minimum spinup period of ∼4 years, after which SKE oscillates quasi-periodically around an equilibrium value, showing a clear seasonal signal. Peak energy values occur in the summertime, consistent with the climatological wind applied at the surface. The seasonal cycle is less clear in the VKE. Figure 4.5b shows the evolution of the surface averaged salinity. There is an initial sharp increase but after about year 12 the curve is stable at around 36.54. A possible reason for the initial adjustment may be differences between the initial sea surface salinity (SSS) from NEAClim and the COADS E-P (towards which the model SSS is restored). Temperature and volume (not shown, see Appendix A.1)

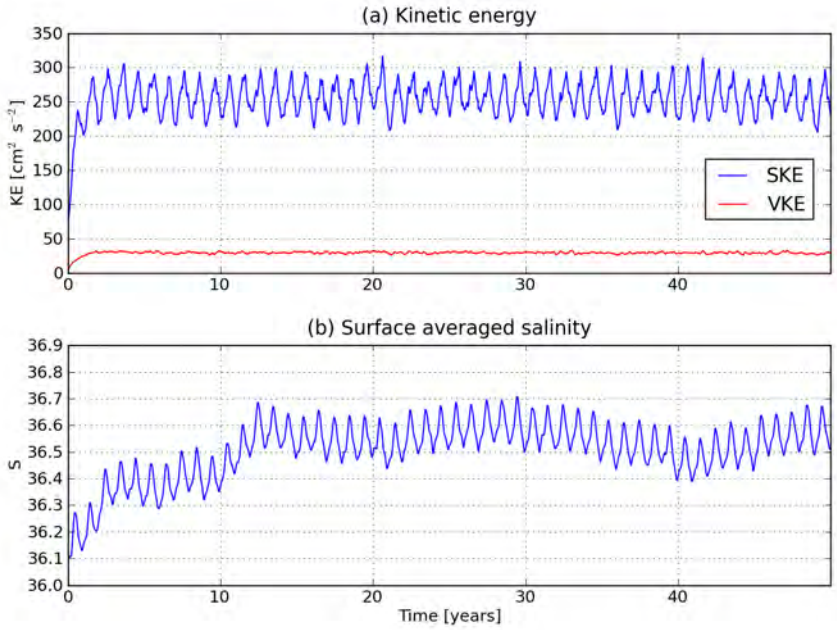

Figure 4.5.: Time evolution of (a) the surface- (SKE) and volume-averaged kinetic energy (VKE) and, (b) the surface-averaged salinity from the L0 model solution.

both show minor adjustments during the first 12 years, but thereafter have clear seasonal cycles around constant values with no drift.

4.3.2. Sea surface temperature

Figure 4.6 compares summer snapshots of L0 SST with summer SST observations obtained from OSTIA (Table 4.2). The L0 fields are 3-day averages, OSTIA are daily with a resolution of 6 km. The temperature ranges and distributions in the model and observed SSTs match closely and structural patterns are consistent: gradients in the isotherms in the offshore region have the typical summertime zonal alignment (Barton et al., 1998); upwelling-related filament activity is evident at the major capes, particularly at Ghir, Juby and Bojador (Barton et al., 1998; Pelegrí et al., 2005b). These figures emphasize the realistic and intrinsic variability within the model solution, despite use of a climatological forcing regime (Marchesiello et al., 2003).

The summertime meridional extent of the upwelling in the south is well captured by the model (Barton et al., 1998): at Cape Blanc (21°N) there is a sharp front between upwelled NACW in the north, where upwelling is permanent, and SACW to the south where the summer winds are weak and unstable (Mittelstaedt, 1991). The front is the CVFZ (Section 4.1.1), which is a permanent feature whose position is shown in L0 by the convoluted intersection of the $S = 36.0$ and $\sigma_t = 26.5$ kg m^{-3} surfaces to the west of Cape Blanc (Figures 4.6a,c) (Pastor et al., 2008). South of the CVFZ, the absence of summertime upwelling permits seasonal strengthening and northward extension of the NECC, spreading

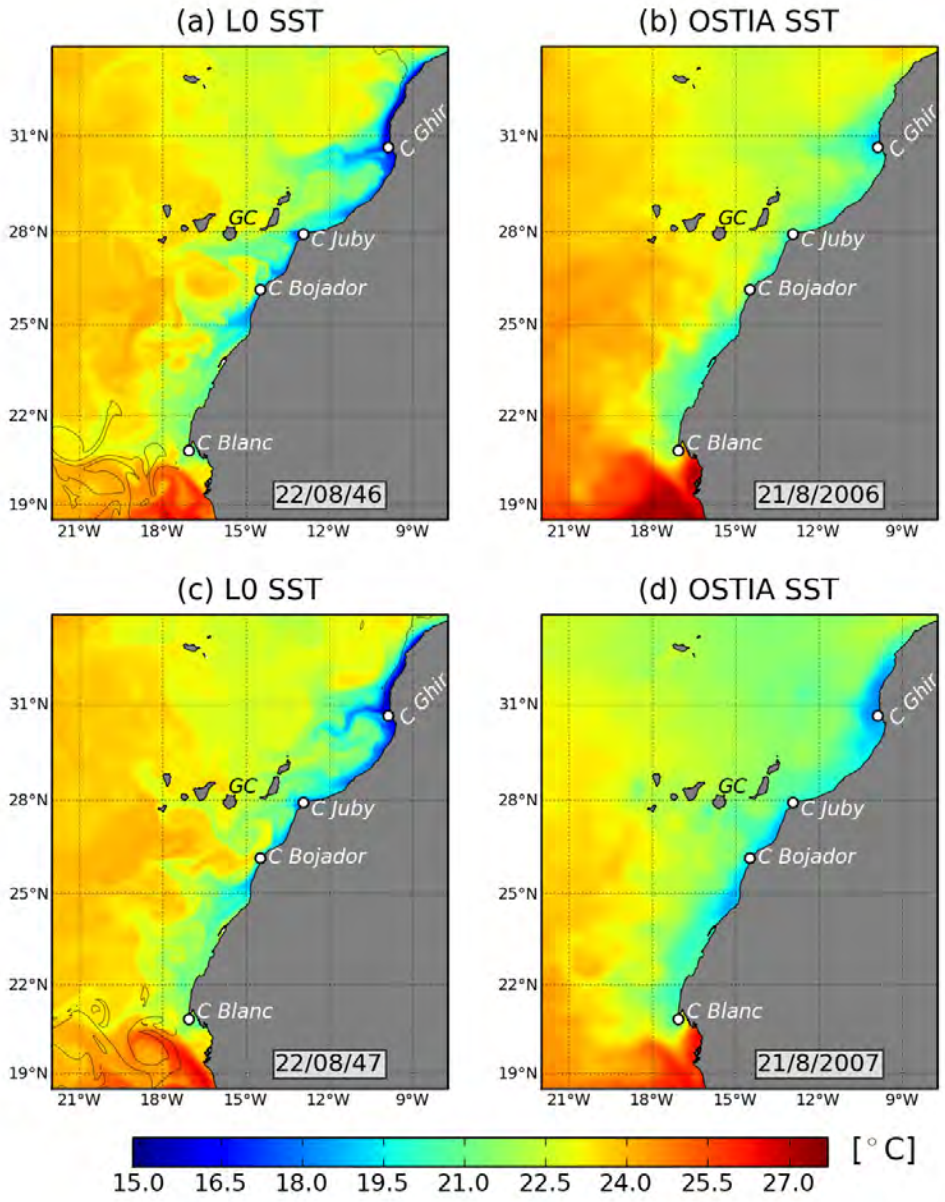

Figure 4.6.: Comparison of L0 ROMS (a, c) and OSTIA (b, d) SST in summer. The L0 SSTs are 3-day averages, dates correspond to day/month/year of the solution. The OSTIA SSTs are daily averages. The dark thin line in the model figures is the intersection of the 26.5-kg-m^{-3} density surface and isohaline 36.0, which marks the location of the Cape Verde Frontal Zone (Pastor et al., 2008).

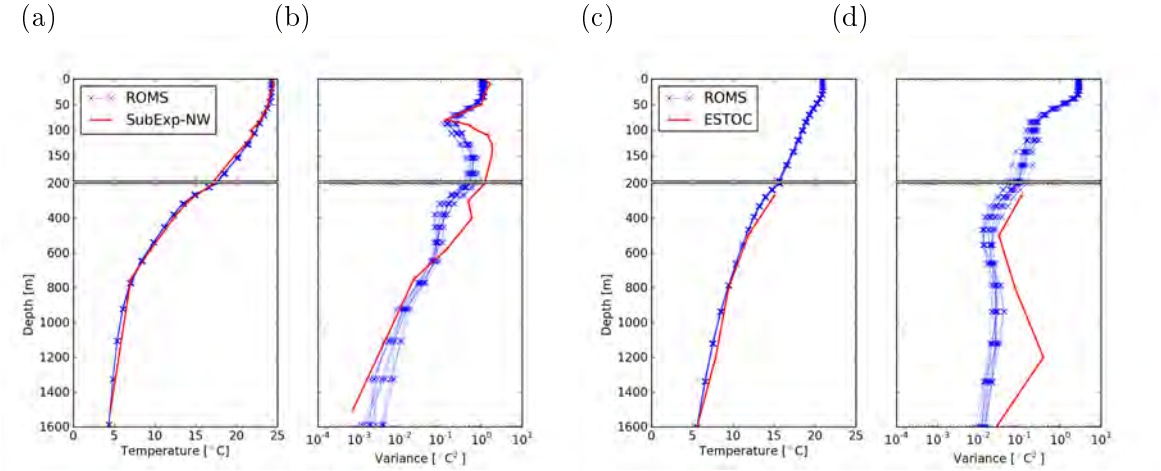

Figure 4.7.: Profiles of (a, c) mean temperature and its (b, d) variance. (a) and (b) compare the SubExp-SW mooring with co-located L0 profiles. (c) and (d) compare the ESTOC mooring with co-located L0 profiles. Note the change of depth-scale at 200 m.

tropical warm surface water (>27°C) from the open ocean towards the coast. The model is seen to capture this spreading south of 21°N. At the Banc d'Arguin just south of Cape Blanc, strong surface heating observed by OSTIA is not captured by the model, possibly a consequence of uncertainty in the nearshore structure of the model wind forcing (Capet et al., 2004).

4.3.3. Temperature profiles

The subsurface performance of the model can be assessed by considering tracer vertical profiles. Observed data are available from several projects where moorings have been deployed in the northeast Atlantic. From the Subduction Experiment (SubExp; Weller et al., 2004) we obtained five 3-year time series of temperature data at various depths. From the ESTOC mooring (Knoll et al., 2002), ∼100 km north of Gran Canaria, we obtained a similar 3-year time series. The locations of the moorings are shown in Figure 4.1 on page 73.

Figure 4.7 shows profiles of the mean temperature and its variance from SubExp-SW and ESTOC, together with ensembles of co-located L0 profiles. The ensembles comprise ten 3-year averages taken from model years 30 - 41.

Figure 4.7a shows mean temperature from the surface to 1600 m. The SubExp-SW and L0 ensemble profiles show generally close agreement at all depths, particularly in the surface layers above ∼100 m. Below 200 m, the L0 ensemble has a slight negative bias (<0.5°C). The variances in Figure 4.7b agree closely above 100 m. Below this depth to ∼600 m, the L0 variance tends to be smaller than SubExp-SW.

Surface ESTOC data are currently only available below 270 m. In Figure 4.7c the mean profiles show that the model has a small consistent negative bias in compare to the ESTOC data: at ∼280 m the L0 means are ∼1°C below the ESTOC values. The profiles then converge to under ∼0.5°C, until the depth range 800 - 1400 m. Here, MW present in the

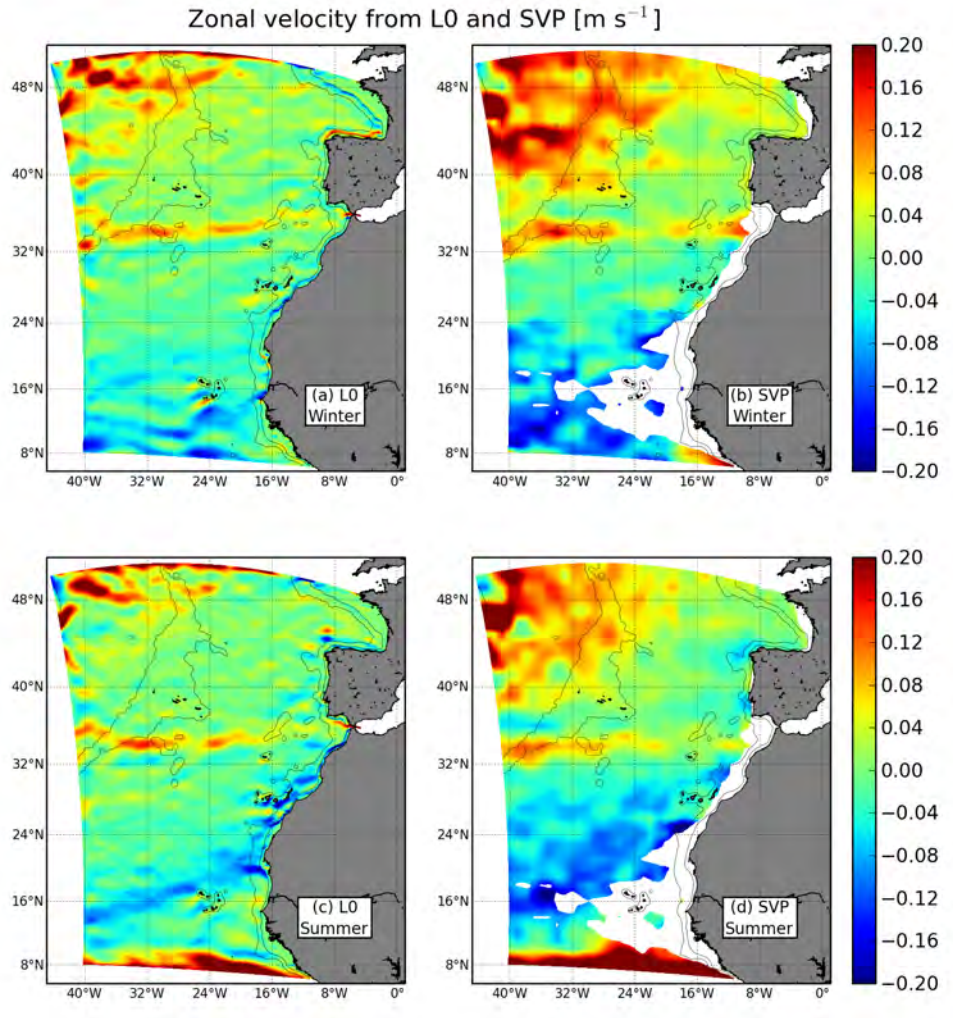

Figure 4.8.: Winter and summer comparisons of mean zonal velocities from L0 (depth-averaged 10 - 20 m) and from the SVP drifter climatology. The 300- and 3000-m isobaths are plotted in black. SVP regions with less than 50 drifter days per square degree are masked.

ESTOC profile is absent in L0 at this location (see Section 4.3.6). For the variances in Figure 4.7d, the L0 ensemble is again lower than the observed, with the largest difference at MW depths. Low-frequency variability is expected to be influenced significantly in the eastern basins by MW water in this depth range (Müller and Siedler, 1992).

4.3.4. Zonal surface currents

Winter and summer distributions of zonal surface currents from L0 and from the SVP drifter climatology are shown in Figure 4.8. The SVP velocity fields have generally broader patterns and greater magnitudes. In part, this may be attributed to the coarse 1° resolution of these data. The highest velocities, eastward in direction, are found in the northwestern quarter of the domain, which covers the southern reaches of the NAC. The current is seen to enter the domain at the western boundary in two adjacent branches (43° and 46°N) just south of the

Flemish Cap (Figure 4.1). The broad eastward flow field is constrained by the MAR (Bower et al., 2002), so that east of ∼24°W the velocities are less than half their western values. The southern reaches of the NAC-related flow field include the Azores islands. In the southern half of the domain the return (westward) flowing NEC is dominant. Its signal is relatively smooth if compared to the NAC. Along the southern boundary, the seasonally-varying NECC is most apparent in summer, when it is at its most northerly position. Intersecting the domain at 34° - 35°N is the AzC, a prominent feature in all seasons, which displays small meanders along its axis. The intensity of the current is variable along its length, being strongest between ∼24° - 40°W.

Qualitatively, there is a reasonable correspondence with the ROMS velocity distributions. The large-scale features, i.e., NAC, AzC, NEC are evident, though have a finer structure than the SVP patterns. The AzC is narrower, and also strongest at ∼24° - 40°W. However, in both seasons, the L0 AzC weakens at ∼26°W. It is noteworthy that southwest of the Canary Islands, the region of the so-called Canary Eddy Corridor (CEC; Sangrà et al., 2009), there is agreement between model and data for a mean eastward counter-flow. The patterns are broad in winter. In summer, the L0 flow is intense and concentrated along ∼26°N. The summer SVP show only a weak flow, perhaps because of their low resolution. Counter-currents have been observed downstream of Hawaii and the Cape Verde islands (Chavanne et al., 2002).

4.3.5. Eddy variability

Eddy statistics are calculated from the model fields and compared with observations from merged satellite altimeter data (AVISO, Table 4.2). SSH variance is defined as $\langle \eta'^2 \rangle^{1/2}$. Angle brackets indicate time means and primes denote deviations from the time-mean quantities: $\eta = \langle \eta \rangle + \eta'$. Where a seasonal mean is used we refer to the product as *non-seasonal* and, conversely, using an annual mean we obtain a *seasonal* product. The EKE, used in Section 4.6.1, is defined as $\left(\langle u'^2 \rangle + \langle v'^2 \rangle \right) /2$.

4.3.5.1. Sea surface height variance

Figure 4.9 compares non-seasonal L0 SSH variance with AVISO SSH variance in winter through autumn. The large-scale distribution of variability is similar in all seasons in both model and altimetry. The largest SSH variability is found in the vicinity of the NAC and AzC, where baroclinic and barotropic instability is responsible for intense eddy generation (Le Traon and De Mey, 1994; Rossby, 1996).

In general, the model variability is lower than the observed, particularly for the AzC which is evident as a narrow but distinct feature at 34°N, extending eastward towards the Gulf of Cadiz. The high variability associated with the turbulent NAC occupies much of the northwestern quarter of the domain (Colin De Verdière et al., 1989; Müller and Siedler, 1992). In the northwest corner, a patch of low variability is associated with the shallow Flemish Cap (Figure 4.1 on page 73). The eastern extent of the NAC variability is constrained by

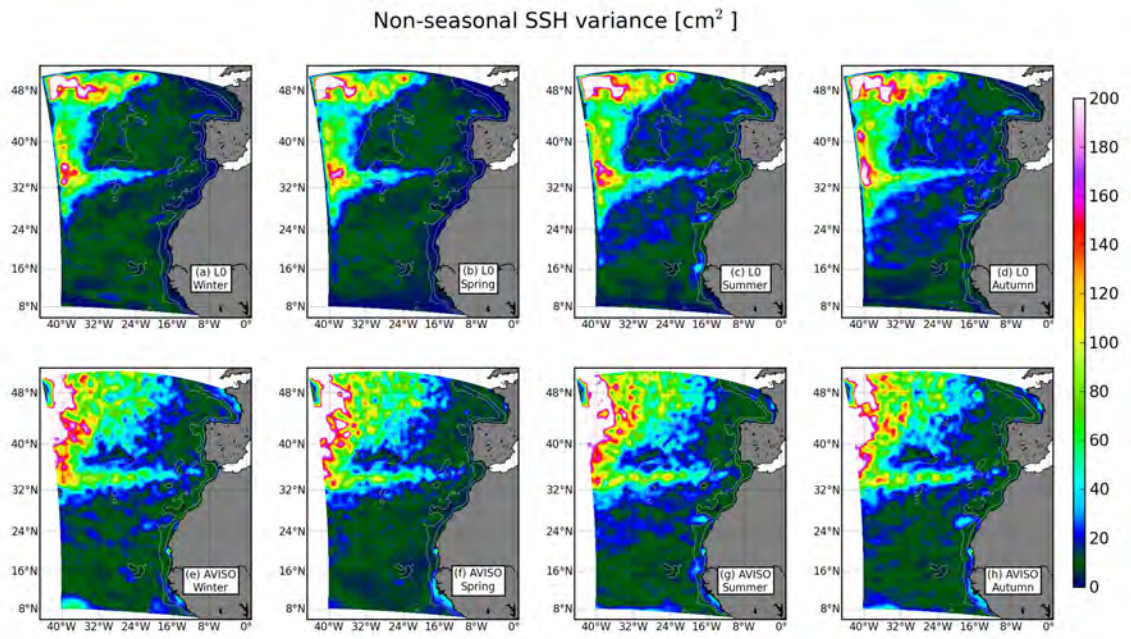

Figure 4.9.: Seasonal fields of non-seasonal sea surface height variance from L0 and from AVISO. The 300- and 3000-m isobaths are plotted in white.

the MAR (Bower et al., 2002), this effect is quite pronounced in the model. The model SSH variance between ∼42° - 46°N is, however, significantly lower than in the observations. This may be because of the exclusion of both low-frequency (i.e., interannual) and high-frequency (i.e., time- and lengthscales shorter than the boundary forcing) signals from the monthly climatological boundary forcing, effectively preventing the input of mesoscale variability through the open boundaries (see Appendix D on page 223).

The localised patches of increased variability south of the Canary Islands and of Madeira have a distinct seasonality, and here there is close correspondence between model and altimetry. The Canary Island variability increases in summer, and peaks in autumn, and is related to eddy activity (Arístegui et al., 1994). For Madeira the cycle is less clear, but is present nonetheless. At Cape Verde the altimetry show a faint positive anomaly in winter and spring. This signal is seen in the model in spring, but is very weak.

Other features of note are the high variability in AVISO over the Arguin Bank at 20°N, this was explained by Capet et al. (2008b) to be a shallow bank which experiences intense winds. Also, in L0 but not in AVISO, there is increased variability off northern Iberia, particularly in summer and autumn. This may be related to anticyclonic slope water eddies (SWODDIES; Pingree and Le Cann, 1992).

4.3.6. Mediterranean water spreading

A major feature of the thermohaline field of the North Atlantic is the Mediterranean salt tongue (Richardson et al., 1989, 2000). Figure 4.10 shows the model annual mean (a) salinity and (c) temperature at 1000 m. For comparison, observed annual mean fields from NEAClim

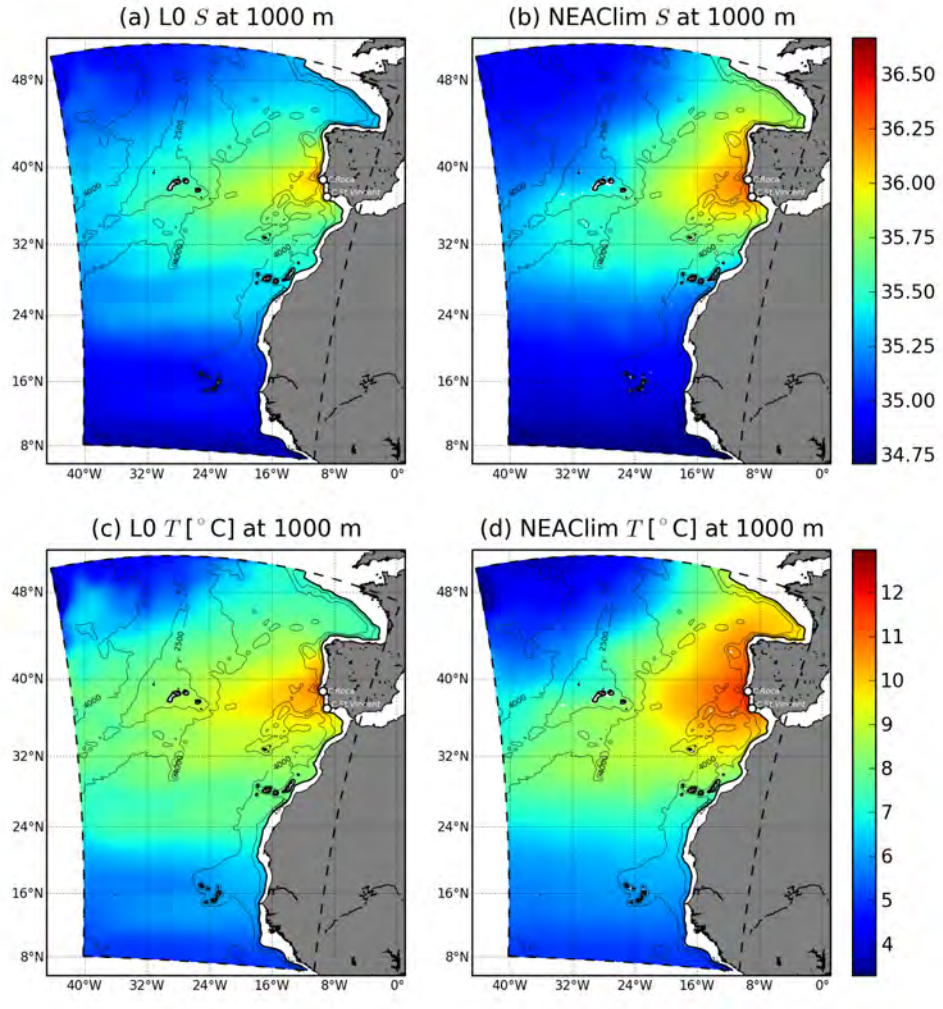

Figure 4.10.: Comparison of annual means of model L0 (a) salinity and (c) temperature, and the NEAClim climatology (b) salinity and (d) temperature, at 1000 m.

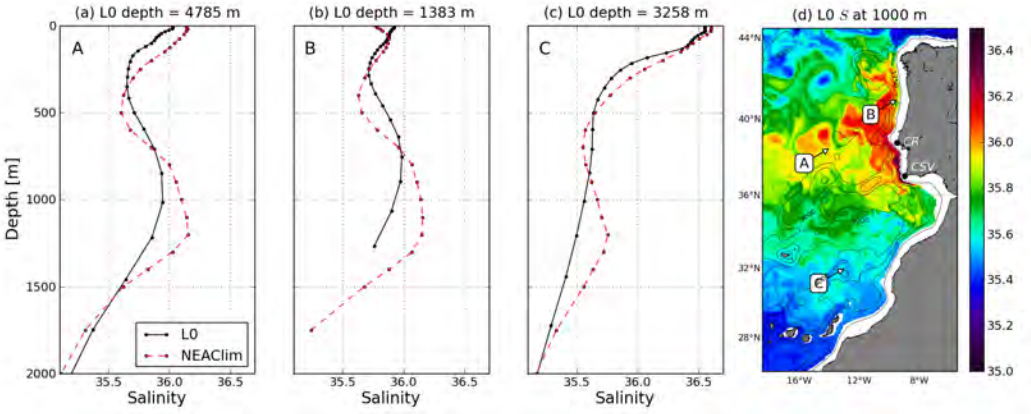

Figure 4.11.: Comparisons (a, b, c) of annual mean salinity profiles from L0 and NEAClim at three locations (A, B, C) off the eastern boundary. (d) Instantaneous L0 salinity field at 1000 m from January of model year 47. Arrows show profile locations. Isobaths are plotted at 500, 1750, 3000 and 4000 m. Capes Roca (CR) and St. Vincent (CSV) are shown.

are presented in Figures 4.10b,d. The NEAClim data show the warm and salty MW signal extending westward away from the Iberian Peninsula (IP), with the largest values for both salinity and temperature found just offshore of Cape Roca at 38.8°N. The model anomalies are similar in their zonal distributions at this latitude. However, their latitudinal ranges are rather smaller than the observed, particularly to the north.

Figure 4.11 compares profiles of annual mean salinity L0 and NEAClim at three locations near to the eastern boundary where MW is present in NEAClim. Location A is in deep water 400 km west of Cape Roca. The salinity profiles from both L0 and NEAClim show the characteristic bulge of MW between 500 and 1500 m depth. However, the L0 maximum is weaker and is located at 1000 m, which is ∼250 m above that of the climatology. Location B is over the western Iberian slope. MW is present in L0, but is again weaker and shallower than NEAClim. Location C is south of the AzFC within the CanC. Here there is still a significant MW presence in NEAClim but, in L0, MW is absent. The differences between L0 and NEAClim at the MW levels (and outside these levels too) most likely arise from spurious diapycnal mixing related to the tracer advection scheme (Marchesiello et al., 2009). A shallow bias in the model in the upper layers above 500 m is observed in all three profiles. This may be a result of the use of climatological wind forcing.

Figure 4.11d shows an L0 snapshot (month 1, year 47) of salinity at 1000 m. MW arrives at 1000 m as it begins to round Cape St. Vincent. The flow follows the slope until it nears Cape Roca, where it begins to spread offshore. The spreading appears to be affected by topography (Wang and Dewar, 2003).

In L0 few *Meddies* are captured. Figure 4.11d shows two eddy-like features which may be *Meddies* offshore of Cape Roca (at 14°W and 17°W). They both originate near to Cape Roca, rather than Cape St. Vincent which is the preferred generation site. A possible reason for the lack of *Meddies* at Cape St. Vincent may be poor resolution of the topography (no canyons) in the Gulf of Cadiz (Serra et al., 2005).

4.4. The Azores Front/Current system (AzFC)

In the last section the model solution has been shown to give a good representation of the mean and eddy circulation of the eastern subtropical gyre. The Azores Current (AzC) is an integral part of the gyre, which is supplied by the Gulf Stream and the North Atlantic Current (Klein and Seidler, 1989; Rossby, 1996; Juliano and Alves, 2007). In the region southeast of the Grand Banks, the Gulf Stream undergoes a complex splitting process: a major part of this division is to the northeast, becoming the North Atlantic Current. A portion of the remainder, which takes the form of streamers and eddies contained within and advected by a large-scale eastward drift, is concentrated into the well-defined baroclinic front which is the AzFC.

The ∼10-Sv baroclinic transport of the AzC is concentrated within a 0.25-m-s^{-1} jet of width ∼60 km, and depth ∼650 m. Early observations south and southeast of the Azores revealed an extensive, meandering, west-east subtropical front (Käse and Seidler, 1982; Käse et al., 1985). Mesoscale eddies were observed on both sides of the front with typical scales of 200 km. The frontal meanders were attributed to quasi-stationary *Rossby* waves originating at the eastern boundary of the Canary Basin, or to baroclinic instability of the jet. Suggested evidence for baroclinic instability is the absence of a strong mean meridional temperature gradient south of the front. The AzC is clearly visible in the geostrophic flow field (Figure 4.8).

Figure 4.12 shows zonally-averaged (18° - 24°W) mean velocity sections from L0, for the four seasons over the meridional range 30° - 38°N. Contours describe the density anomaly. A small seasonal transition is apparent. Autumn and winter have the highest eastward velocities at ∼0.1 m s^{-1}, and the current is at its deepest, ∼800 m. In spring and summer the current is weaker, ∼0.08 m s^{-1}, and closer to ∼700 m depth. Eastward transports range between 7.8 and 9.5 Sv. The Azores Counter-Current is present in the sections throughout the year, both north and south of the AzC, though it is more intense in the south.

A comparative zonal velocity section from the initialisation file (January mean) (not shown) has a similar velocity structure to the mean transport sections of Figure 4.12. The AzC is between 34° - 35°N, with a maximum velocity of 0.065 m s^{-1}. Transports are -1.2 and 8.2 Sv. Westward flow is present north and south of the AzC but is more intense to the south (0.05 m s^{-1}), in agreement with the model results.

4.4.1. Closure of the Strait of Gibraltar

In order to assess the influence of the AzC on the CanC, we ran an additional numerical experiment (hereinafter L0-NOMW) identical to L0 but with the Strait of Gibraltar closed. By blocking the flux at the Strait of Gibraltar, a principal forcing mechanism of the AzC is removed: A recent study by Kida et al. (2008) introduces the topographic β-plume, where the vorticity equation for basin-scale barotropic flow (Stommel, 1982; Pedlosky, 1996) is modified so that the gradient of topographic vorticity, rather than planetary vorticity, provides the primary control on the zonal flow. In the context of the AzC, entrainment by mixing of

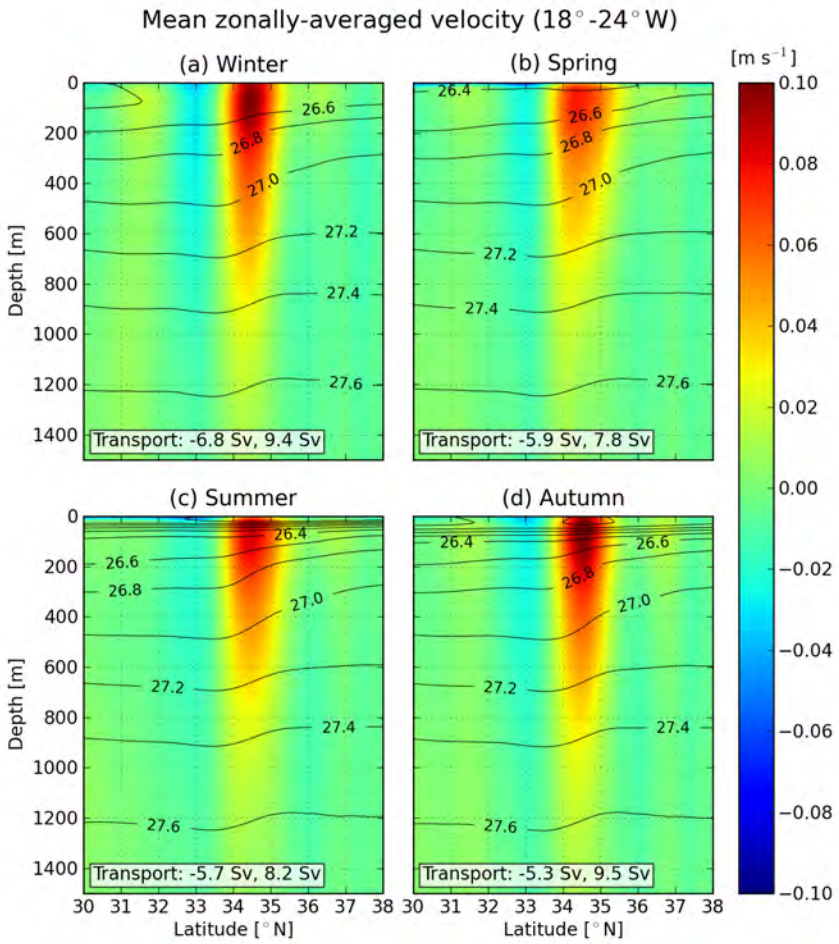

Figure 4.12.: Seasonal mean zonal velocities, averaged between 18° - 24°W from the surface to 1500 m. A clear Azores Current signal is present at 34° - 35°N. Contours of the density anomaly are plotted in black (kg m^{-3}).

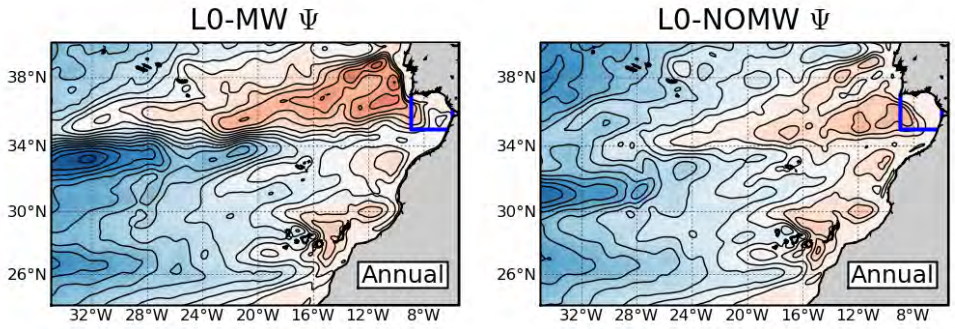

Figure 4.13.: Comparison of the depth-integrated (0 - 600 m) annual mean streamfunction for the L0-MW and L0-NOMW solutions. The L0-MW mean is taken over the same period as L0-NOMW. Contour intervals are equivalent to 1 Sv. Blue (red) corresponds to anticyclonic (cyclonic) circulation. The box region outlined in blue in the Gulf of Cadiz is used for the transport budget analysis of Table 4.3.

Table 4.3.: Annual and seasonal entrainment (Sv; downward positive) in the Gulf of Cadiz, calculated using the 600-m-deep box domain shown in Figure 4.13.

Solution	Annual	Winter	Spring	Summer	Autumn
L0-MW	1.46	1.47	1.28	1.34	1.73
L0-NOMW	0.22	0.22	0.17	0.14	0.34

NACW into the downflowing MW within the Gulf of Cadiz creates a mass sink, which must be balanced by either a mass source at the same latitude as the sink, or by dissipation. This process induces a zonal cyclonic circulatory cell, which may be seen as the AzC (and AzCC). Numerical studies by Jia (2000) and Özgökmen et al. (2001) have demonstrated that the absence of MW in the Gulf of Cadiz results in the absence of the AzC. More recently, Peliz et al. (2007) showed the cyclonic cell associated with the topographic β-plume in a high-resolution ROMS study.

Figure 4.13 compares the annual mean depth-integrated (0 - 600 m) streamfunction for L0-MW[3] and L0-NOMW. The streamfunction is computed following the method of Penven et al. (2005). For L0-MW, the AzC is evident at 34°N, transporting over 7 Sv at ∼21°W. The current appears to have three southward-turning branches: ∼27°, ∼20°, and ∼16°W near Madeira, consistent with observations (Stramma and Siedler, 1988; Juliano and Alves, 2007). In the Gulf of Cadiz and west of southern Iberia, a large zonal cyclonic recirculation cell loops around Cape St. Vincent before detaching and extending offshore. This cell is related to the topographic β-plume.

For L0-NOMW, the AzC is greatly weakened. At 21°W the transport is just 1.5 Sv, less than a quarter the L0-MW value. The remaining AzC signal is possibly related to the wind. Özgökmen et al. (2001) found through sensitivity experiments that while local cyclonic wind forcing in the Gulf of Cadiz may not account for the total transport of the AzC, it may enhance its strength.

A transport budget analysis in the Gulf of Cadiz enables an estimate to be made of the magnitude of the entrainment of MW. A 600-m-deep box region is defined in the Gulf of Cadiz in Figure 4.13. Results from the analysis, comparing L0-MW and L0-NOMW, are shown in Table 4.3. The annual entrainment when the Strait of Gibraltar is open is 1.46 Sv downwards. Seasonally, the largest entrainment is found in autumn, and the smallest in spring. When the Strait of Gibraltar is closed, entrainment falls by an order of magnitude for all seasons; autumn remains the season with the largest entrainment. The seasonal variability is not related to the flux at the Strait of Gibraltar, which is quasi-constant. A similar analysis by Peliz et al. (2007) yielded similar annual values.

The most interesting aspect of the L0-MW and L0-NOMW solutions is the circulation of the Canary Current to the south below about 32°N. The CanC is said to be fed by the AzC.

[3]L0-MW is an L0 mean calculated from L0 years 5 - 15, so as to correspond with L0-NOMW which was run for just 15 years.

Despite the marked differences to the north, the streamlines in Figure 4.13 between Cape Ghir, Madeira and the Canary Islands are remarkably similar. This result suggests that the Canary Current is relatively insensitive to variability in the Azores Current.

4.5. The Canary Current

The Canary Current is recognised as a seasonal boundary current with a well-defined but variable path (Stramma and Siedler, 1988; Navarro-Pérez and Barton, 2001; Pelegrí et al., 2005a; Machín et al., 2006a; Pelegrí et al., 2006). A summer peak in intensity has been observed by Stramma and Siedler (1988) and later Machín et al. (2006a). Stramma and Siedler (1988) related seasonal variability of the position of the CanC to seasonal shifts in the position of the subtropical gyre: they depicted the mean summer CanC at ∼32°N flowing midway between Madeira and the African shelf, while in winter it retreats westward closer to Madeira. Pelegrí et al. (2006) have stressed the importance of the role played by the CanUC, which they consider to be an eastward branch of the CanC. North of Cape Ghir, the CanUC along the coast is strongest in summer following the seasonal Trade wind cycle. In late autumn and winter, the CanUC separates from the coast at Cape Ghir, moving offshore to merge with the CanC (Pelegrí et al., 2005a). It is speculated that this separation away from the coast results in the formation of a large cyclonic loop that has the CanC extending around the western Canary Islands, with a portion recirculating north along the coast towards Cape Ghir. In spite of these efforts, uncertainty remains about the position of the CanC and its seasonal dependence, and the mechanism or mechanisms which govern its variability. A climatological model solution such as L0 is well placed to address these questions, and here we suggest an alternative description.

4.5.1. Meridional velocity at 32°N

Figure 4.14 shows 700-m deep L0 seasonal sections of mean meridional velocity across the CanC at 32°N, between the African coast and Madeira. Several localised regions of relatively intense (>0.03 m s^{-1}) equatorward flow stand out; these correspond to the CanC.

In summer, a comparatively broad surface intensified CanC is centred about 14°W. In the top 200 m the flow exceeds 0.03 m s^{-1}. At the coast, a second significant equatorward flow corresponds to the CanUC, for which there is an associated poleward undercurrent at depth. The undercurrent is the only poleward flux in the summer section, aside from within a thin surface *Ekman* layer. Equatorward flow is also seen at ∼16.5°W, which may be partially related to localised recirculation around Madeira which forms a barrier to the AzC (Zhou et al., 2000), and is present in the other seasons. In winter, there is a core of equatorward flow located at ∼11°W, i.e., within ∼150 km of the coast and ∼250 km east of the summer CanC position. The current profile is deeper than in summer, with speeds >0.03 m s^{-1} between 100 - 600 m, so that it is largely barotropic in character. We argue here that this flow represents the CanC at its winter position. East of the CanC at ∼13°W,

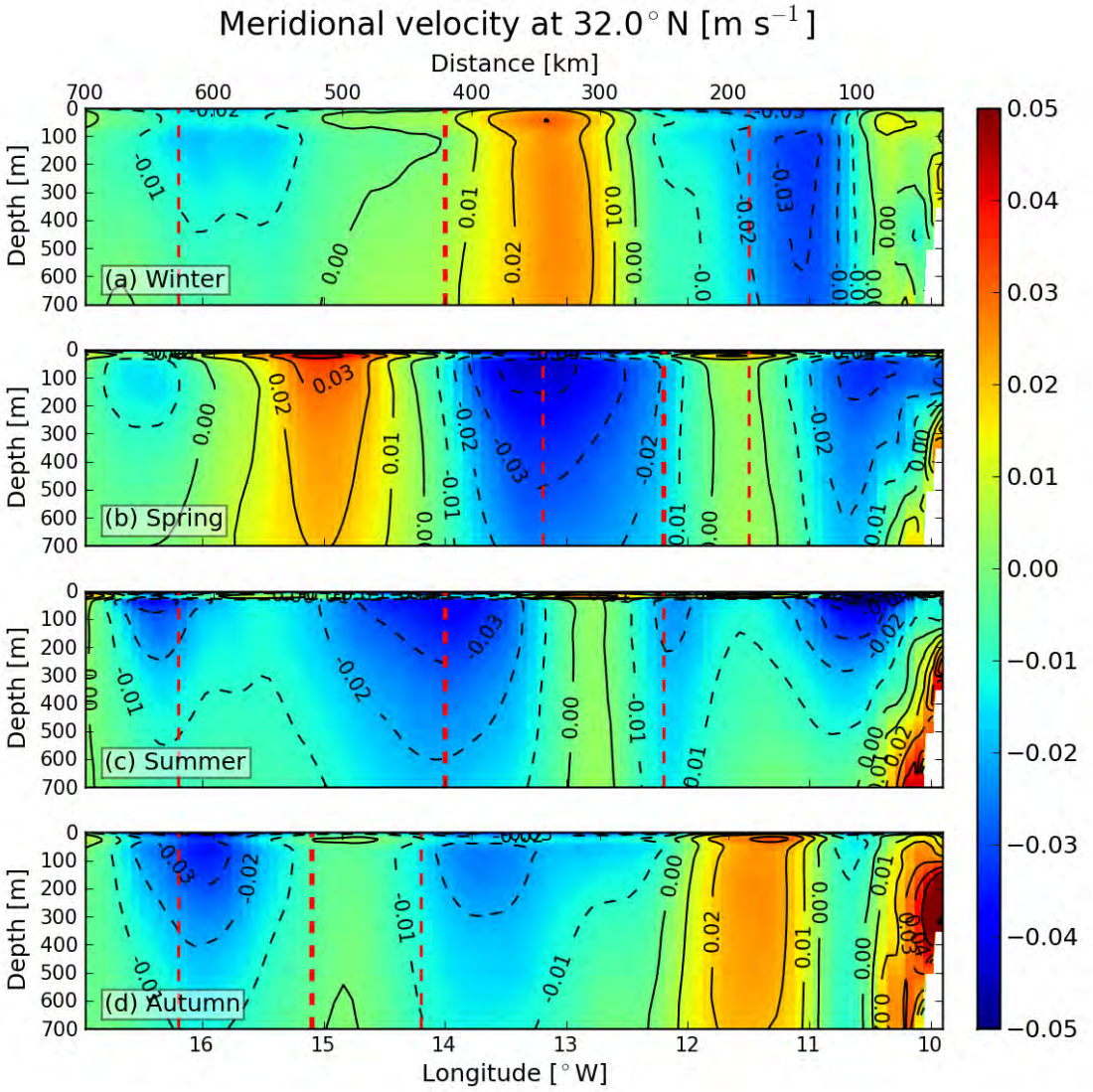

Figure 4.14.: L0 seasonal mean zonal sections of meridional velocity at 32°N. The CanC is visible, particularly in summer where it is centred at ∼14°W and reaches 0.05 m s^{-1}. Velocity contours are plotted every 0.01 m s^{-1}, full (dashed) contours show northward positive (southward negative) velocity. Red dashed lines show the core position (central thick line) and breadth (outer thin lines) of the CanC as determined from four seasonal cruises along ∼32°N by Machín et al. (2006a).

a strong poleward flow, also barotropic, is seen. Weak equatorward flow is also evident at ∼16°W near to Madeira. In spring, the CanC has broadened and strengthened, and is located roughly midway between its summer and winter positions at ∼13°W. It now has a baroclinic structure with the highest velocities (>0.4 m s^{-1}) above ∼200 m. Close to the coast, strong equatorward flow corresponds to the CanUC as the Trade winds begin their seasonal intensification (Wooster et al., 1976). At ∼15°W there is a pronounced poleward flow. Lastly, in autumn, a core of equatorward flow at ∼16°W corresponds to the CanC. A weaker flow is seen at ∼13.7°W. At the coast the CanUC has gone, and is replaced by a strong poleward flow centred at around 300 m. Further offshore at ∼11.5°W, there is a second, weaker, barotropic poleward flow.

The sense from this model sequence is of a CanC that develops in winter close to the coast, and then moves progressively westward at a generally constant rate. Westward progression is also suggested from the positions of the offshore poleward flows, in autumn, winter and spring.

4.5.2. Depth-integrated streamfunction

To make sense of the information in Figure 4.14, we look at seasonal-mean depth-integrated (surface to the depth of the 7°C isotherm) streamfunctions from L0 in Figure 4.15, focusing on the region between Madeira, the Canary archipelago and the African coast. In winter, the circulation is weak with no clear rotational dominance within the domain. However, centred at around 32°N, 12°W is a large anticyclonic flow structure, marked A1. The expected flow (equatorward) on the eastern flank of A1 clearly corresponds with the winter CanC identified in Figure 4.14. Furthermore, the flow on the western flank of A1 corresponds with the winter poleward flow in Figure 4.14a at ∼13°W.

In the subsequent seasons (Figures 4.15b-d) the position of A1 is seen to track westwards across the domain (monthly maps, not shown, confirm this picture). In spring A1 maintains its meridional position at 32°N, but thereafter drifts south, possibly steered by the topography of Madeira. For each season, the CanC identified in Figure 4.14 continues to correspond with the position of the eastern flank of A1. In autumn, when the core of A1 has moved beyond Madeira, it is apparent that at the coast just north of Cape Ghir a new A1, labelled A1$^{\bigstar}$, is growing. Looking back again to winter, the old A1, now labelled A1$^{\blacktriangle}$, is still visible at the western boundary of the domain.

In winter (Figure 4.15a) a cyclonic structure, marked C1, is seen to the southwest of A1. C1 also propagates westward (Figures 4.15b-d) but at a different rate: C1$^{\bigstar}$ marks the birth of C1 in spring, while C1$^{\blacktriangle}$ shows C1 leaving the domain in summer. C1 also shows meridional deviations, moving initially northwards from summer to autumn, then southwards from summer to spring. Interaction between C1 and A1 is evident in all seasons, but is strongest in autumn (Figure 4.15d) when it results in intense northwestward flow (the tail of which is seen in Figure 4.14d at ∼11.5°W).

Figure 4.16 compares annual means of accumulated meridional barotropic transport (start-

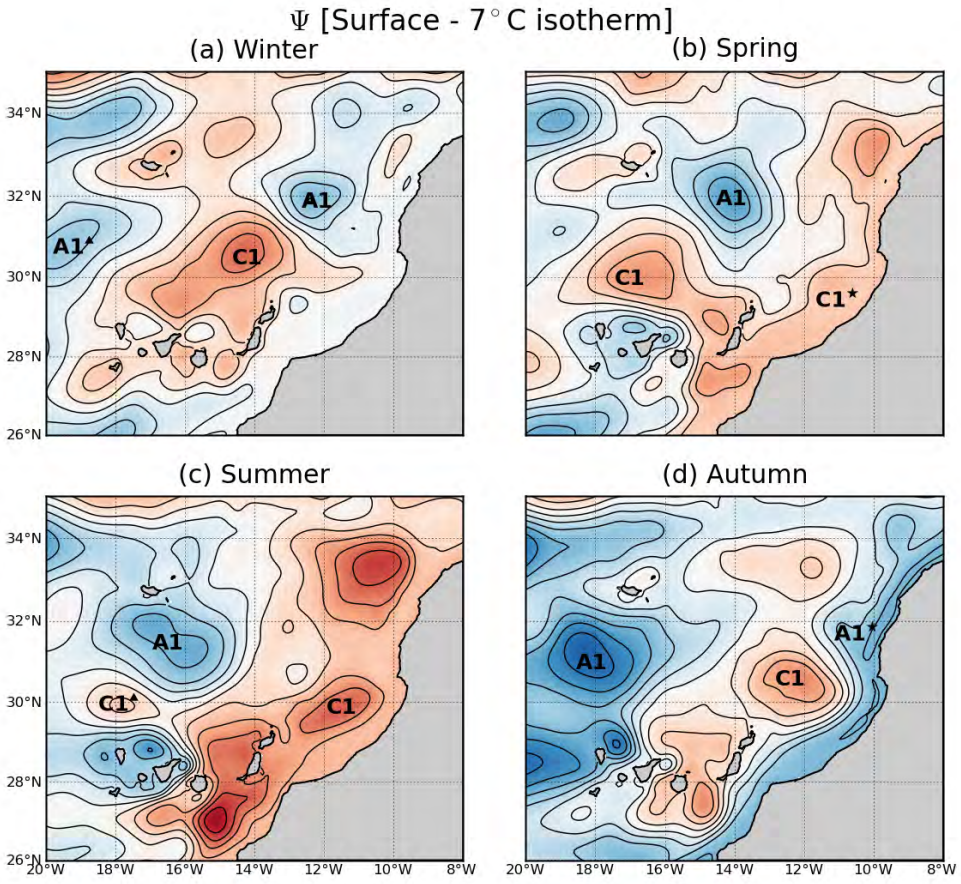

Figure 4.15.: Mean L0 depth-integrated seasonal streamfunction, integrated between the surface and the depth of the 7°C isotherm. Contour intervals are 0.5 Sv. Blue (red) corresponds to anticyclonic (cyclonic) circulation. Label A1 (C1) marks the passage of an anticyclonic (cyclonic) mesoscale structure. A1$^{\bigstar}$ (C1$^{\bigstar}$) shows the assumed location and season of birth of A1 (C1). A1$^{\blacktriangle}$ (C1$^{\blacktriangle}$) shows the position of A1 (C1) from the previous cycle.

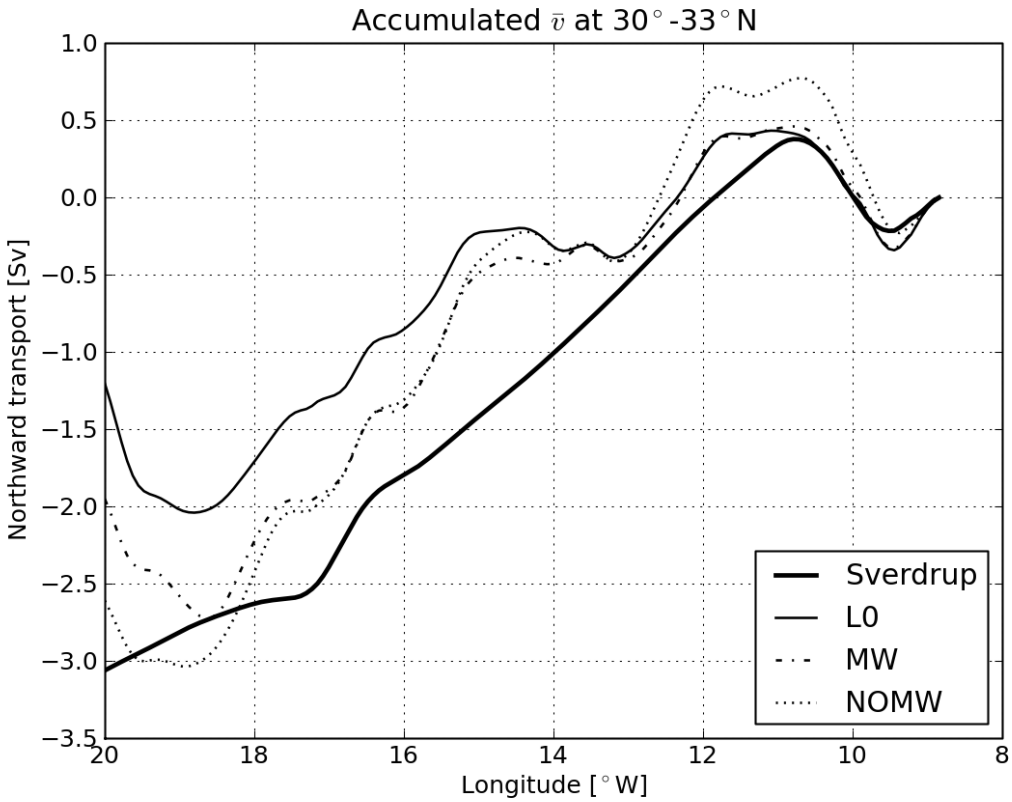

Figure 4.16.: Comparison of annual mean meridional accumulated barotropic transports (starting from the eastern boundary) from the model (L0, MW and NOMW), with the Sverdrup transport derived from the curl of the SCOW wind stress. The transports are averaged over the latitudes 30° - 33°N.

ing from the eastern boundary) over the latitude range 30° - 33°N, from L0, L0-MW and L0-NOMW (see Section 4.4.1 on page 92), with the transport derived through the Sverdrup relation (Sverdrup, 1942):

$$\bar{v} = \frac{\nabla\vec{\tau}}{h \times \beta \times \rho_0} \tag{4.3}$$

where $\nabla\vec{\tau}$ is the curl of the annual mean SCOW wind stress (Table 4.2), β is the meridional gradient of the *Coriolis* parameter ($\sim 2.2 \times 10^{-11}$ m^{-1} s^{-1}) and ρ_0 is the model mean sea water density (1027.4 kg m^{-3}). The model transports follow the Sverdrup relation rather well, indicating that the CanC is largely wind driven. Local departures are likely related to deep flows associated with topographic features (Jia, 2000). Small northward transports between 10° - 11°W possibly correspond to cyclonic and anticyclonic structures identified in Figure 4.15: in autumn, interaction between the emerging A1* and C1 produces a significant northward flux. The transports of L0-MW and L0-NOMW agree very closely, further evidence for the conclusion of Section 4.4 that the CanC path and intensity are independent of the AzC. It is noteworthy, however, that the transports of L0 and L0-MW diverge significantly beyond 14°W, suggesting that the model is still undergoing some adjustment between years 5 and 15.

4.5.3. Observational evidence

Whilst L0 has been extensively validated in Section 4.3, it is useful to compare the results above with available observational evidence. Machín et al. (2006a) describe the seasonal variability of the CanC north of the Canary Islands by means of an inverse box model using data collected during four individual cruises. The seasonal position and breadth of the CanC as interpreted by Machín et al. (2006a) at ∼32°N is marked in Figure 4.14 by red vertical lines (see also Figure 2.11 on page 27). The best correspondence between the L0 CanC and that of Machín et al. (2006a) is obtained in summer. In spring and autumn, the positions remain close. Westward progression of the core of the current (spring through autumn) is evident. In winter the correspondence is weak, they describe a broad generally weak CanC with a central core at ∼14°W, i.e., ∼250 km further offshore than the winter L0 CanC. However, a winter vertical section of absolute geostrophic velocity (see their Figure 19, winter northern section at 200 km) reveals a deep surface-intensified equatorward flow at ∼11°W. This is in clear agreement with the L0 winter CanC.

Table 4.4 presents mean annual and seasonal equatorward transports of the CanC calculated between 10.5° - 17°W at the latitude of Madeira, 32°N. The means are from L0 and from the observed transports of Machín et al. (2006a). Also shown are 11-year means from L0-MW and L0-NOMW (Section 4.4.1). The annual transports are very close for both model and observations. Seasonally, the important discrepancies occur in summer and autumn. The model transports are consistent with each other, but appear reversed when compared with Machín et al. (2006a). However, a credible explanation is that the autumn cruise data used by Machín et al. were collected in September (1997), a summer month in

Table 4.4.: Mean annual and seasonal equatorward transports (Sv) in the CanC in the layer 0 - 700 m, at 32°N between 10.5° - 17°W. Values are shown for the model solutions L0, L0-MW and L0-NOMW, and also from the observational study of Machín et al. (2006a). The L0-NOMW solution is discussed in Section 4.4.1 on page 92.

Solution	Annual	Winter	Spring	Summer	Autumn
L0	3.1	1.5	2.8	5.7	2.5
L0-MW	3.0	1.3	3.0	5.3	2.6
L0-NOMW	3.3	1.7	3.4	5.9	2.3
Machín et al. (2006a)	3.0±1.2	1.7±1.0	2.8±1.2	2.9±1.1	4.5±1.2

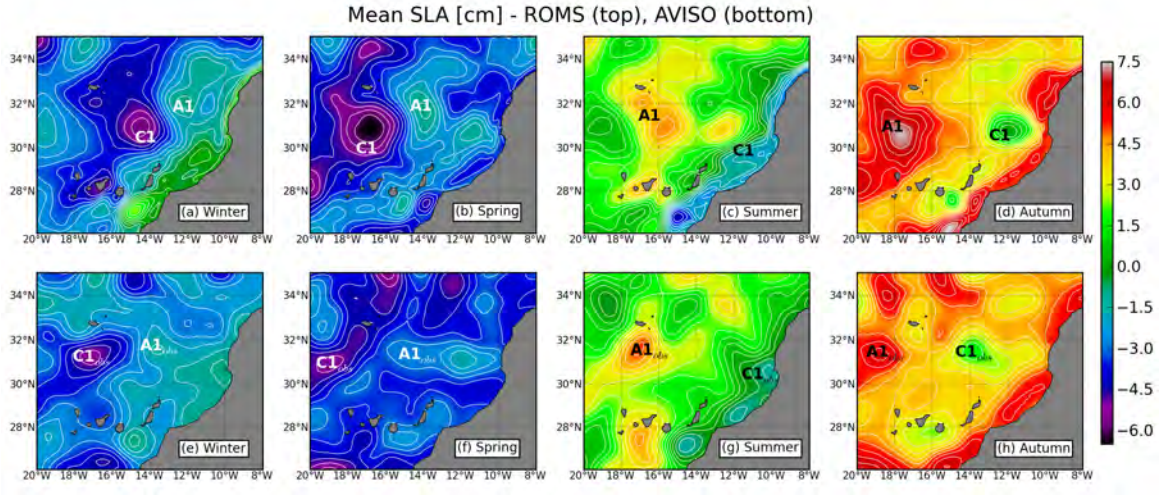

Figure 4.17.: Seasonal mean sea level anomalies. The top panels shows SLAs from L0 and the bottom shows AVISO. Contours are plotted in white every 0.5 cm.

our seasonal means. Considering this fact, the summer and autumn model transports do correspond well with those of Machín et al. (2006a).

Concerning L0-MW and L0-NOMW, the agreement reinforces the point made above in Section 4.4.1 that the near absence of an AzC does not greatly impact the CanC.

In Figure 4.17 we compare mean seasonal sea level anomalies (SLA) from L0 (a-d) and AVISO (e-h) altimetry. The modelled and observed SLAs show good agreement in their overall magnitudes and distributions, with evidence of a seasonal cycle, upwelling and equatorward flow in summer, and a flow reversal along the coast in autumn. For the model fields, the positions of structures A1 and C1 (identified in Figure 4.15 on page 98) are indicated. These coincide closely with features (highs and lows) in the model SLAs. Analogous structures in the altimeter SLA are speculatively labelled $A1_{obs}$ and $C1_{obs}$ in Figure 4.17e-h.

In winter, Figure 4.17e shows the AVISO SLA to have a negative anomaly located directly south of Madeira ($C1_{obs}$) that corresponds with C1. For A1 there is no clear correspondence, although a weak positive anomaly ($A1_{obs}$) is seen at ~31.7°N, 13.7°W. In spring (Figure 4.17f), comparison with AVISO is less clear than in winter. $C1_{obs}$ has moved westwards and

is close to exiting the domain, its magnitude is significantly smaller than C1 in the model. There is no clear closed contour for $A1_{obs}$, however a tongue of weakly-positive SLA at 31°N is its likely location. The summer comparison shows a clear positive SLA ($A1_{obs}$) south of Madeira, in good agreement with A1 (Figure 4.17g). $C1_{obs}$ is also evident, located slightly further north (in the lee of Cape Ghir) than C1 in the model. Lastly, in autumn, there are clear observations of both $A1_{obs}$ and $C1_{obs}$ (Figure 4.17h).

The overall impression from the comparison between the model and altimetry in Figure 4.17 is that, where match-ups between structures are suggested, a small phase shift is evident so that observed structures appear to lead the model structures by a few months.

4.5.4. Planetary waves - a mechanism?

Many reports suggest the presence of westward-propagating baroclinic planetary (*Rossby*) waves within the Canary Basin (Tokmakian and Challenor, 1993; Challenor et al., 2001; Osychny and Cornillon, 2004; Hagen, 2005; Hirschi et al., 2007). Planetary waves have also been observed in model solutions of the region (Lecointre et al., 2008). Hagen (2005), working with hydrographic data from the open ocean in the Canary Basin, describes waves at 32°N with zonal wavelengths of 428 km and periods of 289 days. He showed that waves observed in satellite SLA north of 22°N appear to be seasonally excited. It is argued that the bulk of westward energy propagation at mid-latitudes is more representative of nonlinear vertically-coherent eddies than of linear *Rossby* waves (Chelton et al., 2007). We therefore follow Lecointre et al. (2008) in using the term "planetary wave" as a generic descriptor of westward propagating signals.

Potential instigators of planetary waves exist at the eastern boundary of the Canary Basin, notably temporal variation of the wind stress curl and change of current direction at the boundary. Figure 4.2 shows intense cyclonic curl in summer off Cape Sim at 31.4°N, which is absent in the other seasons (Bakun and Nelson, 1991). Sturges and Hong (1995) showed a link between wind stress and anomalies in the thermocline depth along 32°N. The spectrum of the wind curl showed a peak at 12 months, the intensity decreasing from west to east.

Longitude/time plots (Hovmöler) of the monthly mean SLA from (a) the model and (b) altimetry at 32°N between 9.4° and 17°W are shown in Figure 4.18. Three annual cycles are repeated to better illustrate periodicity in the signals. To filter the seasonal cycle, we take the difference between each time band and its mean, and then bin the output according to its month, prior to averaging. The largest west-east amplitude difference occurs in summer for both L0 and AVISO. In L0 there is clear westward propagation of a growing anomaly with a positive tendency, originating in late autumn near to the coast and arriving at the western boundary in summer. The anomaly corresponds to anticyclonic structure A1 described in Figures 4.15 and 4.17.

Periodicity at annual timescales is evident in both the model and observed SSH anomalies. The structure is less well defined in the AVISO data, possibly because of interannual variability. Examination of Figure 4.18 suggests overall advection rates across the domain

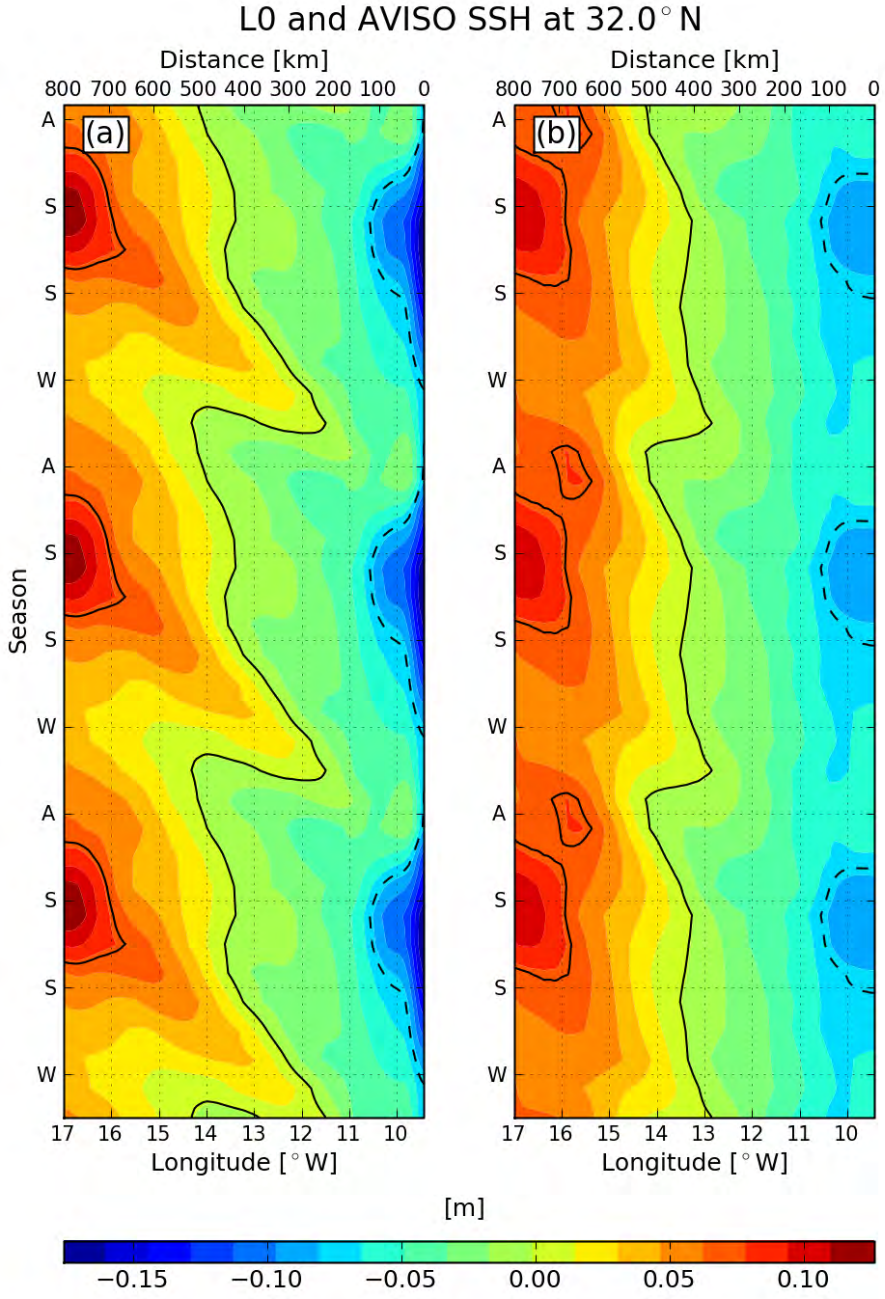

Figure 4.18.: Longitude/time plots showing three repeated yearly cycles of monthly mean SSH from (a) L0 and (b) AVISO altimetry at 32°N. Contours are shown in black at -0.075, 0.0 and 0.075 m. The seasons are labelled W(inter), S(pring), S(ummer), A(utumn). Years 25 - 39 (1992 - 2007) are used from L0 (AVISO).

of ∼0.03 m s^{-1} in both L0 and AVISO, although the structures appear to accelerate as they move offshore, following an initial slow period between the boundary and ∼12°W. This is in good agreement with observations (0.032 m s^{-1}) and theoretical estimates (0.021 m s^{-1}) for the phase speeds of longer period planetary waves in this region (Osychny and Cornillon, 2004; Hagen, 2005).

The nearshore region to the north of Cape Ghir clearly plays a critical role in the dynamics of the CanC. Further analysis of our results, combined with available observational data, is necessary to further define the processes that lead to annual excitation of westward-propagating anomalies at this important region.

4.6. Subtropical eddy corridor

Sangrà et al. (2009) present observational evidence for the existence of zonal corridors of westward-propagating eddies in the northeastern Atlantic. In particular, between ∼22° - 29°N, the Canary Eddy Corridor (CEC) extends westward from the Canary Islands towards the MAR. The CEC is populated by long-lived (>3 months) anticyclonic and cyclonic eddies, which transport water mass- and biogeochemical properties away from the African coastal region to the open ocean. Sangrà et al. (2009) plotted CEC eddy trajectories using 14 years of altimeter data. They reported that approximately 17 eddies are generated each year in the vicinity of the Canary Islands, that are sufficiently long-lived to be considered part of the corridor.

An open question concerns the precise generation sites of the long-lived eddies of the CEC. The trajectories of Sangrà et al. (2009) originate away from the coast but, as they point out, altimetry is known to unreliable near to land. Obvious candidates are the islands (Arístegui et al., 1994; Sangrà et al., 2005, 2007), however eddies are also known to be generated close to the African coast (Navarro-Pérez and Barton, 1998).

4.6.1. Eddy kinetic energy

A comparison of L0 and AVISO eddy kinetic energy distributions at the Canary Islands is shown in Figure 4.19. EKE has been defined in Section 4.3.5 on page 88. The L0 EKE is computed using 3-day averages of geostrophic velocities derived from the model SSH[4]. High EKE south of the islands is visible for both model and altimeter, although the distributions are clearly wider and amplitudes larger in the model. The notable minima nearshore in the altimeter EKE is explained by the altimeter's failure to resolve eddy activity with wavelengths smaller than ∼0.5° (Ducet et al., 2000; Capet et al., 2008b), in contrast to the model.

[4]When model geostrophic EKE is computed for the purposes of validation with altimeter-derived EKE, it is often smoothed in time and space in order to approximate the temporal and spatial scales of the altimeter product (for AVISO: ∼7 days, ∼35 km) (Capet et al., 2008b). However, because here we are interested in the EKE at the maximum resolution provided by the model (i.e., 3 days, 7.5 km), and also near to land, we apply no temporal or spatial smoothing to the L0 fields.

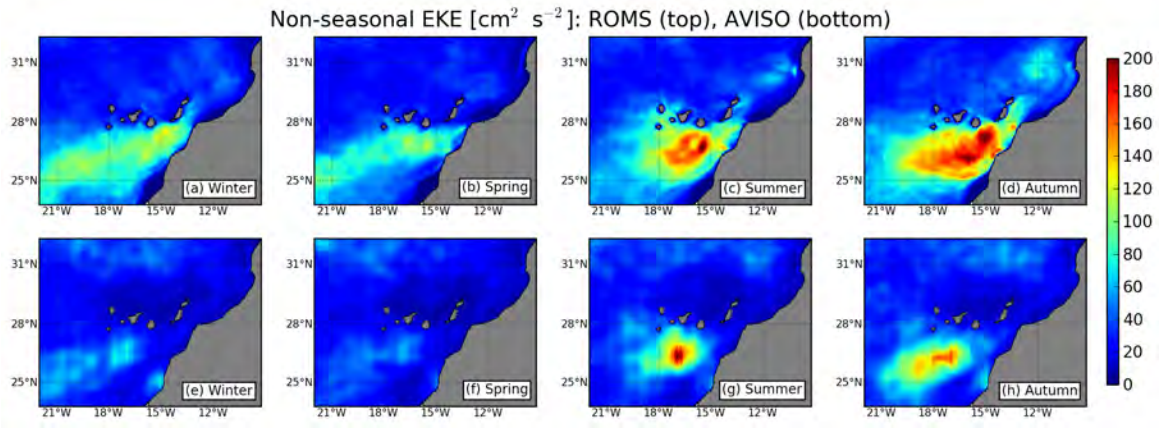

Figure 4.19.: Non-seasonal geostrophic eddy kinetic energy at the Canary Islands from L0 (a-d) and AVISO (e-h).

The seasonal cycle is evident in both the L0 and AVISO EKE. The energy increases sharply in summer when the Trade winds reach their peak. In autumn, the energy is dispersed as eddies interact and propagate, generally westwards. This process continues in winter through spring, although the levels of energy are seen to progressively decrease. Close to the coast and islands, the model shows high EKE. Adjacent to Capes Juby and Bojador, there is elevated EKE all year. In autumn, the highest EKE is found southeast of Gran Canaria. Also, levels are high throughout the Lanzarote Passage; autumn is the season when the surface coastal flow reverses (Section 2.6 on page 30).

Figure 4.19 indicates that the origins of eddies that contribute to the CEC may be better determined from the model solution than from altimetry. We therefore apply an eddy-tracker to the model solution to find out where CEC eddies are generated.

4.6.2. Eddy tracker

The *Okubo-Weiss* technique is used for eddy tracking as described by Chelton et al. (2007); Sangrà et al. (2009). The *Okubo-Weiss* parameter (W) measures the relative contributions of deformation and vorticity over a flow field, such that a coherent vortex can be defined within a closed contour, where W is negative. The *Okubo-Weiss* parameter takes the form:

$$W = S_n^2 + S_s^2 - \omega^2 \tag{4.4}$$

where the first two right-hand-side terms are the normal and shear components of the strain, and ω is the relative vorticity:

$$S_n = \frac{\partial u}{\partial x} - \frac{\partial v}{\partial y}, \qquad S_s = \frac{\partial v}{\partial x} + \frac{\partial u}{\partial y}, \qquad \omega = \frac{\partial v}{\partial x} - \frac{\partial u}{\partial y} \tag{4.5}$$

W was calculated using surface velocities within a subdomain (>20°N) from the 3-day averages of L0 years 11 through 50. The search radius was 15 km (based on a timescale of 1 day). W contours were plotted at W_c = -1.75×10^{-11} s^{-2}. Eddy centroids were defined at

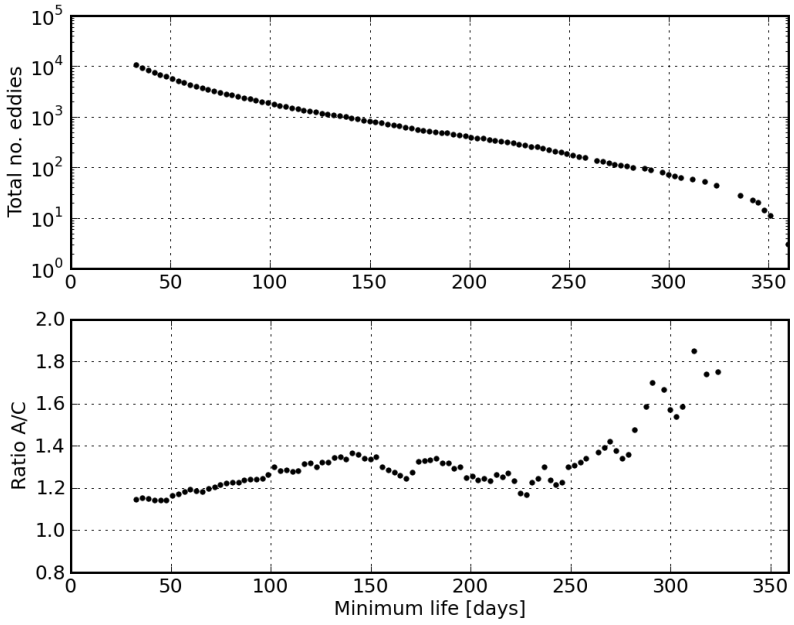

Figure 4.20.: (a) Total numbers of eddies (log scale) and (b), ratios of anticyclones to cyclones as functions of minimum life periods (days) in the L0 domain between 22° - 29°N, calculated using an *Okubo-Weiss* parameter-based eddy tracker applied to L0 years 11 to 50.

the model *rho*-points within each closed contour where $|\omega|$ is maximum.

Figure 4.20 presents statistics related to the eddy tracking. Figure 4.20a shows the total number of eddies tracked as a function of their minimum lifespan in days. Eddies of duration less than 30 days are omitted. As eddy lifespan increases there is a sharp fall in eddy population. In Figure 4.20b, the ratio between anticyclones and cyclones is plotted against minimum eddy lifespan. The ratio is always greater than one, indicating a slight dominance of anticyclones over cyclones in agreement with Sangrà et al. (2009).

4.6.3. The Canary Eddy Corridor

Figure 4.21 shows eddy trajectories from Section 4.6.2 with lifetimes greater than six months that represent the model Canary Eddy Corridor. The tracks are filtered so that time and location of origin corresponds to, respectively, the seasons and the boxed region (in green) south of the islands. The box is split into two subdomains, an island domain and a coastal domain, following the notional division by Barton et al. (1998), who attributed variability in the west to island wake effects, while to the east upwelling-related phenomena (e.g., generation of eddies by frontal instabilities) play a more prominent role.

There is a notable difference in the patterns of the tracks relative to the season of origin[5]. The winter tracks are generally concentrated into a narrow meridional band. In the other

[5] In this discussion the tracks are classified according to their season of origin, however it should be kept in mind that the tracks shown have durations greater than two seasons, so that the later stages of each track do not correspond to the season stated.

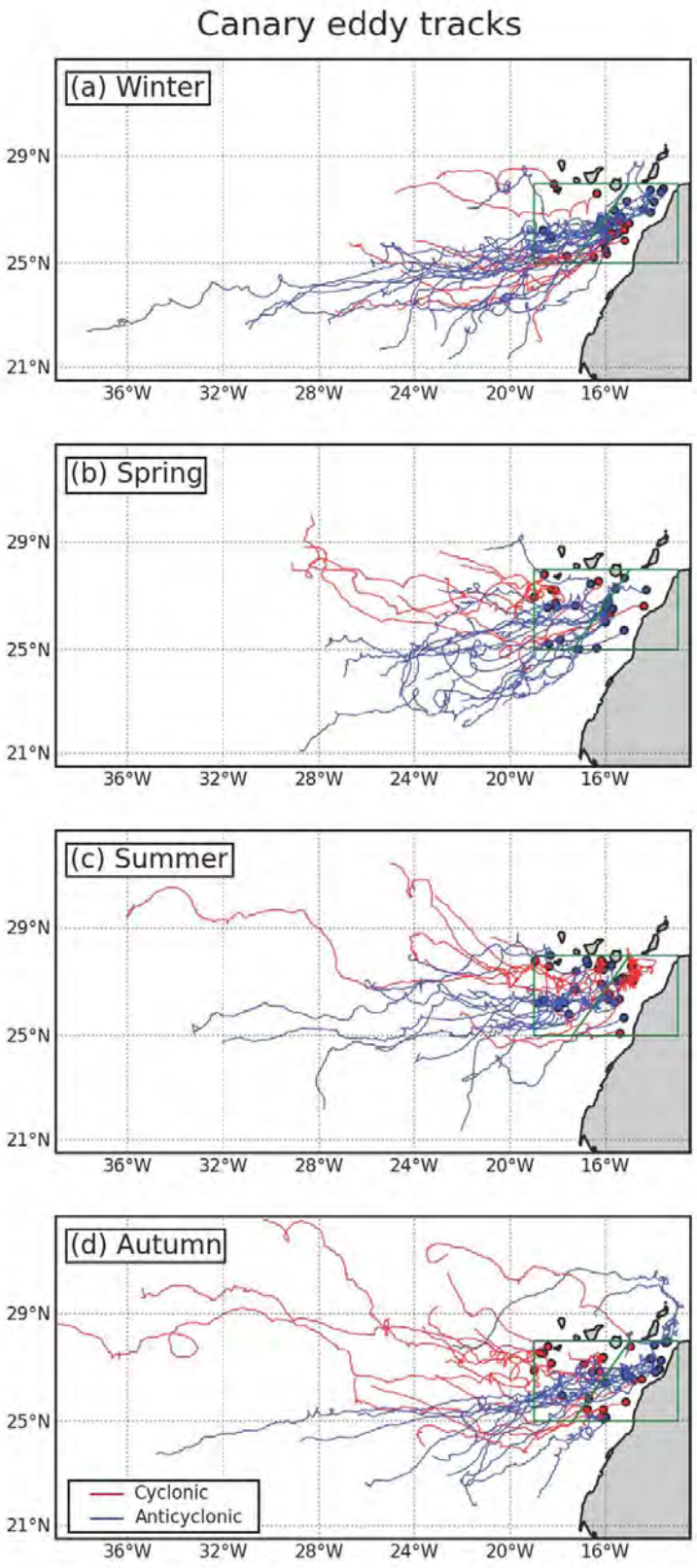

Figure 4.21.: Tracks of L0 cyclonic and anticyclonic eddies with lifetimes greater than six months originating within the green box domain south of the Canary Islands. A dot marks the beginning of each track. The tracks are from L0 years 11 to 50. The green box is divided into two subdomains to separate eddies of wholly island origin (left side) and those which may also be generated at the coast or through instabilities of the upwelling front (right side).

Table 4.5.: Total numbers of cyclonic (C) and anticyclonic (A) eddies tracked in Figure 4.21. The tracks follow eddies with lifetimes greater than 6 months, from L0 years 11 through 50. See Figure 4.21 for the locations of the island and coastal subdomains.

	Island C	Island A	Coast C	Coast A	Island total	Coast total
Winter	3	5	8	17	8	23
Spring	6	7	2	12	13	14
Summer	8	10	7	6	18	13
Autumn	9	2	6	15	11	21
					50	71

seasons, the meridional distributions are more disperse. In autumn, some of the coastal eddies initially flow northwards, probably as a result of the poleward inshore flow during this season. The tendency for separation of the tracks, anticyclones to the south and cyclones to the north, is evident in all seasons bar the winter. This can be explained by observing that the majority of the winter cyclones originate a degree or so south of the anticyclones. The later stages of the trajectories of the winter cyclones begin to show a northward deflection, hence the convergence in cyclone and anticyclone trajectories west of about 22°W.

Concerning locations of origin, there is a clear distinction between spring and summer, and autumn and winter. The former show more eddies originating in the island domain: in summer several eddies originate close to the islands, whereas in spring they originate further south. In the latter, generation in the coastal domain dominates: anticyclones appear in both autumn and winter between Fuerteventura and Capes Bojador and Juby. In addition, in winter, there is a cluster of eddy births (anticyclonic and cyclonic) offshore of Cape Bojador at ∼15°W. These results are summarised in Table 4.5. Coastally-generated eddies dominate in winter, with a preference for anticyclones, while in summer island generated eddies are more common, with a roughly even split between cyclones and anticyclones. In total, 121 eddies originating at the Canary Islands of lifetime greater than 6 months were tracked, giving an average of 3 per year.

The eddy tracks presented demonstrate that the model is able to simulate long-lived eddies with characteristics similar to those of the Canary Eddy Corridor eddies reported by Sangrà et al. (2009). The eddies originate in all seasons in the model solution. Eddies originating in spring and summer tend to be generated away from the African coast in the open ocean island wake region. Conversely, autumn and winter eddies are more often generated closer to the coast. The average number of eddies tracked per year (3) is significantly below the 17 reported by Sangrà et al. (2009), who use a larger domain (22° - 29°N, 32°W to the coast). Using their domain we obtain 13 eddies per year, which is comparable. Differences are likely to arise from the relatively short altimeter time series, and from deficiencies in the tracking methodologies applied to the respective datasets.

4.7. Summary and conclusions

In this paper, results have been presented from a high-resolution regional model simulation for the Canary Basin. The focus was on the mean circulation, the seasonal cycle, and mesoscale variability. The model solution reaches statistical equilibrium after a few years, and is integrated for 50 years. A model/data comparison of seasonal mean and eddy quantities shows the model to attain a credible representation of the known dynamics of the Canary region.

Analysis of the solution has focused primarily on the Canary Current. The main finding concerns the seasonal cycle of this current between Madeira and the Canary Islands. The position of the CanC is mediated by two large-scale, westward-propagating anomalous structures. An anticyclonic anomaly originates north of Cape Ghir in autumn, while a cyclonic counterpart appears south of Cape Ghir in spring. They are therefore phase-locked to the annual cycle. The pair propagate westwards at similar speeds of $\sim$3 cm s^{-1} (2.6 km day^{-1}), which is the approximate phase speed for baroclinic planetary (*Rossby*) waves in this region. Because they are rotating, both structures have a component of meridional velocity at their flanks; the southward component is the Canary Current.

The seasonal position of the current is defined by the progress of the structures. We show through the Sverdrup relation that a large portion of the transport of the Canary Current is related to the wind. The anticyclonic structure originates in a region which experiences intense cyclonic wind stress curl in summer. The relaxation of the wind with the progression to autumn may be involved in the generation of this structure.

The anomalies have a surface expression, and so are visible to satellite-borne altimeters. Sea level anomaly fields from the model and from altimetry are comparable, the cyclonic and anticyclonic structures show up as negative and positive anomalies, respectively. The position of the Canary Current identified in historical *in situ* observations is also in agreement with these results. Concerning reports of a wintertime offshore excursion of the CanC at around 31°N (Pelegrí et al., 2006), this can be related to the anticyclonic anomaly, following its autumn generation north of Cape Ghir. These comparisons make this a credible description of the seasonal cycle of the Canary Current. Another aspect of the structures is that they may be involved in the generation and maintenance of the Cape Ghir filament (Hagen et al., 1996).

Concerning the origin of the Canary Current, studies have shown the Azores Current to supply the current through a southward branch east of Madeira. However, a 15-year model simulation where the AzC transport was reduced by about 85% by closing the Strait of Gibraltar had minimal impact on the CanC. Its mean transport and position did not change significantly. This supports the idea of the CanC being a wind-driven current, and suggests that in terms of dynamics it is only weakly connected to the Azores Current.

The perturbation of the Canary Current and the Trade winds at the Canary Island archipelago leads to significant mesoscale variability. Whilst island-generated eddies have frequently been observed and described in the lee of the archipelago, a recent article shows

that such eddies may have a remote impact (Sangrà et al., 2009). Altimetry data reveal a large population of long-lived mesoscale eddies that occupy a zonal corridor at around 26°N. The so-called Canary Eddy Corridor is resolved in the model solution through the use of an eddy tracker based on the *Okubo-Weiss* parameter.

The eddy tracks provide new insight into the origins of the CEC eddies. This information cannot be obtained from altimeters because of their inability to resolve the nearshore region. The eddies in the model have mixed origins. They are generated primarily near to the coast, rather than at the islands. Island generation becomes important in summer only. Eddy kinetic energy fields from the model confirm these findings.

In future work this model solution will be downscaled to force higher-resolution model domains at the Canary Islands. The focus will be the on the variability of the incident current at the islands, and the impact that this has on mesoscale and submesoscale variability in the region.

Acknowledgments

Evan Mason is supported by the Spanish Government through project RODA (CTM2004-06842). ROMS development at UCLA is supported by the Office of Naval Research (currently grant N00014-08-1-0597). This work was partially supported by the National Center for Supercomputing Applications under grant number OCE030007 and utilised the *abe* system. The altimeter products were produced by SSALTO/DUACS and distributed by AVISO, with support from CNES. The Subduction Experiment and ESTOC mooring data were obtained from http://www.cmrecords.net/.

5. High-resolution modelling at the Canary Islands

A numerical study of the circulation and turbulent wake at the Canary Islands[1]

Evan Mason[1], Francois Colas[2], Jeroen Molemaker[2], Alexander Shchepetkin[2],

James C. McWilliams[2], Pablo Sangrà[1] and Mimi Hughes[2]

1. *Departamento de Física, Universidad de Las Palmas de Gran Canaria, 35017, Las Palmas de Gran Canaria, Spain*
2. *Institute of Geophysics and Planetary Physics, University of California Los Angeles, Los Angeles, California, USA*

Abstract

Mesoscale variability has been intensively studied at the Canary Islands, by *in situ* and remote sensing methods. The archipelago straddles the coastal transition zone that divides the open ocean Canary Current and the northwest African coastal upwelling. Mesoscale eddies have been observed in the lee of the archipelago in all seasons, but the eddy kinetic energy calculated from altimetry peaks in summer. Eddies are assumed to be generated by the islands, acting as obstacles to the incident flow, with wind shear playing an additional role. There are reports also of large standing eddies between the African coast and the eastern islands.

In this paper we present results from a high-resolution numerical model at the Canary Islands. Previously, process-oriented model studies have focused on the islands. The model is climatologically forced, and is part of a suite of nested model solutions that cover the Canary Basin. Model transports between the island passages are consistent with the few observations that exist, indicating that the mean island circulation is well resolved. The solution captures the full seasonal cycle at a resolution approaching the submesoscale. An array of different phenomena are seen, some not previously described. In particular, headlands on the islands appear to play an important role in the generation of vorticity. For instance, highly unstable anticyclones are frequently seen being generated at a small peninsula at the north of the island of Gran Canaria. In common with submesoscale solutions in other regions, there is evidence of outbreaks of submesoscale-related turbulence in winter.

[1]This article is in preparation and is expected to be submitted for publication in 2010.

5.1. Introduction

The Canary Island archipelago straddles the transition zone between coastal and oceanic waters offshore of northwest Africa (Figure 5.1) (Barton et al., 1998). The island grouping is an abrupt feature that lies within the path of the southwestward flowing Canary Current (CanC) (Machín et al., 2006a). The easternmost islands, Fuerteventura and Lanzarote, are separated from the African landmass by a deep (>1000 m) and wide (>95 km) channel, known as the Lanzarote Passage (Hernández-Guerra et al., 2003). The remaining five islands, including Gran Canaria which is the main focus of the present work, lie upon a steep-sided, zonally-orientated, ∼2500-m deep plateau that extends ∼500 km offshore. Deep water separates the offshore islands. North and south of the plateau depths greater than 3000 m are quickly reached.

The perturbation of the CanC as it passes the archipelago leads to high levels of mesoscale variability, readily seen through satellite altimetry (Tejera et al., 2002; Sangrà et al., 2009). Maps of eddy kinetic energy reveal elevated values downstream of the archipelago, with pronounced seasonality that shows correspondence to the prevailing Trade-wind cycle: constant all year but increasing in summer (Wooster et al., 1976). The observed mesoscale energy has primarily been attributed to island-generated eddies but there is also a large, if not greater, contribution from instabilities associated with the wind-forced coastal upwelling along the African coast (see Section 4.6 on page 104). Strong surface fronts and filaments are frequently observed extending offshore, sometimes interacting with the island eddy field (Arístegui et al., 1994, 1997; Basterretxea et al., 2002; Barton et al., 2004). An additional mesoscale feature is a large semi-permanent cyclonic eddy that has been observed south of Fuerteventura (Navarro-Pérez and Barton, 1998). Eddy activity at the Canary Islands has been demonstrated by Sangrà et al. (2009) to have a remote impact. Long-lived vortices, whose origins are the Canary Island region, have been detected in altimetry maps across a zonal corridor to as far west as 32°W. Fourteen years of altimeter data showed an average of 17 such eddies per year may populate the so-called Canary Eddy Corridor (CEC).

Topographic forcing as an eddy-generation mechanism at Gran Canaria has been studied by Sangrà (1995). High stagnation pressure where the incident CanC meets the island impels the flow around the eastern and western flanks. The boundary layer separates from the island, forming two shear layers that trail downstream. The shear layers roll-up into the near wake region behind the island, and may coalesce into discreet swirling vortices that are alternately released into the wake: the Von Karman vortex street (Blevins, 1995). The Reynolds number (Re), the ratio of inertial to viscous forces, determines the likelihood of eddy shedding in an idealised current/obstacle regime. Gran Canaria is nearly circular in shape with a diameter of ∼50 km, and is thought to be cleanly exposed to the incident CanC. Results from a quasigeostrophic model, configured with an obstacle (representing Gran Canaria) embedded within a constant current ($U = 0.1$ m s^{-1}), showed eddy shedding for Re greater than 60, with the proviso that the current persisted for at least 36 days[2].

[2] $Re = (UL)/A_H$, where U is the incident current velocity, $L = 54000$ m is the diameter of Gran Canaria,

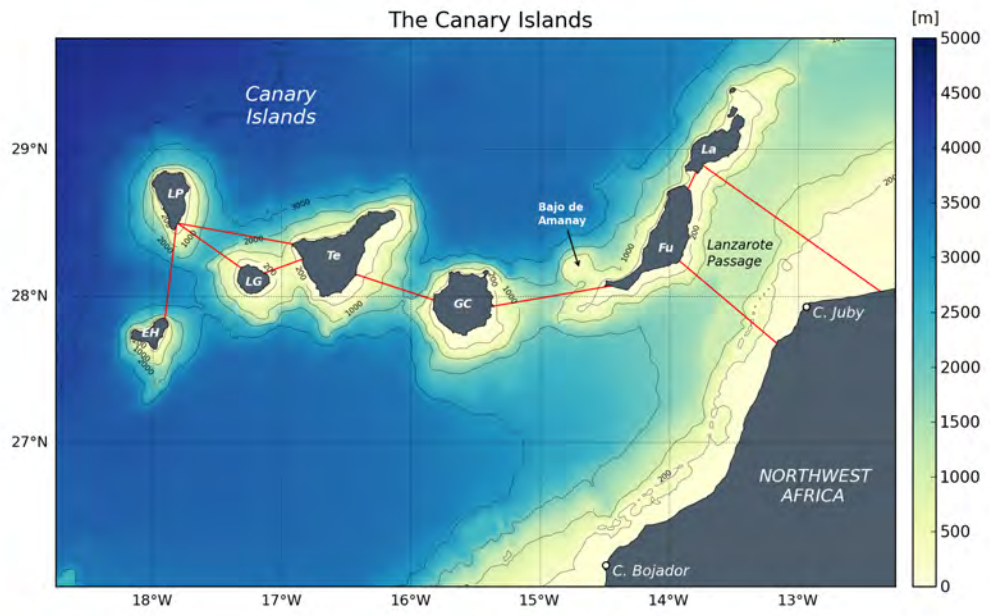

Figure 5.1.: Map showing the Canary Islands off the northwest African coast. Islands are labelled: EH - El Hierro, LP - La Palma, LG - La Gomera, Te - Tenerife, GC - Gran Canaria, Fu - Fuerteventura, La - Lanzarote. Also shown are the inter-island transect locations (red lines) for transport estimates in Section 5.3.3. Isobaths are plotted at 200, 1000, 2000, 3000 and 4000 m.

For greater velocities, the frequency of eddy shedding increased, and the required minimum persistence time was lowered. Jiménez et al. (2008) used a similar model setup to investigate the response with the addition of constant wind forcing, and found that eddy shedding was initiated at lower values of the incident current ($U = 0.04$ m s^{-1}, $Re = 20$). These results support the view that topography-induced wind shear may play an important role in eddy generation in the lee of the islands (Basterretxea et al., 2002; Sangrà et al., 2007; Piedeleu et al., 2009).

As relatively-intense mesoscale turbulence is associated with all four of the world ocean eastern boundary upwelling systems (EBUS) (Capet et al., 2008b), the presence of the Canary Islands cannot be the only source of eddies. Eddies, fronts and filaments result in large part from instabilities in alongshore upwelling currents (Batteen, 1997). In offshore regions, baroclinic conversion (i.e., mean potential to eddy kinetic energy) is the principal source of eddy energy. Nearshore, barotropic conversion (i.e., mean to eddy kinetic energy) also plays a role (Marchesiello et al., 2003). However, energy levels in the northwest Africa upwelling system are shown to be generally lower than those of the other EBUS, notably the California Current System, owing to differences in stratification between the two systems (Marchesiello et al., 2004; Marchesiello and Estrade, 2009).

The studies cited in this section hint at considerable mesoscale variability occurring at the Canary Island archipelago. However, owing to the complexity of the circulation and

and $A_H = 100$ m^2 s^{-1} is the horizontal eddy viscosity coefficient.

topography, continuing sparseness of observations, and uncertainty about the character of the incoming CanC flow, relatively little is known about circulation in and around the islands. The objectives of this paper are two-fold. We present climatologically-forced high-resolution numerical ocean model results from an offline, multiply-nested ROMS configuration. The model solution provides an estimation of the seasonal and monthly mean circulation at the Canary Islands, permitting a description to be made of the incident flow regime at the archipelago and, in particular, at Gran Canaria (Section 5.3). In a second section, we present a characterisation of the Canary Island eddy field using a solution at a horizontal resolution of 1 km (Section 5.4). This grid resolution is at the threshold of the mesoscale-submesoscale transition (Capet et al., 2008c). The main finding is the intense production of vorticity that occurs at island capes and headlands, particularly the small La Isleta peninsula in the north of Gran Canaria. We comment also on the seasonal modulation of the eddy field by submesoscale dynamics (Capet et al., 2008a), present in the high-resolution model results.

5.2. The model configuration

In this section, the nested ocean model configuration is described. We use the UCLA version of the Regional Ocean Modelling System (ROMS) (Shchepetkin and McWilliams, 2005, 2009b). ROMS is a free-surface, primitive-equation, curvilinear-coordinate ocean model, where the barotropic and baroclinic momentum equations are resolved separately. ROMS uses a terrain-following (or *sigma*) vertical coordinate system (Haidvogel and Beckmann, 1999). Island wake studies that use ROMS include Dong et al. (2007) and Dong and McWilliams (2007). The former is a 3D idealised study of the wake, while the latter uses a realistic model solution to investigate island wakes within the Southern California Bight.

In order to ensure the realism of the large-scale geostrophic mean flow at the Canary Islands, we downscale our boundary forcing from a 7.5-km validated ROMS solution of the Canary Basin (Chapter 4). This is a climatologically-forced solution, yet contains interannual variability owing to the non-linear nature of the primitive equations (Lorenz, 1963). To achieve the target 1-km resolution at the Canary Islands, we adopt a 2-stage nesting by the inclusion of an intermediate 3-km grid. Hereinafter, we refer to the 3- and 1-km solutions as L1 and L2, respectively. The 7.5-km parent is referred to as L0.

5.2.1. The model domains (L1 and L2)

The L1 3-km domain, which includes the Canary Island archipelago and Madeira to the north, is located within the Canary Basin in the northeast Atlantic (Figure 5.2). L2, at 1-km resolution, is focused on the Canary archipelago. Both domains are rotated so that their closed eastern boundaries run parallel to the African coast. The northern, southern and western boundaries are open. The topography is treated as described in Section 3.2.2 on page 53 using the 1-minute resolution General Bathymetric Chart of the Oceans dataset (GEBCO) (Hunter and Macnab, 2003) . Depths greater than 5 m are set to 5 m. Table 5.1

Table 5.1.: Grid and configuration parameters for the L1 and L2 model configurations.

	L1	L2
Horizontal resolution [km]	3	1
Length [years]	12	3
Latitude [°N]	20° - 37°	24° - 32°
Longitude [°W]	8° - 25°	11° - 20°
Domain rotation [°]	028	038
Grid dimensions [km^2]	1002 × 1608	592 × 612
Grid size	334 × 536 × 42	592 × 612 × 60
Minimum depth [m]	5	5

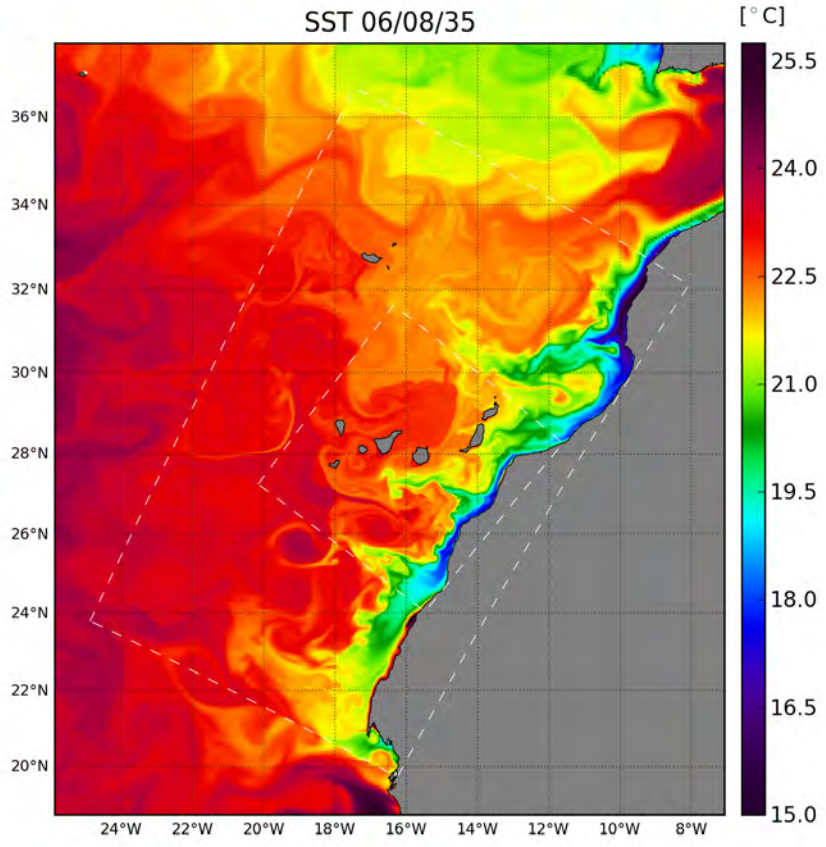

Figure 5.2.: Instantaneous SST in August of model year 35 from the full nested configuration: L2 (L1) SST is superimposed upon L1 (L0) SST. White dashed lines demark the nested 3- (outer) and 1-km (inner) model grid boundaries.

Table 5.2.: Maximum and minimum depths in metres of the top and bottom vertical layers in the 3- (L1) and 1-km (L2) model domains.

Level	L1		L2	
	Min	Max	Min	Max
Top	0.11	3.41	0.08	2.20
Bottom	0.12	252.43	0.09	145.77

provides a summary of the details of the L1 and L2 configurations.

L1 and L2 have 42 and 60 vertical levels, respectively. The surface- and bottom-stretching parameters are set as $\theta_s = 6$ and $\theta_b = 2$. Table 5.2 shows the maximum and minimum depths at the top and bottom levels that result from these parameter choices. Interaction between currents and topography is an important source of vorticity. Therefore higher resolution at the bottom, better resolving the bottom boundary layer, is expected to increase vorticity production, especially near the coasts and islands.

Initial and boundary conditions for L1 (L2) were obtained by extracting the required prognostic variables from L0 (L1) and interpolating to the L1 (L2) grid, following methods described in Chapter 3. L0 years 34 to 44 were used to force L1, and L1 years 35 to 37 were used for L2 (see Figure 5.4 for a schematic of the coupling). Averages are saved from L1 (L2) every 2 (1) days, giving 15 (30) records per month.

5.2.2. Climatological forcing

L1 and L2 use identical climatological surface forcings. Wind stress at 0.25° resolution is taken from the QuikSCAT-based Scatterometer Climatology of Ocean Winds (SCOW, Risien and Chelton, 2008). Figure 5.3a shows the wind stress curl and wind speed vectors from SCOW in August, interpolated to the L2 grid. Heat fluxes and precipitation come from the Comprehensive Ocean-Atmosphere Dataset (COADS; Worley et al., 2005). A mild sea surface temperature (SST) and sea surface salinity (SSS) restoring (360 days) is applied (Barnier et al., 1995). The SST climatology is a monthly 4-km global product from the NOAA/NASA AVHRR Oceans Pathfinder Program (Version 5^3, built upon the Version 4 product at 9.28 km by Kilpatrick et al., 2001). The surface forcing files are created using the tools described by Penven et al. (2008). Initial and lateral boundary forcing files are prepared following the procedures of Chapter 3. See Chapter 4 for more on the preparation of L0.

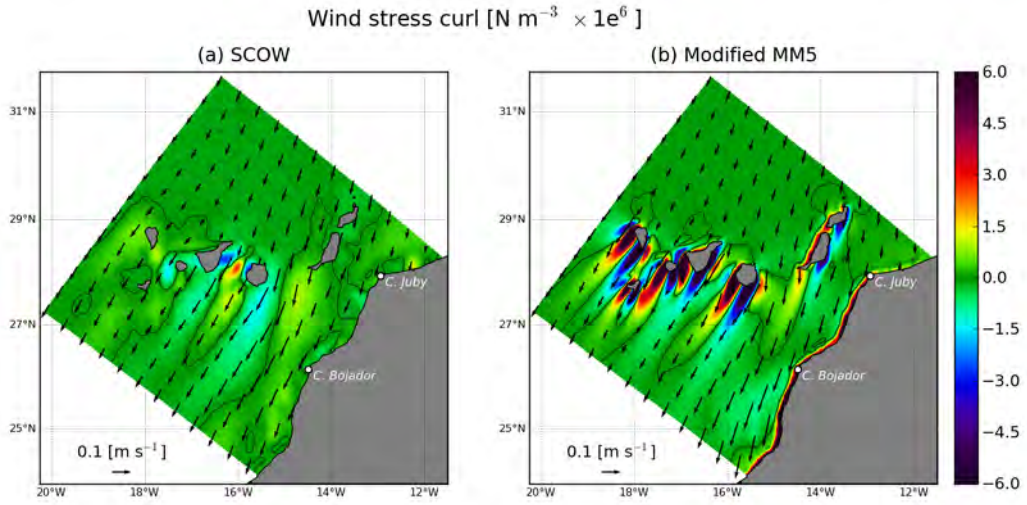

Figure 5.3.: L2 August wind stress curl from (a) SCOW and (b) MM5. Vectors show the wind speed and direction. The zero wind stress curl is contoured in black.

5.2.3. MM5 runs

Three additional L2 runs were made where wind stress derived from MM5 atmospheric model outputs was used in place of SCOW. These runs were each just 3 months in duration, because the MM5 solution covers only the period July through September 2006. This time period coincides with a month-long eddy-sampling cruise that took place at the Canary Islands (RODA1). The MM5 solution has been validated with QuikSCAT and with wind observations at Gran Canaria (Appendix B).

Although MM5 provided us with hourly outputs, we chose to make monthly means out of the data for use in the MM5 experiments. This is because the main aim of the MM5 runs was to examine the role of increased wind shear downwind of the islands in the generation of eddies (Basterretxea et al., 2002; Jiménez et al., 2008; Piedeleu et al., 2009). Hourly, or even daily, MM5 wind stress fields were highly variable, with the atmospheric wake changing its size, shape and position, and therefore markedly different from SCOW. Monthly averages provide a stationary wake similar to the SCOW wake but with the requisite increases in intensity and shear. To ensure that the mean MM5 fields (i.e., July, August, September) scale as closely as possible with the equivalent SCOW fields, the MM5 stresses are modified as follows: the mean differences between the u- and v-components[4] of the respective products are added to the MM5 components. In practice, we only modified the v-components, because of an anomaly identified in the MM5 u-components that would have generated a bias across the domain (see Appendix B.2 on page 207). The modified MM5 wind product is hereinafter called MM5. Figure 5.3 shows the respective August wind stress curls for SCOW and MM5.

[3] As well as offering higher resolution, the 4-km Version-5 Pathfinder SST has reduced biases related to atmospheric aerosols, an important consideration for the northeast Atlantic which is strongly affected by Saharan dust (Mahowald et al., 2005).

[4] Throughout this article, the terms u- and v-components will refer to the orientation of the model grid.

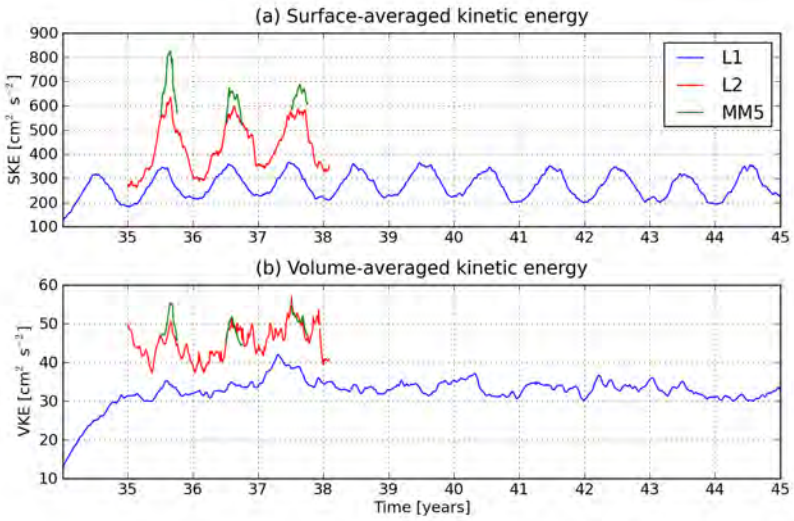

Figure 5.4.: Timeseries of surface- and volume-averaged kinetic energy from L1, L2, and the three MM5 runs. Years correspond to the L1 period of the L0 parent solution.

The MM5 ROMS results are presented in Section 5.4.5).

5.3. Equilibrium solution and mesoscale circulation

Time series of the surface- (SKE) and volume-averaged kinetic energy (VKE) from L1 and L2 are presented in Figure 5.4. The seasonal cycle is evident in the SKE, peaks correspond to the summertime Trade-wind maximum. In the VKE, the seasonal cycle is less clear, but is distinguishable in L2. L1 VKE shows a spinup period of about one year following initialisation at the beginning of year 34.

Whilst it is expected that L2 energy levels are higher than L1, any comparison is compromised because of the different domain sizes. However, Figure 5.4 also shows kinetic energies from the three MM5 runs of Section 5.4.5, which are run on the L2 domain. There is a marked increase in the SKE of the MM5 runs over that of L2, consistent with the application of a higher resolution wind.

5.3.1. General description

Figure 5.2 shows a composite [L2 (L1) superimposed onto L1 (L0)] instantaneous sea surface temperature (SST) field in the Canary region in summer. The wind-driven upwelling is evident along the coast as a band of cool water from the Gulf of Cadiz (35.5°N) in the north to Cape Blanc (20.8°N). The solutions show the typical mesoscale variability patterns as seen in satellite images (Van Camp et al., 1991). Several large filaments extend offshore. The Cape Ghir filament at 20.8°N (Pelegrí et al., 2005b) and the filament between Capes Juby and Bojador (~27.0°N) (Barton et al., 1998) are both frequently observed. There is the suggestion of warm-wake formation in the lees of both Gran Canaria and Tenerife.

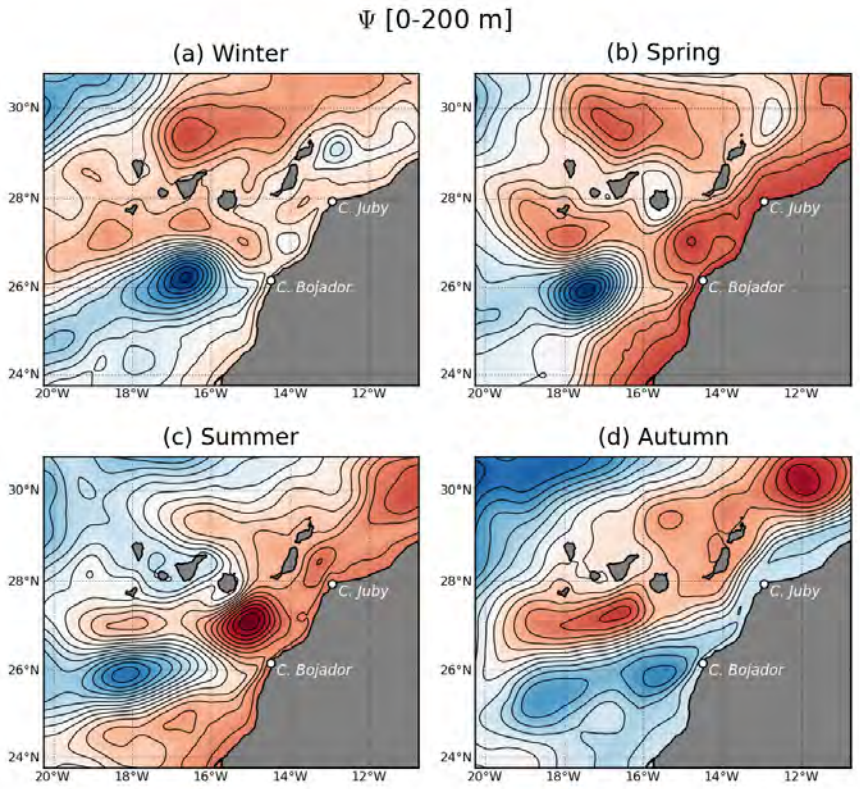

Figure 5.5.: Streamfunction (Ψ) derived from seasonal mean L1 velocities between the surface and 200 m depth. Cyclonic (anticyclonic) circulation is shown in red (blue). Intervals between streamlines correspond to 0.2 Sv.

Warm wakes are common features in satellite SST images of the islands. They arise from a combination of strong diurnal surface heating and low winds in the sheltered lee (Basterretxea et al., 2002). Warm wakes are not expected to be realistically reproduced in the model given the relatively low-resolution climatological wind and heat fluxes used to force the surface. An anticyclonic eddy is visible at ~26.2°N, 16.8°W (see also Figure 5.11). Mesoscale structures that straddle the open model boundaries are mostly coherent; inconsistencies generally occur where there is outflow across the boundary, such as at the southern L1 boundary.

5.3.2. Mesoscale circulation

In this section, seasonal and monthly averages calculated from the final 10 years of the L1 solution provide information about the flow regime at the Canary Islands. Firstly, we wish to know the character of the incident flow: What is the mid-term variability (months to seasons) of the mean path of the current that impinges upon the islands?

Figure 5.5 shows seasonal plots of the L1 non-divergent streamfunction (Ψ) integrated over the top 200 m at the Canary Islands [see Penven et al. (2005) for the calculation of the streamfunction]. Use of the streamfunction enables a description of the geostrophic

flow (i.e., the Canary Current) incident to the archipelago. In winter, a low-pressure centre to the north of Tenerife induces flow towards La Palma, and eastward along the northern coast of Tenerife. Gran Canaria experiences a weak flow from the north. In spring, the northern low-pressure centre persists, and is joined by the development of a second low-pressure cell just south of El Hierro (i.e., south of the archipelago). The two low-pressure cells are connected by anticyclonic streamlines which pass around Gran Canaria. In summer, as the subtropical gyre moves inshore (Navarro-Pérez and Barton, 2001), the low-pressure cells weaken. Gradients increase, and there is a clearly-defined intense eastward flow passing the northern tip of Tenerife which turns southward to impact against Gran Canaria (see also Appendix C.2 on page 218). The westward return flow has a small northward component, passing between El Hierro and La Palma. In autumn, the flow at the Canary Islands is weak, particularly to the north. Two bands of strong gradients run parallel to the coast, one is located inshore of the archipelago, the other is offshore. The inshore flow is anticyclonic, suggesting poleward flow along the African coast (Hernández-Guerra et al., 2002).

These results are in agreement with descriptions showing a shift in the mean position of the eastern subtropical gyre between west and north in winter, and south and east in summer (Stramma and Siedler, 1988; Navarro-Pérez and Barton, 2001) (see also Figure 2.10). There is confirmation of the intensification of the incident flow at Gran Canaria in the summer months (Piedeleu et al., 2009). The results also suggest that the incident flow tends to come from the northwest during this time.

South of the archipelago there are conspicuous high- and low-pressure centres. An anticyclonic cell is present all year. Associated with the cell is an eastward flow at $\sim$26.5°N (confirmed in the SVP drifter observations of Figure 4.8 on page 87). The cell is most intense in winter, when it dominates the wake region. This region is frequently associated with the generation of anticyclonic CEC eddies (Figure 4.21 on page 107). In spring a cyclonic (low-pressure) structure appears at the coast north of Cape Bojador. This may be related to the large semi-permanent cyclonic eddy reported at this location by Navarro-Pérez and Barton (1998). By the summer it has grown and moved offshore near to Gran Canaria, where it interacts with the anticyclonic cell. In autumn the two cells are zonally elongated, the cyclonic cell to the north. Their interaction results in intense eastward flow, which extends towards the coast and then northward into the Lanzarote Passage. Autumn is the season when the flow in the passage reverses towards the north.

5.3.3. Island passage transports

Observations of transports within the island channels have mostly been made in the east, especially in the Lanzarote Passage adjacent to the African coast (Hernández-Guerra et al., 2002; Knoll et al., 2002; Hernández-Guerra et al., 2003; Machín et al., 2006a). For the western passages few reports exist, most notable is Navarro-Pérez and Barton (2001).

Figure 5.1 shows the positions of nine transects, whose seasonal transports above 600 m are presented in Table 5.3. The Lanzarote Passage (Lanzarote - Africa and Fuerteventura

Table 5.3.: Seasonal transports (Sv) through the Canary Island passages in the layer 0 - 600 m from L1. La - A: Lanzarote - Africa, Fu - A: Fuerteventura - Africa, Fu - La: Fuerteventura - Lanzarote, GC - Fu: Gran Canaria - Fuerteventura, Te - GC: Tenerife - Gran Canaria, LG - Te: La Gomera - Tenerife, LP - LG: La Palma - La Gomera, LP - Te: La Palma - Tenerife. Transport directions are normal to the transects in Figure 5.1; northward/eastward positive. The full depths of the passages are given.

	Depth [m]	Winter	Spring	Summer	Autumn
La - A	1250	-0.40	-2.02	-0.98	2.16
Fu - A	1500	-0.43	-2.00	-0.93	2.18
Fu - La	70	-0.02	-0.06	-0.08	-0.04
GC - Fu	1600	0.30	-1.11	-1.24	-0.22
Te - GC	2100	0.00	-0.01	-1.51	-0.75
LG - Te	280	0.01	0.09	-0.04	-0.05
LP - LG	2500	-0.70	-0.05	-0.41	-0.70
LP - Te	2750	-0.69	0.04	-0.50	-0.75
EH - LP	3400	-0.85	-1.27	-1.41	-0.94

- Africa) shows the strongest transports and the most striking variability, with an abrupt reversal from southward to northward flow in autumn (Hernández-Guerra et al., 2002). Small differences between the two transects are explained by persistent westward flow between Fuerteventura and Lanzarote. Figure 5.6 shows seasonal vertical velocity sections at Fuerteventura - Africa. The coastal upwelling jet over the African shelf is evident all year, although it weakens in winter, concurrent with mixed layer deepening. A poleward return flow is seen all year at ∼200-m depth. In the centre and west of the channel the flow is weak or weakly southward in winter, spring and summer. The autumn reversal occupies the full breadth of the channel, down to ∼600 m. It is noteworthy that the surface upwelling jet remains in operation. Below ∼600 m there is year-round equatorward flow in the west.

Between Gran Canaria and Fuerteventura (Table 5.3) transports above 600 m are weaker than in the Lanzarote Passage. In spring and summer, southward transports exceed 1 Sv. In autumn and winter they are very weak, with a slight northward component in winter. Seasonal vertical velocity sections at Fuerteventura - Africa (Figure 5.7) show that northward transport is present at mid-channel all year, being strongest at ∼500 m. The variability in the transport stems from southward flow which appears along the flank of Gran Canaria in spring and summer. At depth (>∼800 m) there is southward flow all year, concentrated towards Gran Canaria.

Transports are southward and below 1 Sv all year between La Palma and Tenerife. Figure 5.8 shows the current structure to be rather uniform in the vertical in all seasons. In the surface layers in summer, a northward flow appears. This agrees with Navarro-Pérez and Barton (2001)'s observations using sea level differences between La Palma and Tenerife.

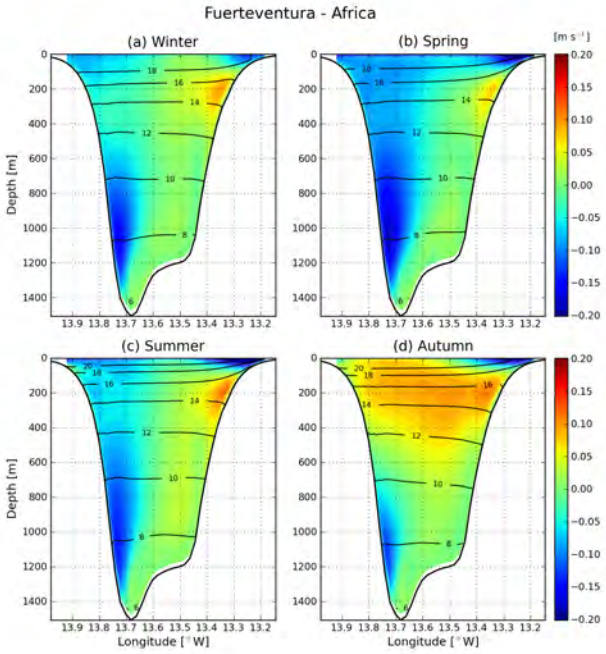

Figure 5.6.: Seasonal velocity sections across the Fuerteventura - Africa passage from L1. Contours in black show the vertical temperature structure.

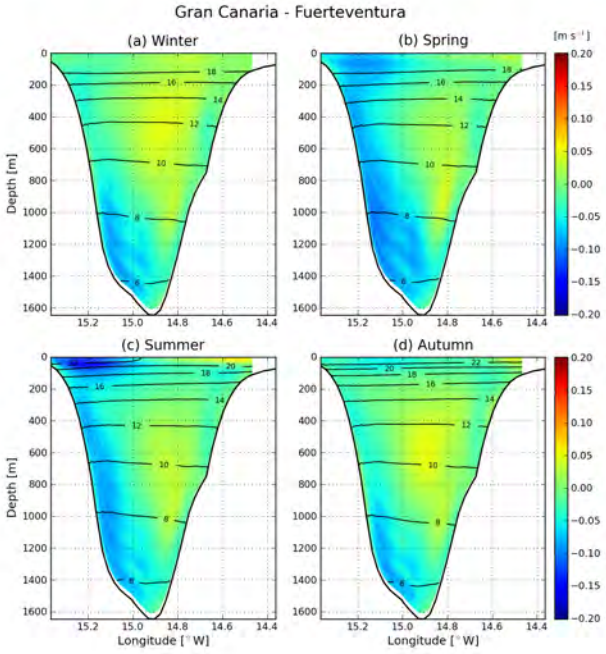

Figure 5.7.: Seasonal velocity sections across the Gran Canaria - Fuerteventura passage from L1. Contours in black show the vertical temperature structure.

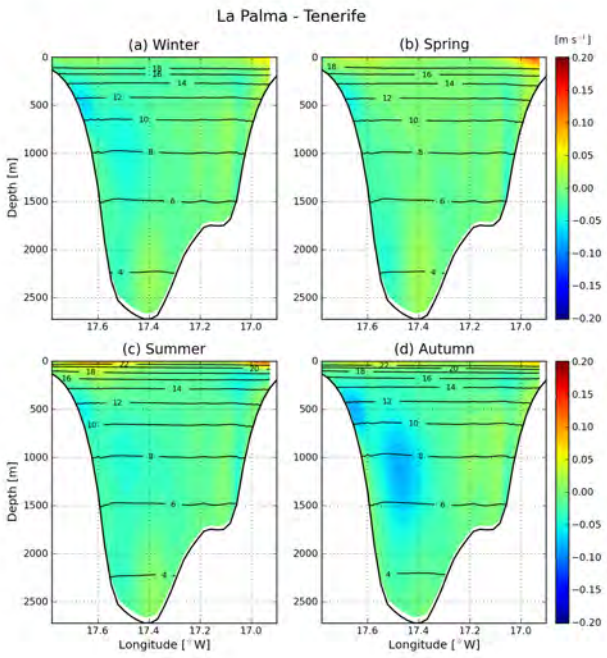

Figure 5.8.: Seasonal velocity sections across the La Palma - Tenerife passage from L1. Contours in black show the vertical temperature structure.

Figures 5.9 and 5.10 show monthly channel transport values (0 - 600 m) in the eastern and western channels. In addition to the total values, net northward and southward values are given. In the Lanzarote Passage, transports over the two transects follow each other closely as expected (Figure 5.9a). Whilst the net reversal to northward flow begins in September, Figure 5.9b shows that significant northward flows begin as early as July, concurrent with weakening of the southward flow (Figure 5.9c). In the shallow channel between Fuerteventura and Lanzarote, the flow is westward all year. Between Gran Canaria and Fuerteventura, most of the variability arises from the southward transport. This is the case also for the channel between Tenerife and Gran Canaria. Figure 5.9c reveals a phase lag of 1 - 2 months in the maximum southward transport values of the eastern passages: the Lanzarote Passage peaks in May, followed by Gran Canaria - Fuerteventura in July, and Tenerife - Gran Canaria in August.

Figure 5.10 shows monthly transports for two western passages. Between La Palma and Tenerife the transport is westward all year, apart from a weak eastward flow that occurs in May. The transect between El Hierro and La Palma indicates westward flow all year, which is strongest in July ($\sim$2 Sv).

The mean surface-layer flow speeds given in this section are weak, $\sim$0.05 m s^{-1}. However, the instantaneous flows are expected to be much higher as larger-amplitude mesoscale variability typically dominates (Navarro-Pérez and Barton, 2001).

Currents below $\sim$500 m are assumed to be weak in the island channels. However, Figures 5.6 - 5.8 all indicate a tendency for deep southward flows on the eastern flanks of the islands,

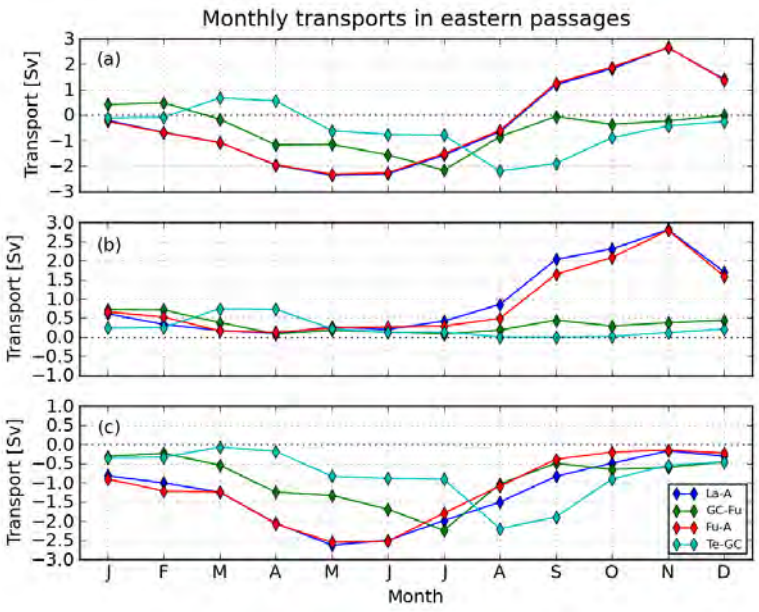

Figure 5.9.: Monthly transports (Sv) in the eastern passages. (a) Net transport. (b) Net northward transport. (c) Net southward transport. Transport directions are normal to the transects in Figure 5.1. Values are in Sv, northward/eastward positive.

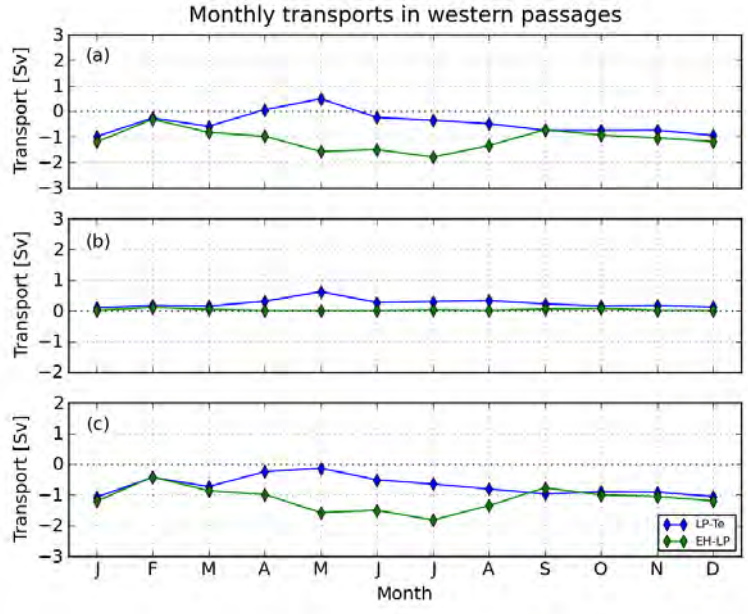

Figure 5.10.: Monthly transports in the western passages. (a) Net transport. (b) Net northward/eastward transport. (c) Net southward/westward transport. Transport directions are normal to the transects in Figure 5.1. Values are in Sv, northward/eastward positive.

which sometimes exceed 0.2 m s^{-1}. This is also the case for Gran Canaria - Fuerteventura, La Palma - La Gomera, and El Hierro - La Palma (see Appendix C).

5.4. The Canary Island eddy field (submesoscale regime)

In this section we give a phenomenological description of the principal types of eddy generation observed in the model solution. Although we concentrate our study on Gran Canaria eddies, we also describe coastal eddies that originate in the Lanzarote Passage, and between Gran Canaria, Fuerteventura and the African coast. We include these eddies because they appear frequently, typically have larger diameters than the island-generated varieties, and are likely to be contributors to the Canary Eddy Corridor (Sangrà et al., 2009).

An examination of the full three-year sequence of daily surface fields of relative vorticity from L2 reveals a complex flow pattern around the islands. An example in August of year 35 is given in Figure 5.11 (see Figure 5.2 on page 117 for the corresponding SST), which shows depth-averaged (0 - 100 m) relative vorticity. Meso- and submesoscale features in the form of fronts, eddies and filaments are numerous. Along the coast south of Cape Juby there are many small-scale phenomena, but the clearest feature is a filament extending offshore at 27°N between Juby and Cape Bojador. Strong westward flow through the shallow gap between Lanzarote and Fuerteventura forms an intense front (cyclonic to the south, anticyclonic to the north) that extends southwest in the direction of Gran Canaria (see also Figure C.2 on page 216). In the south of the domain there is an anticyclone, A1, which is to be discussed in Section 5.4.4.

5.4.1. Incident flow and eddy generation at Gran Canaria

Southwest of Gran Canaria in Figure 5.11 an early-stage (∼7 days) anticyclonic eddy (A2) is in the process of being spun off from the southwest of the island. The incident flow (indicated by the white arrow) fits the idealised scenario for topographic generation of eddies at the island, i.e., inflow from the north/northeast (Section 5.1). However, examination of the flow pattern upstream suggests that this setting may be transient: the incident flow is part of the recirculation of a large diffuse anticyclonic structure with origin at the northern tip of Tenerife. Along the axis of the incident current there is a strong front, evidenced by cyclonic vorticity (horizontal shear) at ∼28.5°N, 15°W, and also visible in SST (Figure 5.2). How common is such a flow pattern? It may not be uncommon, because the patterns (vorticity and SST) agree very well with the summertime mean streamfunction of Figure 5.5c (note that the streamfunction is calculated with L1).

Eddy A2 originates at the capes along the eastern flank of Gran Canaria. Bands of intense negative vorticity can be seen in Figure 5.11 extending around the the south of Gran Canaria towards A2. A similar situation exists to the north, where cyclonic vorticity is being generated and advected westward from a prominent cape (La Isleta, Section 5.4.2). Figure 5.12 presents a vertical section of relative vorticity through A2, showing the eddy to be

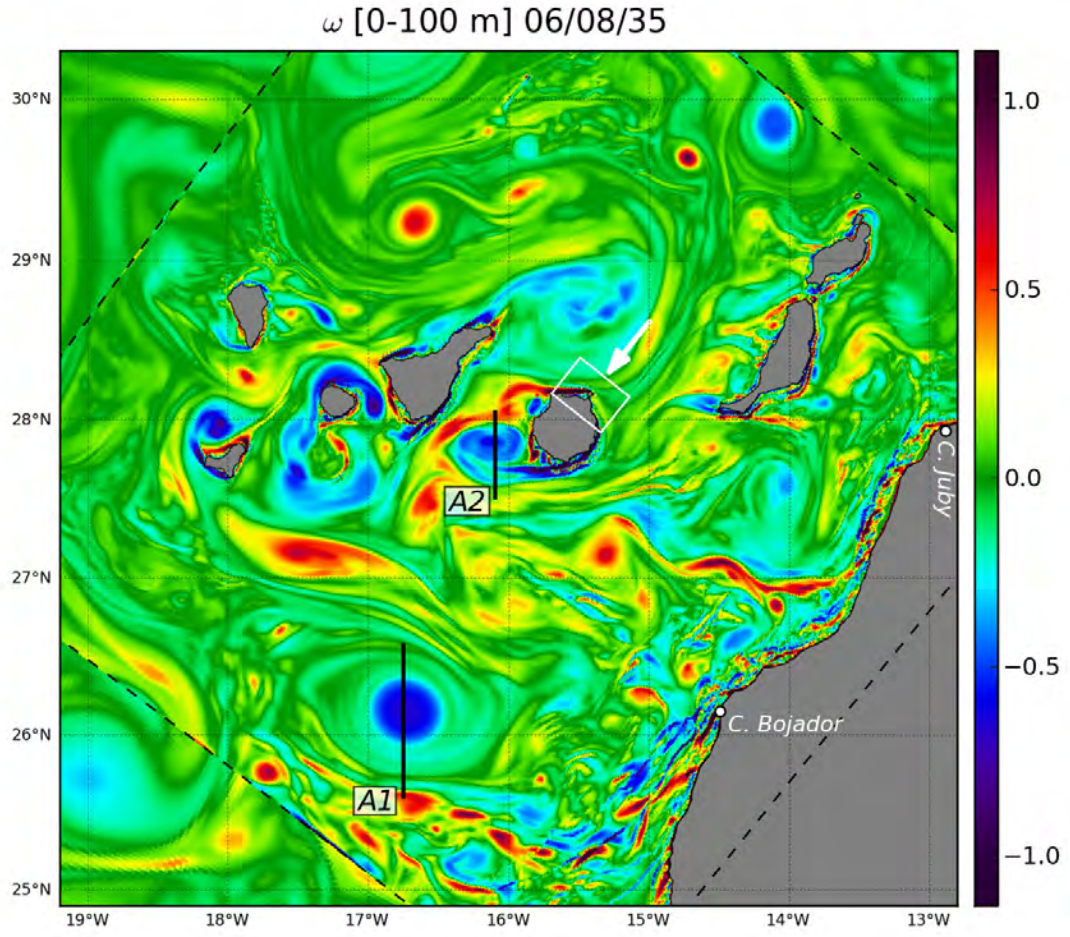

Figure 5.11.: Snapshot of depth-averaged relative vorticity, ω, (normalised by f) in August of model year 35. Two anticyclones, A1 and A2, are identified. The area demarked by the white box plotted over the northern part of Gran Canaria is used to calculate respective timeseries of v-velocity (direction indicated by white arrow), and ω. These are shown in Figure 5.13. The black dashed line demarks the boundary between L1 and L2.

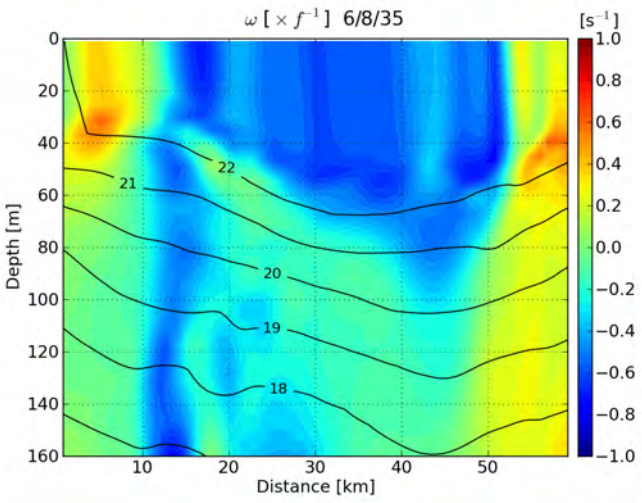

Figure 5.12.: Vertical section of normalised relative vorticity through anticyclone A2 identified in Figure 5.11, which was generated at Gran Canaria. Contours in black show temperature (°C).

shallow with a maximum depth of ∼75 m and generally confined within the 22°C isobath. Anticyclones observed south of Gran Canaria tend to be 2 - 3 times deeper than A2 (Arístegui et al., 1994). Its core is composed of vertical bands of variable-strength anticyclonic vorticity, with cyclonic vorticity at the periphery. A2 turns out to be short-lived, diffusing within one week.

How important is the incident flow for the generation of eddies such as A2 (and longer-lived eddies) at Gran Canaria? A subjective analysis was done to identify cases of eddy shedding in the lee of Gran Canaria by examining animations of surface vorticity in both L1 and L2. Identified events are marked in Figure 5.13, which also shows timeseries of the depth- and area-averaged incident flow from L1 and L2 at Gran Canaria for the period of the L2 solution. In the L2 velocity a clear seasonal cycle shows the incident flow increasing in spring and peaking in summer. However, the magnitude, timing and duration of the summertime peak is variable: year 35 is stronger (>0.2 m s^{-1}) and longer (July through November) in comparison with years 36 and 37. These differences are not surprising and appear to be primarily a result of intrinsic variability generated within L2. The effect in terms of eddy generation in L2 in the lee of Gran Canaria is evident: eddies were observed only between May and October, with the majority in year 35. Anticyclones (11) outnumber cyclones (2). On four occasions eddies were generated under weak incident flow conditions (<0.1 m s^{-1}). The L1 velocities have a less pronounced seasonal cycle than L2.

Figure 5.14 describes a cyclonic eddy (C1) found to the south of Gran Canaria in September of year 36. C1 first appears as a coherent eddy in July in the passage between Gran Canaria and Tenerife (hence it is not included in the eddy count of Figure 5.13). Its original vorticity source is a cape at the northwest of Gran Canaria but it entrains vorticity from Tenerife and remains trapped in the passage, becoming more intense, until the end of August.

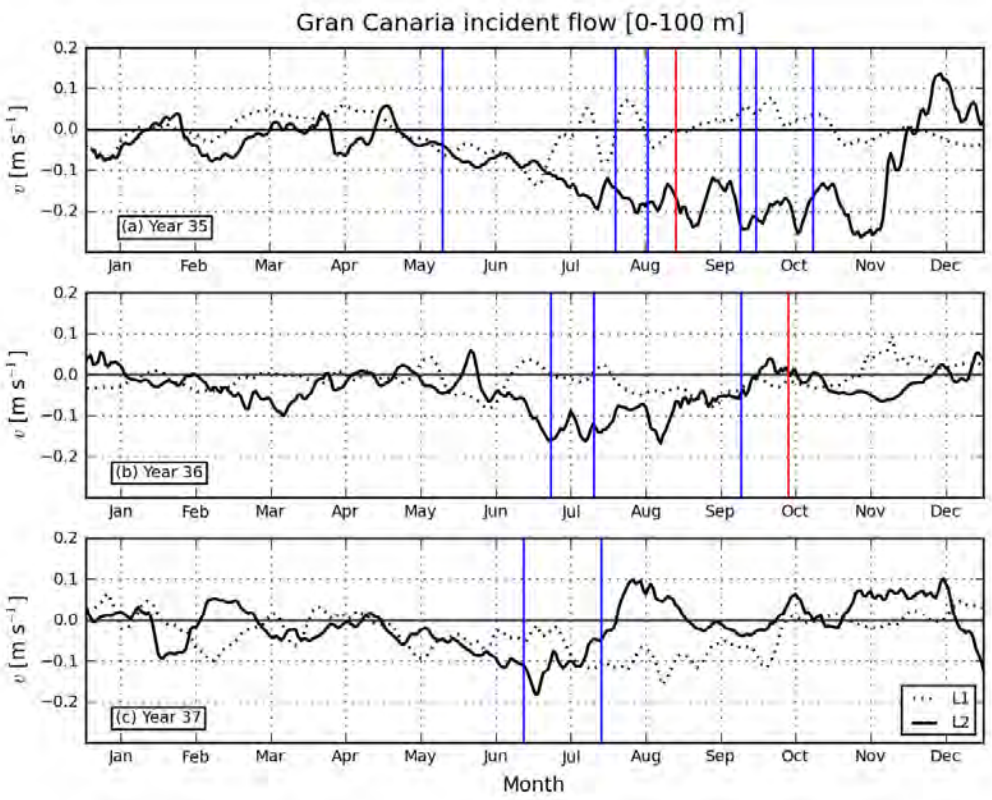

Figure 5.13.: Timeseries of L1 and L2 incident current at Gran Canaria for years (a) 35, (b) 36 and (c) 37. The values are averages of the v-velocity component from each solution over a 100-m-deep box region identified in Figure 5.11. The v-component from L1 is rotated to have the same angle as L2. Blue (red) vertical lines show periods when anticyclonic (cyclonic) eddies were generated and shed south of the island in L2.

(a) (b)

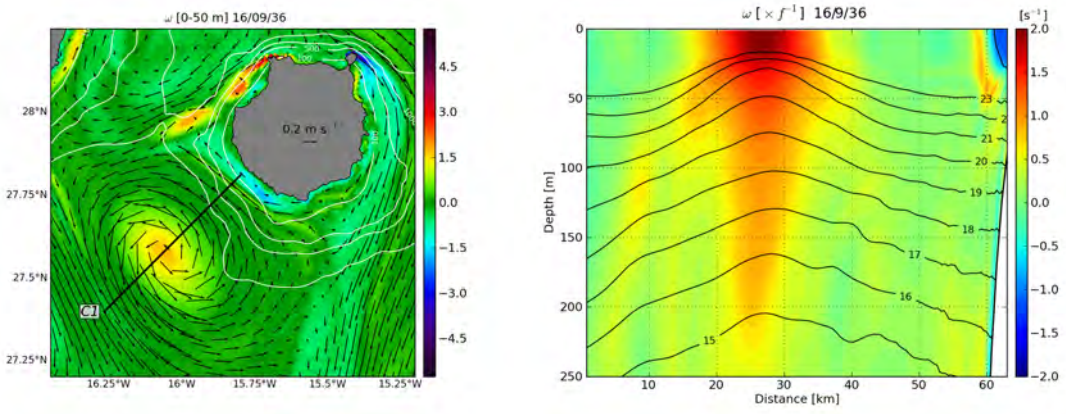

Figure 5.14.: Cyclonic eddy C1 southwest of Gran Canaria. (a) Depth-averaged normalised relative vorticity, ω, in the lee of the island. (b) Vertical ω section through C1 [transect shown in (a)]. Note different colour-bar scales. Contours in black show temperature (°C).

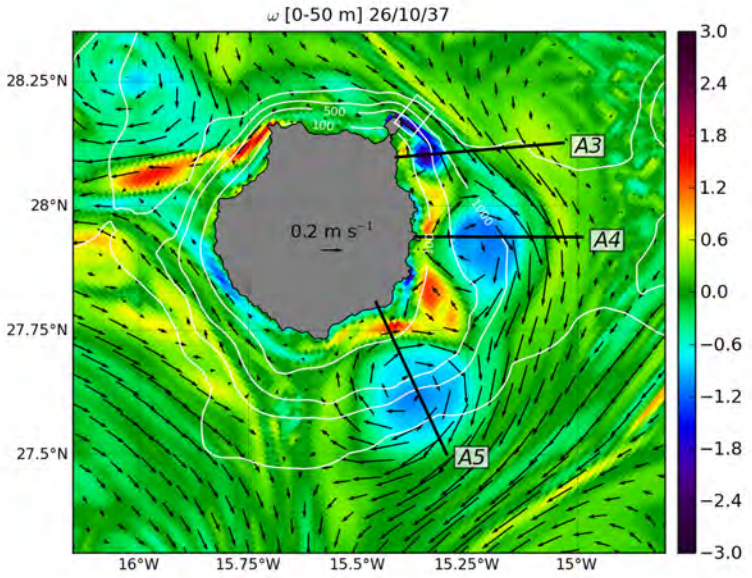

Figure 5.15.: Snapshot of normalised (by f) depth-averaged (0 - 50 m) relative vorticity at Gran Canaria. Black arrows show the current velocity. A sequence of anticyclonic eddies (A3, A4, A5) is spun off from La Isleta under the effect of southeastward flow. The rectangular box in white demarks the averaging area for the timeseries in Figure 5.18. Isobaths in white are at 100, 500, 1000 and 2000 m.

Early in September, C1 abruptly exits the passage and moves rapidly to the south of Gran Canaria, where it is shown in Figure 5.14a. The depth-averaged (0 - 50 m) ω field shows C1 to have an elliptical shape, its diameter approaches that of Gran Canaria. Figure 5.14b shows C1 to have a much deeper structure than A2. The isotherms shows the characteristic cyclonic-eddy uplifting in the centre.

5.4.2. Eddy shedding at La Isleta

Figure 5.15 shows a snapshot of normalised ($\times f^{-1}$) depth-averaged (0 - 50 m) relative vorticity during an eddy-shedding event at the north of Gran Canaria. The location is La Isleta, a small peninsula which extends a few kilometres seaward and where the bathymetry is very steep. A sequence of three anticyclones generated at La Isleta is seen to the east and southeast of Gran Canaria. The anticyclones are generated in response to a steady southeastward flow of $\sim$0.15 m s^{-1} that passes La Isleta, generating strong horizontal shear. Although these are separate eddies, their coincident place and near time of birth makes it is convenient to consider them as the same eddy at different stages of evolution. A3 is the youngest eddy at 2 days. A4 (A5) is about 10 (18) days old. The eddies appear to follow the 1000-m isobath.

Sections of relative vorticity through eddies A3, A4 and A5 are shown in Figure 5.16. The eddies are shallow structures ($\sim$50 m), their cores concentrated within the mixed layer,

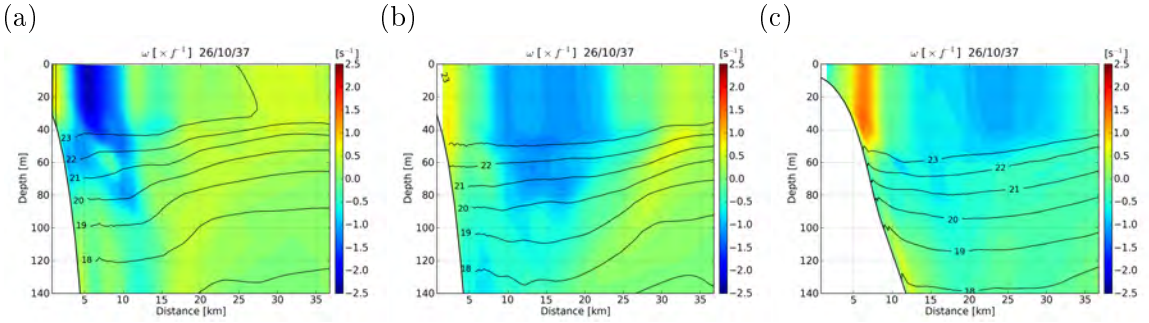

Figure 5.16.: Vertical sections of normalised relative vorticity, ω, through the La Isleta anticyclones (a) A3, (b) A4 and (c) A5, identified in Figure 5.15. Isotherms are contoured in black. The horizontal scales are the same so that the relative sizes are apparent.

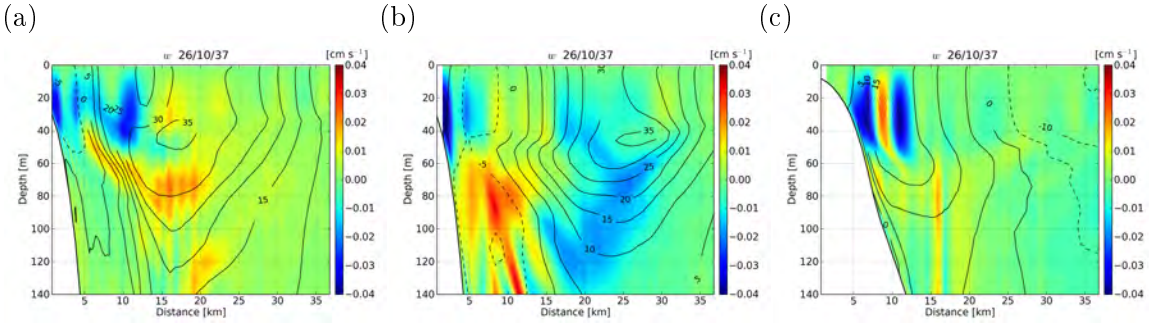

Figure 5.17.: Sections of vertical velocity, w, through the La Isleta anticyclones (a) A3, (b) A4 and (c) A5, identified in Figure 5.15. Contours show the velocity normal to each section in cm s^{-1} (dashed negative).

which contrasts with observed eddy depths of ∼300 - 400 m in the region (Arístegui et al., 1994; Sangrà et al., 2007). Whilst their depths do not change, the eddy radii increase with a corresponding decrease in vorticity, suggesting an adjustment under the condition of conservation of potential vorticity. Vertical velocities within the eddies are shown to be small and tending to negative in the sections in Figure 5.17. A3 (Figure 5.17a) has the largest velocities of ∼0.02 cm s^{-1} (∼17 m day^{-1}) downwards. In this figure the core of the southeastward current (>0.35 m s^{-1}) is shown northeast of the eddy (17 km, 40 m; see also Figure 5.15). Eddy A4 (Figure 5.17b) has positive (upward) vertical velocities on its landward side and negative on the seaward. Eddy A5 (Figure 5.17c) has the weakest vertical velocities of 0.005 cm s^{-1} (∼4 m day^{-1}). The up- and downward flows are arranged in a series of ∼2-km-wide vertical bands that span the depth of the eddy. However, at the landward periphery of A5 the strongest vertical velocities of the sections are seen: two downward vertical bands (∼0.04 cm s^{-1}, ∼35 m day^{-1}) surround an upward flow of ∼0.025cm s^{-1} (∼22 m day^{-1}). There is strong horizontal shear in this region associated with the passage of eddy A5 and the coastal boundary (Figure 5.15).

The absolute relative vorticity (when normalised by f as shown in Figure 5.15) of all three anticyclonic eddies at their time of generation exceeds 1, suggesting that they are

Table 5.4.: Parameters related to the anticyclonic La Isleta eddies (A3, A4, A5) of Figure 5.16. L is eddy radius [m], H is eddy depth [m], $\triangle\rho$ is the density difference between the surface and the base of the eddy [kg m^{-3}], g' is the reduced gravity [m s^{-2}], R is the *Rossby* radius of deformation [m], and Ro is the non-dimensional *Rossby* number.

Eddy	L	H	$\triangle\rho$	g'	R	Ro
A3	2296	50	0.18	0.002	4109	3.2
A4	5357	51	0.15	0.001	3970	0.5
A5	5358	59	0.16	0.002	4483	0.7

inertially unstable ($|\omega|>f$). The short radius[5] of eddy A3 ($\sim$2300 m) suggests that it is firmly in the cyclostrophic regime where centrifugal force dominates *Coriolis*. The *Rossby* number (Ro) can be used to classify the eddies into the cyclogeo- or cyclostrophic regime (Cushman-Roisin, 1994):

$$Ro = \left(\frac{R}{L}\right)^2, \tag{5.1}$$

where the radius of deformation $R = (g'H)^{1/2}/f$, with $g' = g\frac{\triangle\rho}{\rho_0}$ the reduced gravity, H the vertical scale of the eddy, and L the eddy radius. Table 5.4 summarises the results for each eddy. In the case of A3, $Ro \gg 1$, $L \ll R$, centrifugal force dominates the *Coriolis* force so that the eddy is likely to be unstable. While A4 and A5 appear to be near to the stable regime, their histories are the same as A3 and they are already in the process of decay. Within one week from the image shown the eddies have mostly dissipated.

To demonstrate that periodic eddy generation at La Isleta is not uncommon in the solution, Figure 5.18 shows 3-year timeseries from L2 of the tangential velocity and relative vorticity at La Isleta. The timeseries are depth averages (0 - 100 m) taken from within the white box in Figure 5.15. Light blue shading indicates periods of eddy generation at La Isleta. There is clear anti-correlation between u and ω. During most of the year u tends to be negative, i.e., cyclonic flow around the island, and ω is positive. However, there are periods where the flow reverses, and each of the four eddy-generation events coincides with such a period. In years 36 and 37, events occur in summer and autumn. The timing of the event seen in Figure 5.15 (October, year 37) is marked in deep blue. Comparing the present figure with Figure 5.13, it is noteworthy that frequent lee-generation occurs in the summer of year 35, when there are no eddies shed at La Isleta, while the reverse is true for years 36 and 37. This indicates that interannual variability of the incident flow may affect not only the frequency of eddy generation, but also the location. The generation of anticyclonic eddies is a frequent occurrence at La Isleta, although the resulting eddies are short-lived.

[5]Eddy radii (L) are estimated using the vorticity profiles in Figures 5.16a-c. The eddy centre is established as the location where $|\omega|$ is maximum just below the surface. L is then the minimum horizontal distance (projecting left and right) from the centre to a point where $|\omega|$ has decreased by 85%.

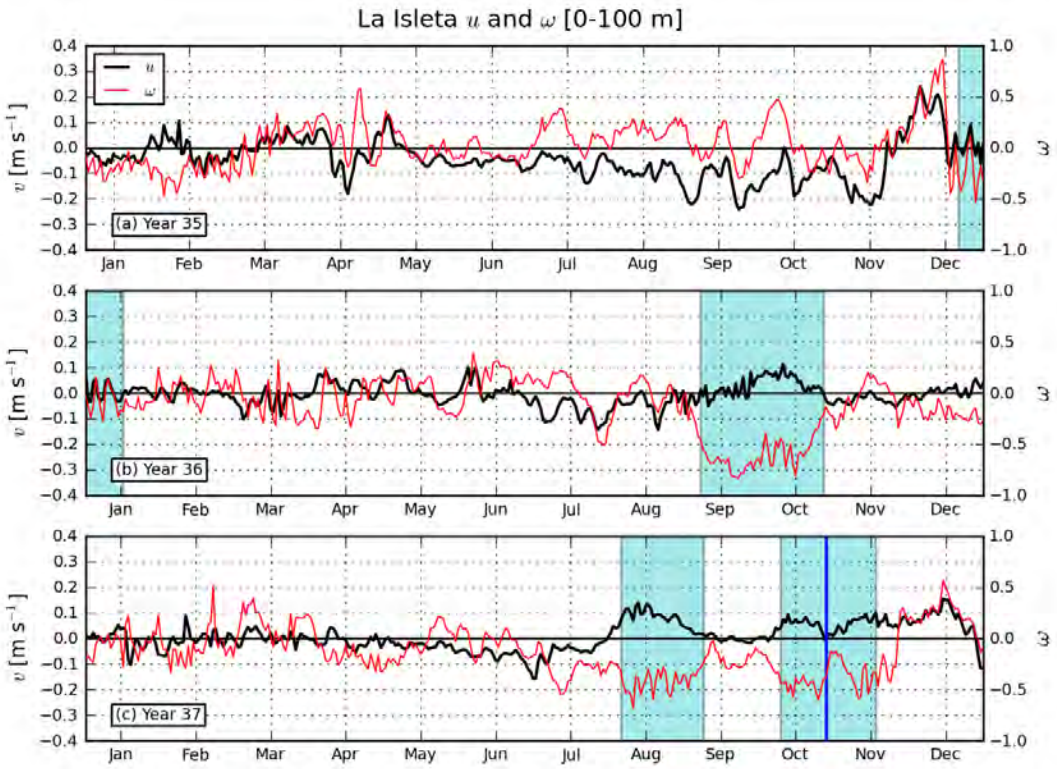

Figure 5.18.: Timeseries of L2 u-velocity and relative vorticity, ω, for years (a) 35, (b) 36 and (c) 37. The values are averages over a 100-m deep region north of La Isleta (see white box in Figure 5.15). Periods of anticyclonic eddy generation observed at La Isleta are shaded in light blue. The deep blue line in October of year 37 corresponds to the event shown in Figure 5.15.

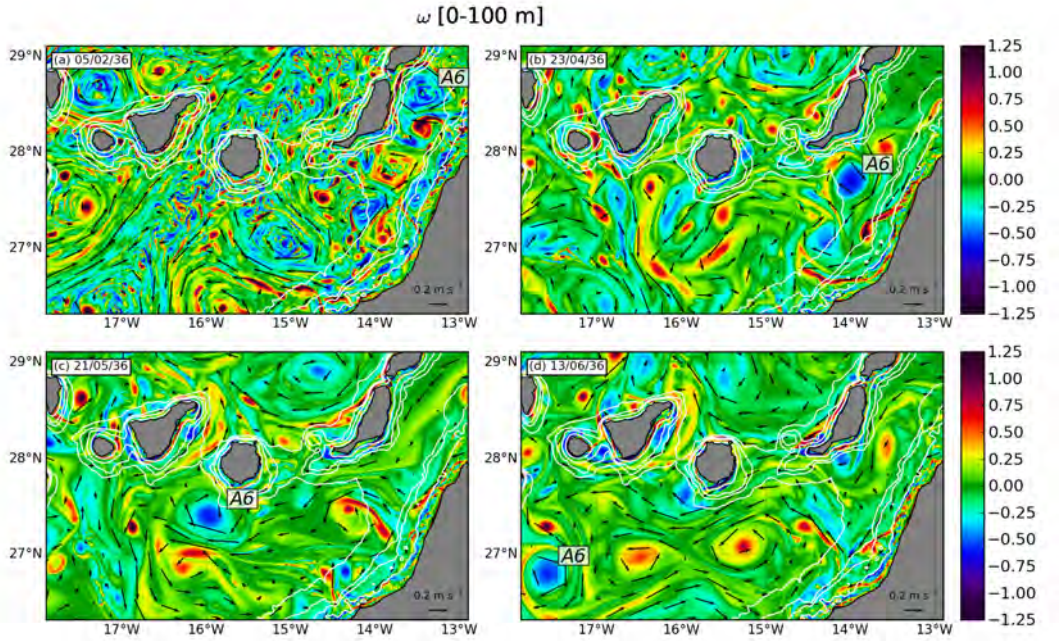

Figure 5.19.: Evolution of L2 anticyclone A6 shown by depth-averaged (0 - 100 m) fields of relative vorticity, ω, normalised by f. (a) The vortex originates southeast of Lanzarote in the Lanzarote Passage in February. (b) In April the vortex passes out of the passage. (c) The vortex is south of Gran Canaria in May. (d) By June, the vortex is seen south of La Gomera.

5.4.3. Lanzarote Passage eddy

Figure 5.19 shows fields of depth-averaged relative vorticity (0 - 100 m), detailing the progression of an anticyclone generated in the Lanzarote Passage over the period of about 7 months. The eddy forms just east of Lanzarote in November of year 35. It remains at this location, growing as it entrains surrounding patches of anticyclonic vorticity.

In February year 35, Figure 5.19a shows that the eddy has a diameter of ∼60 km. The isobaths indicate that it occupies the centre of the passage, across which the mean flow in the surface layers in winter is sheared: northward to the west and southward to the east (see Figure C.1 in Appendix C on page 215). The body of the eddy is composed of concentric rings of stronger and weaker anticyclonic vorticity. Along its northern periphery, there is strong cyclonic vorticity. In March, the eddy begins to coalesce into a single coherent body, and moves southwards. Figure 5.19b shows the eddy in April as it leaves the Lanzarote Passage, taking a southwestward trajectory. It advances rapidly into deep water, and by mid-May is located south of Gran Canaria (Figure 5.19c). Without prior knowledge of the evolution of this eddy, it may easily be mistaken for a Gran Canaria generated anticyclone. By mid-June, the anticyclone is found about 1° to the south of El Hierro (Figure 5.19d). Over the following 30 days it abruptly turns inshore, and then dissipates rapidly at ∼26.3°N, 16°W.

Figure 5.19 also indicates that there is seasonality in the submesoscale regime. Figure

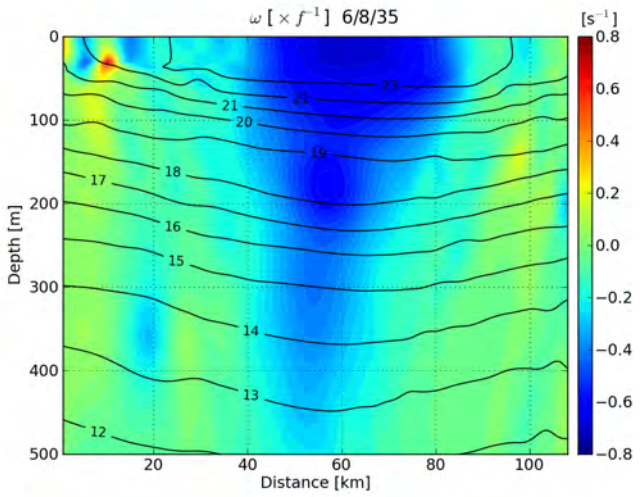

Figure 5.20.: Vertical section of normalised relative vorticity, ω, through anticyclone A1, identified in Figure 5.11 on page 128. Isotherms are contoured in black.

5.19a is in winter, and the overall vorticity field is quite distinct from that of Figures 5.19b-d, which are in spring and early summer. The wintertime image shows a dominance of small-scale turbulent features throughout the domain (Capet et al., 2008a).

5.4.4. Coastal eddy

Figure 5.20 shows a vertical section of relative vorticity through the anticyclonic eddy (A1) identified in Figure 5.11 on page 128. A1 originated in early April between Gran Canaria, Fuerteventura and the African coast: its anticyclonic signature first appears as a cluster of disperse patches of negative vorticity on the north side of a filament at Cape Bojador (similar to the situation seen at the same location in Figure 5.11). The patches converge and, by the summertime, A1 is an intense anticyclone with a depth of ∼400 m. At the surface, its temperature anomaly has nearly double the breadth of the vorticity anomaly (see also the SST field of figure 5.2 on page 117). A1 would seem a likely candidate for a CEC eddy, but by October it has dissipated and passes out of the L2 domain at the southern boundary.

5.4.5. MM5 experiments

The main aim of the MM5 experiments is to test if a higher-resolution wind product has an impact on eddy generation in the lee of Gran Canaria (Basterretxea et al., 2002; Jiménez et al., 2008). Three 3-month MM5-forced runs were made for the L2 domain. Each run was initialised using June 30 instantaneous outputs from L2 years 35, 36 and 37. Figure 5.4 on page 120 showed the evolution of the surface- and volume-averaged kinetic energy for these runs. The effect of the higher-frequency wind forcing is clear, the surface kinetic energies consistently exceed those of L2.

Surface vorticity fields in the three MM5 runs diverge rapidly (∼1 month) from the SCOW-forced solutions, so that their mesoscale patterns are very different. We therefore focused

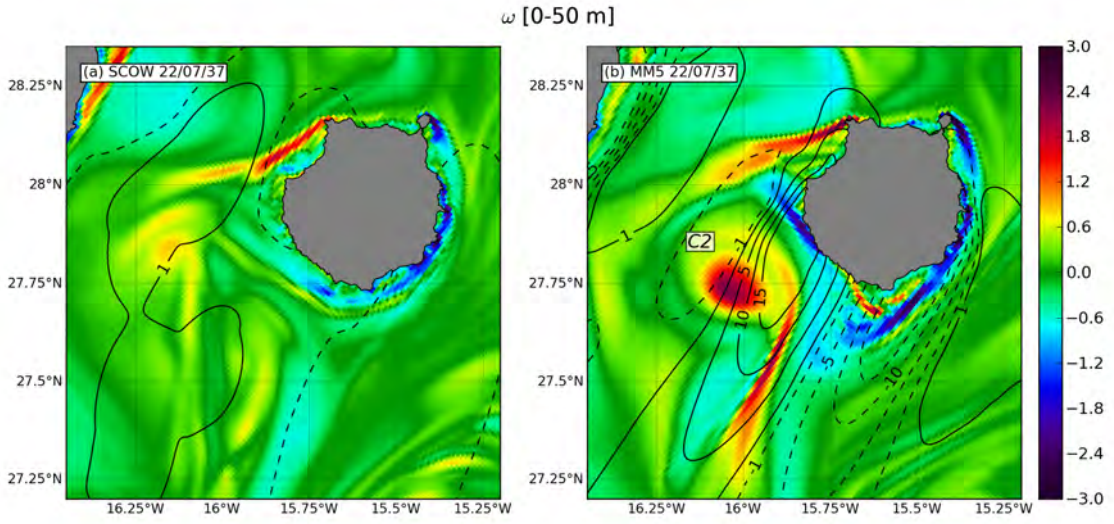

Figure 5.21.: Comparison of depth-averaged (0 - 50 m) L2 relative vorticity south of Gran Canaria from (a) SCOW- and (b) MM5-forced simulations after a spin-up of 19 days. A cyclonic eddy C2 is identified in (b). Contours in black show *Ekman* pumping velocities, w = -15, -10, -5, -1, 1, 5, 10 and 15 m day^{-1} [positive, upwards; negative (dashed), downwards].

on the first month (i.e., July) of the MM5 runs. Figure 5.21 compares vertically averaged (0 - 50 m) relative vorticity at Gran Canaria for L2 and MM5 on 22 July of model year 37. There are some similarities in the two fields which is expected after only 19 days of spin-up, but there are striking differences downstream of Gran Canaria. In the MM5-forced solution a large cyclonic eddy (C2) has formed which is not present in the SCOW solution. It is likely that this eddy is generated through the action of cyclonic wind stress shear. Jiménez et al. (2008) showed in a process-oriented modelling study that wind stress shear in the lee of Gran Canaria can induce the formation of eddies when the incident current is not quite strong enough to do so alone. In the present case the incident current is ∼0.05 m s^{-1} (Figure 5.13). Also plotted in Figure 5.21 are contours of the *Ekman* pumping velocity calculated as $w = \nabla\overrightarrow{\tau}/\rho \times f$, where $\nabla\overrightarrow{\tau}$ is the curl of the wind stress, $\rho = \rho_{z=0}$ is the model density at the sea surface and f is the *Coriolis* parameter. *Ekman* pumping velocities in the SCOW solution are $|w|$<5 m day^{-1} throughout the domain shown, whereas in the MM5 solution $|w|$ exceeds 15 m day^{-1} in the wake region. Overall there is an order of magnitude difference in the *Ekman* pumping velocities for the two wind products. In the region of C2 there are strong positive (upward) velocities, consistent with a cyclonic eddy. This simple experiment is a confirmation of the model results of Jiménez et al. (2008), and also a demonstration of why using high-resolution wind stresses from atmospheric models may be important for numerical island wake studies.

5.5. Discussion and conclusions

Mesoscale and near-submesoscale variability at the Canary Islands is described using a one-way nested regional ocean model configuration. Under the influences of mean seasonal atmospheric forcing and high-frequency open boundary forcing from parent ROMS solutions, two solutions (3 and 1 km) are generated.

The main features of the mesoscale circulation from the 3-km solution (L1) (Section 5.3) are as follows: While coarse-resolution observational studies point to the Canary Current impinging on the archipelago from the northeast, the simulated current shows a highly-variable pathway to the islands. In summer the incoming flow at Gran Canaria arrives from the northwest. The transport onto the island is nearly 0.5 Sv in the top 200 m. South of the archipelago, the lee is characterised by tightly packed flow streamlines. In spring and summer a strong cyclone develops between Gran Canaria and the African coast. Interplay between the cyclone and an intense offshore anticyclone in summer and autumn appears to lead to the well-known autumn flow reversal in the Lanzarote Passage. The streamlines of the two cells are zonally elongated from near the coast to west of the islands. A corresponding zonal extension of the autumn EKE is seen in the L0 solution (Figure 4.19 on page 105). The eddy tracking experiments of Section 4.6.3 (page 106) show that a large proportion of long-lived eddies are generated off the African coast in autumn and winter. We can speculate that these eddies arise as a combination of barotropic instability associated with the onshore/eastward flow, and baroclinic instability associated with the upwelling front which is in place even in winter.

Transports calculated in the Lanzarote Passage are in agreement with observations. Velocity sections show that autumn flow reversal occurs throughout the Central Water layer (near surface to ∼500 m) in the passage. This suggests that local relaxation of the upwelling winds which occurs in autumn is not the cause of the flow reversal as has been speculated. In fact, in the model the upwelling jet persists throughout year over the African shelf and slope, accompanied by a poleward flowing undercurrent centred at about 250 m over the slope (Barton, 1989).

At depth, the passage velocity sections show surprisingly strong anticyclonic currents along the flanks of the islands. At Gran Canaria for example southward velocities greater than 0.05 m s^{-1} are present all year between 800 m and the bottom of passage (Figure 5.7). These may be Taylor columns (Huppert and Bryan, 1976; Goldner and Chapman, 1997) or an anomalous island circulation of the type mentioned by Chopra (1973). See Appendix C for more examples of these deep flows.

The near-submesoscale regime is revealed by the three-year 1-km solution (L2) (Section 5.4). High-resolution observations that resolve the submesoscale have not been conducted at the Canary Islands, with the exception of Sangrà et al. (2001). These authors studied effects on the biology of internal waves at the shelf break at Gran Canaria, finding that productivity was greatly enhanced as a result of vertical fluxes associated with internal wave mixing. Productivity is limited by the availability of nutrients, which are at depth, and light, which is

at the surface. Submesoscale fronts support large vertical fluxes (~ 100 m day^{-1}, typically an order of magnitude higher than mesoscale fronts; Thomas et al., 2008), providing a pathway for exchange between the lower layers and the photic zone. At the surface, patchiness in property distributions may be attributed to submesoscale processes. Capet et al. (2008a) demonstrated that convergence associated with submesoscale near-surface currents rapidly concentrates passive particles; this has implications for passive or semi-passive organisms such as fish larvae. Patchiness may affect biological production by limiting access to nutrients or oxygen. A shift towards submesoscale studies and observations may therefore be in order in the Canary region. As well as biological productivity, submesoscale processes have a significant impact on the ocean energy cascade and near-surface restratification (Capet et al., 2008c; Klein and Lapeyre, 2009; McWilliams et al., 2009).

Variability in the incident flow at Gran Canaria is shown to lead to two distinct regimes for eddy generation at the island. The first year of the solution had a relatively strong summertime incident flow at the north. Counts of eddies generated at the south at this time were correspondingly high. In the two subsequent years, the incoming flow had a northeastward component and eddy counts were down. However, a greater number of headland eddies were seen generated at La Isleta, a small peninsula at the north of the island. Eddies at this location have not been reported in the literature.

Three anticyclones (A3, A4, A5) generated in quick succession in October year 37 at La Isleta during a period of northeastward flow were shown in Figure 5.15. An analysis of the eddies indicated them to be inertially unstable, and all three were dissipated away within a short time. It was shown that vertical velocities associated with the eddies were generally small apart from at their peripheries, especially the nearshore edges: A5 had up/downwelling of $\sim$30 m day^{-1}. This is a localised transient event but the substantial associated vertical transports may be expected to have significant consequences on biological production even at such short timescales (Hernández-León, 1991). Eddies similar to the La Isleta anticyclones are also observed at Tenerife.

Headland eddies have been widely studied (Signell and Geyer, 1991; Aiken et al., 2002, 2003; Edwards et al., 2004; McCabe et al., 2006). The generation mechanism for the La Isleta eddies may be internal form drag, where high stratification forces the flow around the obstacle (i.e., the submerged ridge associated with the headland), resulting in downstream flow separation and formation of eddies (Edwards et al., 2004). Figure 5.18 showed that most periods of anticyclone formation at La Isleta occurred in summer and early autumn, when stratification is high. A clear exception is December-January of year 35; the eddies observed at this time possibly arise as a combination of the current shear and winter submesoscale instabilities in the surface mixed layer. Cyclonic vorticity is also generated at La Isleta under conditions of northwestward flow, viz Figure 5.11. The La Isleta results demonstrate that headlands and capes in the Canary Islands may make a significant contribution to the total vorticity production at the archipelago.

Outbreaks of small-scale turbulence across the domain in winter were observed in the solution, demonstrating the seasonal cycle in the submesoscale regime. That many of the

vortices are found far from land indicates that their existence is not necessarily associated with topography. Capet et al. (2008a) reported similar submesoscale turbulence over the Argentinian shelf in winter that was attributed to mixed-layer instabilities brought about by a deep surface boundary layer and a cross-shelf density gradient. Vertical velocities associated with mixed layer instabilities lead to rapid restratification of the mixed layer, which are important for biological production (Thomas et al., 2008).

Additional L2 experiments using 6-km winds from an atmospheric model showed the advantages of using a high-resolution surface wind stress. Despite temporal averaging to match the monthly SCOW climatology, the MM5 outputs retained a high degree of spatial resolution relative to SCOW. *Ekman* pumping velocities computed from the curl of the wind stress in the lee of Gran Canaria were an order of magnitude higher for MM5 than SCOW. Comparison of the ocean model solutions revealed the formation of a cyclonic eddy downstream of Gran Canaria soon after initialisation in the MM5 forced run.

In this final chapter a variety of eddies of differing origins within the Canary Island region has been presented. This result underlines the complexity of the region, and the need for further investigation into the processes and mechanisms behind these phenomena. This characterisation of the mean circulation and the eddy field at the Canary archipelago may be a useful aid in the planning of future observational efforts towards these objectives.

Acknowledgments

Evan Mason is supported by the Spanish research project RODA (CTM2004-06842-C03-03). ROMS development at UCLA is supported by the Office of Naval Research (currently grant N00014-08-1-0597). This work was partially supported by the National Center for Supercomputing Applications under grant number OCE030007 and utilised the *abe* system.

6. Discussion and conclusions

6.1. Synthesis of results and general discussion

The goal of this thesis work has been to study the ocean circulation in the Canary Basin using a numerical ocean model. To this end, a high-resolution regional ocean model (ROMS) configuration has been designed and implemented. In order to achieve $\mathcal{O}1$-km resolution at the Canary Islands, and also to ensure a valid large-scale circulation pattern, an offline nesting approach has been used. The configuration therefore consists of three independently-run domains, which feature successively higher resolutions. Our interest is the equilibrium dynamics of the study region. We therefore use a combination of monthly and, where available, higher-frequency downscaled means of the prognostic variables to force the model boundaries. Interannual variability is omitted from the applied forcing.

6.1.1. Results

6.1.1.1. Model and methodology (Chapter 3)

It is shown that in regional ocean modelling one-way offline nesting is a valuable technique, provided that the boundary forcing is carefully prepared. A methodology is described that incorporates the essential ingredients of an effective boundary forcing. It is demonstrated that inconsistencies between the interior model solution and the external boundary information are minor, mesoscale structures readily enter and/or leave the domain. The methodology is in use with ROMS users at UCLA and elsewhere (Capet et al., 2008a; McWilliams et al., 2009).

A series of sensitivity tests were applied to test the robustness of the model open boundary condition. Perturbations were introduced to the surface wind stress forcing field, to the volume conservation enforcement in the boundary forcing, and to the vertical density structure in the boundary forcing. The tests revealed that volume conservation across the open boundaries of the child grid is an important consideration in building a boundary forcing.

The methodology of Chapter 3 was applied to the offline nested simulations of Chapter 5. In addition, lessons learned during the methodology work forced us to go back and reevaluate our L0 boundary forcing procedure, which was based initially on the methodology of Penven et al. (2008)[1]. The subsequent improvements we introduced to the preparation of the climatological forcing for the L0 outer domain are documented in Chapter 4.

6.1.1.2. Seasonal study of the Canary Basin (Chapter 4)

A validated high-resolution numerical model solution of the Canary Basin in the subtropical northeast Atlantic has been presented. The model boundaries, surface and lateral, are forced with climatological data. Interannual variability nevertheless exists within the outputs, as a result of the intrinsic variability of the evolving solution. The solution is 50 years long, so

[1] In total, three complete nested configurations have been made. The first (2007) and second (2008) were discarded in favour of the 2009 solution. The methodology work of Chapter 3 was based on the 2008 solution.

that the sample size for a statistical analysis is large. Means and variances of the dynamic variables largely conform to the values obtained from observations.

The main physical oceanographic result obtained from the solution concerns the Canary Current. The path of this current between the latitudes of Madeira and the Canary Islands has been observed to display considerable seasonal variability (Pelegrí et al., 2006), yet a definitive characterisation of the seasonal cycle has not emerged. The L0 solution shows that the path of the Canary Current is constrained by westward-propagating planetary-wave-like (Rossby) structures that originate near to the northwest African coast. Two structures are identified. A closed-contour cyclonic anomaly develops south of Cape Ghir in spring. Its counterpart is a similar anticyclonic anomaly that develops near to Cape Sim in autumn. As the two anomalous structures propagate away from the coast at $\sim$3 cm s^{-1}, the path of the Canary Current coincides with the southward-directed flank of each anomaly. These structures have a surface expression and so are visible in altimetry, confirming their existence. Comparisons with *in situ* data from a series of seasonal cruises between Madeira and the African coast in the 1990s provide additional confirmation.

The circulatory system outlined above is surprisingly robust, according to a sensitivity experiment with a closed Strait of Gibraltar. The Canary Current is said to be fed by the Azores Current. This prompts the question: What would happen if the Azores Current were removed? The Azores Current is strongly affected by the presence of the Mediterranean Outflow plume in the Gulf of Cadiz (Jia, 2000). A model experiment was therefore performed where the Strait of Gibraltar was closed, preventing exchange between the Mediterranean and the Atlantic. The Azores Current was significantly weakened. However, the Canary Current was essentially unchanged. Meridional transports of the Canary Current between Madeira and the African coast, with and without the Azores Current, were in close agreement. The transports were also very similar to transports calculated using the Sverdrup relation, confirming the wind to be a dominant mechanism in forcing the Canary Current. Whilst the Azores Current does function as a source for the Canary Current, a dynamic relationship between the two appears to be weak.

The long-lived eddies of the recently identified zonal Canary Eddy Corridor (CEC) are shown to have mixed origins, and to be seasonally dependent. The CEC stretches westward at $\sim$26°N. Altimetry has shown the eddies to be generated in the lee of the Canary Island archipelago, but poor resolution of the sensor precludes a more detailed study. An eddy tracker applied to the model results is used to plot the trajectories of the CEC eddies. It is found that the majority of the eddies, both cyclonic and anticyclonic, are generated towards the African coast. Only in summer does island generation become important.

6.1.1.3. High-resolution Canary Island modelling (Chapter 5)

The aim from this early look at the Canary Island solution is to characterise both the seasonal mesoscale circulation at the islands, and also the eddy field (Chapter 5). Streamfunction fields conform to the known seasonal cycle of the Canary Current, showing more intense

currents in the summer months. In addition, the model gives an indication of the direction of the incoming flow at the archipelago. At Gran Canaria, the mean summertime incident flow arrives from the northwest. Strong flows are sometimes seen rounding the northern tip of Tenerife. South of the island, the current recirculates westward.

Transports are computed within the island channels. Between the African coast and the eastern islands (Lanzarote and Fuerteventura), the model reproduces the observed autumn flow reversal, from equatorward to poleward. It has been speculated that poleward flow is associated with the seasonal relaxation of the upwelling-favourable winds. However, in the model the (equatorward) upwelling current is maintained in autumn. It is seen as a year-round intense jet in the top 100 m of the water column, close to the African shelf. The autumn reversal, however, occupies the full width of the channel down to ∼500 m. This suggests that another mechanism (likely to be remote) independent of the Trade winds should be responsible for the seasonal reversal of the flow along the African coast.

The model results point to the roles of capes, headlands and small peninsulas on the Canary Islands as significant sources of vorticity. At Gran Canaria, for example, La Isleta on the north of the island is a peninsula where intense vortices are frequently generated. When the current is from the northwest, anticyclones are formed that are advected east and south around the island. A current from the northeast leads, conversely, to the generation of cyclonic vorticity on the western side of La Isleta. There are no reports in the literature of observations of such phenomena.

Also at Gran Canaria, it is shown that the application of a spatially higher-resolution wind stress obtained from an atmospheric model (MM5) resulted in lee eddy generation that did not occur under climatological wind stress forcing conditions.

6.1.2. Perspectives on the model configuration and approach

It is important to include a mention of the known deficiencies in our approach and use of the model. Some of these are previously known issues, others have come to light during the course of this study and may be corrected in the future.

- Climatological approach: In adopting a monthly climatological approach it is implicit that we exclude sub-monthly and interannual scales. Higher-frequency winds may be important, consider for example the case of a two-week summer relaxation of the upwelling winds. At lower frequencies, the consequences of a change of sign of the North Atlantic Oscillation will not be captured by our model.

- One-way nesting: When using one-way nesting there is no feedback from the child to the parent solution. This may be important for the large-scale structure, as has been shown through the use of a two-way nested model configuration for the Agulhas retroflection off South Africa (Biastoch et al., 2008). In the Canary Basin, a two-way nesting applied at the Gulf of Cadiz may improve the Mediterranean outflow and subsequent spreading of MW.

- Open boundary artifacts: The problem of open boundary artifacts is not solved for the parent domain (L0). In Figure 1.1 on page 4 we showed anomalous L0 rim currents along the western boundary. These artifacts show up whenever an alien data source (e.g., outputs from an Ocean General Circulation Model as opposed to ROMS) is used to force the open lateral boundaries. A possible solution to at least minimise the problem is a basin-scale domain, which would reduce the open-boundary area.

- Vertical resolution and discretisation: The conventional approach when designing a ROMS configuration is to increase the vertical resolution in the surface layers. The bottom layers are neglected, the reasoning being that we are usually interested in surface aspects of the circulation only. However, topographic features can exert an important control on the surface circulation, even if these features are in deep water such as the Mid-Atlantic Ridge (Bower and von Appen, 2008). The large-scale L0 solution does not resolve the bottom boundary layer in deep water, so that this important component of the forcing may be missing or incorrect. In the high resolution solutions (L1 and L2) the increased vertical resolution is implemented. No systematic comparison has been made so far between realistic solutions with and without the increased bottom resolution, so it is not really known what difference this may make.

- Wind resolution: The SCOW global wind climatology is currently the best observed wind product available. It is based on 8 years of wind data at 0.25° resolution from the SeaWinds scatterometer aboard the QuikSCAT satellite. It was shown in Chapter 5 (page 136) that an order of magnitude difference in *Ekman* pumping velocities downstream of the Canary Islands arises when using the 6-km resolution MM5 wind stresses rather than SCOW. On this basis alone it is possible to conclude that the present model solutions may be improved with a higher-resolution wind product from an atmospheric model.

- Riverine input was not included in the configuration. Off northwest Africa river discharges are minimal, but they may be dynamically important off western Iberia (Peliz et al., 2002).

6.2. Conclusions

The main conclusions that arise from this thesis are divided into two sections that reflect the contrasting contributions between Chapter 3, and Chapters 4 and 5. The content of Chapter 3 concerns numerical modelling procedures related to open boundaries. Chapters 4 and 5 are the result of application of the above procedures to model domains in the Canary Basin, enabling an oceanographic study to be carried out. We start with the oceanography:

Oceanographic contribution

- Insight is provided by the model solution into the circulation of the Canary Current north of the Canary Islands. The path of the current is mediated by the westward propagation of annually-excited planetary (Rossby) waves which originate near to the African coast. The seasonal cycle of the mean zonal position of the simulated Canary Current at 32°N agrees well with published *in situ* estimates. Mean transports within the range ∼3 - 6 Sv are likewise in agreement with observations; peak transport is in summer. Sea surface height anomalies from altimetry confirm the existence of the planetary waves.

- The Canary Current is shown not to be highly sensitive to variability in the Azores Current. A sensitivity experiment where the Azores Current was removed by closing the Strait of Gibraltar had little effect on the Canary Current: seasonal transports and circulatory pathways were essentially the same with and without the Azores Current.

- The origins of the long-lived eddies that constitute the Canary Eddy Corridor (CEC) at ∼26°N are seasonally dependent. During most of the year, especially in autumn and winter, CEC eddies are formed off the African coast; they are not generated at the islands. Only in summer does topographic generation by the islands become dominant. The inability of altimetry to resolve nearshore sea surface height anomalies precludes an observational confirmation of this result for the present.

- The mesoscale seasonal circulation at the Canary Islands has been described. The upstream incident current at Gran Canaria is predominantly from the northwest in summer, contrary to the northeast as determined from low-resolution climatologies. In the immediate lee of the Canary archipelago the circulation is weakly cyclonic for much of the year. Slightly further to the south (∼1°) an intense anticyclonic cell is present all year. In autumn seasonal reversal of the flow in the Lanzarote Passage occurs, apparently as result of interaction between the anticyclonic cell and the summertime intensification of the cyclonic circulation.

- The flow reversal occupies the full Central Water layer of the Lanzarote Passage, making local relaxation of the upwelling winds an unlikely mechanism for the reversal.

- An eddy census reveals a large variety of eddies in the Canary Island wake region with different origins.

- Headlands on the islands, especially Gran Canaria, are important sources of vorticity. Transient cyclostrophic eddy events are frequently seen at La Isleta on the north of the island. Vertical transports at the peripheries of these eddies are significant, with possible biological implications.

- At the submesoscale the wintertime is characterised by outbreaks of mixed layer instabilities, in common with other eastern boundary and shelf regions.

Modelling aspects

- One-way offline nesting is still a valuable approach in regional ocean modelling, despite the emergence of two-way methods.
- The boundary forcing file creation process is critical. Artifacts are introduced into the model solution if the boundary forcing is not approached with care.
- In a ROMS-to-ROMS context, the downscaling methodology to create boundary files described in this thesis produces good model results.
- Perturbation experiments suggest that the most critical aspect to get right is enforcement of volume conservation at the boundaries.
- When downscaling to a ROMS configuration using boundary information from a source other than ROMS, the methodology is less reliable.

The results outlined above serve to validate the choice of a climatological modelling approach to the questions addressed in this thesis, as opposed to an interannual or event-based study. A climatological configuration aims to simulate the mean state of a system, including its variability which arises intrinsically within the model. The mean and eddy state of the circulation in the Canary Basin as obtained from the solutions presented here has been validated through comparison with a range of observed quantities. There may therefore be considerable confidence in the oceanographic conclusions drawn from these model results.

6.3. Future work

There is wide scope for future work with the model solutions presented in this thesis. The parent domain covers a large portion of the northeast Atlantic and is at an ideal resolution for downscaling to very high resolutions using a minimum number of nesting stages. The model outputs can conceivably be used to support the following studies:

- A submesoscale study at Gran Canaria. A 300-m grid is envisaged.
- The northwest African upwelling: A modelling study using a solution downscaled from L0 is presently underway looking at the Cape Ghir filament (Troupin et al., 2009b).
- Fronts such as the Cape Verde Frontal Zone: Steven Herbette (personal communication) has started work on mixing at the CVFZ using a solution downscaled from L0.
- Other island archipelagos of Macaronesia: Rui Caldeira (personal communication) is downscaling from the L0 solution to a 2-km grid at Madeira.
- *Meddy* generation in the Gulf of Cadiz and along the Portuguese slope at the submesoscale. Such a study would complement high-resolution observations of *Meddies* made using seismic reflection profiling (Buffett et al., 2009; Klaeschen et al., 2009).

- Larval advection studies: Model velocity outputs can be used by Individual-Based Models (IBM) to study the advection of larvae and other passive or semi-passive particles. An IBM, using velocities from an early lower-resolution version of L1, has been applied at the Canary Islands (Brochier et al., 2008, 2009). The objective of the reported experiments is to characterise the arrival of sardine larvae at Gran Canaria, which are advected towards the archipelago within upwelling filaments originating between Capes Bojador and Juby.

- Biogeochemical (BGC) studies: ROMS includes an NPDZ-type ecosystem/BGC module (Gruber et al., 2006). ROMS has also been coupled to the PISCES BGC model to study the Peruvian upwelling [Echevin et al. (2008) and references therein]. The physical model presented here may form the backbone to a future coupled physical/BGC study at the Canary Islands.

- Seamount studies: Seamounts are common features of the Canary Basin region and are of growing physical and biogeographical interest (Bashmachnikov et al., 2009; Mohn et al., 2009). The present configuration could be used to support studies of *Meddy*/seamount interactions, or an interdisciplinary study of seamounts with the inclusion of BGC modules.

- The L0 grid may be used for an interannual study if questions should arise about the region that could not be addressed with the climatological solution. The effects of changes in the North Atlantic Oscillation is one possible motive, for example.

- The present solutions could be much improved by using surface forcing data from a regional atmospheric model such as WRF (Weather and Research Forecasting model, a successor to MM5) (Skamarock et al., 2008). The benefit of the use of MM5 winds for the L2 configuration at the Canary Islands was demonstrated in Section 5.4.5 on page 136. Similar benefits may be expected for the coastal upwelling.

- Finally, creation of a new parent solution to cover the Atlantic Ocean is anticipated, thereby replacing L0.

7. Resumen en español (Spanish summary)

7.1. Introducción

El resumen en español se organiza de la siguiente manera. Sección 7.2 presenta las principales metas y objetivos de la tesis. Sección 7.3 describe la oceanografía física del margen noreste del Océano Atlántico, con una sección dedicada a la región Canaria. El enfoque adoptado en el modelo utilizado en este trabajo de tesis se describe en la sección 7.4. Los principales resultados y una discusión general de los tres capítulos centrales (capítulos 3, 4 y 5) se presenta en la sección 7.5. Las principales conclusiones se exponen en la sección 7.6. La sección 7.7 concluye con un resumen de las futuras líneas de investigación.

7.2. Objetivos de la investigación

El objetivo general de este estudio es investigar la circulación y la variabilidad mesoescalar y submesoescalar en la Cuenca de Canarias a través de un modelo numérico. Dada la vasta extensión del área, el estudio se centra en la zona de las Islas Canarias y el noroeste de África. Actualmente existen pocos estudios numéricos para esta región y, de éstos, ninguno a las resoluciones que aquí se describen.

Las Islas Canarias se encuentran en la zona de transición entre el mar y el afloramiento del noroeste de África, conocido como el Canary Upwelling Ecosystem (CUE). El CUE es uno de los cuatro sistemas de afloramiento más importantes del océano global, que con tan sólo el 0,1 % de su superficie representa el 30 % del total de las capturas de mundiales pesca (Durand et al., 1998). Debido a la importancia del ecosistema en la CUE, en los últimos años se han llevado a cabo estudios intensivos de la dinámica de mesoescala asociada al afloramiento y su interacción con las estelas de las islas. La producción biológica es altamente dependiente de esta dinámica, por lo que es necesario comprenderla. Básicamente, el intercambio horizontal y vertical de masa, causado en origen por la tensión de corte del viento junto con la topografía, hace que los nutrientes queden disponibles para el plancton, al ser bombeados hacia la zona fótica. Con respecto a otros afloramientos importantes, la dinámica de la CUE es particularmente compleja debido a la presencia de las Islas Canarias. En la actualidad sólo tenemos un conocimiento parcial del campo de remolinos asociados a las islas y del papel de los frentes asociados al afloramiento e inestabilidades del mismo en los intercambios plataforma-océano (Barton et al., 2004). La visión general de estos aspectos de la CUE está descrita en algunos artículos de revisión (Barton, 1998; Arístegui et al., 2006, 2009).

Con esta perspectiva, en el presente trabajo se han desarrollado un conjunto de configuraciones *anidadas*[1] del modelo , con resoluciones cada vez más altas en áreas más pequeñas

[1] En este capítulo, en relación con los modelos oceánicos regionales se adoptan los siguientes términos en español como traducciones adecuadas del inglés:

- anidación o acoplamiento - *nesting*
- anidamiento unidireccional - *one-way nesting*
- anidamiento bidireccional - *two-way nesting*
- malla de mayor resolución (o similar) - *parent*
- malla interior (o similar) - *child*

(Figura 7.1. A gran escala (es decir, la Cuenca de Canarias), esta tesis se centra en el carácter de las corrientes geostróficas que impactan contra las Islas Canarias. La Corriente de Canarias es el flujo incidente en el archipiélago, por lo que se espera que su intensidad, dirección y persistencia determine en gran medida la compleja variabilidad mesoescalar asociada a las islas. La importancia de estos factores se desprende de estudios recientes que sugieren que la Corriente de Canarias no se ajusta al arquetipo de corriente de contorno oriental (débil y ancho flujo hacia el ecuador), sino que más bien aparece como una corriente bien definida y con marcada estacionalidad (Pelegrí et al., 2005a; Machín et al., 2006a). Sin embargo, quedan muchas cuestiones pendientes relativas tanto a su cinemática y dinámica.

También se ha visto que la variabilidad mesoescalar generada en la región de las Islas Canarias exporta efectos no locales: los datos de altimetría muestran remolinos persistentes propagándose hacia el mar abierto desde las Islas Canarias. Este "pasillo de remolinos" se ha venido a denominar el *Canary Eddy Corridor* (CEC; Sangrà et al., 2009). Las primeras estimaciones sugieren que el flujo de la masa asociada con el CEC puede alcanzar la cuarta parte del transporte en la Corriente de Canarias, lo cual tiene importantes implicaciones en los transportes biogeoquímicos. Se especula que los remolinos se generan por el efecto de las islas, pero la altimetría no alcanza una resolución adecuada para dar respuestas definitivas. El modelo numérico desarrollado y validado en el presente trabajo ha demostrado ser adecuado para responder a estas y otras cuestiones sobre el CEC: ¿Dónde y cuándo se generan los remolinos? ¿Existe alguna dependencia estacional para su generación y las trayectorias posteriores?

Algunos estudios cuantifican los transportes entre los distintos pasajes de las Islas Canarias. El de Lanzarote, que separa el archipiélago del continente africano, es el que ha recibido una mayor atención (Hernández-Guerra et al., 2003). La Corriente Canaria de Afloramiento (CanUC), asociada al afloramiento canario-sahariano, está presente todo el año aunque se observan cambios significativos en la dirección del flujo en otoño. Se especula que esta inversión está relacionada con la relajación otoñal de los Alisios. El modelo puede dar una idea de los procesos relacionados con esta inversión otoñal, así como cuantificar los transportes en los pasajes menos estudiados.

Además de los remolinos más persistentes, hay muchos fenómenos transitorios de pequeña escala que contribuyen a la variabilidad en la región de las Islas Canarias. La modelización numérica a escala regional es actualmente capaz de resolver los procesos de submesoescala. Esto se puede aplicar también a los métodos observacionales. Los estudios más recientes han puesto de manifiesto multitud de características submesoescalares relativamente desconocidas hasta hace poco, lo cual tiene su implicación frente a procesos biogeoquímicos (Capet et al., 2008a; Thomas et al., 2008). Los frentes y remolinos más conspicuos se forman y disipan en cortas escalas temporales. Las velocidades verticales asociadas con estas estructuras superan en un orden de magnitud a las asociadas a los fenómenos de mesoescala, lo cual supone un incremento del bombeo y disponibilización de nutrientes hacia la superficie.

• reducción (incremento) de escala - *downscaling (upscaling)*

El capítulo 3 proporciona una explicación completa del concepto y el significado de *anidación*.

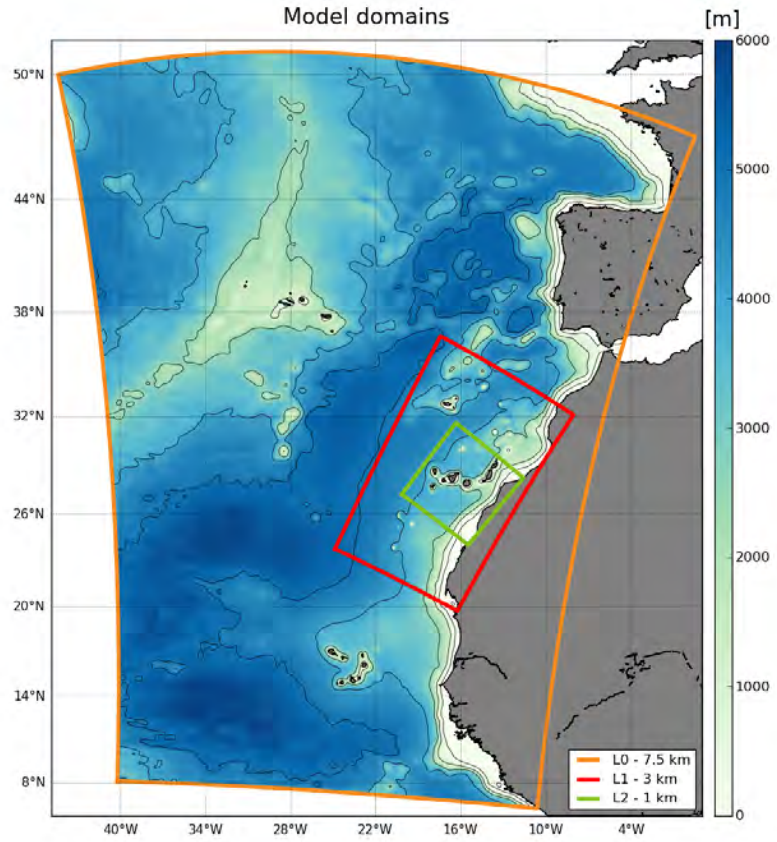

Figura 7.1.: Los dominios del modelo acoplado: L0, L1 y L2. La topografía de cada malla se muestra. Isóbatas de L0 se representan a 200, 1000, 2500, 4000 y 5000 m.

El dominio anidado más fino tiene una resolución horizontal de 1 km (Figura 7.1), lo cual lo sitúa en el límite de resolver la transición meso-submesoescala (Capet et al., 2008c). Esta solución muestra campos superficiales ricos en remolinos submesoescalares, frentes y filamentos, no vistos en las soluciones de menor resolución. El primer paso para el estudio detallado de este nueva visión es la identificación y caracterización de los fenómenos observados: ¿Cómo interpretamos las estructuras de mesoescala, como los remolinos generados en las islas, al aumentar la resolución y observar la rica estructura submesoescalar? ¿Existen "nuevas" estructuras, que simplemente no existen en el régimen de mesoescala? ¿Cuáles son las características del ciclo estacional en el régimen submesoescalar?

Esta introducción plantea una amplia gama de preguntas. El intento de darles respuesta requiere una solución numérica de alta calidad, asumida tras un estricto proceso de validación. Antes de resumir los resultados obtenidos de este modelo, se esboza la oceanografía de la Cuenca de Canarias en la siguiente sección.

7.3. Oceanografía de la Cuenca de Canarias

7.3.1. Introducción

La región de la Cuenca de Canarias localizada en el Océano Atlántico noreste ha sido bien conocida por la gente de mar durante muchos siglos. En el año 1400, los navegantes portugueses siguieron el camino de la Corriente de Canarias en sus viajes por África hacia el Oriente. En 1492, Cristóbal Colón se detuvo en La Gomera, isla occidental de las Islas Canarias, en su camino hacia el descubrimiento de las Américas. El interés de Colón en la navegación hacia el oeste, surgió de la tentación de encontrar un atajo hacia las riquezas de Asia. Pasó varios años familiarizándose con la región de las Canarias. En septiembre de 1492, usando una plomada, realizó las primeras observaciones de la Corriente Norecuatorial (Peterson et al., 1996). Colón, además de por un sinnúmero de otros exploradores europeos, fue seguido más tarde por comerciantes, muchos de los cuales surcaban una ruta triangular, tomando esclavos desde África hacia el Caribe y las Américas, y llevando de vuelta a Europa azúcar y algodón. A lo largo de estos viajes de comercio circular, los veleros utilizaron los sistemas de vientos predominantes en el Atlántico Norte, aprovechando los vientos Alisios del este de bajas latitudes para el viaje de ida, y los vientos del oeste de latitud media para el viaje de vuelta a casa. Las Islas Canarias por lo tanto se convirtieron en un enclave importante para las transacciones comerciales, así como un lugar clave para la emigración hacia las Américas. Hoy en día, la importancia económica y científica de la región de las Islas Canarias se deriva de su ecosistema. La pesca representa en la actualidad unas capturas anuales de alrededor de 2 millones de toneladas, en medio de informes de una disminución en las capturas, que es posiblemente impulsada por el clima (Arístegui et al., 2009).

7.3.2. Topografía

La cuenca de Canarias se sitúa aproximadamente entre los 40°W y la costa occidental de Europa y África y entre las latitudes 10° – 40°N. Ésta cubre un área de más de 3 millones de kilómetros y la parte más profunda es de 4500 m en las Llanuras Abisales de Madeira, que se encuentra a unos 1000 km al oeste de la costa de africana. En contraste, los archipiélagos volcánicos de Canarias y Madeira alcanzan altitudes mayores de 1800 m sobre el nivel del mar. El macizo volcánico del Teide en Tenerife (la mayor de las Islas Canarias), a 3718 m, es la montaña más alta de España.

La topología de la Cuenca de Canarias se ilustra en la figura 7.2. En el oeste, la cuenca está delimitada por la Dorsal Centro-Atlántica, que alcanza una altura aproximada de 2000 m sobre la llanura abisal. La costa africana, de unos 2000 km de longitud, está principalmente orientada en dirección noreste-suroeste. La anchura media de la plataforma a lo largo de la costa es de 50 a 60 km, con un máximo de 100 a 120 km en la latitud 25°N, y un mínimo de 20 a 30 km a 21°N (Mittelstaedt, 1991; Carr and Kearns, 2003). En el sur, entre 7° y 13°N, la plataforma se amplía a más de 300 km. El borde de la plataforma está bien definido por la isóbata de 200 metros. En la extensión norte del transecto se encuentra el Golfo de Cádiz,

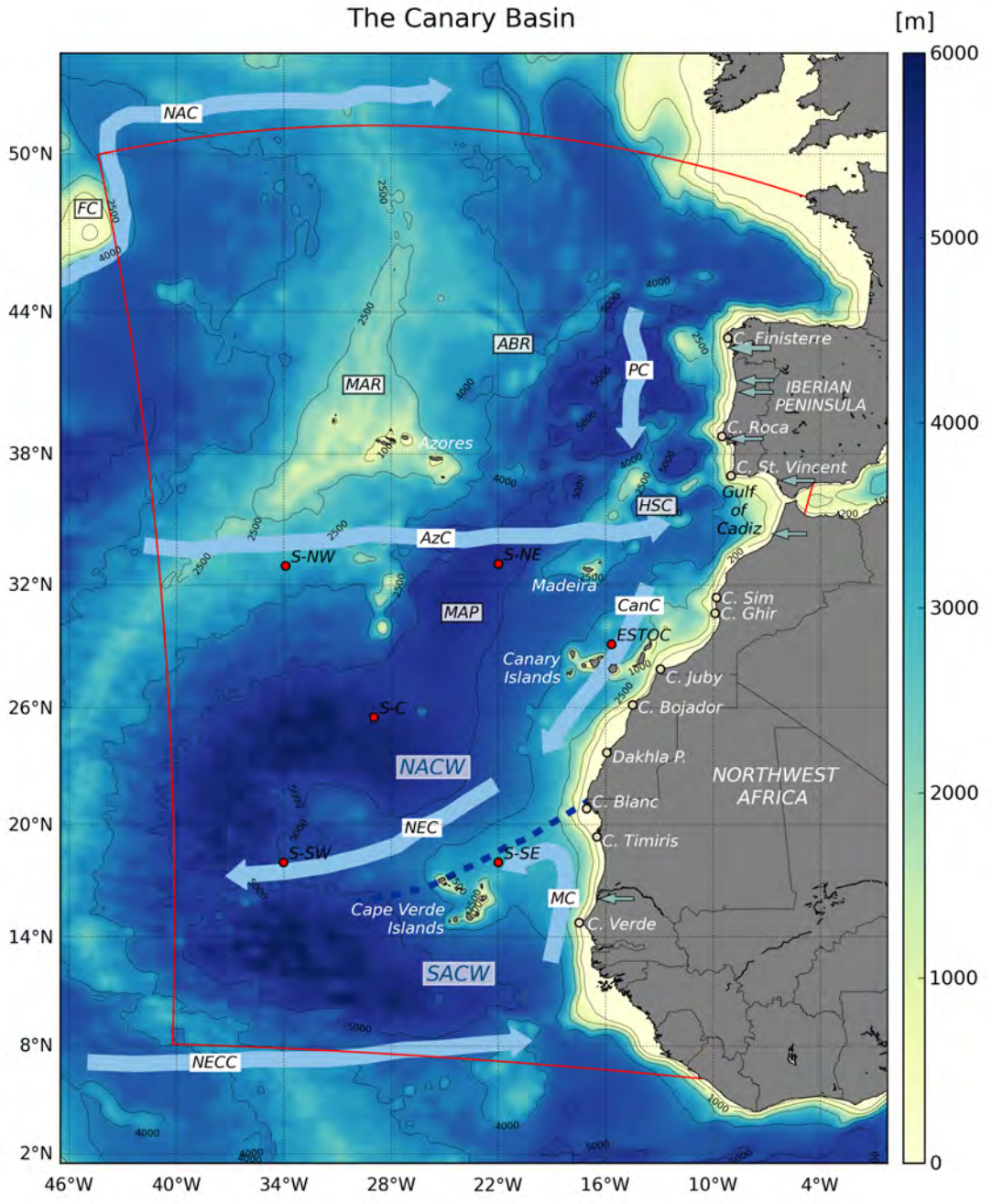

Figura 7.2.: Principales características oceanográficas de la Cuenca de Canarias en el océano Atlántico Nororiental. El Frente de Cabo Verde que separa las zonas del Agua Central del Atlántico Norte (NACW) y el Agua Central del Atlántico Sur (SACW) está marcado por la línea punteada de color azul oscuro. Los puntos rojos muestran las posiciones de los fondeos del Subduction Experiment (SubExp). Las desembocaduras de los ríos se indican por las flechas horizontales de color azul claro. Abreviaturas: AzC - Corriente de Azores, CanC - Corriente de Canarias, MC - Corriente de Mauritana, NEC - Corriente Norecuatorial, NECC - Contra-Corriente Norecuatorial; ABR - Azores-Vizcaya Rise, FC - Flemish Cap, HSC - Horseshoe Seamount Chain, MAP - Llanuras Abisales de Madeira, MAR - Dorsal Centro-Atlántica. Se marcan en negro las isóbatas de 200, 1000, 2500, 4000, 5000 m. El límite del dominio del modelo L0 (Capítulo 4) está marcada en rojo. Los datos topográficos son proporcionados por GEBCO (Hunter and Macnab, 2003).

donde el Estrecho de Gibraltar facilita el intercambio de las propiedades del agua entre el Atlántico Norte y el Mar Mediterráneo. A lo largo de la costa africana se localizan diversos cabos importantes, entre los que se encuentran Cabo Ghir (30.6°N), Juby (28.0°N), Bojador (26.1°N), Blanco (20.8°N) y Verde (14.8°N). Por otro lado, a lo largo de la costa occidental de la Península Ibérica, los cabos principales son el de San Vicente (37.0°N), Roca (38.8°N) y Finisterre (42.9°N).

La topografía del fondo mostrada en la figura 7.2, incluye las características morfológicas típicas del margen continental: la plataforma, el talud y la pendiente continental. A lo largo del margen continental se desarrollan varios cañones sumergidos, principalmente en la zona occidental de la Península Ibérica (Peliz and Fiúza, 1999). Los cañones están asociados con la generación de remolinos, y son también lugares donde se depositan los sedimentos costeros (Fiúza et al., 1998; Peliz et al., 2002). El Cañón del Portimão, en el Golfo de Cádiz, es una importante interrupción topográfica en el avance del Agua Mediterránea, el cual está implicado en la formación de *Meddies* (Serra and Ambar, 2002). En el Cañón de Agadir, al suroeste de Cabo Ghir, se ha observado un remolino anticiclónico subsuperficial durante dos campañas sucesivas (Pelegrí et al., 2005b). Se sugiere que los remolinos pueden estar asociados con la interacción entre la contra-corriente que fluye hacia el polo a lo largo del talud y el cañón.

Los archipiélagos insulares de la Cuenca de Canarias han llegado a ser conocidos en conjunto como la Macaronesia. El archipiélago canario está situado sobre los 28.5°N, 15°W. Las siete islas que lo componen se encuentran sobre una meseta con orientación zonal que se extiende mar adentro desde el límite continental. El archipiélago de Madeira se encuentra a unos 500 kilómetros al norte las Islas Canarias a 33°N y 16.5°W. Las islas de Cabo Verde se encuentran a 700 km de la costa de Cabo Verde. El archipiélago de las Azores se encuentra al este del eje principal de la Dorsal Centro-Atlántica a 38°N, 28°W.

Las montañas submarinas de origen volcánico son estructuras comunes fuera de la plataforma continental entre la costa de Cabo Blanco y el suroeste de la Península Ibérica (Ye et al., 1999). Al oeste del Golfo de Cádiz hay un grupo de montes submarinos llamados Horseshoe Seamount Chain (Epp and Smoot, 1989). Estos montes submarinos, en particular el Gorringe Bank, se cree que limitan las trayectorias de los *Meddies* generados cerca del Cabo de San Vicente (Richardson et al., 2000; Serra and Ambar, 2002; Wang and Dewar, 2003).

La Dorsal Centro-Atlántica (MAR) es una importante característica topográfica que presenta una importante barrera frente a los intercambios de aguas en el Atlántico. En un análisis de derivadores subsuperficiales, Bower et al. (2002) sugieren que para cruzar el MAR las corrientes (es decir, la Corriente del Atlántico Norte) fluyen preferentemente sobre los canales más profundos, limitada por la conservación de vorticidad potencial (f/H donde f es el parámetro de *Coriolis* y H es la profundidad de la columna de agua). Estas observaciones están apoyadas a través de mapas de corrientes geostróficas actuales sobre el MAR, calculado a partir de la altimetría por (Bower and von Appen, 2008), y las medidas *in situ* por (Søiland et al., 2008).

En el extremo oeste del dominio, fuera de la Cuenca de Canarias, el Flemish Cap 47°N, 45°W, es una característica notable. Esta ancha meseta submarina tiene poco más de 100 m de profundidad, y presenta una fuerte influencia topográfica sobre la corriente del Atlántico Norte que lo rodea (Heywood et al., 1994; Rossby, 1996).

7.3.3. Forzamiento superficial

La Cuenca Canaria se encuentra bajo la influencia del sistema de alta presión atmosférica conocido como el Anticiclón de las Azores (AzH). En las proximidades de la costa del noroeste de África, sobre la que predominan las bajas presiones, los gradientes de presión son bruscos, resultando en intensos vientos del noreste paralelo a la costa, conocidos como los vientos Alisios. En las latitudes ecuatoriales de baja presión, la zona de convergencia entre los vientos Alisios del hemisferio norte y del hemisferio sur es conocida como la Zona de Convergencia Intertropical (ITCZ; Molinari et al., 1986; Waliser and Gautier, 1993). La ITCZ se asocia con aire ascendente y altas precipitaciones. Los cambios latitudinales de la AzH y de la ITCZ dan lugar a variaciones estacionales. Durante el verano boreal, tanto el cinturón de los vientos Alisios como la ITCZ se desplazan hacia el norte alejándose de sus posiciones ocupadas durante el invierno. El ciclo estacional de las corrientes de superficie refleja la respuesta oceánica a los campos de viento de variación estacional, que están relacionados con las migraciones de estos fenómenos atmosféricos.

7.3.3.1. Esfuerzo del viento

El cinturón de Alisios sopla del nordeste a lo largo de la península Ibérica y África noroccidental, lo cual origina un extenso sistema de afloramiento costero en ambas regiones (Wooster et al., 1976; Mittelstaedt, 1991; Nykjær and Van Camp, 1994). La figura 7.3 muestra los campos estacionales del rotacional del esfuerzo del viento sobre el Atlántico nororiental subtropical. Ésta muestra gran variabilidad en la estructura del viento para un amplio rango de escalas espaciales.

Los vectores muestran magnitud y dirección del viento a 10 metros de la superficie. Los datos provienen de SCOW, una climatología de velocidad y esfuerzo del viento generada por Risien and Chelton (2008). Ésta está basada en 8 años de datos del dispersómetro SeaWinds, abordo del satélite QuikSCAT (Chelton et al., 2004). También se muestran las isobaras de 1016 y 1020 mbar provenientes de COADS (Comprehensive Ocean-Atmosphere Dataset, Release 2.1; Worley et al., 2005), para ilustrar la posición del Anticiclón de las Azores (AzH). Mientras que los promedios sobre intervalos temporales superiores a un mes muestran un declive en la magnitud de los vectores de viento de sureste a noroeste, los promedios escalares producen mucha menos variabilidad lo cual indica una variabilidad direccional mucho mayor en el noroeste (Weller et al., 2004).

En invierno y otoño, con el AzH localizado en su posición más austral (33°N), los Alisios, que soplan en dirección nordeste, se extienden mucho más hacia el sur. Este desplazamiento permite que circulen depresiones ciclónicas hacia el este por el borde norte. En la región

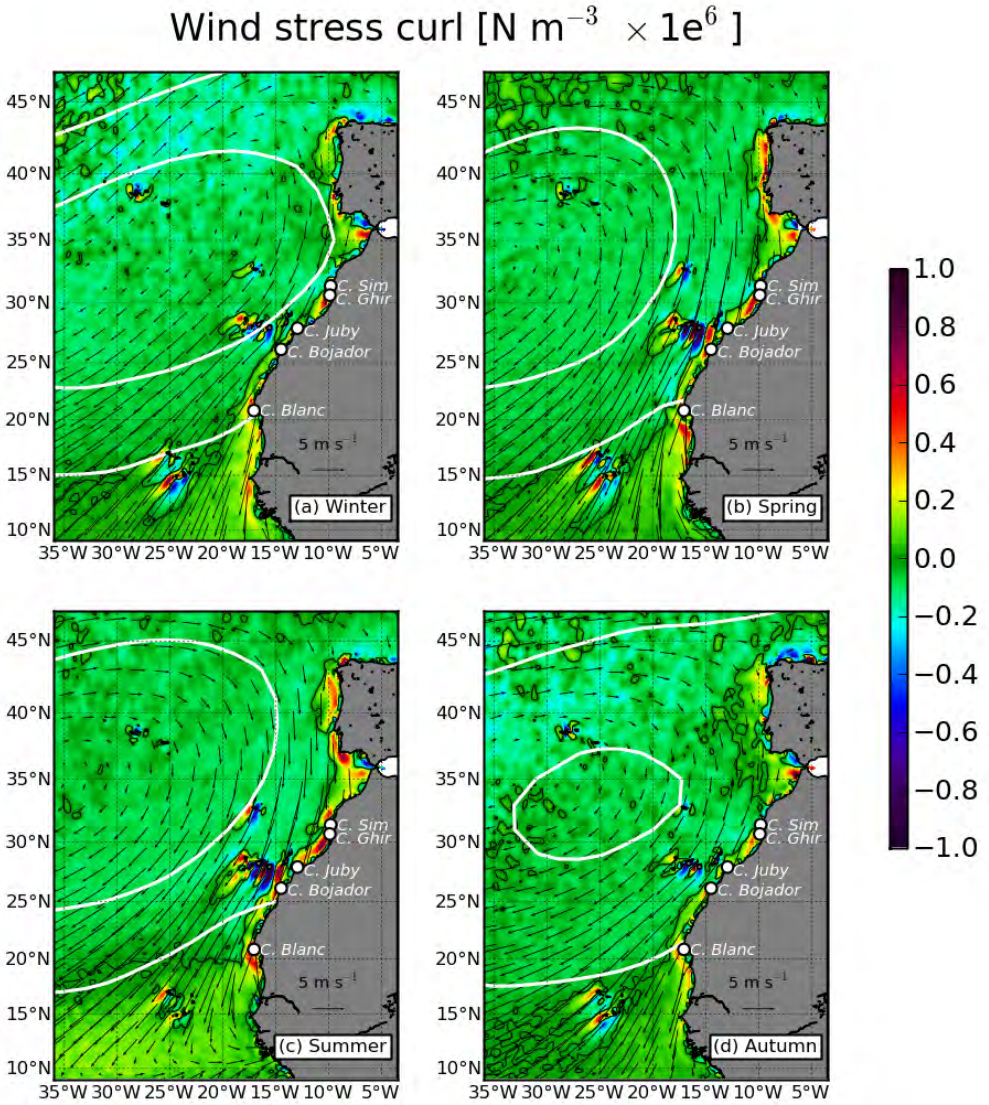

Figura 7.3.: Promedios estacionales del rotacional de la tensión del viento normalizado obtenido de la climatología de la tensión del viento SCOW derivada del QuikSCAT (Risien and Chelton, 2008) en el noreste del Atlántico subtropical. El contorno de rotacional nulo se muestra en negro. Los contornos de los isobaras 1016 y 1020 mbar, procedente de la climatología COADS (Worley et al., 2005) de los flujos océano-atmósfera, se muestran en blanco. Los vectores en negro muestran la velocidad y dirección del viento a 10 m.

noroccidental el rotacional del esfuerzo del viento es moderadamente anticiclónico y, en consecuencia, ésta es una región de subducción de aguas frías superficiales por convergencia de *Ekman* en la superficie. Weller et al. (2004) observó valores de 50 m año^{-1} cerca del punto de fondeo S-C (Figura 7.3).

A lo largo de las costas de África noroccidental y la Península Ibérica el rotacional del esfuerzo del viento es fuertemente ciclónico, sobre todo a sotavento de los principales cabos. Un ejemplo lo observamos en Cabo Ghir, donde los valores del rotacional son positivos durante todo el año, si bien acentuando su magnitud hacia el verano boreal. En la zona del Cabo Sim, un poco más al norte, el rotacional es ciclónico sólo en verano, y no se observan estructuras relevantes durante el resto del año. Ya en la Península Ibérica la estación de afloramiento comienza en primavera prolongándose durante el verano, de forma consistente con la migración del AzH hacia el norte. El rotacional ciclónico extiende el afloramiento costero hacia regiones más oceánicas (más de 100 km de la costa). En el sur, este afloramiento oceánico se extiende más allá del archipiélago de Cabo Verde. Weller et al. (2004) estiman velocidades de afloramiento en verano de 60 m año^{-1} en 15°N, 27°W.

Es importante destacar la capacidad del producto QuikSCAT/SCOW para resolver las estelas atmosféricas en los archipiélagos (véase por ejemplo en Madeira, las islas Canarias y Cabo Verde) las cuales se encuentran bajo la influencia de los Alisios. La canalización de los vientos al pasar entre las islas origina la formación de chorros que se extienden varios kilómetros a sotavento. Comparando las estelas de Cabo Verde y Canarias se puede notar que el desarrollo de las estelas en el primer archipiélago antecede al del segundo aproximadamente en una estación, lo que está de acuerdo con la migración del AzH. El rotacional asociado al chorro de viento es un potencial generador de remolinos oceánicos (Barton, 2001; Chavanne et al., 2002; Jiménez et al., 2008).

7.3.3.2. Flujos de calor

Los ciclos anuales de la insolación y de la fuerza y la posición del AzH son responsables de gran parte de la variabilidad espacial y temporal en las aguas de la termoclina en la Cuenca de Canarias. La variabilidad a escala anual de la superficie de forzamiento es alta, y, a gran escala, los gradientes latitudinales son considerables. Así, los gradientes latitudinales de temperatura son una fuente importante de la energía potencial disponible en la zona.

La figura 7.4 muestra los campos estacionales de la media del flujo neto de calor (NHF) de COADS. Valores positivos (negativos) muestran la ganancia (pérdida) de calor del océano. La primavera y el otoño difieren de las otras estaciones en la zona mostrada en que hay una ganancia o pérdida de calor casi total, respectivamente. Las regiones costeras con latitudes menores de 38°N presentan una ganancia de calor constante, menos en otoño. Weller et al. (2004) analizaron tres años de datos meteorológicos de superficie obtenidos en cinco fondeos del Subduction Experiment (SubExp), cuya ubicación se muestra en la figura 7.4. Los fondeos se colocaron al norte y al sur de la línea media anual NHF=0, de modo que se muestrease tanto el calentamiento neto hacia el sur, como el enfriamiento hacia el norte. Sin embargo, en

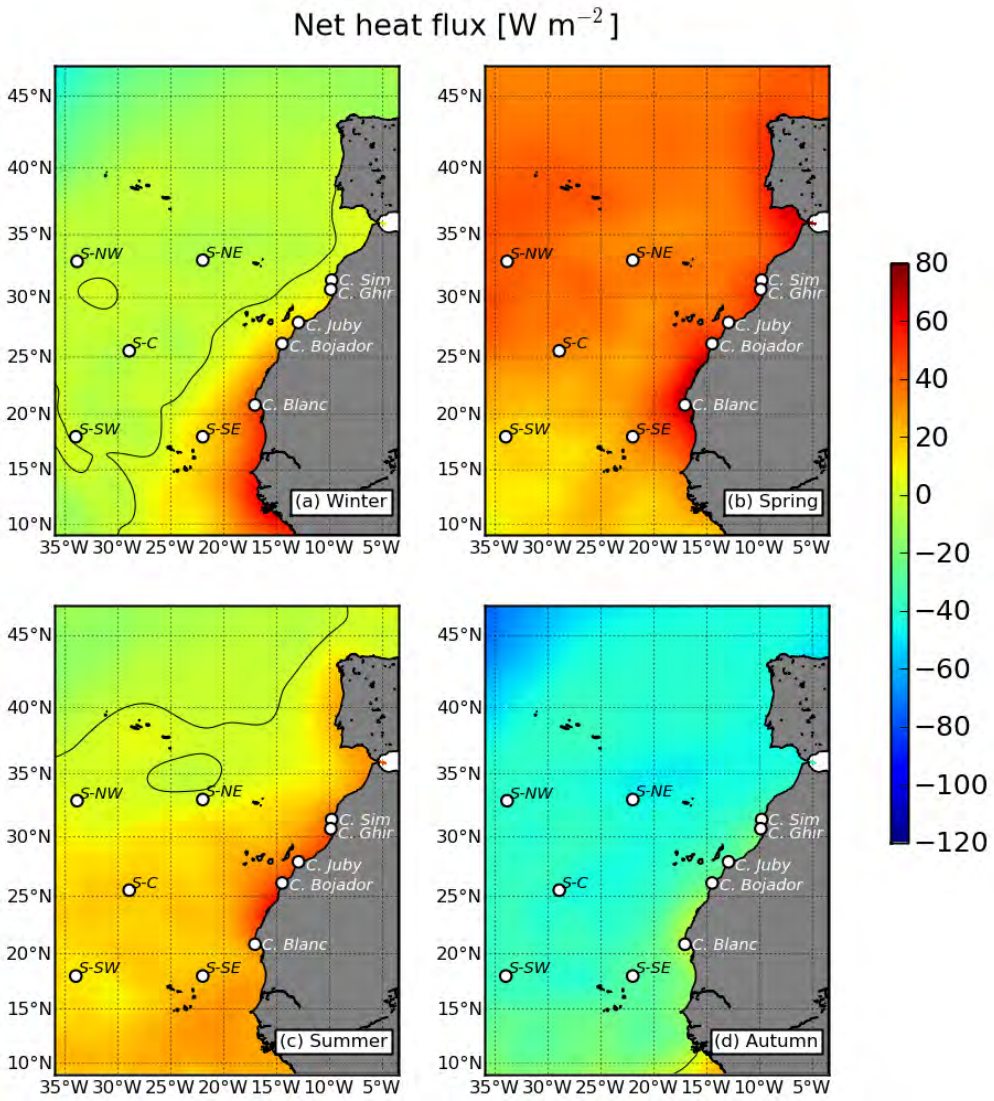

Figura 7.4.: Campos estacionales del flujo de calor neto (NHF) en superficie, procedente de la climatología COADS de los flujos océano-atmósfera según Worley et al. (2005). Valores positivos (negativos) representan ganancia (pérdida) de calor por parte del océano. El valor de NHF = 0 se muestra en negro. La localización de los cinco fondeos del Subduction Experiment están marcados en blanco.

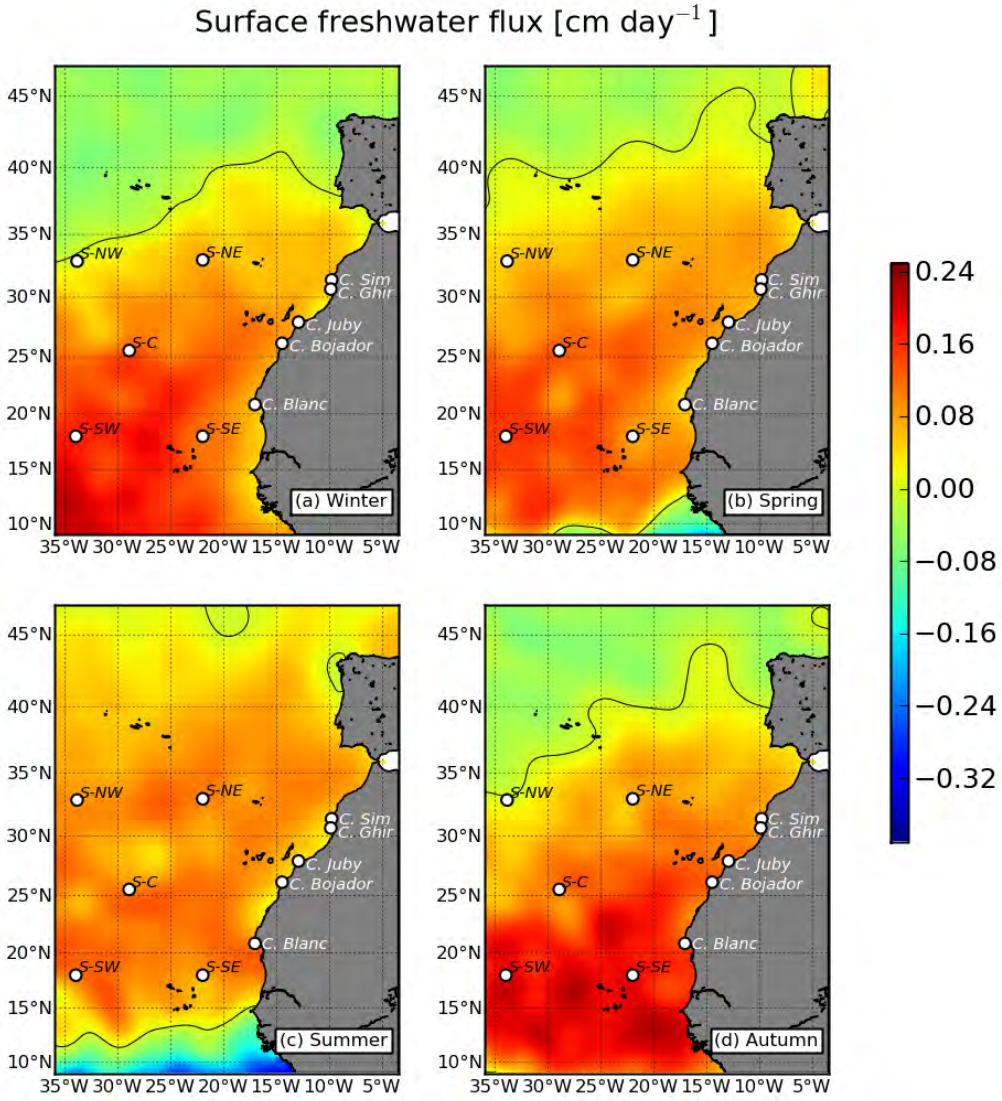

Figura 7.5.: Campos estacionales de evaporación menos precipitación (E-P) de la climatología COADS de los flujos océano-atmósfera según Worley et al. (2005). El valor de E-P = 0 se muestra en negro. La localización de los cinco fondeos del Subduction Experiment están marcados en blanco.

estas localizaciones, a partir de los datos COADS, los promedios anuales del NHF son todos cercanos a cero. Por otro lado, Weller et al. (2004) reportaron un promedio anual positivo (en el rango de ∼20 a 40 W m^{-2}) a partir de las observaciones de los fondeos[2], de acuerdo con el estudio de Josey (2001). En los cinco sitios se registró una ganancia neta de calor en verano y una pérdida neta en invierno. En la región de las Islas Canarias, el NHF es positivo de marzo a agosto, y negativo de septiembre a febrero (Pelegrí et al., 2005a).

7.3.3.3. Flujos de agua dulce

La figura 7.5 muestra las medias estacionales de la evaporación menos precipitación (E-P) de COADS. Alrededor de los 15°N y 35°N, la evaporación supera la precipitación en todas las estaciones. En verano, las precipitaciones altas están asociadas con la ITCZ, ya que ésta ocupa su posición más al norte dentro de una banda de E-P negativo a lo largo de 10°N.

Schmitt et al. (1989) presentó una recopilación de datos de evaporación y precipitación para el Atlántico Norte. En este trabajo se demostraba que, en la Cuenca de Canarias, la evaporación supera la precipitación anual alrededor de 50 cm por año en el norte, y más de 100 cm por año en el sur. En contraste con el resto del Atlántico Norte, estas diferencias se mantienen constantes. En la Cuenca Canaria, Schmitt et al. (1989) mostraron que los flujos de densidad térmica son superiores a los flujos de densidad salina entre 2 y 20, con valores crecientes hacia la costa. La evaporación relativamente alta se asocia con la NHF elevada y constante, y las temperaturas altas de la superficie del mar (SST) (Pelegrí et al., 2005a).

En general, en la región de la Cuenca de Canarias la precipitación supone sólo una pequeña contribución a la flotabilidad. En Canarias, la lluvia es mínima en mayo (0.04 cm $día^{-1}$ en Gran Canaria). En diciembre y enero, la precipitación es máxima (0.06 cm $día^{-1}$ en Gran Canaria) (Pelegrí et al., 2005a). En los sitios de los fondeos SubExp, Weller et al. (2004) se observaron bajas tasas de lluvia (hasta 1 cm $día^{-1}$) desde la primavera hasta el verano. En otoño, el aumento de la precipitación se observó en los fondeos del sur, y éste fue disminuyendo con la llegada del invierno. En el fondeo del noroeste (S-NW), la presencia de determinados fenómenos meteorológicos sinópticos en el otoño y el invierno han contribuido a aumentar las tasas de lluvia (hasta 3.8 cm $día^{-1}$).

Las zonas costeras con mayor aporte fluvial en la zona se muestran en la figura 7.2. Esa contribución fluvial es importante al noroeste de las costas de Portugal y España, con valores máximos en invierno (Peliz et al., 2005). Sin embargo, no hay descargas de los ríos principales de gran parte de la costa noroeste de África. En la costa marroquí, a unos 34°N, hay un pequeño número de ríos, cuyas plumas son a veces visibles en las imágenes de satélite después de fuertes inundaciones (Warrick and Fong, 2004). Estas plumas son típicamente transportadas hacia el polo. El efecto de las fuertes descargas de los ríos a lo largo de la costa de África ecuatorial afecta a las masas de agua al sur de 18°N. Este agua dulce tiene una anomalía cálida, y puede ser vista propagándose hacia el norte en las imágenes SST de

[2]El forzamiento del modelo en esta tesis utiliza el flujo neto de calor de la climatología COADS. Por lo tanto, la ganancia de calor en la Cuenca de Canarias modelado (al menos en la región de los fondeos SubExp) se puede suponer que tienen un sesgo negativo.

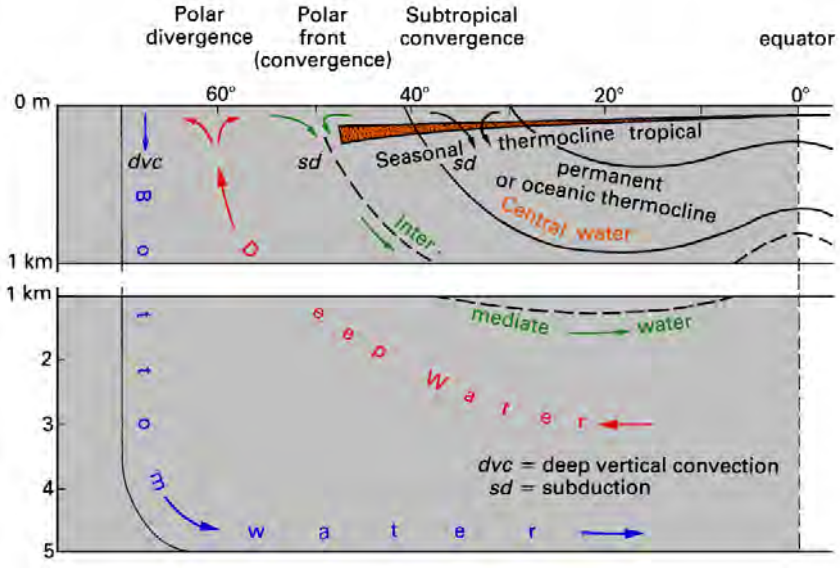

Figura 7.6.: Esquema de la distribución de las principales masas de agua. Se muestra la posición de la zona de convergencia subtropical, así como la profundidad de la termoclina permanente y estacional. Tener en cuenta el cambio de escala por debajo de los 1000 m. Tomado de Tomczak and Godfrey (2003).

invierno (Van Camp et al., 1991).

7.3.4. Masas de agua

En la Cuenca de Canarias aparecen los tres tipos característicos de masas de agua de latitudes medias: Aguas Centrales, Intermedias y Profundas. Su distribución ha sido ampliamente descrita en Barton, 1998 y Arístegui et al., 2006. La figura 7.6 resume las distribuciones verticales y horizontales de las masas de agua de un océano hipotético. El agua superficial en la Cuenca de Canarias tiende a ser salada, debido a la elevada insolación y la escasez de precipitaciones. El Agua Central ocupa la capa subsuperficial, hasta la base de la termoclina principal (que varía con la latitud), típicamente localizada entre 200 y 1000 m. Este agua se forma en gran medida como resultado de la acción del viento. Las Aguas Intermedias se encuentran bajo de los Aguas Centrales a una profundidad máxima de 1500 m. Debajo de las Aguas Intermedias se sitúan las Aguas Profundas, que se extienden hasta los 4000 m, y son los más voluminosas de todas las masas de agua en los océanos del mundo. En contacto con los fondos oceánicos, debajo de las Aguas Profundas se encuentran las Aguas de Fondo.

7.3.4.1. Aguas Centrales

En el Atlántico Norte subtropical, los vientos Alisios y los vientos del oeste fuerzan la circulación oceánica que define el Giro Subtropical del Atlántico Norte a nivel de cuenca. En el giro, especialmente en los meses de invierno, las inestabilidades conducen a una intensa mezcla vertical que homogeniza las capas superiores, dando lugar al Agua Central del

Atlántico Norte (NACW). Esta masa de agua es dominante por encima de 600 m (Harvey, 1982), y se caracteriza generalmente por isotermas (10° - 12°C) e isohalinas (35.405 - 35.650) cuasi-horizontales (Arhan et al., 1994). Existe cierta variabilidad meridional en la composición del NACW, de tal manera que puede definirse en función de su lugar de origen, ya sea subtropical o subpolar.

La variedad subtropical del NACW es el Agua Central del Este del Atlántico Norte ($ENACW_T$), cuya temperatura oscila entre 13° y 15°C. El $ENACW_T$ ha sido identificada al sur de la Península Ibérica y se cree que se origina en el Frente de las Azores (Fiúza and Halpern, 1982; Fiúza, 1984; Ríos, 1992), extendiéndose con el flujo general hacia la Península Ibérica. En el límite norte del $ENACW_T$ (42.9°N, Cabo de Finisterre), una fuerte masa de agua subsuperficial (∼200 m) separa el $ENACW_T$ de las aguas más frías y dulces de origen subpolar del $ENACW_P$ (11° - 13°C) hacia el norte (Fraga et al., 1982). Este frente se denomina a veces como Frente de Galicia (Fiúza, 1984; Peliz and Fiúza, 1999). El $ENACW_T$ y el $ENACW_P$ son transportadas hacia el norte y hacia el sur en el complejo sistema de corrientes y contracorrientes paralelas a la costa oeste de la Península Ibérica (Ríos, 1992; Álvarez-Salgado et al., 1993, 2003).

Al sur de Cabo Blanco (20.8°N), se identifica otro tipo de masa de agua central procedente del sur, el Agua Central del Atlántico Sur (SACW). SACW es más fría y menos salina (10° - 16°C, 35.21 - 35.77) que el NACW (Tomczak and Hughes, 1980), y también es más rica en oxígeno y nutrientes. En esta región existe una zona frontal entre estas dos masas de aguas centrales: NACW y SACW, que se conoce como Zona Frontal de Cabo Verde (CVFZ) (Zenk et al., 1991; Arhan et al., 1994; Pastor et al., 2008), cuyo frente se extiende zonalmente a través del Atlántico en torno a 15°N (Lozier et al., 1995; Stramma and Schott, 1999). Entre 30°W y la región de la plataforma africana de Cabo Blanco, el frente adquiere una orientación suroeste-noreste (Figura 7.2). A pesar de sus diferentes rangos de temperatura y salinidad, SACW y NACW tienen el mismo rango de densidades, de forma que la CVFZ es un frente termohalino compensado en densidad, dando lugar a una gran cantidad de inestabilidades en forma de intrusiones, filamentos y lentes (Tomczak and Godfrey, 1994; Pastor et al., 2008).

7.3.4.2. Aguas Intermedias

Las Aguas Intermedias generalmente se forman en las zonas de convergencia de latitudes altas (Figura 7.6), y por lo tanto tienden a ser más frías y dulces. Sin embargo, la Cuenca de Canarias tiene una masa de agua intermedia anómala que es el agua del Mediterráneo (MW). El MW se forma en el Mar Mediterráneo, donde la evaporación es alta y las entradas de agua dulce son bajas. Este agua cálida y salada del MW abandona el mar Mediterráneo en el Estrecho de Gibraltar. A medida que desciende la pendiente en el Golfo de Cádiz, la pluma turbulenta del MW se va situando debajo de NACW. Alrededor de los 1000 metros, el MW alcanza un nivel de densidad neutra, con la que se va propagando por el noreste Atlántico (NEA) (Richardson et al., 2000). La figura 7.7 muestra la extensión de la anomalía de salinidad resultante asociada con el MW, así como una recopilación de la localización

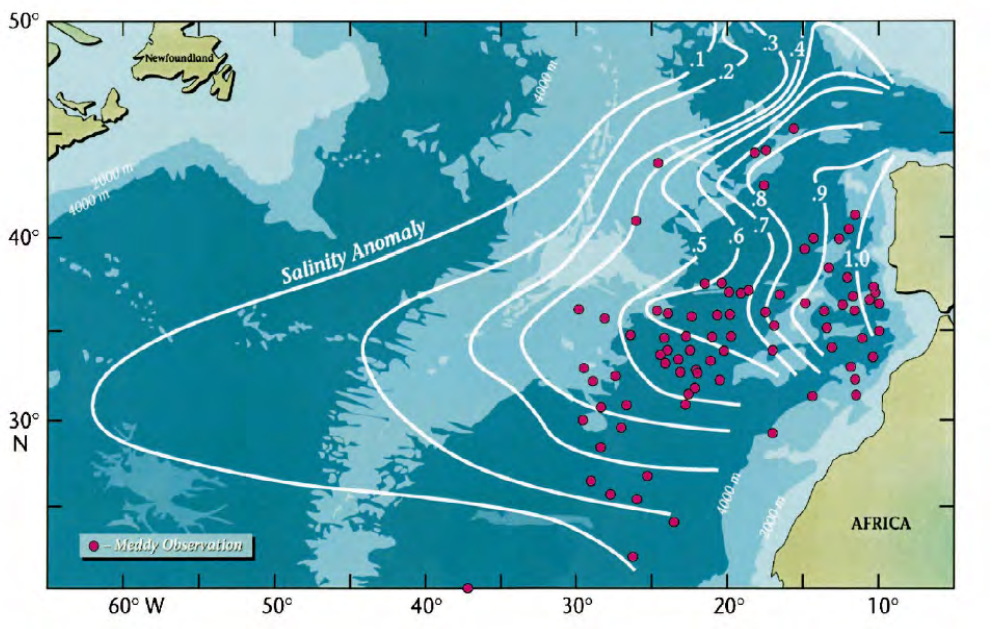

Figura 7.7.: Anomalía de salinidad del Agua Mediterránea. Se muestra un resumen de las observaciones históricas de los *Meddies*, reproducida de Richardson et al. (2000). Se muestran los contornos de la anomalía de la salinidad relativa a 35.01 cerca de una profundidad de 1100 m.

de *Meddies* (remolinos de agua Mediterráneo) identificados en el NEA. Los *Meddies* son remolinos anticiclónicos en forma de lentes que se generan a lo largo del Golfo de Cádiz y en el talud occidental de la Península Ibérica , entre 800 - 1400 m (Bower et al., 1997), profundidades en las que se encuentra MW. Con diámetros de 40 - 150 km y espesores de alrededor de 600 m, los *Meddies* se extienden hacia el NEA, donde contribuyen de manera importante a la difusión al encontrarse con agua de diferentes características a las suyas durante su propagación (Wang and Dewar, 2003).

El Agua Intermedia Antártica (AAIW) es la más convencional de las masas de agua intermedias de la Cuenca de Canarias. Tras su formación en el Zona Frontal Polar Antártica, AAIW entra en el Atlántico Sur, y continúa hacia el Atlántico Norte, a profundidades entre 600 - 1100 m (Suga and Talley, 1995). La figura 7.8 muestra una sección vertical de la salinidad en el Atlántico Norte occidental, en la cual el avance de la lengua del AAIW es visible a unos 800 m, y encontrándose con el MW sobre los 20°N. Parece que hay dos vías adoptadas por el AAIW en la cuenca de Canarias, una es desde el oeste a través de la Corriente del Golfo (véase la sección 7.3.5), mientras que la otra es una penetración hacia el norte a lo largo de la frontera oriental, es decir, el noroeste de África (Machín and Pelegrí, 2009). Estos autores demostraron que la extensión del AAIW hacia el polo es máxima en otoño, cuando se puede observar al norte de Cabo Ghir. El AAIW es la masa de agua intermedia más difundida en los océanos.

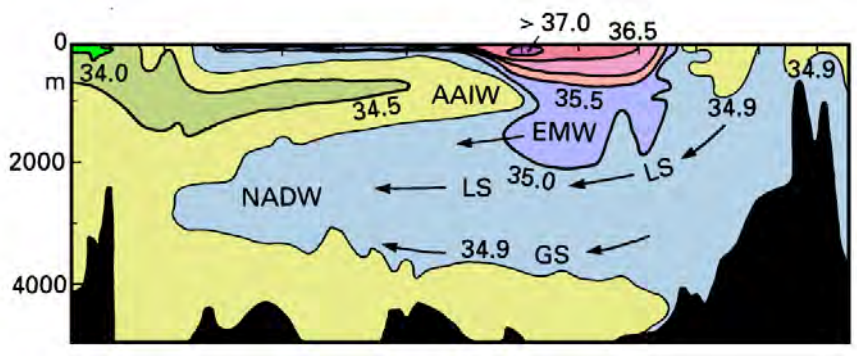

Figura 7.8.: La salinidad a lo largo de una sección meridional (55°S - 65°N) en el Atlántico norte occidental. EMW es Agua Mediterránea Euro-africana. Reproducido de Tomczak and Godfrey (2003).

7.3.4.3. Aguas Profundas

El Agua Profunda del Atlántico Norte (NADW) se encuentra por debajo del AAIW y del MW en la Cuenca de Canarias. El NADW está formada por procesos de convección en los giros subpolares del Mar de Noruega y Groenlandia. Después, se adentra en el Atlántico Norte a través de los profundos canales que separan las cordilleras submarinas de Escocia, Islandia y Groenlandia. El NADW se encuentra en todo el océano Atlántico en el rango de profundidades entre 2000 - 4500 m (McCartney, 1992; van Aken, 2000).

7.3.5. Corrientes principales

La Cuenca de Canarias es una región compleja, rica en actividad dinámica en múltiples escalas (Arhan et al., 1994; Le Traon and De Mey, 1994; Reverdin et al., 2003; Weller et al., 2004; Machín et al., 2006a). La circulación media está dominada por las componentes del giro anticiclónico subtropical oriental (ESG): la Corriente de Azores (AzC), la recirculación de ésta hacia el sur formando la corriente de Canarias (CanC), y un flujo de retorno hacia el oeste formando la corriente Ecuatorial norte (NEC) (Figura 7.2) (Klein and Seidler, 1989; Mittelstaedt, 1991). El transporte total de la ESG se ha estimado en 12 Sv (Stramma, 1984; Siedler and Onken, 1996). La ESG se caracteriza por que la termoclina se localice a menor profundidad en dirección este, y por un flujo de poca intensidad que se extiende hacia el ecuador. La transición zonal entre el flujo hacia el este y hacia el oeste en el giro subtropical oceánico viene marcada por el frente termohalino que constituye el sistema Frente de Azores/Corriente de Azores (AzFC; Juliano and Alves, 2007). En las latitudes tropicales por debajo de los 10°N, el rasgo característico es la Contra-Corriente Norecuatorial (NECC), que fluye hacia el este, y cuya intensidad es altamente estacional (Stramma et al., 2003).

La figura 7.9 muestra un mapa de las corrientes superficiales del Atlántico Norte y de la energía cinética turbulenta (EKE), determinado por Reverdin et al. (2003) a partir de un análisis de un conjunto de varios años de datos de boya de deriva. Las situaciones de inestabilidad en las corrientes más importantes son una fuente importante de EKE. Es ge-

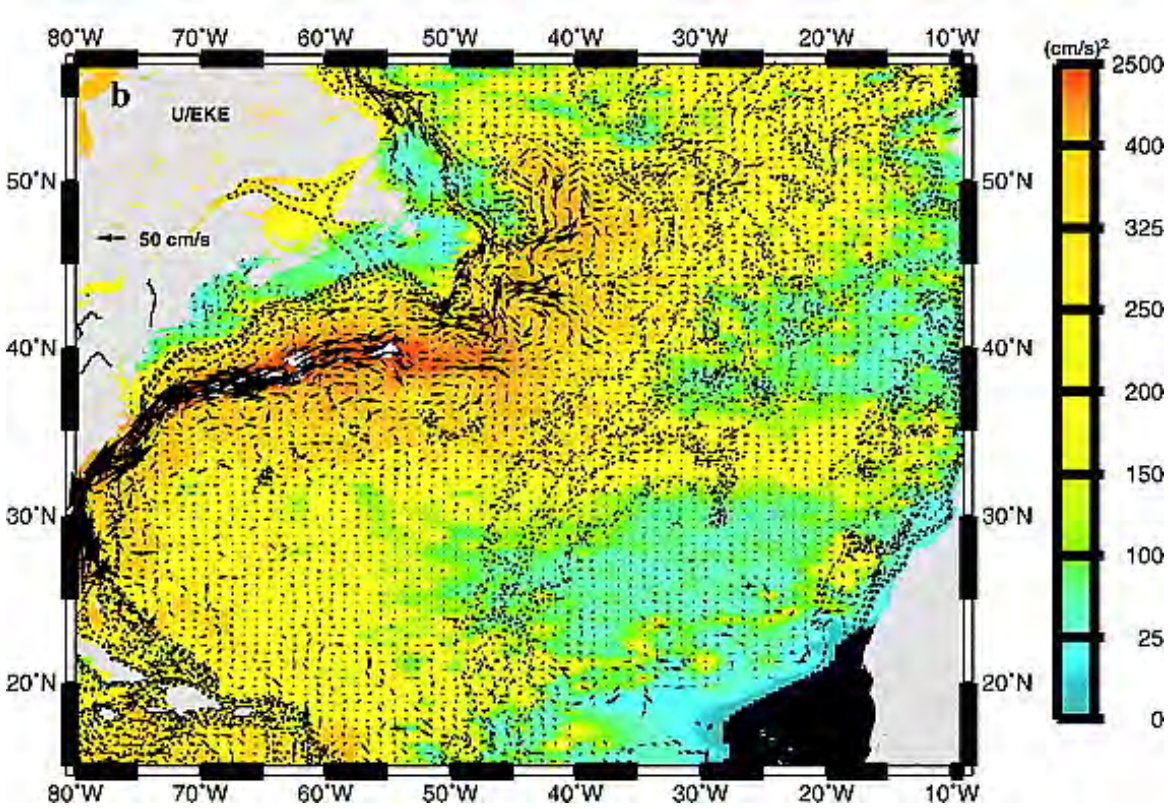

Figura 7.9.: Mapa mostrando la media de las corrientes superficiales y el EKE en el Atlántico Norte, a partir del estudio con boyas de deriva de Reverdin et al. (2003). Los contornos muestran las isóbatas a 200, 1000, 2000, 3000 y 4000 m de profundidad.

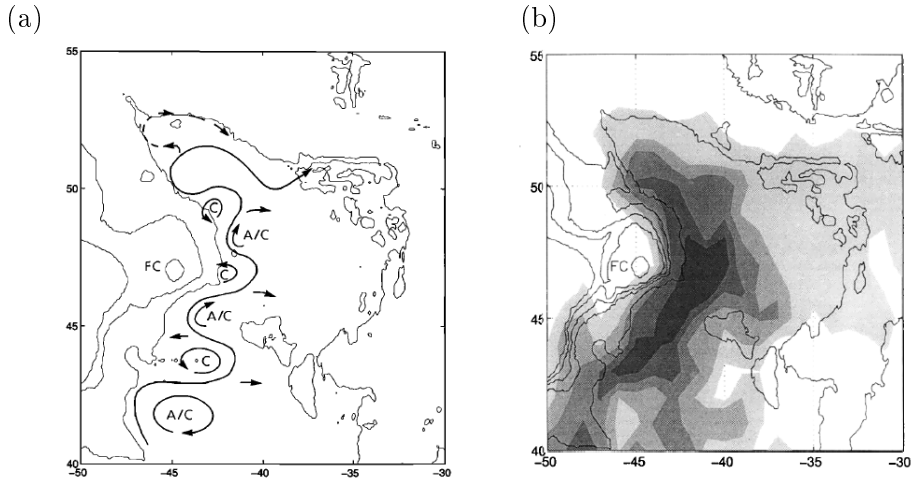

Figura 7.10.: Diagrama esquemático que ilustra (a) la trayectoria de la Corriente del Atlántico Norte, sus meandros y la recirculación asociada; (b) la energía cinética de los remolinos calculada a partir de boyas lastradas entre 50 y 100 m de profundidad. El sombreado representa incrementos de 250 $cm^2\ s^{-2}$. La alta EKE corresponde a la Corriente del Atlántico Norte, cuando rodea el poco profundo Flemish Cap (FC). La batimetría corresponde a los contornos de 200, 2000 y 4000 m. Reproducido de Rossby (1996).

neralmente aceptado que, lejos de la influencia de la topografía, las regiones de EKE altas coinciden con la localización de corrientes de gran energía, de modo que la EKE puede ser considerada como un indicador de las trayectorias seguidas por las corrientes principales (Heywood et al., 1994; Reverdin et al., 2003). La recirculación de la ESG destaca en el mapa EKE: la corriente zonal y con meandros AzFC del 34°N, el límite oriental CanC, con EKE elevada aguas abajo de las Islas Canarias, y el NEC extendiéndose hacia el oeste, entre el 20° - 25°N. El rasgo más llamativo de esta cifra es la Corriente del Golfo (GS) en el oeste, de gran energía. Alrededor del 40°N, 55°W, se sabe que la GS se bifurca en dos sistemas distintos, el de la Corriente del Atlántico Norte hacia el norte, y la AzC hacia el sureste. A pesar de que la bifurcación no está del todo clara en los datos de boyas de deriva de la figura 7.9, la continuidad hacia el norte y el sureste, es evidente. Se cree que ambas ramas influyen en la estructura y la dinámica de la ESG (Schmitz and McCartney, 1993; Rossby, 1996).

7.3.5.1. La Corriente del Atlántico Norte

La Corriente del Atlántico Norte (NAC) es una corriente de frontera oeste bien definida, con una trayectoria estable pero serpenteante (Rossby, 1996), que transporta a unos 42 Sv a una latitud de 42°N (Kearns, 1996; Carr et al., 1997). La NAC fluye hacia el norte desde los 40°N a lo largo del lado este de las zonas poco profundas de Grand Banks y Flemish Cap, girando bruscamente hacia el este a 51°N y continuando su recorrido a través del Atlántico. Esta corriente es bien conocida por su papel crucial en el transporte de calor hacia Europa occidental. La NAC es un frente baroclínico, que separa las frías aguas costeras de las cálidas aguas oceánicas (subtropicales) . Durante su paso hacia el norte, la NAC presenta una serie de grandes meandros cuyas características indican que ha sido generados por prominentes

estructuras topográficas (por ejemplo, Grand Banks y Flemish Cap) (Kearns and Paldor, 2000). Su trayectoria se muestra esquemáticamente en la figura 7.10a. Como resultado de la inestabilidad de los meandros, o de su crecimiento o decadencia, hay un intercambio de masa entre la corriente y las aguas circundantes. Las trayectorias de boyas indican que la mayor parte de esta "pérdida" de masa se produce hacia el este (Rossby, 1996). En la figura 7.10a, las flechas zonalmente orientadas indican la trayectoria probable de la masa "perdida".

La figura 7.10b muestra la EKE asociada con la NAC y su paso hacia el norte, a medida que rodea el Flemish Cap. La EKE en esta región muestra un gradiente negativo agudo hacia el este, lejos de la NAC. Rossby (1996) explica este descenso en la EKE debido a la pérdida de masa de la NAC, así las parcelas de agua expulsada se desaceleran rápidamente a medida que avanzan hacia el este en aguas más tranquilas. Estas aguas pasan a formar parte del agua subtropical que circula a gran escala hacia el este, una parte de la cual forma parte del la parte oriental del Giro Subtropical (ESG)Klein and Seidler, 1989; Krauss et al., 1990; Rossby, 1996), contribuyendo a la formación de las aguas poco profundas pero bien definidas de la AzFC.

7.3.5.2. La Corriente de las Azores

La AzC es una corriente zonal, cuyo origen es una ramificación hacia el sureste de la Corriente del Golfo, es una estructura permanente situada entre 33° - 35°N que atraviesa el MAR y fluye hacia el golfo de Cádiz, con un transporte entre 10 y 12 Sv (Gould, 1985; Stramma and Muller, 1989). Juliano and Alves (2007) identificaron un meandro ciclónico casi-permanente en 35°N, 47.5°W como el vínculo entre la AzC y su fuente en el GS. La AzC es profunda, hasta 1000 m, con una anchura típica de 50 km de ancho, propagándose en forma de *jet* con oscilaciones, que dan lugar a la forma de meandro típicamente observada en AzC (Siedler et al., 1985; Le Traon and De Mey, 1994; Juliano and Alves, 2007). La velocidad media determinada a partir de un análisis con correntímetros en la cuenca Canarias por Zhou et al. (2000) está comprendida entre 0,10 a 0,15 m s^{-1}. A lo largo de la trayectoria de la AzC, se han descrito una serie de brazos que se dirigen hacia el sur, de modo que sólo alrededor de 4,5 Sv llegan al Golfo de Cádiz (Klein and Seidler, 1989; Paillet and Mercier, 1997). Pelegrí et al. (2005b) sugieren que sólo el último de estos brazos, al este de la meseta de Madeira (17°W), debe considerarse que presenta una posición permanente (véase también Zhou et al., 2000). Por otro lado, observaciones en los brazos más occidentales parecen estar relacionados con la naturaleza inestable de la corriente. Tanto al norte como al sur de la AzC hay evidencia de un flujo hacia el oeste de la Contracorriente de las Azores (AzCC) (Onken, 1993; Le Traon and De Mey, 1994; Cromwell et al., 1996; Alves and Colin de Verdière, 1999; Juliano and Alves, 2007).

Stramma and Siedler (1988) describieron un desplazamiento de unos 2°hacia el norte del eje zonal de la AzC en el verano (Figura 7.11), sin embargo, otros autores no han encontrado evidencia de esta variación estacional de la posición de la AzC (Le Traon and De Mey, 1994; Cromwell et al., 1996). Le Traon and De Mey (1994), a partir de datos de altimetría,

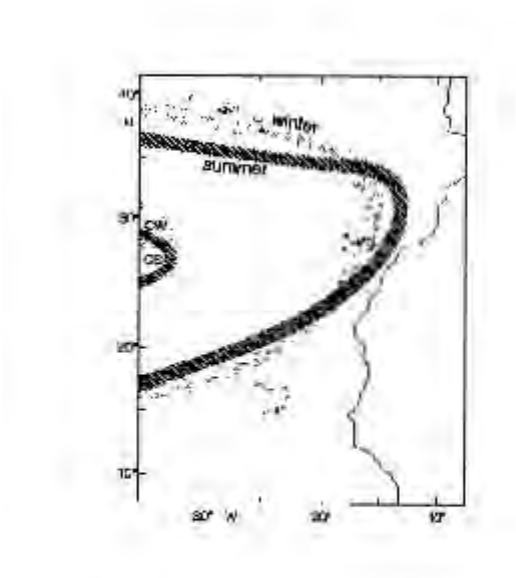

Figura 7.11.: Representación esquemática de Stramma and Siedler (1988) del margen oriental del Giro Subtropical (ESG) en el verano y el invierno, en los primeros 200 m del océano.

afirmaron que la corriente es más coherente y tiene una mayor penetración hacia el este en verano que en invierno.

La parte occidental del sistema frontal AzFC que se asocia con la AzC, se separa las Aguas Modales Subtropicales de 18°C y 13°C (Pollard et al., 1996). Käse et al. (1985) determinaron saltos de temperatura y salinidad al este de las Azores del orden 2°C y 0.3, respectivamente, en el frente. En el plano vertical, el frente contiene el NACW situada sobre MW (Harvey and Arhan, 1988). La complicada trayectoria del frente ha sido atribuida a ondas de Rossby cuasi-estacionarias, que se originan en el límite oriental de la Cuenca de Canarias (Le Traon and De Mey, 1994), y también a la inestabilidad baroclínica del *jet* (Alves and Colin de Verdière, 1999). Meandros ciclónicos (anticiclónicos) se forman típicamente en el norte (sur) del eje principal de la corriente. Además se han observado remolinos de mesoescala en ambos lados del frente, con escalas típicas de 200 km. Los remolinos y el serpenteo del frente conllevan una alta variabilidad en la trayectoria de la corriente y, dando lugar a una alta señal de la EKE, como se aprecia en la figura 7.9. Zhou et al. (2000) observaron máximos valores de la EKE en el flanco sur de la corriente.

Aunque en un principio se pensó que AzC se originaba por el forzamiento del viento (Käse and Krauss, 1996), cada vez hay más trabajos que relacionan su dinámica con procesos de *entrainment* en el Golfo de Cádiz (Jia, 2000; Peliz et al., 2007; Kida et al., 2008).

7.3.5.3. La Corriente de Canarias

La CanC constituye la frontera oriental del Giro Subtropical del Atlántico Norte (NASG), y la componente más oriental del ESG, fluyendo hacia el ecuador paralelamente a la costa noroeste africana. El transporte del NACW es de aproximadamente 3 Sv hacia el sur, con en torno a un ∼1 Sv adicional asociado con el afloramiento costero (Machín et al., 2006a). La CanC ha sido generalmente aceptada como una corriente extensa y débil, conducida por

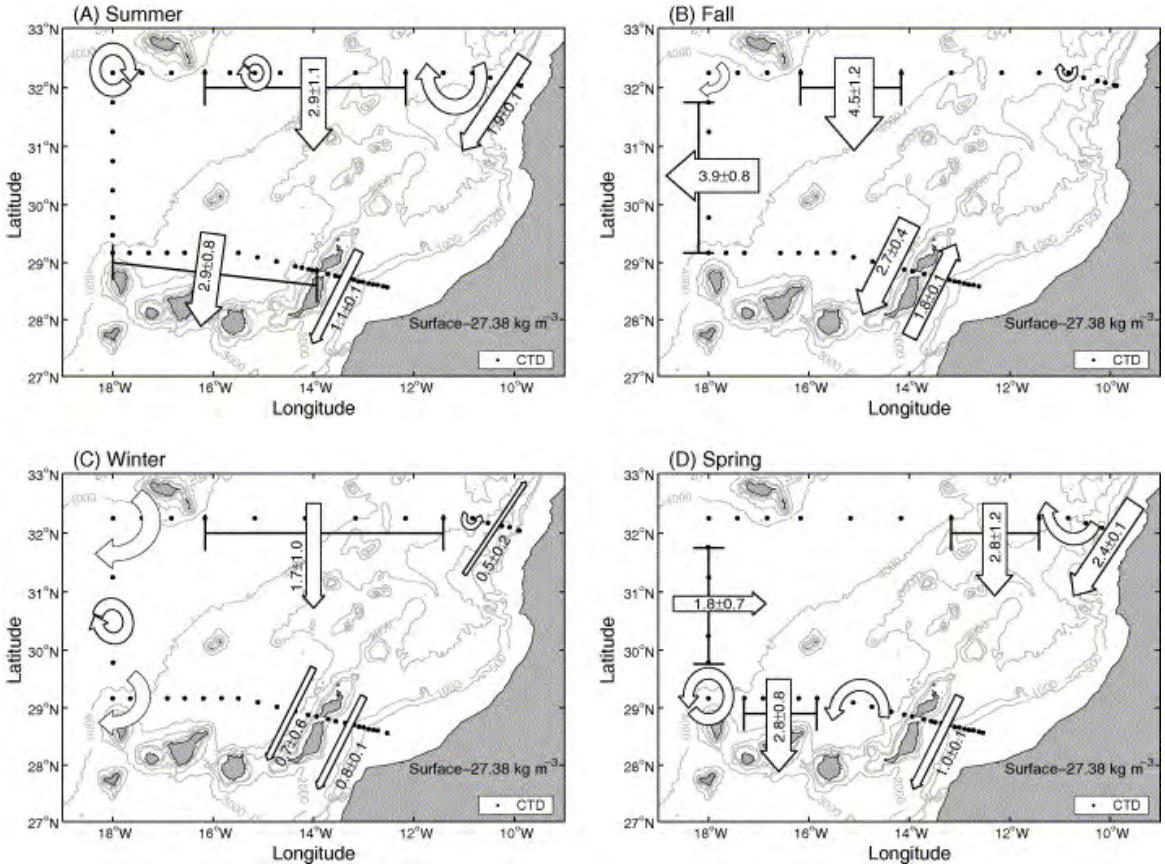

Figura 7.12.: Esquemas del transporte estacional de la Corriente de las Canarias reproducido por Machín et al. (2006a). El ancho de las flechas es proporcional al transporte de masa (Sv). Flechas curvadas (sin transporte en cifras) sugieren la presencia de estructuras de mesoescala.

el viento, que abarca la zona de transición entre el océano abierto y la región costera norte africana, donde el afloramiento tiene lugar la mayor parte del año. La CanC es la continuación de la AzC, que se ramifica hacia el sur al pasar por el norte de Madeira a 17°W. Después de atravesar el Archipiélago Canario, el flujo principal de la CanC continúa hacia el sur hasta que se separa de la costa africana cerca de Cabo Blanco para unirse a la Corriente Norecuatorial (NEC) (Stramma, 1984).

Stramma and Siedler (1988), analizando el campo de flujos geostróficos usando datos históricos, relacionaron el desplazamiento estacional de la CanC al del ESG. La figura 7.11 muestra como en invierno se observó la CanC lejos de la costa, cerca de Madeira, mientras que en verano la CanC ocupa una posición central entre Madeira y la costa africana. Estudios recientes indican que la descripción general anterior de la CanC omite una variabilidad considerable, incluso a escalas de tiempo estacionales. Zhou et al. (2000) encontraron que las boyas de deriva en la CanC tienden a ocupar una banda estrecha, en lugar de la amplia franja prevista a partir de datos climatológicos. Estas representaciones están de acuerdo con las secciones meridionales estacionales de la velocidad geostrófica presentadas en Machín et al. (2006a). En éstas, por ejemplo, en verano de 1998, la CanC fue vista como una corriente intensa centrada a unos ∼800 m de profundidad alrededor de 14°W.

La CanC, por lo tanto, tiene una estructura de corriente estrecha, una posición bien definida, aunque con cierta variabilidad estacional. Además, su comportamiento parece estar fuertemente vinculado al afloramiento costero. Así, Pelegrí et al. (2005a) subrayan la estrecha interconexión entre la región del afloramiento costero y el mar abierto (que se discute en profundidad más adelante, en la sección 7.3.6). Sin embargo, debido a que las observaciones en esta región aún son relativamente escasas, lograr una descripción definitiva de la ruta y la variabilidad estacional de la CanC parece difícil de alcanzar.

7.3.5.4. La Corriente y Contra-Corriente Norecuatorial

La Corriente Norecuatorial (NEC) define el límite sur de la dinámica del ESG, y es la corriente más septentrional del complejo sistema de corrientes del Atlántico ecuatorial (Stramma and Schott, 1999; Stramma et al., 2003). El NEC es una corriente superficial extensa conducida por el viento, que fluye hacia el oeste a través del Atlántico Norte al norte del frente Cabo Verde (Stramma and Muller, 1989; sección 7.3.4). Stramma et al. (2005) observaron que la NEC parece estar compuesta por varias bandas distintas en lugar de por un único flujo principal (Figura 7.13), de tal modo que la profundidad de cada banda aumenta de sur a norte. La figura 7.14 muestra el transporte de masa acumulado asociado la NEC entre 20° y 24°N, a partir de la sección occidental de un muestreo en caja (Hernández-Guerra et al., 2005) y la estructura de bandas es evidente. El transporte medio de la NEC es de unos 5 Sv (Fiekas et al., 1992; Hernández-Guerra et al., 2005). La NEC recibe agua de la CanC, transportando una mezcla de NACW y SACW, siendo este última advectada hacia el norte a través de la CVFZ (Arhan et al., 1994). Stramma and Siedler (1988) describieron las variaciones estacionales en la posición de la NEC. En el otoño, la corriente se encontraba

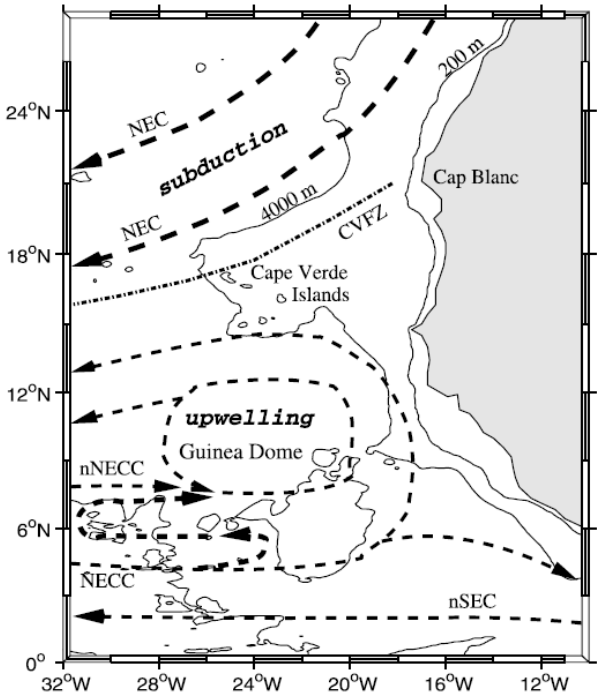

Figura 7.13.: Mapa de la Corriente y Contra-Corriente Norecuatorial (NEC, NECC) en África occidental. También se muestra el Domo de Guinea al sur de las islas de Cabo Verde. Tomado de Stramma et al. (2005).

más al norte que en primavera, probablemente como resultado del desplazamiento hacia el norte el de la ITCZ (Molinari et al., 1986; Waliser and Gautier, 1993).

La Contracorriente Norecuatorial (NECC), que fluye hacia el este, es parte del sistema de corrientes ecuatoriales que conforma el flanco sur de un giro ciclónico tropical (Figura 7.13). La NECC se encuentra entre ∼3° - 10°N, y tiene velocidades máximas en otoño, cuando la ITCZ se encuentra en su posición más septentrional. Stramma et al. (2005) describieron un transporte de 11,5 Sv en octubre / noviembre de 2002. La NECC se debilita en primavera, o incluso invierte el flujo hacia el oeste en el Atlántico tropical occidental (Lumpkin and Garzoli, 2005). A medida que se acerca a la masa de tierra de África, la NECC se divide, con una porción que gira hacia el norte a lo largo de la costa como la Corriente de Mauritana (MC), mientras que el resto continúa hacia el este como la corriente de Guinea (Lázaro et al., 2005). La recirculación hacia el norte es una componente del Domo de Guinea, una estructura ciclónica permanente cuasi-estacionaria, que se encuentra al sur de las islas de Cabo Verde, bordeada por la NEC y la NECC. El Domo de Guinea es una región de fuerte afloramiento, y que muestra una cierta variabilidad estacional (Lázaro et al., 2005). La MC fluye hacia el norte a través del CVFZ, transportando SACW que se mezcla con el NACW de la NEC.

Stramma et al. (2005) afirmaron la importancia de la presencia de un estructuras similares a remolinos en la NEC y la NECC. Por lo tanto, estos remolinos pueden aumentar el intercambio de agua entre los giros subtropicales y tropicales.

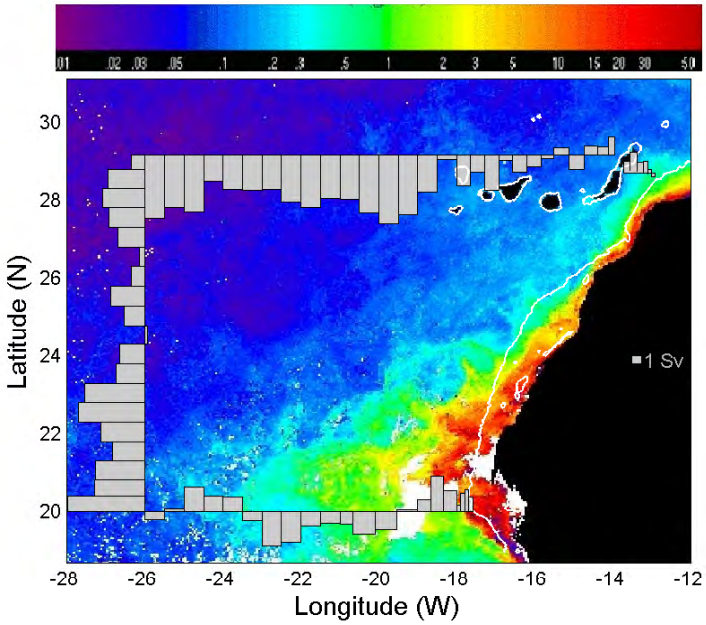

Figura 7.14.: Transporte acumulado de masa en la capa superficial, al sur de las Islas Canarias, obtenida a partir de modelos inversos (Hernández-Guerra et al. (2005)). También se muestran las concentraciones medias de pigmentos de fitoplancton (mg m^{-3}) a partir del sensor de color del océano, SeaWiFS (McClain et al., 1998) para septiembre de 2003. La línea blanca delimita la isóbata de 200 metros. Tomado de Hernández-Guerra et al. (2005).

7.3.6. El afloramiento en el noroeste africano

El sistema de afloramiento en el noroeste africano (CUS), que incluye el afloramiento de la Península Ibérica en el norte, es uno cuatro mayores sistemas de afloramiento de margen oriental (EBUS) en los océanos del mundo (Carr and Kearns, 2003). Estos EBUS presentan también una importante actividad económica derivada de la industria de la pesca (Arístegui et al., 2006). El aporte constante de nutrientes en aguas superficiales derivado de la dinámica de *Ekman*, conduce a la producción primaria característicamente alta en estos sistemas de afloramiento. Carr (2002) define la zona activa de un sistema de afloramiento como la zona donde las concentraciones de clorofila exceden el 1 m mg^{-3}. El CUS tiene la mayor zona activa de todos los EBUS.

El afloramiento en Canarias se mantiene por la presencia de los vientos Alisios (sección 7.3.3.1). Entre Cabo Blanco y el Estrecho de Gibraltar, el afloramiento es activo durante todo el año, aunque es menos intenso hacia el norte del archipiélago canario. En verano, la influencia de los Alisios se extiende hacia el norte hasta el oeste de la Península Ibérica, mientras y, en invierno, hacia el sur hasta Cabo Verde (Wooster et al., 1976; Mittelstaedt, 1991; Van Camp et al., 1991; Nykjær and Van Camp, 1994). El NACW subsuperficial es transportada a lo largo de la costa en la zona fótica, como se explicaba en el clásico ejemplo de Ekman (1905), en el que una célula de agua vertical se crea en respuesta a los vientos paralelos a costa, en conjunción con la creación de un *jet* también paralelo a costa. En el CUS, Pelegrí et al. (2006) afirman que el *jet* costero puede ser considerado como una rama

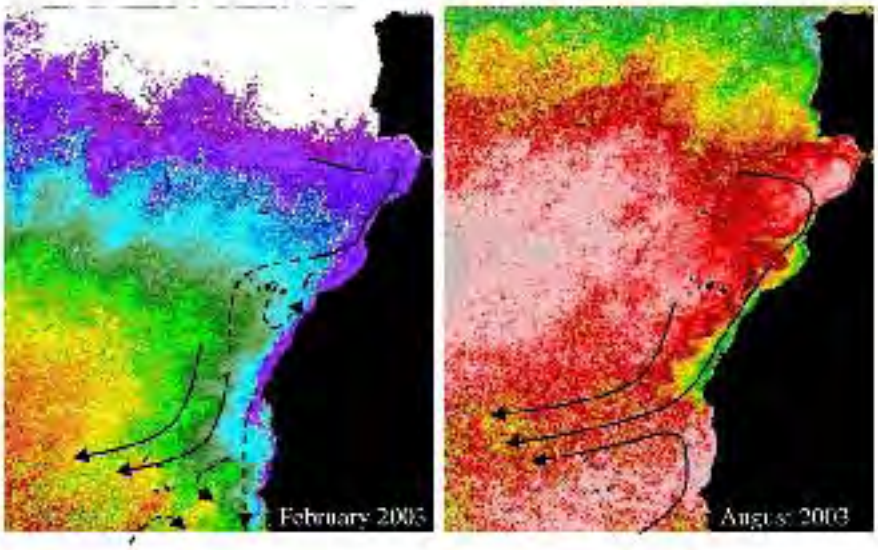

Figura 7.15.: Medias mensuales de SST para el margen oriental del Giro Subtropical (ESG) en el invierno (izquierda) y verano (derecha) de 2003. Se ha superpuesto un esquema de los patrones de flujo de la CanC y CanUC. Las líneas continuas indican la circulación bien establecidas del flujo, mientras que las líneas discontinuas marcan posibles conexiones. Tomado de Pelegrí et al. (2006) (barra de colores no disponible).

oriental de la CanC, la Corriente Canaria de Afloramiento (CanUC).

La CanUC presenta una marcada estacionalidad a lo largo de toda su extensión, que es el resultado de la variabilidad espacial y temporal del estrés del viento. La CanUC parece originarse entre el Estrecho de Gibraltar y Cabo Ghir, donde varios estudios han demostrado la existencia de un flujo del NACW (∼1 - 2 Sv) desde mar abierto hacia la región costera (Stramma, 1984; Lozier et al., 1995; Pelegrí et al., 2005a; Machín et al., 2006b). Este agua fluye hacia el ecuador, al igual que la CanUC, como se muestra esquemáticamente en la figura 7.15. En invierno, este flujo hacia la región costera es casi zonal y recircula hacia el sur dentro de una estrecha banda paralela a costa. En verano, el flujo se intensifica, pero recircula en una región más amplia (Machín et al., 2006b). En la zona de Cabo Ghir, durante el verano la CanUC continúa su viaje hacia el sur adyacente a la costa, mientras que en invierno parece que dar un rodeo grande en alta mar ∼30°N para fusionarse con la CanC. En las Islas Canarias, se produce una recirculación ciclónica de tal manera que su camino de retorno se observen inversiones del sentido de la corriente en las corrientes costeras de estas islas (Pelegrí et al., 2005a). Aunque las inversiones del flujo costero interior en la latitud de las islas Canarias en otoño son bien conocidas (Hernández-Guerra et al., 2002; Knoll et al., 2002; Machín et al., 2006a) y han sido atribuidas a la relajación del afloramiento, los detalles de la magnitud y la estructura del ciclo de la recirculación invierno entre el archipiélago y Cabo Ghir no están claros.

El CUS presenta las características típicas de mesoescala asociadas con los EBUS. Así, las aguas del afloramiento de la costa africana, frías y ricas en nutrientes, interaccionan con la CanC, produciendo variables frentes, remolinos y filamentos. Los filamentos casi-

permanentes de Cabo Ghir y Cabo Blanco (Pelegrí et al., 2005b), extendiéndose ambos cientos de kilómetros mar adentro, son los ejemplos más notables. El filamento de Cabo Ghir puede verse claramente en las imágenes de satélite SST de la región (Figura 7.15) (Van Camp et al., 1991; Pelegrí et al., 2005b). Otros filamentos importantes son aquellos frecuentemente observados entre Cabo Bojador y Cabo Juby (Barton et al., 1998), que están asociados con el transporte de material orgánico al este de las Islas Canarias (Bécognee et al., 2006; Moyano et al., 2009). De hecho, la región al sur de las Islas Canarias es donde se presenta una mayor variabilidad dentro del CUS (véase la EKE en la figura 7.9). Las interacciones complejas entre los remolinos generados por las islas, el frente de afloramiento y los filamentos de afloramiento se observan con frecuencia (Arístegui et al., 1994; Barton et al., 1998; Basterretxea et al., 2002; Barton et al., 2004; Sangrà et al., 2009).

En su límite sur, la CanUC converge con el SACW en la región de la CVFZ. En verano y otoño, cuando el MC penetra hacia el norte hasta Cabo Blanco, aparece una intensa convergencia (entre el NACW y el SACW), junto con transporte hacia el océano. Por otro lado, en invierno y primavera, como el límite del afloramiento se encuentra más al sur, hacia Cabo Verde (Figura 7.15), la convergencia y el transporte hacia mar abierto se reduce, aunque sigue estando presente (Pelegrí et al., 2006). El transporte hacia mar abierto conlleva un transporte de altas cantidades de nutrientes, de ahí la elevación de las concentraciones de fitoplancton comúnmente visto la costa de Cabo Blanco, como se observa en la figura 7.14. El filamento asociados a la zona de convergencia, conocido como el filamento gigante de Cabo Blanco, tiene unas características únicas de bajas temperaturas y altas concentraciones de clorofila, detectables varios cientos de kilómetros mar adentro (Gabric et al., 1993).

Asociada a la circulación del afloramiento, se encuentra una corriente subsuperficial hacia el polo que se desplaza paralela a la plataforma del noroeste de África, a una profundidad de unos 300 m (Barton, 1989). Esta corriente transporta el SACW en profundidad hacia el norte, una parte del cual penetra más allá de la CVFZ en Cabo Blanco. Otra corriente subsuperficial también es observada en la costa oeste de la Península Ibérica, pero la naturaleza su continuidad con la proveniente del noroeste de África es incierta debido a la interacción de del MW en Gibraltar (Barton, 1998; Hagen, 2005).

7.3.7. El Archipiélago Canario

El archipiélago canario está constituido por siete islas y varios islotes que forman una cadena frente a las costas del noroeste de África (Figura 7.16). Las islas se encuentran a una latitud entre $\sim$27.5° y 30°N, a nivel de la porción sur de la gran ensenada que separa Cabo Juby y Cabo Ghir, y tiene una extensión este-oeste de unos 500 km. Aunque sólo distan 95 km entre Fuerteventura y la masa continental de África, el pasaje que las separa alcanza profundidades de más de 1000 m. Todas las islas, a excepción de Lanzarote y Fuerteventura, son montañosas y presentan picos que sobrepasan los 1000 m. Las islas, que se cree que surgen de la corteza oceánica (Roest et al., 1992), forman parte de un cinturón de 3000 kilómetros de extensión de islas y montañas submarinas que se han tenido actividad volcánica durante más de 16

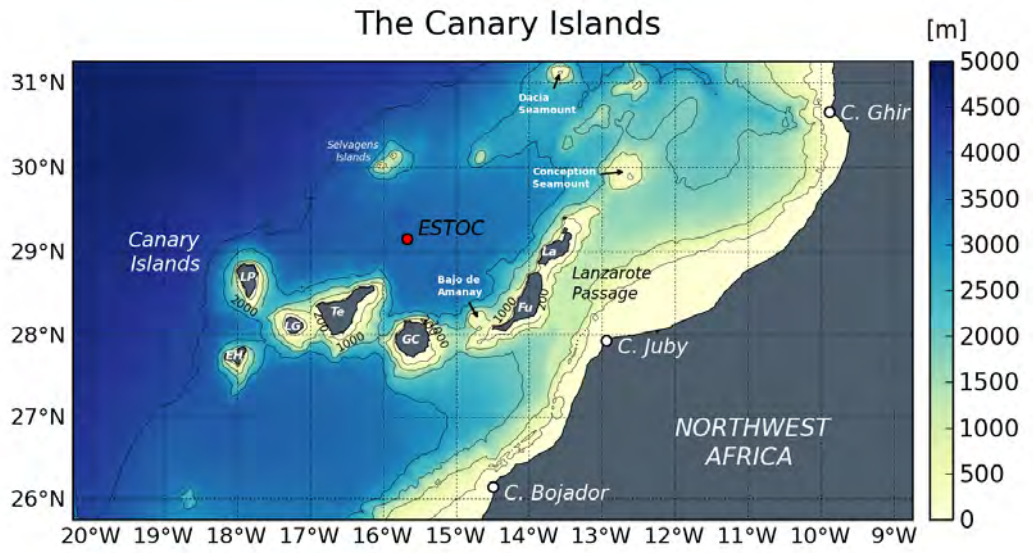

Figura 7.16.: El archipiélago Canario: LP - La Palma; EH - El Hierro; LG - La Gomera; Te - Tenerife; GC - Gran Canaria; Fu - Fuerteventura, La - Lanzarote. El fondeo ESTOC se muestra al norte de Gran Canaria. En negro se representan las isóbatas de 200, 1000, 2000, 3000, 4000 m. Fuente de los datos topográficos: GEBCO (Hunter and Macnab, 2003).

Ma, y que se extiende desde aproximadamente 37°N (Madeira-Tore Rise) hasta 15°N (Cabo Verde). La mayor densidad de islas y montañas submarinas se encuentran entre 20° - 35°N, lo que incluye los archipiélagos de Canarias y Madeira. Las siete islas muestran un gradiente en edad hacia el oeste, así Lanzarote y Fuerteventura son las más antiguas (>35 Ma), y La Palma (2 Ma) y El Hierro (<1 Ma) las más recientes.

El Archipiélago canario supone una de las características topográficas más importantes de la región, debido a que se encuentra directamente en el camino de la CanC y la CanUC, extendiéndose en la zona de transición entre las aguas costeras y oceánicas (Barton et al., 1998; Pelegrí et al., 2005a).

7.3.7.1. Topografía

La topografía de Canarias se muestra en la figura 7.16. Las islas se encuentran sobre una meseta oceánica localizada a unos 2500 m, que se extiende hacia el oeste lejos del margen continental. Los lados de la meseta son muy escarpados, llegándose a alcanzar profundidades de más de 3500 m rápidamente en los flancos norte, sur y oeste. Las islas se alzan sobre la meseta, constituyen una barrera al paso de la CanC, que debe pasar a través de los pasajes profundos que los separan.

Hay cuatro pasajes principales que separan las islas. El Pasaje de Lanzarote es el más oriental, que se extiende entre las islas de Lanzarote y Fuerteventura, y la costa africana. Aquí el fondo oceánico se eleva muy suavemente hacia el continente. Dos pasos secundarios, relativamente poco profundos, separan Tenerife y La Gomera, y Fuerteventura y Lanzarote, respectivamente. Además, las islas se caracterizan por una plataforma muy estrecha y

topografía escarpada.

En la región, otras características batimétricas de interés son las Islas Salvajes, y la presencia de montes submarinos en mar abierto. Los dos pequeños islotes de las Islas Salvajes se encuentran en aguas profundas a unos 200 km al norte de Tenerife, a mitad de camino entre Madeira y las Islas Canarias. Ocupan una superficie de sólo 2,73 kilómetros. El monte submarino Concepción se encuentra a aproximadamente 120 km al noreste de Lanzarote, y a 130 km al noroeste de éste, se encuentra el monte Dacia. Ambos montes submarinos apenas alcanzan más de 100 m sobre la superficie, y entre ellos se encuentran varias pequeñas montañas submarinas. Cabe destacar que estas estructuras se encuentran al norte de las Islas Canarias, y así es de esperar que perturben el paso de la CanC al norte del archipiélago. También, a unos 8 km al noroeste de la punta sur de Fuerteventura, se encuentra un pequeño monte submarino, el Bajo de Amanay, que se eleva a menos de 25 m de la superficie.

7.3.7.2. La circulación atmosférica y forzamiento

Las islas oceánicas que presentan una orografía elevada modifican tanto la circulación oceánica como la atmosférica. Cuando los vientos Alisios soplan en las Islas Canarias en primavera y verano, están limitadas por una fuerte inversión de temperatura de la atmósfera entre 400 y 1000 m sobre la superficie de los océanos (Naya, 1984). Gran Canaria, Tenerife y La Palma presentan un relieve escarpado que se extienden por encima de la capa de inversión. En la vertiente norte de estas islas, el viento ascendiende y a menudo forma una capa de estratocúmulos en la base de la inversión. Esta capa de inversión estable forma una barrera adicional a la convección, de tal manera que el aire se ve forzado a circular hacia los flancos de la isla. A sotavento de estas islas raramente se forman nubes extensas, debido a la subsidencia atmosférica por las laderas de sotavento.

Las observaciones sobre la estela atmosférica persistente en Gran Canaria fueron descritas mucho antes que los de la estela oceánica (Chopra and Hubert, 1964, 1965a,b; La Violette, 1974). La figura 7.17a muestra una fotografía presentada por Chopra and Hubert (1964) el satélite meteorológico *Tiros V* sobre las Islas Canarias en julio de 1962. Se aprecia una estela de vórtices atmosféricos que se extiende varios cientos de kilómetros a sotavento de Gran Canaria. Una imagen más reciente presenta el mismo fenómeno, como se muestra en la figura 7.17b. Los remolinos, cuyas propiedades características fueron descritas por Hubert and Krueger (1962), son visibles en los estratocúmulos que se encuentran por debajo de la inversión de la temperatura. La vida de estos remolinos, según Chopra and Hubert (1964), se estimó en 35 horas. Estos autores señalaron la semejanza entre estos vórtices y aquellos del patrón de las calles de remolinos de *Von Karman*, observado en experimentos de laboratorio. Una calle de vórtices a sotavento de la vecina isla de Tenerife aún está en discusión.

En el trabajo de Zimmerman (1969), se estudiaron un mosaico de imágenes de formaciones de nubes en las cercanías de las Islas Canarias tomadas por la nave *Gemini-6*, donde las calles de vórtices eran claramente visibles. Tras la propuesta de Wilkins (1968), que se afirmaba que el vórtice de una isla con elevado relieve debe causar cambios periódicos de la presión en

(a) (b)

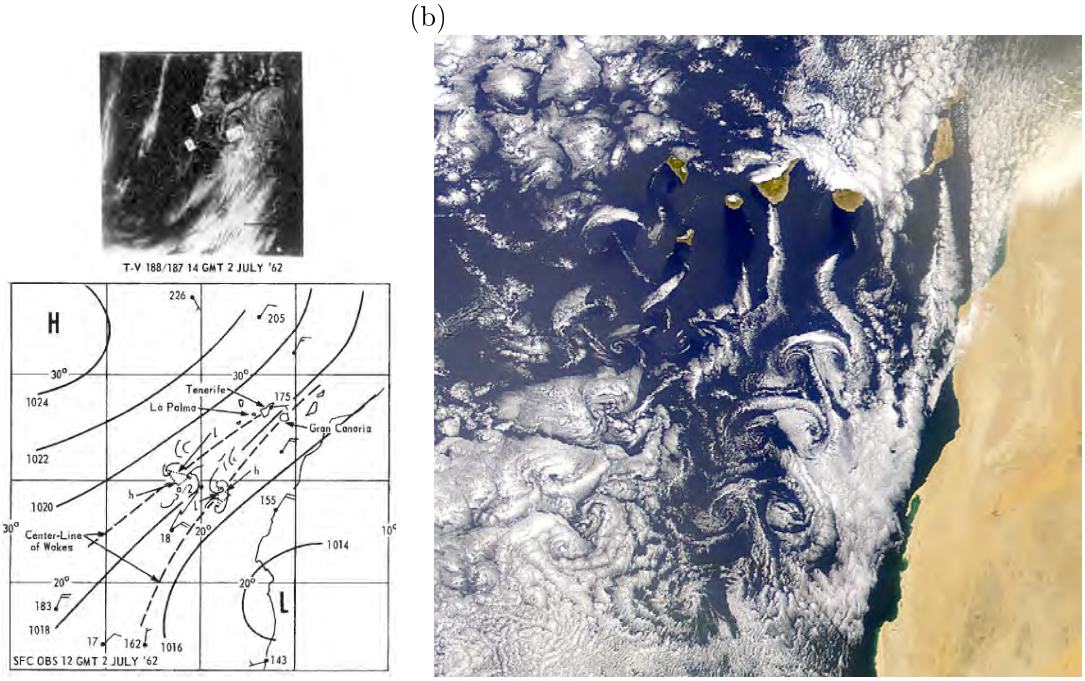

Figura 7.17.: Patrones de remolinos atmosféricos sotavento de las Islas Canarias. (a) Esquema y foto del satélite meteorológico *Tiros-V* el 2 de julio de 1962, reproducido de Chopra and Hubert (1964). (b) Los patrones de vórtices atmosféricos en las Islas Canarias observados desde el sensor MODIS a bordo del satélite *Terra*, el 4 de junio de 2000.

los costados de la isla, Zimmerman (1969) analizó las fluctuaciones de presión en seis lugares diferentes del archipiélago. En una estación situada en Santa Cruz de Tenerife registraron las mayores fluctuaciones, que alcanzaron 2.5 mbar. Zimmerman (1969) atribuyó un 1.5 mbar de estas fluctuaciones a la génesis de remolinos, teniendo en cuenta cambios de presión semidiurnos de 1 mbar. Las mayores fluctuaciones de presión se encontraron en los flancos de las islas. Un examen completo de los anteriores artículos mencionados pueden ser encontrados en Chopra (1973).

En la figura 7.18, se muestra el ciclo estacional del estrés y velocidad del viento en las Islas Canarias, a partir de datos tomados de la climatología SCOW Risien and Chelton (2008). Se detallan los promedios de los meses de febrero, mayo, agosto y noviembre. La persistencia de los vientos Alisios, que favorecen el afloramiento, es evidente. Éstos alcanzan su máxima intensidad entre marzo y septiembre, cuando el Anticiclón de las Azores se acerca a su límite norte (Wooster et al., 1976; Nykjær and Van Camp, 1994). Los valores máximos mensuales de velocidad del viento, según los datos SCOW, ocurren en agosto (12.3 m s^{-1}), en un lugar al este de Gran Canaria. Esto es superior a la media de 8.7 m s^{-1} dada por Pelegrí et al. (2005a). Por otro lado, el mínimo de la velocidad del viento tiene lugar en febrero (1.4 m s^{-1}), en un lugar alejado de la costa.

Los campos de rotacionales de la figura 7.18 ilustran la constricción de los vientos a su paso por los pasajes entre islas del archipiélago canario. Cuando el viento es lo suficientemente intenso, se forman *jets* en estos pasajes. Al ver los límites laterales de estos chorros de viento,

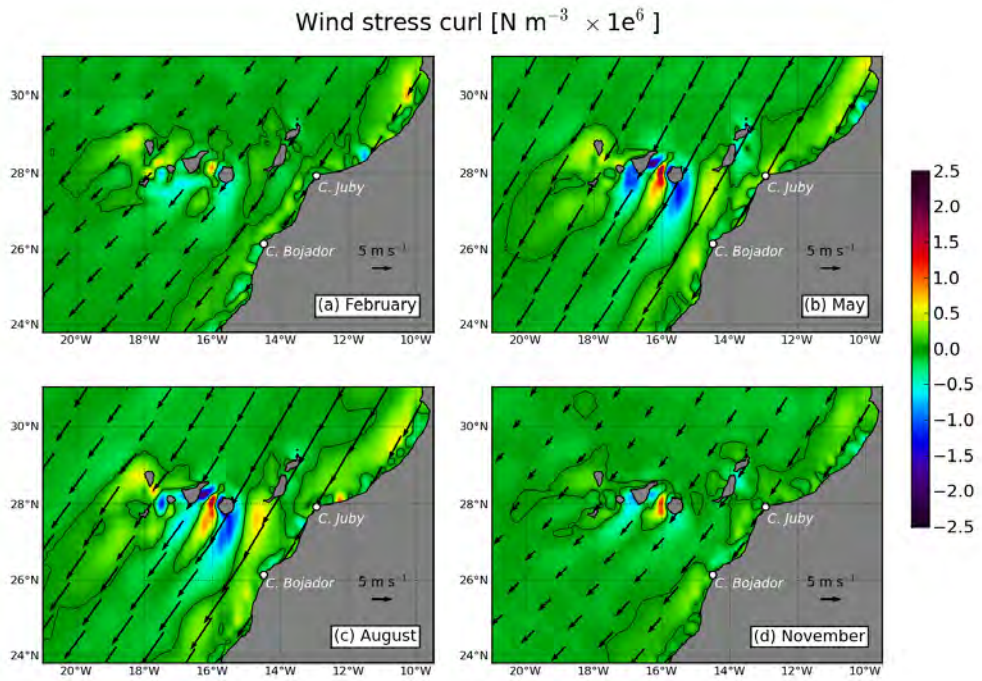

Figura 7.18.: Promedios mensuales del rotacional de la tensión del viento normalizado obtenido de la climatología de la tensión del viento SCOW derivada del QuikSCAT (Risien and Chelton, 2008) en las Islas Canarias. El contorno de rotacional nulo se muestra en negro. Los vectores en negro muestran la velocidad y dirección del viento a 10 m.

el rotacional es alternativamente positivos (derecha) y negativos (a la izquierda). Entre estos *jets*, a sotavento de cada isla, se sitúa la zona de sombra de vientos de la isla, donde los vientos son débiles. El efecto de estos *jets* de viento en el océano es inducir rápidas variaciones en el transporte de *Ekman*, fuertes afloramientos o *downwelling*, y la generación de remolinos de mesoescala (Basterretxea et al., 2002; Chavanne et al., 2002). Estos patrones de *jets* de viento y las zonas de sombra de viento también se observan en las islas de Cabo Verde y en Madeira.

7.3.7.3. Las corrientes y la variabilidad en las Islas Canarias

La variabilidad estacional de la Corriente de las Canarias al norte de las Islas Canarias ya se discutió en la sección 7.3.5.3. Ya ahí se enfatizó la importancia de los trabajos recientes sobre la CanC, y también sobre la CanUC. Sin embargo, las teorías expuestas hasta el momento son incompletas y requieren una mayor investigación, sobre todo porque, en las Islas Canarias, la ruta de acceso y la variabilidad de estas corrientes tiene una relevancia directa, debido a su papel como el flujo incidente en el archipiélago (Sangrà, 1995).

Las primeras observaciones en la región sugerían una CanC que fluía constante hacia el ecuador CanC, incidiendo en las islas y continuando hacia el sur (Stramma, 1984; Stramma and Siedler, 1988). Estos estudios se vieron obstaculizados por la baja resolución, por lo que las perturbaciones del flujo de la CanC asociadas a las islas se quedó sin resolver.

Sin embargo, en una imagen estacional de Stramma and Siedler (1988) (véase la figura 7.11), se confirmaba que la variabilidad a gran escala está asociada con la variabilidad del ESG (Barton et al., 1998; Navarro-Pérez and Barton, 2001). Utilizando los datos del nivel del mar desde mareógrafos ubicados en las islas occidentales (La Palma y Tenerife) y en las islas orientales (Lanzarote y Tenerife), Navarro-Pérez and Barton (2001) calcularon las velocidades geostróficas meridionales y encontraron flujos mayores cerca de la costa africana en verano, mientras que en invierno es más fuerte en mar abierto, en consonancia con el avance y el retroceso del ESG. Los valores medios del flujo en las capas superficiales de todo el archipiélago es débil ($\sim$0.02 m s^{-1}), de modo que el caudal instantáneo es tradicionalmente dominado por una variabilidad de mesoescala a mayor escala. Navarro-Pérez and Barton (2001) pusieron de manifiesto que, en el oeste, había una tendencia de flujo hacia el sur (norte) en invierno (verano), mientras que en el este, el flujo promedio fue hacia el sur durante todo el año. En este sentido, se ha de tener en cuenta que este flujo hacia el este está al oeste del Paso de Lanzarote, donde el flujo hacia el norte se produce en otoño.

Varios autores han hecho mención de un serpenteo de flujo ciclónico alrededor del archipiélago (Mittelstaedt, 1991; Navarro-Pérez and Barton, 2001). Navarro-Pérez and Barton (2001) especularon que este flujo podría ser dirigido topográficamente, ya que parece seguir los contornos de profundidad de la meseta en la que se encuentran las islas. Pero también se ha señalado que los pasajes que separan las islas son profundos ($\sim$2000 m), y por lo tanto deberían tener poca influencia sobre las corrientes, que son débiles por debajo de los 500 m. Hay evidencias de que el flujo es variable entre las islas (p.ej., a través de los pasajes), aunque esto ha sido más estudiado en los pasajes del este (Hernández-Guerra et al., 2002; Knoll et al., 2002). Hernández-Guerra et al. (2002), a partir de perfiles de XBT (*expendable bathythermograph*) obtenidos cada dos meses entre noviembre de 1996 y septiembre de 1998, encontraron un transporte geostrófico hacia el sur casi idéntico ($\sim$1 Sv) entre Gran Canaria y Fuerteventura, y Fuerteventura y África. En la sección Fuerteventura - África, el transporte fue hacia el sur, a partir de noviembre de 1996 y 1997. Knoll et al. (2002) registraron valores medios de velocidad de la corriente hacia el sur de 0.05 m s^{-1}, a partir de medidores de corriente en los 200 primeros metros del Paso de Lanzarote durante los años 1997 y 1998, y también observaron una inversión del flujo hacia el norte en otoño. Hernández-Guerra et al. (2002) sugirieron que esta inversión está asociada con la presencia en superficie de la corriente subsuperficial hacia el polo (*poleward undercurrent).* Por otro lado, en la sección Gran Canaria - Fuerteventura, se produjo un transporte anómalo hacia en norte en mayo de ambos años.

A pesar de que el caudal medio en todo el archipiélago se ha demostrado que es hacia el sur con velocidades de hasta 0.05 m s^{-1}, a escala interanual, puede haber largos períodos de inversión de flujo, es decir, contra el sentido de giro (Navarro-Pérez and Barton, 2001; Barton et al., 2004). Navarro-Pérez and Barton (2001) calcularon las velocidades geostróficas a partir de una serie temporal de 20 años de la altura de la superficie del mar obtenida de las estaciones de mareógrafos situados en extremos opuestos del archipiélago (La Palma y Lanzarote). Estos autores hallaron varios períodos de flujo hacia el norte, con magnitudes

de hasta 0.04 m s^{-1} y la duración típica de unos pocos meses.

Los estudios citados en esta sección reflejan la alta variabilidad de mesoescala que ocurren en y alrededor del archipiélago canario. Sin embargo, debido a la complejidad de la circulación y la topografía, la ausencia de observaciones continuas, y la incertidumbre sobre el carácter del flujo de CanC entrante, se sabe relativamente poco acerca de la circulación en los alrededores de las Islas Canarias.

7.3.7.4. La estela de las Islas Canarias

El flujo de la CanC a través del Archipiélago Canario favorece la generación de remolinos de mesoescala, lo que contribuyente de manera importante a la variabilidad de la región inducida por el afloramiento norafricano (Figura 7.19) (Barton et al., 2004). Los remolinos se observan principalmente a sotavento de las islas (La Violette, 1974; Hernández-Guerra et al., 1993; Arístegui et al., 1994, 1997; Barton et al., 2004; Sangrà et al., 2005, 2007; Piedeleu et al., 2009), pero también han sido muestreados en los pasajes (Molina et al., 1996; Knoll et al., 2002) y al norte de las islas (Hernández-Guerra et al., 2005).

Los estudios anteriores utilizaron los métodos de teledetección para registrar anomalías de SST asociadas con remolinos de mesoescala a sotavento de las Islas Canarias. Arístegui et al. (1994) presentó por primera vez medidas *in situ*, a partir de datos recopilados al suroeste de Gran Canaria. En este trabajo se muestrearon tres remolinos ciclónicos (núcleo frío) y uno anticiclónico (de núcleo caliente) utilizando tanto AXBTs (*Airborne Expendable Bathythermograph*) y CTDs (*Conductivity, Temperature, Depth sensor*). Los remolinos tenían diámetros de 40 - 60 km, en la misma escala que el diámetro de 50 km de Gran Canaria, y profundidades de hasta 265 m. Arístegui et al. (1997) describieron las interacciones entre estos remolinos generados por la isla y los filamentos que se extienden hacia mar abierto desde la costa.

Navarro-Pérez and Barton (1998) encontraron un gran remolino ciclónico (100 km de diámetro) situado al suroeste del paso entre Fuerteventura y la costa africana. Esos autores sugieren que su génesis es debida a la topografía de la zona, vorticidad ciclónica se produce al encontrarse el remolino con aguas más profundas en su desplazamiento. Imágenes de SST mostradas en La Violette (1974) y Barton et al. (1998) apoyaron que esta corriente es una característica recurrente. Knoll et al. (2002) registraron grandes valores de cizalla horizontal en la parte superior 300 m del Paso de Lanzarote, señalando que esto a veces es causado por los remolinos en esta zona. Molina et al. (1996) observaron un remolino ciclónico entre Tenerife y La Gomera, que también sugirieron que era permanente.

Los remolinos de Gran Canaria han sido objeto de supervisión mediante boyas dragadas (Sangrà et al., 2005, 2007). Las trayectorias de las boyas indicaron que tanto los remolinos ciclónicos y anticiclónicos son estructuras coherentes de larga duración, que pueden durar varios meses. Sangrà et al. (2009) describieron cómo estos remolinos contribuyen a un corredor zonal de remolinos que se extiende hacia el MAR en torno al 26°N. El llamado *Canary Eddy Corridor* (CEC) transmite de carbono y materia orgánica al interior del océano oligotrófico.

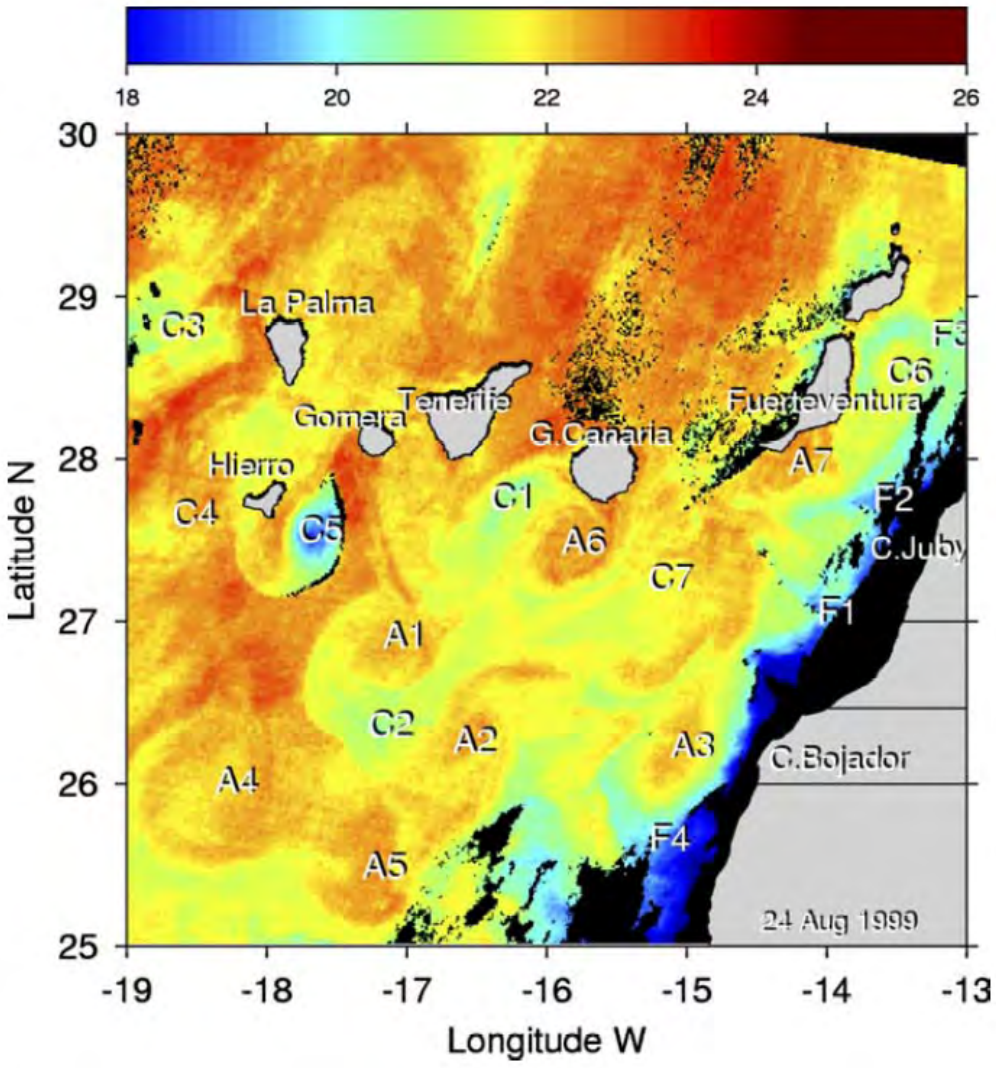

Figura 7.19.: Imagen de temperatura superficial del mar (SST, °C) de AVHRR en las Islas Canarias para 24 de agosto de 1999. Se indica la localizaciones de remolinos (C - ciclónico, A - anticiclónico) y filamentos (F). Reproducido de Barton et al. (2004) (barra de colores no disponible).

7.3.8. Preguntas abiertas

En el transcurso de esta revisión de la oceanografía física de la Cuenca de Canarias, han surgido una serie de preguntas abiertas y algunos problemas, algunos que están en la literatura, y algunos que se me han ocurrido a mí. Son los siguientes:

- Se dice que la Corriente de las Azores "alimenta" a la Corriente de Canarias. ¿Significa esto que existe una relación dinámica entre las dos corrientes? En el contexto del desarrollo de la configuración del modelo por las Islas Canarias, esta es una pregunta importante porque, sin este conocimiento, la inclusión dentro del dominio de una Corriente de las Azores realista es esencial.

- ¿Es posible una mejor descripción de la ruta y variabilidad estacional de la Corriente de Canarias? ¿Qué es lo que gobierna su dinámica? La Corriente de Canarias se ha descrito como una corriente que tiene un camino claro y bien definido. Sin embargo, la descripción se limita generalmente a una distinción general entre escenarios del verano y del invierno mediada por el avance y el retroceso del giro subtropical. Se sabe que la región del Cabo Ghir desempeña un papel fundamental a finales de verano.

- ¿Cuál es la naturaleza del flujo incidente (es decir, la Corriente de Canarias) en las Islas Canarias? Se sabe que alcanza su máxima intensidad en los meses de verano, pero ¿qué pasa con su dirección? ¿Cambia? ¿Es sistemática? La presencia, dirección y fuerza del flujo incidente que se espera para determinar una gran parte del carácter de la variabilidad de mesoescala y submesoescala en el archipiélago, que incluye los remolinos generados por las islas. La importancia potencial de estos remolinos se ha destacado por la reciente descripción del *Canary Eddy Corridor*.

En los siguientes capítulos que describen el desarrollo, análisis y resultados del modelo de la Cuenca Canaria, se abordarán estos temas. En algunos casos las respuestas definitivas están fuera del ámbito de aplicación de la presente obra. Sin embargo, se abren nuevas perspectivas e ideas para el trabajo de modelización y de observación futuro.

7.4. Planteamiento y metodología

En el modelaje se ha adaptado un enfoque *climatológico* para el cual se ha simulado una dinámica de equilibrio en la región. En relación a ello, nuestro principal interés reside en el estudio de la circulación media, del ciclo estacional y de la variabilidad en el rango de mesoescala y cercano a la submesoescala. No se ha considerado el forzamiento interanual y con ello la variabilidad interanual. En este tipo de aproximaciones la variabilidad a mesoescala es implícita a la técnica de modelaje. Esto ha sido demostrado en el caso particular de sistemas de afloramientos (Marchesiello et al., 2003), apuntando que es caótica y difícil de predecir. Su generación está vinculada a situaciones de inestabilidad dentro de grandes estructuras a gran escala, como las corrientes y frentes de afloramientos. La circulación a gran escala

está determinada por (1) el forzamiento atmosférico a gran escala o de baja frecuencia (que puede ser local o remoto) y, (2) por las corrientes de borde que entran y/o salen de nuestro dominio numérico

En este estudio, a fin de garantizar el realismo de la circulación media en las Islas Canarias, el dominio numérico se extiende mucho más allá de las aguas cercanas a las Islas. A la hora de decidir los límites del dominio numérico se ha tomado en consideración que la circulación en las Islas Canarias está modulada por la Corriente de Canarias. Ésta se desarrolla a escala de cuenca y de ahí la necesidad de extender el dominio más allá de las aguas cercanas al Archipiélago. La corriente de Canarias se origina en un ramal de la Corriente de las Azores localizada a la latitud del Estrecho de Gibraltar, es decir a latitudes bastante más altas que la correspondiente a las Islas Canarias. Por otro lado, el Estrecho de Gibraltar constituye una singularidad de la frontera septentrional de nuestro dominio. En esta región la densa masa de Agua Mediterránea (MW) fluye hacia el Atlántico con un transporte de $\sim$1 Sv (1 Sv = 10^6 m^3 s^{-1}). Aunque está todavía en discusión, cada vez es más aceptado que el arrastre de las aguas superficiales (Aguas Centrales Noratlánticas) por parte del MW juega un papel determinante en la formación de la Corriente de las Azores (Peliz et al., 2007; Kida et al., 2008). Por ello, dada la clara relación entre la Corriente de Azores, la Corriente de Canarias y las Islas Canarias, se ha creído necesario incluir en el dominio del modelo actual la región de la Corriente de las Azores y en su borde oriental dejar el Estrecho de Gibraltar con el fin de incluir los procesos relacionados con la salida del Mediterráneo. Después de diversos pruebas con dominios y pasos de malla diferentes se optó por extender el dominio a gran escala del modelo mas allá de las aguas del Archipiélago Canario y Golfo de Cádiz abarcando por tanto toda la Cuenca Canaria (Figura 7.1 en la página 155).

Teniendo en cuenta el costo computacional para el dominio a gran escala (en lo sucesivo, L0) se adoptó una resolución espacial de 7.5 km. Utilizando las técnicas de reducción de escala y anidación se ha ido aumentado sucesivamente la resolución espacial hasta alcanzar el kilómetro en nuestra región objetivo (Archipiélago Canario). En base a ello, como se muestra en la figura 7.1 (página 155) se han generado dos subdominios; uno intermedio, el L1, de 3 km de resolución y uno pequeño, el L2, con una resolución de 1 km. Las soluciones se han ejecutado de forma independiente, y los resultados de cada dominio exterior se reducen proporcionalmente para suministrar información a los bordes de cada dominio secundario o subdominio. De esta manera, la estructura a gran escala generada en L0 se pasa a la L1, y posteriormente a la L2. Antes de la reducción de escala, los resultados de L0 se han validado con detalle comparado sus resultados con las climatologías de diversas fuentes de datos. La validación ha sido una parte crucial en el desarrollo de la configuración del modelo, sobre todo para el acoplamiento entre los subdominios L1 y L2 con el dominio a gran escala L0.

Los remolinos a mesoescala generados por las islas que conforman el Archipiélago Canario se han resuelto en cada uno de los dominios acoplados. También hemos sido capaces de resolver los procesos a mesoescala/submesoescala en la cercana costa africana tales como el sistema de afloramiento costero con su sistema de filamentos que pueden interactuar con los remolinos generados por las islas (Figura 7.1). La región de afloramiento del noroeste de

África no se incluye en el dominio más pequeño L2 pero sí en el dominio intermedio L1 y en el dominio a gran escala L0. La solución para el dominio a gran escala es una solución multidecadal de un total de 50 años que proporcionará estadísticas sólidas para el sistema de reducción de escala hacia los subdominios intermedio (L1) y pequeño (L2). Asimismo esta solución es suficientemente robusta como para validarse con observaciones y para hacer los análisis de la dinámica de la región correspondientes. Básicamente se ha tomado el dominio L0 para hacer los estudios de la variabilidad estacional de los distintos procesos presentes en la Cuenca Canaria. Al ser mayor su costo computacional se ha integrado el dominio intermedio (L1) sólo a lo largo de 11 años. Sin embargo creemos que este rango de tiempo es suficiente para resolver la variabilidad estacional y mensual. La solución en el dominio pequeño (L2), la más costosa computacionalmente, sólo se ha integrado a lo largo de 3 años, lo que limita el hacer un análisis estadístico.

En el dominio circunscrito al Archipiélago Canario (L2) se han generado tres simulaciones correspondientes a los tres años de L2, aplicando un forzamiento de vientos de los meses julio, agosto y septiembre (de 2006) obtenidos a partir de un modelo numérico de la atmósfera (MM5). Los resultados de estas soluciones se incluyen en los resultados del capítulo 5.

Finalmente se ha utilizado el código numérico del *Regional Ocean Modelling System* desarrollado en la Universidad de California en Los Ángeles (ROMS-UCLA, Shchepetkin and McWilliams, 2005, 2009b).

7.5. Síntesis de resultados y discusión

El objetivo de este trabajo de tesis ha sido estudiar la circulación oceánica en la Cuenca de Canarias mediante un modelo numérico del océano. Con este fin, se ha diseñado e implementado una configuración de un modelo regional de alta resolución del océano (ROMS). A fin de lograr una resolución de $\mathcal{O}1$ km en las Islas Canarias, y también para asegurar un patrón válido de circulación a gran escala, se ha utilizado un enfoque de anidación unidireccional. La configuración se compone de tres dominios independientes, que presentan resoluciones cada vez más altas. Nuestro interés es la dinámica promedio de la región de estudio. Por lo tanto, se utiliza una combinación de forzamiento mensual y, cuando esté disponible, un forzamiento de alta frecuencia de las variables pronóstico en los contornos del modelo. En superficie siempre se utiliza un forzamiento mensual y la variabilidad interanual se omite en la aplicación del forzamiento. Los principales resultados de los capítulos 3, 4 y 5 se resumen a continuación.

7.5.1. Modelo y metodología (Capítulo 3)

En el capítulo 3, se propone una nueva formulación de la condición barotrópica de contorno en la frontera abierta (OBC) del modelo oceánico ROMS que minimiza la reflexión de ondas en las fronteras abiertas. Si se emplea extremo cuidado al crear los ficheros de forzamiento en las fronteras es posible conseguir soluciones numéricas de calidad minimizando los artificios

en los contornos empleando técnicas de anidamiento unidireccionales. Los componentes fundamentales del método de forzamiento aquí descrito es la interpolación exacta de los datos de la malla de menor resolución hacia la malla de mayor resolución, de forma que se asegure la congruencia entre la topografía, la máscara de tierra y una corrección a la velocidad normal en las fronteras, para garantizar la conservación del volumen en la malla de mayor resolución (Sección 3.2.3).

La OBC lleva implícita el uso de ficheros de forzamiento bidimensionales. La ventaja de emplear forzamientos bidimensionales frente a la región de *nudging* 3D es la capacidad de los primeros de proporcionar información de alta frecuencia a la malla interior a lo largo de un mayor periodo temporal. Esto posibilita que la malla interior sea forzada con una solución exterior que contiene varianza meso- e incluso submesoescalar en los campos de trazadores y velocidad.

Esta estrategia de acoplamiento ofrece un enfoque único y adecuado para estudiar fenómenos como la inestabilidad frontal y remolinos submesoescalares (Capet et al., 2008a; Thomas and Ferrari, 2008) en un campo realista del dominio interno, de mayor resolución (Capet et al., 2008c; McWilliams et al., 2009). Al promediar la solución externa en, por ejemplo, promedios mensuales (Dong et al., 2009) se retira la variabilidad mesoescalar en las fronteras, la cual es esencial para generar adecuadamente la variabilidad submesoescalar en el dominio interior. Cuando un dominio computacional es lo suficientemente grande, parte de la variabilidad de mesoescala puede ser recuperada por medio de la inestabilidad baroclina. Al hacer múltiples acoplamientos para conseguir cada vez dominios con mayor resolución (pero también menor extensión físico), es esencial conservar toda la variabilidad proveniente de la soluciones de la malla mayor.

Una limitación del trabajo del capítulo 3 es que aún falta conocer en detalle cuáles propiedades de la solución en la malla mayor son esenciales de transferir con exactitud a la malla fina. Los experimentos de sensibilidad realizados en el presente estudio sugieren la importancia de la conservación de volumen a través de las fronteras abiertas. Pequeñas correcciones a las velocidades en los contornos conllevan velocidades tangenciales anómalas en la región cerca de los contornos del dominio más fino. Otro tipo de perturbaciones producen respuestas menos acusadas en la solución de la malla interna. Sin embargo, la experiencia con experimentos similares para diferentes configuraciones de las mallas anidadas son poco concluyentes. Esto significa que en la actualidad, utilizando la metodología del capítulo 3, es posible obtener soluciones de alta calidad cuando redimensionamos una solución de ROMS a otra configuración de ROMS. Sin embargo, la capacidad de redimensionar datos arbitrarios como observaciones o soluciones calculadas por diferentes modelos no está tan avanzada. En estos últimos casos, las deficiencias de la metodología son evidentes, como muestra la figura 3.1 en la página 46. Se pueden ver corrientes en el borde de la solución de gran escala (L0), la cual fue forzada con una climatología mensual basada en observaciones.

Por último, mostramos que pequeños cambios en los datos del forzamiento del contorno pueden dar lugar a diferencias considerables en la solución de todo el dominio numérico (véase la figura 3.11 en la página 66). Incluso en casos en que la región de interés se encuen-

tre lejos de los contornos del dominio computacional, sigue siendo importante realizar un redimensionamiento adecuado de la solución en el dominio mayor hacia la malla más fina.

7.5.2. Variabilidad estacional en la Cuenca Canaria (Capítulo 4)

En el capítulo 4 se presentaron los resultados de una simulación obtenida con una modelo regional de alta resolución para la Cuenca Canarias. La atención se centró en la circulación media, el ciclo estacional y la variabilidad de mesoescala. La solución del modelo alcanzó el equilibrio estadístico después de unos años y estaba integrada por 50 años. Una comparación modelo/datos de las valores estacionales promedios y sus fluctuaciones muestra que el modelo puede alcanzar una representación creíble de la dinámica conocida de la región de Canarias.

El análisis de la solución se centró principalmente en la Corriente de Canarias (CanC). La preocupación principal está relacionada con el ciclo estacional de esta corriente entre Madeira y las Islas Canarias. La posición de la CanC está influenciada por estructuras anómalas de gran escala que se propagan hacia el oeste. Una anomalía anticiclónica se origina al norte de Cabo Ghir en otoño, mientras que por contra una ciclónica aparece al sur de Cabo Ghir en primavera. Por lo tanto, tienen una periodicidad anual. Ambas estructuras se propagan hacia el oeste a una velocidad similar de $\sim$3 cm s^{-1} (2,6 km $día^{-1}$), que es aproximadamente la velocidad de fase para una onda planetaria baroclínica (Rossby) en esta región. Debido a que son estructuras rotatorias, ambas estructuras tienen una componente de velocidad meridional en su contorno; esa componente hacia el sur es la Corriente de las Canarias.

La posición estacional de la corriente se define por el progreso de las estructuras. Nuestros resultados están de acuerdo con la relación de Sverdrup, de forma que gran parte del transporte de la Corriente de Canarias está relacionada con el viento. La estructura anticiclónica se origina en una región que experimenta un intenso rotacional ciclónico de la tensión del viento en el verano. La relajación del viento en otoño puede estar involucrada en la generación de esta estructura.

Las anomalías tienen una expresión en superficie, por lo que son visibles para los altímetros de satélites. Los campos de anomalía del nivel del mar obtenidos con el modelo y con altimetría son comparables, las estructuras ciclónica y anticiclónica aparecen como anomalías negativa y positivas, respectivamente. La posición de la Corriente de Canarias identificada en las observaciones históricas *in situ* también está de acuerdo con estos resultados. En cuanto a los trabajos sobre la separación de la CanC en invierno hacia al océano interior a $\sim$31°N (Pelegrí et al., 2006), esto puede estar relacionado con la anomalía anticiclónica generada al norte de Cabo Ghir en otoño. Estas comparaciones hacen de esto una descripción fidedigna del ciclo estacional de la Corriente de Canarias. Otro aspecto de las estructuras es que pueden estar involucrados en la generación y mantenimiento del filamento de Cabo Ghir (Hagen et al., 1996).

En cuanto al origen de la Corriente de Canarias, los estudios han demostrado que la Corriente de Azores mantiene la CanC a través de una rama hacia el sureste de Madeira. Sin embargo, una simulación del modelo a 15 años en que el transporte AzC se redujo en

un 85 % por el cierre del Estrecho de Gibraltar tuvo un impacto mínimo en la CanC. Su transporte media y su posición no ha cambiado significativamente. Esto apoya la idea que la CanC es impulsada por el viento, y sugiere que, en términos de la dinámica está sólo débilmente conectada a la Corriente de Azores.

La presencia de las Islas Canarias perturbando el paso de la Corriente de Canarias y la circulación de los vientos alisios conduce a la presencia de una variabilidad de mesoescala significativa. Si bien los remolinos generados por islas han sido frecuentemente observados y descritos a sotavento del archipiélago, según un artículo reciente, tales remolinos pueden tener un impacto a distancia (Sangrà et al., 2009). Datos de altimetría revelan una gran población de remolinos de mesoescala de larga duración, que ocupan un corredor zonal en torno a ∼26°N. El llamado *Canary Eddy Corridor* (CEC) se resuelve en la solución del modelo mediante el uso de un programa de seguimiento de remolinos basado en el parámetro Okubo-Weiss.

Las trayectorias de los remolinos proporcionan una nueva visión de los orígenes de los remolinos del CEC. Esta información no puede obtenerse a partir de los altímetros, debido a su incapacidad para resolver la región cercana a la costa. Los remolinos en el modelo tienen un origen mixto. Son generados principalmente cerca de la costa, en lugar de en las islas. La generación de la isla llega a ser importante sólo en verano. Los campos de energía cinética turbulenta del modelo confirman estos hallazgos.

Como trabajo futuro la solución de este modelo será empleada para forzar modelos de mayor resolución en el dominio de las Islas Canarias. El enfoque será el de la variabilidad de la corriente incidente en las islas, y el impacto que esto tiene sobre la variabilidad de mesoescala y submesoescala en la región.

7.5.3. Modelación de alta resolución en las Islas Canarias (Capítulo 5)

En este capítulo se ha descrito la variabilidad mesoescalar y cercana a la submesoescalar en las Islas Canarias mediante un modelo oceánico regional con una configuración de anidamiento unidireccional. Para ello se ha integrado el modelo en los dominios a media escala (L1, 3 km de resolución) y pequeña escala (L2, 1km de resolución) con un forzamiento atmosférico bajo condiciones medias estacionales de alta y baja resolución. En los contornos externos se han tomado las soluciones de los modelos de mayor escala. A continuación se discuten las principales características de la circulación de mesoescala de la solución de 3 km (Sección 5.3).

Mientras que las climatologías indican que el flujo incidente sobre el archipiélago procede del nordeste, la corriente simulada muestra una alta variabilidad. En verano el flujo incidente sobre Gran Canaria llega del noroeste con un transporte próximo a 0,5 Sv en los primeros 200 m de la columna de agua. Al sur del archipiélago, la estela se caracteriza por una zona de una alta dinámica según se observa en las líneas de corriente. En primavera y verano se desarrolla una intensa estructura ciclónica entre Gran Canaria y la costa africana. En mar abierto se origina, en cambio, una circulación anticiclónica más intensa en verano y

en otoño. Ello da lugar a la inversión del flujo en el Pasaje de Lanzarote tal como ha sido observado en diferentes trabajos observacionales (Hernández-Guerra et al., 2003). Las líneas de corriente de las dos células se alargan hacia la costa al sur de las islas en otoño, lo cual coincide con una extensión zonal de la EKE observada en la solución del dominio a gran escala L0 (Figura 4.19 on page 105). En relación a ello, los experimentos de seguimiento de remolinos de la sección 4.6.3 (página 106) muestran que una gran proporción de los remolinos de larga duración se generan fuera de la costa de África en otoño y invierno. Estos remolinos se generan posiblemente debido a la combinación de la inestabilidad barotrópica asociada con el flujo de la corriente hacia la costa y la inestabilidad baroclina asociada al frente del afloramiento costero africano.

Volviendo al Pasaje de Lanzarote los transportes, tanto en orden de magnitud como en sentido, están en concordancia con las observaciones de que se disponen. La inversión del flujo se produce durante el otoño en la capa de Agua Central (0 - 500 m). Ello sugiere que la relajación local de los vientos del afloramiento, que se produce en el otoño, no es la causa de la inversión del flujo. De hecho, el modelo muestra que el *jet* costero del afloramiento persiste durante todo el año sobre la plataforma y el talud de África. Este *jet* va ligado a una corriente subsuperficial que fluye hacia el polo pegada al talud continental y centrada a unos 250 metros de profundidad (Barton, 1989).

En las capas profundas de las secciones de los pasajes interinsulares se observan, sorprendentemente, intensas corrientes anticiclónicas a lo largo de los flancos de las distintas islas. Así, por ejemplo en la parte sur de Gran Canaria se observan en estas capas velocidades superiores a 0,05 m s^{-1}, presentes durante todo el año entre 800 metros y el fondo (Figura 5.7). Esta circulación anticiclónica podría estar asociada a columnas de Taylor debido a la interacción con la topografía insular (Huppert and Bryan, 1976; Goldner and Chapman, 1997) o a una circulación anómala asociada a islas, tal como se describe en Chopra (1973). A este respecto, véase el Apéndice C para más ejemplos de estos flujos profundos anticiclónicos.

Pasemos ahora a discutir el régimen de mesoescala obtenido a partir de la integración del modelo a lo largo de tres años en el dominio de pequeña escala L2 (Sección 5.4 on page 127). Los estudios observacionales en el archipiélago se han restringido a la mesoescala, no existiendo a nuestro conocimiento estudios observacionales en el rango de la submesoescala. De hecho, existe un sólo estudio donde se estudian los efectos biológicos de las ondas internas de marea en el talud insular de Gran Canaria (Sangrà et al., 2001). Tal como se demuestra en este estudio, los procesos a submesoescala pueden modular fuertemente la componente biológica del sistema marino al promover la accesibilidad a los nutrientes y a la luz mediante flujos verticales. En este sentido se ha observado que en los frentes de submesoescala se pueden dar velocidades verticales de 100 m $día^{-1}$, un orden de magnitud mayor que en los frentes de mesoescala (Thomas et al., 2008). Esto puede proporcionar una vía de intercambio significativa entre las capas profundas ricas en nutrientes y la zona fótica. Otro proceso importante relacionada con la submesoescala es la concentración superficial de propiedades. Capet et al. (2008a) demostraron que la convergencia asociada con la submesoescala origina corrientes superficiales que concentran partículas pasivas, lo que puede tener implicaciones

importantes para trazadores pasivos o semi-pasivos como el meroplancton. Estas agregaciones puede afectar a la producción biológica, limitando el acceso a los nutrientes y a el oxígeno.

Retomando el tema que nos ocupa, el flujo incidente a la isla de Gran Canaria obtenido por nuestra modelo, diferencia entre dos regímenes distintos para la generación de remolinos por la isla. En el primer año de integración, la solución muestra un intenso flujo incidente en verano que origina un pulso en la generación de remolinos por la isla. En los dos años siguientes el flujo incidente es del noreste mas débil, lo que conduce a una población menor de remolinos a lo largo del año. En muchos de los experimentos se ha observado el nacimiento de remolinos en La Isleta que es una pequeña península localizada en el extremo noreste de la isla de Gran Canaria. No se tienen evidencias observacionales de generación de remolinos en esta región dado que, como ya se ha comentado, no se han desarrollado estudios observacionales en el rango a mesoescala. En octubre del año 37 de la simulación se observa la generación de tres anticiclones sucesivos (A1, A2, A3) originados por La Isleta, coincidiendo con un periodo de flujo incidente del noroeste (Figura 5.15). El análisis de su estabilidad inercial concluye que estos remolinos rotan demasiado rápido y son posiblemente inercialmente inestables disipándose en un lapso de tiempo relativamente corto. La distribución de velocidades verticales asociadas a estas estructuras muestra velocidades verticales bastantes altas en su periferia, especialmente en sus bordes costeros. En el remolino A3 se observaron velocidades de afloramiento/hundimiento en su borde costero del orden de 30 m día^{-1}. Aunque sea un evento transitorio localizado, los transportes verticales asociados pueden tener consecuencias significativas en la producción biológica incluso en escalas de tiempo cortas (Hernández-León, 1991). También se observaron el nacimiento de este tipo de remolinos en el extremo norte de Tenerife.

La generación de remolinos de submesoescala por cabos y penínsulas es una tema ampliamente investigado (Signell and Geyer, 1991; Aiken et al., 2002, 2003; Edwards et al., 2004; McCabe et al., 2006). El mecanismo de generación de los remolinos de La Isleta puede ser atribuido a la fricción con la topografía que da lugar al despegue de la capa límite del obstáculo y la consiguiente generación de remolinos asociado a una fuerte estratificación y cizalla (Edwards et al., 2004). En la figura 5.18 se ilustra cómo la mayor frecuencia de generación de anticiclones por la isleta se produjo en verano y principios de otoño con condiciones de alta estratificación y flujo incidente. En diciembre-enero del año 35 ocurre una anomalía, donde nuestra hipótesis es que los remolinos se generan debido al efecto conjunto de una fuerte cizalla y/o inestabilidades de la capa de mezcla. En su parte occidental, La Isleta es también una fuente de vorticidad ciclónica cuando el flujo incidente es del noreste (Figura 5.11). Todo ello sugiere que los cabos y penínsulas de las islas que configuran el archipiélago pueden contribuir significativamente a la variabilidad a mesoescala de la región y por ende en la producción de vorticidad.

En invierno se observaron eventos de turbulencia a pequeña escala lo que sugiere un ciclo estacional en el régimen de la submesoescala. Dado que muchos vórtices de submesoescala se originan lejos de la zona costera puede haber otra causa diferente a la topográfica asociada

con su generación. En este sentido en un estudio de la variabilidad a submesoescala en la plataforma continental argentina realizado por Capet et al. (2008a), se observó una intensa variabilidad a mesoescala también en invierno. Estos autores la atribuyeron a inestabilidades de la capa de mezcla vertical y los gradientes de densidad a través de la plataforma. Thomas et al. (2008) observaron que las reestratificaciones asociadas a dichas inestabilidades y sus correspondientes velocidades verticales pueden tener un fuerte impacto sobre la producción biológica.

En lo referente al forzamiento del viento en el dominio L2 a parte de los datos climatológicos SCOW (resolución de 30 km) se ejecutó el modelo atmosférico MM5 con una resolución de 6 km. La sensibilidad del modelo a la resolución del campo de vientos es crítica. En este sentido las soluciones con el MM5 aumentaron significativamente la vorticidad y consiguiente variabilidad en el dominio. Ello está relacionado con una mayor cizalla del viento y consiguiente bombeo de *Ekman* al forzar el modelo con los resultados del modelo MM5 que puede ser de un orden de magnitud mayor que el obtenido con la climatología de menor resolución SCOW. A modo de ejemplo en la figura 5.21 en la página 137 se observa cómo se genera un remolino ciclónico al suroeste de Gran Canaria con el forzamiento MM5 que no se observa con el forzamiento SCOW.

7.5.4. Perspectivas de la configuración del modelo y enfoque

Es importante incluir en este estudio las limitaciones/deficiencias y rango de aplicabilidad inherentes a las aproximaciones vinculadas a nuestro modelo y consiguientes razonamientos. Algunos ya se conocían *a priori* pero otros han surgido a lo largo del desarrollo de este estudio.

- Enfoque con climatologías (campos medios): Al adoptar un enfoque climatológico viene implícito que se excluyen las escalas sub-mensuales e interanuales. Así por ejemplo en el caso del campo de viento (forzamiento atmosférico), oscilaciones de una semana podrían modificar significativamente la estructura del afloramiento costero, hecho que no se considera al ser la escala temporal resultado de un promedio mensual. En este sentido algunas observaciones han mostrado que el sistema de afloramiento puede reaccionar a pulsos de vientos semanales especialmente en verano cuando se intensifican los Alisios. A escala interanual el forzamiento climatológico no es capaz de considerar variabilidades decadales como es el caso a las asociadas por ejemplo a la Oscilación del Atlántico Norte (NAO).

- Anidación de dominios unidireccional: En este caso las soluciones de los dominios de mayor resolución (L1, L2) no interactúan con la solución respectiva del dominio de menor resolución (L0, L1) como sería el caso de un anidamiento bidireccional. Esto puede ser importante para la estructura a gran escala, como se ha demostrado mediante el uso de una configuración bidireccional para el modelo anidado para la retroflexión de la Corriente de las Agulhas en la costa sudafricana (Biastoch et al., 2008). En la

Cuenca de Canarias, la anidación de dos vías aplicada en el Golfo de Cádiz, podría mejorar el flujo de salida del Mediterráneo y posterior difusión de la MW.

- Artefactos relacionados con la frontera abierta: El problema de los artefactos de la frontera abierta no se ha resuelto para el dominio principal (L0). En la figura 1.1 (página 4) se mostraron corrientes de borde anómalas a lo largo de la frontera occidental del dominio a gran escala (L0). Estos artefactos aparecen cualquiera que sea la fuente de datos externa (por ejemplo salidas de un modelo de circulación global en lugar de ROMS) utilizada para forzar los contornos abiertos. Una posible solución, al menos para minimizar este problema, es agrandar el dominio de escala sub-cuenca a escala de cuenca lo que reduciría el área de la frontera abierta.

- Resolución vertical: El enfoque mas común en el diseño de una configuración del ROMS es aumentar la resolución vertical en las capas superficiales. Ello provoca a veces filtrar demasiado la dinámica de las capas mas profundas respecto a las superficiales. Esto puedo ser, en determinados casos, crítico dado que la batimetría puede ejercer un importante control sobre la circulación de superficie, transmitiéndose la dinámica de las capas profundas hacia las capas superficiales como de hecho ocurre en la región de la Dorsal Centro-Atlántica (Bower and von Appen, 2008). La solución del dominio a gran escala (L0) no resuelve la capa límite de fondo en aguas profundas, de modo que pudiéramos estar filtrando importantes procesos que podrían afectar a las capas superficiales remotas. En las soluciones de alta resolución (dominios L1 y L2) la resolución vertical es mayor que en la del dominio a gran escala (L0) y este posible filtraje debería ser menor. Al no haberse hecho un análisis de sensibilidad a la resolución vertical del modelo desconocemos su posible efecto.

- Resolución de viento: La climatología global del campo de viento SCOW, es actualmente la más precisa entre las distintas climatologías globales del campo de vientos disponibles. Se basa en los 8 años de datos del campo de vientos global de 0,25° de resolución obtenidos por el dispersómetro SeaWinds a bordo del satélite QuikSCAT. En el capítulo 5 (página 136) se ha mostrado que la resolución del campo de vientos puede ser crítica en la inyección de vorticidad relativa al océano a través del mecanismo de bombeo de *Ekman*. De esta forma nuestras soluciones se podrían mejorar si se dispusiese de climatologías de resolución superior a la SCOW.

- La configuración del modelo no considera entradas costeras de agua dulce asociadas a ríos. El caudal de los ríos en el noroeste africano es mínimo, pero pueden ser dinámicamente importante frente a la Península Ibérica (Peliz et al., 2002).

7.6. Conclusiones

Las principales conclusiones que se derivan de esta tesis se dividen en dos secciones que reflejan las contribuciones entre el capítulo 3, y los capítulos 4 y 5. El contenido del capítulo

3 se refiere a los procedimientos de elaboración de modelos numéricos con fronteras abiertas. Los capítulos 4 y 5 son el resultado de la aplicación de los procedimientos anteriores al dominio de la Cuenca de Canarias, lo que permite que se lleve a cabo el estudio oceanográfico.

Contribución oceanográfica

- La solución del modelo de gran escala nos proporciona una visión de la circulación de la Corriente de las Canarias al norte de las Islas Canarias. El camino de la corriente está condicionado por la propagación hacia el oeste de las ondas planetarias (Rossby) que se originan cerca de la costa africana cada año. El ciclo estacional de la posición zonal media de la Corriente de Canarias simulada en 32°N concuerda bien con las estimaciones publicadas. El promedio de transporte está en el rango de ∼3 a 6 Sv, el cual está igualmente de acuerdo con las observaciones, siendo el transporte pico en verano. La anomalía en la altura de la superficie libre del mar obtenida con altimetría confirma la existencia de las ondas planetarias.

- La Corriente de Canarias no presenta una alta sensibilidad a la variabilidad en la Corriente de Azores. Un experimento de sensibilidad donde la Corriente de las Azores fue eliminada por el cierre del Estrecho de Gibraltar ha tenido poco efecto sobre la Corriente de Canarias: el transporte estacional y las vías de circulación son esencialmente los mismos con y sin la Corriente de las Azores.

- El origen de los remolinos de larga vida que constituyen el *Canary Eddy Corridor* (CEC) de ∼26°N varía con la estación. En verano, los remolinos son predominantemente generados por las islas. El resto del año, sin embargo, los remolinos de la CEC se forman frente a la costa de África, sobre todo en otoño e invierno. La incapacidad de la altimetría para resolver las anomalías de superficie cerca de la costa impide la confirmación de este resultado por el momento.

- Se ha descrito la circulación estacional de mesoescala en las Islas Canarias. La corriente incidente que llega a Gran Canaria es predominantemente del noroeste en verano, en lugar del noreste que se determina a partir de las climatologías de baja resolución. En la estela del archipiélago canario la circulación es débilmente ciclónica durante gran parte del año. Un poco más al sur (∼1°) se hace presente una celda anticiclónica intensa durante todo el año. En el otoño se produce la reversión estacional del flujo en la costa africana, al parecer como resultado de la interacción entre la celda anticiclónica y la intensificación en verano de la circulación ciclónica.

- La inversión del flujo ocupa la capa de Agua Central en todo el Pasaje de Lanzarote, lo que sugiere que sea improbable la relajación local de los vientos del afloramiento como mecanismo para la inversión.

- Los cabos en las islas, especialmente en Gran Canaria, son importantes fuentes de vorticidad. Con frecuencia se observan eventos de generación de remolinos ciclostróficos

en La Isleta, en el norte de la isla. Los transportes verticales en la periferia de estos remolinos son significativos, con posibles implicaciones biológicas.

- En invierno, la submesoescala se caracteriza por episodios de inestabilidad en la capa de mezcla, al igual que en otras corrientes de frontera este y en otras regiones de plataforma.

Aspectos del modelaje

- A pesar de la aparición de los modos bidireccionales, el enfoque de anidación unidireccional es todavía un enfoque valioso en la modelización del océanos a nivel regional.
- El proceso de la creación de los ficheros de forzamiento es fundamental. Si no se enfocase con cuidado el forzamiento de los contornos, se introducirían artificios en la solución del modelo.
- En el contexto de ROMS a ROMS, esto es, siempre que ambos modelos anidados se hayan desarrollado con ROMS, la metodología para crear los ficheros de forzamiento de los contornos descrita en esta tesis produce buenos resultados.
- Experimentos con perturbaciones sugieren que el aspecto más crítico para obtener una solución correcta es la aplicación de la conservación de volumen en las contornos.
- La metodología es menos fiable cuando se combinan soluciones de ROMS con otras soluciones generadas con otros esquemas de simulación numérica.

Los resultados del modelo mencionados anteriormente sirven para validar la elección de un enfoque climatológico para las cuestiones abordadas en esta tesis, en contraposición a un estudio basado en escalas interanuales o de eventos. Esta configuración climatológica pretende simular el estado medio de un sistema, incluyendo su variabilidad intrínseca que se plantea en el modelo. El estado medio y la fluctuación de la circulación en la Cuenca de Canarias presentados en este trabajo se ha validado mediante la comparación con una serie de variables observadas. Por lo tanto, esto puede dar una confianza considerable a las conclusiones oceanográficas extraídas de los resultados del modelo.

7.7. Futuras líneas de investigación

Este trabajo es el punto de partida para un importante número de trabajos futuros a la vista de las soluciones del modelo presentado en esta tesis. La malla principal cubre gran parte del noreste del Atlántico y tiene una resolución ideal para la reducción de escala a resoluciones muy altas, con un número mínimo de etapas de anidación. Los resultados del modelo podrían ser utilizados para apoyar los siguientes estudios:

- En Gran Canaria: un estudio a escala submesoescalar. Está prevista una malla de 300 m.

- En el afloramiento noroeste africano: actualmente ya se está trabajando en un modelo utilizando una solución de reducción de escala de L0 en busca del filamento de Cabo Ghir (Troupin et al., 2009b).

- En frentes tales como la Zona Frontal de Cabo Verde: Steven Herbette (comunicación personal) ha comenzado a trabajar en la mezcla en el CVFZ utilizando una solución de reducción de escala de L0.

- En otros archipiélagos insulares de la Macaronesia: Rui Caldeira (comunicación personal) está trabajando en una reducción de escala de L0 a una malla de 2 km en Madeira.

- En el Golfo de Cádiz y el talud portugués: el estudio de la generación de *Meddies* submesoescalares en esta región. Este estudio servirá para complementar las observaciones de alta resolución de *Meddies* realizadas con perfiles de sísmica de reflexión (Buffett et al., 2009; Klaeschen et al., 2009).

- En estudios de la advección de larvas: las salidas de velocidad del modelo pueden ser utilizados por los diferentes modelos basados en individuos (IBM) para estudiar la advección de larvas y otras partículas pasivas o semi-pasiva. En las Islas Canarias se ha aplicado una IBM usando velocidades obtenidas de una versión anterior del dominio L1 (Brochier et al., 2008, 2009). El objetivo de los experimentos publicados es caracterizar la llegada de las larvas de sardina en Gran Canaria, que se ha advectado hacia el archipiélago en filamentos de afloramiento originarios entre los cabos Bojador y Juby.

- En estudios biogeoquímicos (BGC): ROMS incluye un módulo *ecosystem*/BGC de tipo NPDZ (Gruber et al., 2006). Para estudiar el afloramiento de Perú, ROMS también ha acoplado el módulo BGC PISCES (Echevin et al., 2008, y las referencias incluidas). El modelo físico que se presenta en este trabajo puede servir de base para estudiar el acoplamiento físico-biogeoquímico en la región de las Islas Canarias.

- En estudios de los montes submarinos: en la Cuenca de Canarias existen numerosos montes submarinos, y hay un creciente interés por el estudio de sus influencias tanto físicas y biogeoquímicas (Bashmachnikov et al., 2009; Mohn et al., 2009). La configuración actual se podría utilizar para apoyar los estudios de *Meddies* y sus interacciones con los montes submarinos, así como estudios interdisciplinares con la inclusión de módulos de BGC.

- En estudios de variabilidad interanual: La malla L0 puede ser utilizada para un estudio interanual cuando el problema estudiado no queda resuelta con soluciones climatológicas. Por ejemplo permitiría incluir el efecto de los cambios en la Oscilación del Atlántico Norte.

- En mejora de las soluciones al modelo: Las soluciones actuales se podrían mejorar mucho mediante el uso de datos de forzamiento superficial obtenidos de un modelo atmosférico regional, tales como WRF (*Weather and Research Forecasting model*, un sucesor de MM5) (Skamarock et al., 2008). La ventaja de la utilización de los vientos MM5 para la configuración de L2 en las Islas Canarias se ha demostrado en la sección 5.4.5 (página 136). Caben esperar mejoras similares para el afloramiento costero.
- En la generación de una malla principal mayor: la creación de una solución principal mayor permitiría cubrir el Océano Atlántico y sustituiría a L0.

A. Seasonal study

In this section, further results related to the L0 modelling work of Chapter 4 are presented. This additional material is relevant to the validation of the model (Section 4.3 on page 82), but is not expected to be included in the published paper because of lack of space.

A.1. Model spin-up

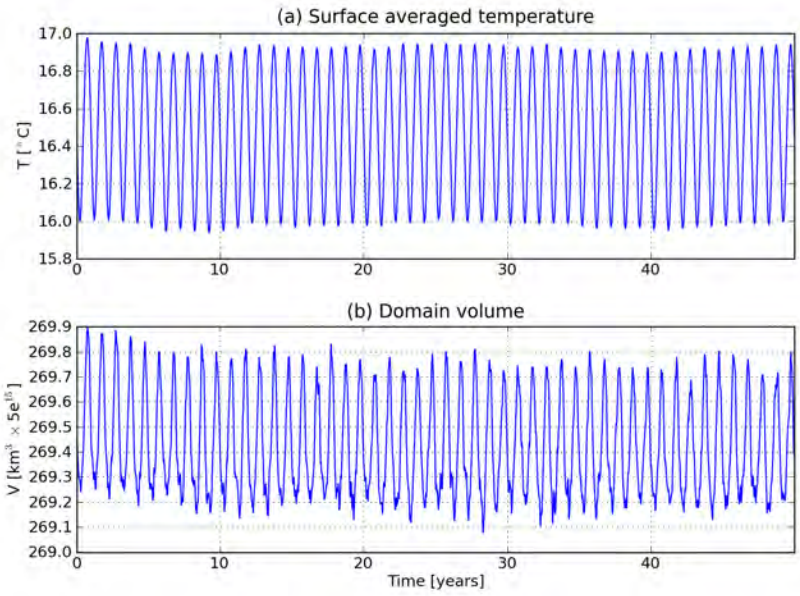

Figure A.1.: Time evolution of (a) the surface-averaged temperature (°C) and (b), the domain volume ($km^3 \times 5e^{15}$) from the L0 model solution.

Figure A.1 shows the evolution of the surface-averaged temperature and the domain volume from the 50-year L0 solution. The seasonal cycle is evident in both variables. The temperature (Figure A.1a) steadily decreases during the first 10 years from an initial high at initialisation. It then increases sharply until year 12, whereafter it remains relatively stable. The first 12 years are in contrast to the salinity, which increased during this time (Section 4.3.1 on page 83). The domain volume (Figure A.1b) decreases similarly to the temperature over the first 10 years of simulation, but does not change significantly for the rest of the simulation.

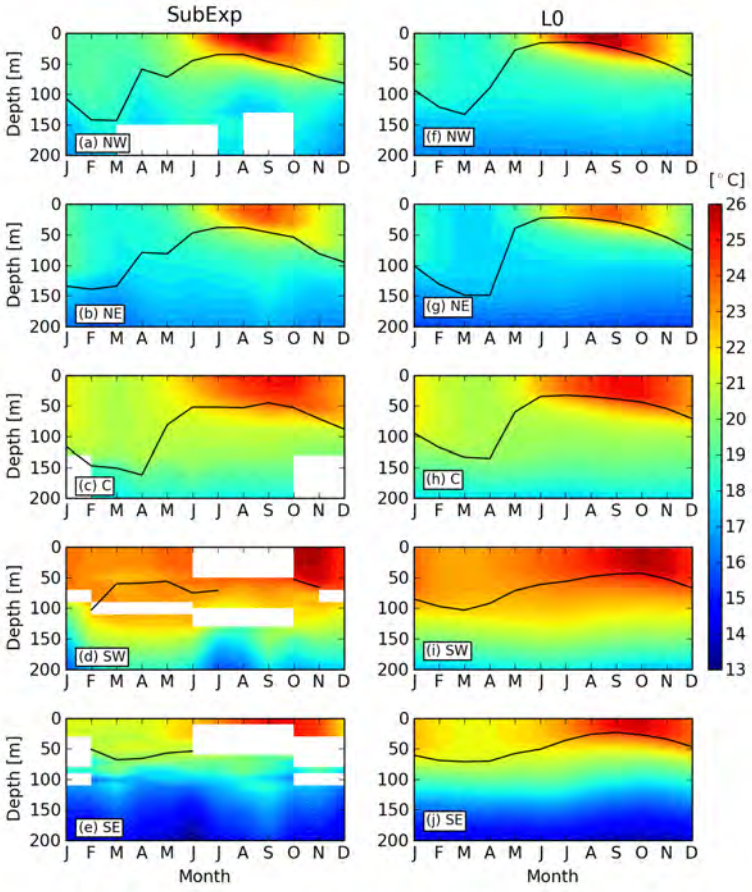

Figure A.2.: Comparison of monthly mean temperature in the top 200 m from the five SubExp moorings (left) and L0 (right). Periods/depths with missing SubExp data are left blank. The mixed layer depth is plotted in black. See Figure 2.1 on page 12 for the locations of the SubExp moorings.

A.2. Subduction experiment moorings

Figure A.2 compares monthly means of temperature from the five Subduction Experiment (SubExp) sites with L0 temperatures taken from the same locations. The plots show that the model has a good response to local forcing, and that spatial and temporal variability of the mixed layer depth is well simulated.

The temperature records show seasonal evolution that penetrates down to about ∼100 m in both the moorings and L0. A shallow seasonal thermocline grows in spring and summer, followed by its erosion in autumn and winter. A time delay between the warming of the upper thermocline, which continues to warm after SST has begun to cool, and the surface layers, is evident at the central and northern locations.

Mixed layer depths are also plotted in Figure A.2, estimated following the criterion of de Boyer Montégut et al. (2004). The spikes in SubExp at NW and NE in April are both

likely to be caused by the passing of eddies; eddy variability was dominant in the moored velocity records at NE. Weller et al. (2004) noted that, contrary to expectation, winter mixed layer depth does not shoal significantly to the south in the SubExp records. This behaviour is seen also in L0. The Trade winds at the central and southwestern moorings drive *Ekman* pumping, deepening the mixed layer at C and NW. At SE, the winter mixed layer depth is associated with upwelling and shoaling towards the African continent. Mixed layer temperature, however, shows a clearer spatial trend, with the temperature at NW and NE the coldest in winter, and that at SW the warmest for much of the year.

This figure indicates that the model performs exceptionally well in terms of simulating the offshore seasonal thermocline.

B. MM5 atmospheric model

In Chapter 5, several ocean model simulations were made where the surface momentum stress was provided by a high-resolution atmospheric model, rather than the QuikSCAT-based SCOW wind stress climatology of Risien and Chelton (2008). In this section, a brief description of the atmospheric model and related methodology is presented, as well as a validation of the results. In addition, we make note of the pitfalls related to poor choice of interpolation method when interpolating data between atmospheric and ocean model grids.

B.1. Methodology

The MM5 wind stress used in the L2 simulations of Chapter 5 were created using the Penn State/NCAR mesoscale model version 5 (MM5; Grell et al., 1995), release 3.6.0. Figure B.1a shows the boundaries of the three coupled MM5 domains. A 6-km domain centred over the Canary Island archipelago is nested within an 18-km domain, which is likewise nested within a 54-km domain that spans the northeast Atlantic. Two-way nesting was used for the two interior domains. Also shown is the ROMS L2 domain, which fits within the inner MM5 grid. Figure B.1b shows the mean wind stress curl on 10 July 2006 from the 6-km solution. All seven of the Canary Islands are well resolved, as well as the African coast between ∼24° - 29°N. Bands of alternating positive and negative curl downstream of the islands correspond to shear lines in the wind field, which arise as the airflow is forced around the islands and through the channels which separate them. The easternmost islands, Fuerteventura and Lanzarote, produce a weaker wake because of their lower altitude.

Each MM5 domain has 29 vertical levels, with the vertical grid stretched so as to place the highest resolution in the lower troposphere. For the 54-, 18-, and 6-km domains the dimensions are, respectively, 77×63, 102×102 and 159×150. In the outer two domains, a Kain-Fritsch 2 cumulus parameterisation scheme is used. In the 6-km domain, only explicitly resolved convection is permitted. In all domains, we use the MRF boundary layer scheme, Dudhia simple ice microphysics, and a radiation scheme simulating longwave and shortwave interactions with clear-air and cloud.

The boundary conditions come from the National Center for Environmental Prediction (NCEP) Global tropospheric analysis data at $1° \times 1°$ resolution (Kalnay et al., 1996). The time period covered is from July to mid-October 2006, with outputs saved every 1 hour. Throughout this period, MM5 was initialised every 3 days at 18:00 and run for 78 hours, with the first 6 hours being discarded as model spin-up. The interior boundary conditions and sea-surface temperatures were updated at each initialisation, with the lateral boundary

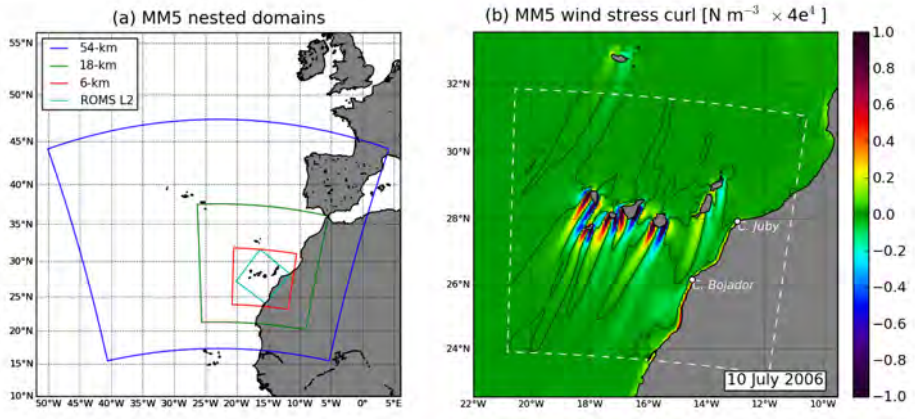

Figure B.1.: (a) MM5 domain boundaries. Also shown is the ROMS L2 boundary, which is forced with the MM5 wind stress (Chapter 5). (b) Mean normalised wind stress curl on 10 July 2006 from the MM5 simulation. The white dashed line shows the boundary of the inner (6-km resolution) MM5 domain. The zero-curl line of the inner solution is contoured in black.

conditions updated continuously throughout the run. Thus the simulation in the 6-km nest acts as a reconstruction of the local atmospheric conditions based on known large-scale atmospheric conditions.

Wind stresses are obtained from the MM5 output u- and v-wind velocity components at 10 m above the sea surface. The stresses are calculated following the bulk aerodynamic formula (Gill, 1982):

$$\tau = \rho C_d \mid U \mid U, \tag{B.1}$$

where τ is the stress vector, $\rho = 1.22$ kg m^{-3} is the air density, U is the wind velocity, and $\mid U \mid$ is the wind speed. C_d is a dimensionless drag coefficient calculated following Yelland and Taylor (1996) and Yelland et al. (1998): for lower wind speeds the data are fitted by the relationship

$$1000C_{d10m} = 0.29 + \frac{3.1}{U_{10m}} + \frac{7.7}{U_{10m}^2} \qquad \left(3 \leq U_{10m} \leq 6\ m\,s^{-1}\right), \tag{B.2}$$

where U_{10m} is the 10-m neutral wind speed. At higher wind speeds

$$1000C_{d10m} = 0.50 + 0.071 * U_{10m} \qquad \left(6 \leq U_{10m} \leq 26\ m\,s^{-1}\right). \tag{B.3}$$

Once calculated, the wind stresses are interpolated to the ocean model grid.

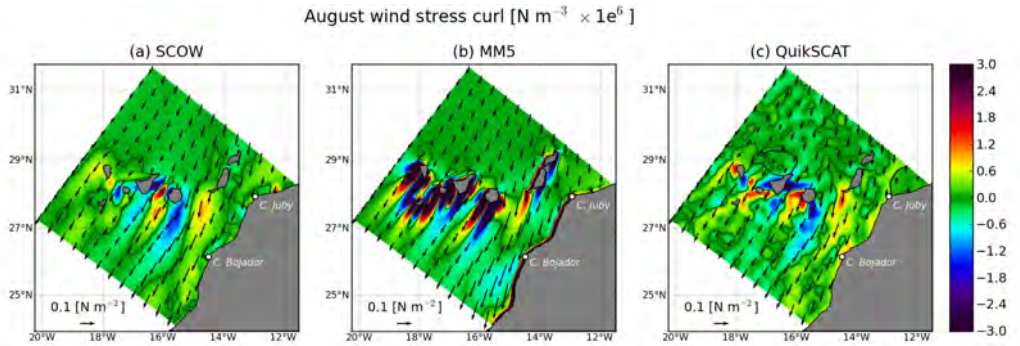

Figure B.2.: August wind stress curl and wind stress from (a) SCOW, (b) modified MM5 and (c) QuikSCAT. SCOW is an average of eight years (1999 - 2007). MM5 and SSMI both correspond to August 2006.

B.2. MM5 validation

Here a brief validation of the MM5 wind simulations is presented, using data from the QuikSCAT scatterometer, and from wind stations on Gran Canaria.

Comparison with QuikSCAT

Figure B.2 compares three August-averaged fields of the wind stress curl: (a) and (b), computed from SCOW and MM5[1], respectively. Also shown are vectors representing the wind stress components from which the curl is derived. Both SCOW and MM5 are used to force the L2 model configuration in Chapter 5. Figure B.2c shows August 2006 wind stress curl and wind stress from SSMI QuikSCAT[2]; we assume this to be the true August 2006 wind field. The wind stress curl of the SCOW and MM5 products match closely in the open ocean. At and downstream of the islands, and close to the coast, there are strong differences as expected. However, downstream of Cape Bojador (∼25.5°N, 15.7°W), MM5 shows a large patch of anticyclonic curl, whereas SCOW at this location is cyclonic. To determine if MM5 is correctly simulating the August 2006 wind field at this location, we consider the August 2006 QuikSCAT mean of Figure B.2c. Owing to its smaller sample size, the field is considerably noisier than SCOW. Off Cape Bojador the QuikSCAT curl is largely cyclonic, and therefore is more similar to SCOW than MM5.

The SCOW and MM5 wind stresses show good agreement in both magnitude and direction. The largest differences are seen near to the African coast, where the MM5 wind stress magnitude tends to be larger. In the Cape Bojador region identified above, the MM5 vectors have a slight onshore component that is not seen in SCOW (this is more evident in fields of the u-component of the wind stress, where MM5 has a pronounced positive anomaly). In

[1] See Section 5.2.3 on page 119 for an explanation for the choice of averaged rather than instantaneous MM5 wind stresses to force the L2 ocean model configuration.

[2] SSM/I data are produced by Remote Sensing Systems and sponsored by the NASA Earth Science MEaSUREs DISCOVER Project. Data are available at www.remss.com.

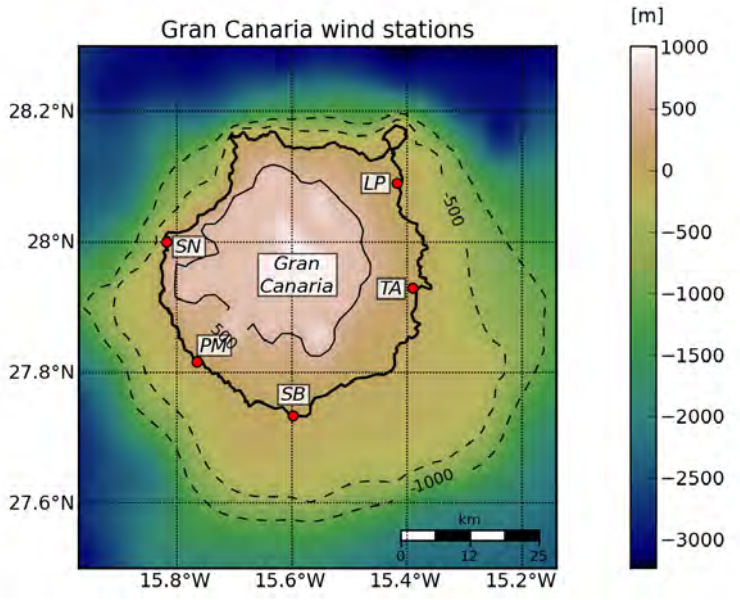

Figure B.3.: Map showing locations of wind stations on Gran Canaria. SN - San Nicolás, PM - Puerto de Mogán, SB - San Bartolomé de Tirajana, TA - Telde/Aeropuerto de GC, LP - Las Palmas de GC. Topographic data from GEBCO (Hunter and Macnab, 2003).

July and September the MM5 vectors have a similar onshore bias to that of August.

Overall, MM5 performs reasonably well when judged against the QuikSCAT products. There are some differences in the wind stress fields near to Cape Bojador, where MM5 has an onshore bias. MM5 produces a more intense island wake, with strong boundary layer shear, which is the reason we want to use it to force the model. QuikSCAT is unable to adequately resolve the nearshore wind structure, because of the resolution of the scatterometer and missing data nearshore.

Comparison with meteorological stations

The locations of five meteorological stations located at coastal regions on Gran Canaria are shown in Figure B.3. The data, provided by AEMAT[3], are hourly records of wind speed and direction; the directions are grouped into 10-degree bins. Each time series begins 1 July 2006 and ends 31 September 2006, and contains 2208 data points. The stations are all coastal, lying inland not more than a few kilometres from the shore. The position and altitude of each station is given in Table B.1. The wind patterns at individual stations are expected to display distinct patterns that depend largely on their location Gran Canaria, which may be generalised for all of the Canary Islands as follows: Sites on the northern parts of the islands display moderate north/northeasterly winds; sites on the flanks (east or west) of the islands display intense persistent winds flowing parallel to the coast; sites on the southern

[3]Spanish Meteorological Agency (La Agencia Estatal de Meteorología).

Table B.1.: Details of the meteorological stations on Gran Canaria that provide wind data for the validation of the MM5 model outputs.

Station	Longitude [°W]	Latitude [°N]	Altitude [m]
San Nicolás	15.49	28.00	10
Puerto de Mogán	15.45	27.49	10
Aeropuerto de G. C.	15.23	27.55	24
Las Palmas de G. C.	15.25	28.05	56
San Bartolomé de Tirajana	15.35	27.44	25

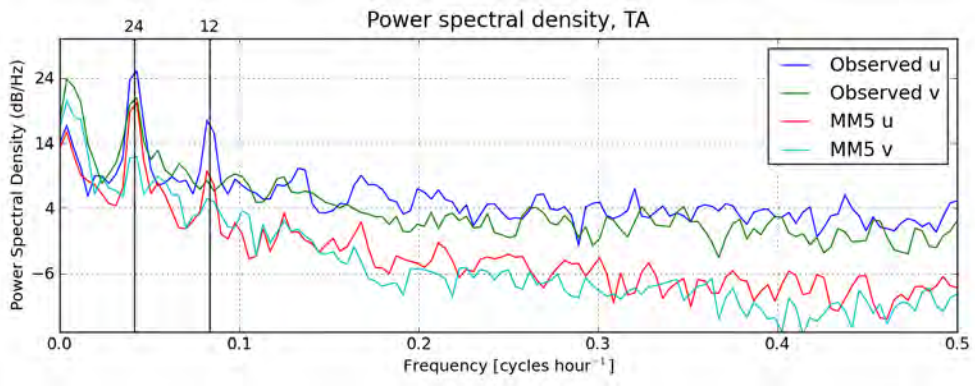

Figure B.4.: Power spectra for the u- and v-wind velocity components from the observations at Telde/Aeropuerto (TA) and from the corresponding location in the MM5 model output. Periods of 12 and 24 hours are shown.

parts of the islands display weak winds with considerable variability in direction. Other local factors may also influence the winds, such as the presence of large ravines that extends inland normal to the coastline, a notable example is a 15-km ravine (Barranco de la Aldea) at San Nicolás.

To identify possible periodic components in the data, power spectra for the hourly data for each series are calculated. Power spectra for the wind station records at the Gran Canaria airport location (TA) are shown alongside those from the co-located MM5 records in Figure B.4. The spectra, from both the observations and the MM5 model, exhibit monotonic decrease of the spectral variance with increasing frequency; at the same time, there is divergence between the model and observed values, the model being weaker, most likely because of unresolved scales below the model grid resolution (6 km). Two spectral peaks stand out, these are at frequencies that correspond to ∼12 and ∼24 hours. The 24-hour peak is associated with the sea-breeze, while the 12-hour peak is related to the semi-diurnal solar component of the atmospheric tide (Simpson, 1994). Spectra at all of the stations are perturbed to some degree at these periods.

Before proceeding to a vector correlation analysis, the winds are low-pass filtered to remove

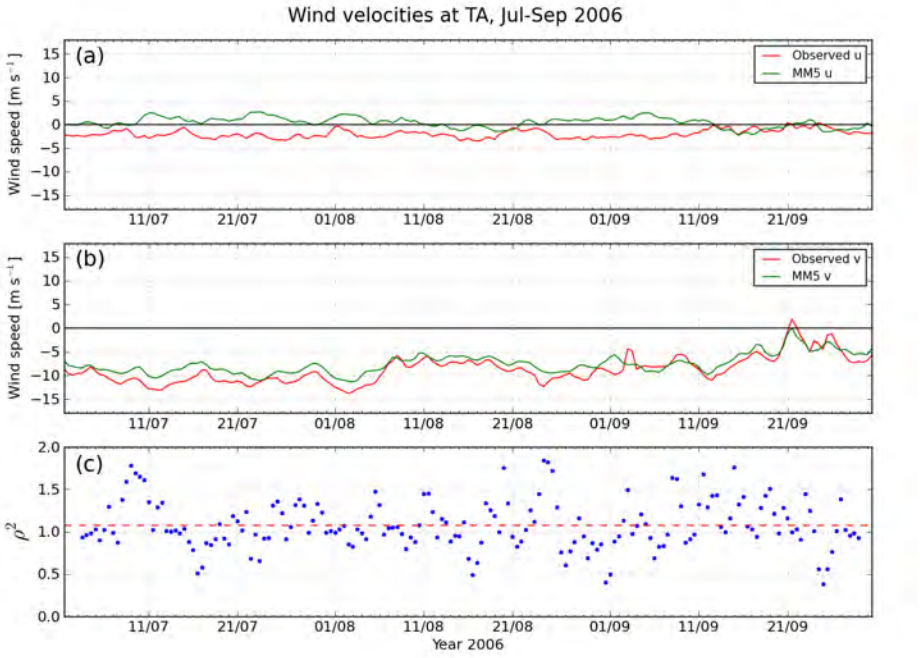

Figure B.5.: Comparison of (a) u- and (b) v-velocity components from the observations at Telde/Aeropuerto (TA) and from the corresponding location inside the MM5 model output. In (c), the Crosby vector correlation coefficient (ρ^2) for a sample size of 8 (equivalent to a period of 96 hours) between the wind time-series is shown (blue dots); the red dashed line gives the mean.

Table B.2.: Mean wind speeds [$\bar{U}$; m s^{-1}] and the variance [$\bar{U}'^2$; m^2 s^2] at meteorological stations on Gran Canaria for July through September 2006, as observed (u_O, v_O) and from MM5 (u_M, v_M).

Station	$\bar{u}_O$	$\bar{u}_M$	$\bar{v}_O$	$\bar{v}_M$	$\bar{u}'^2_O$	$\bar{u}'^2_M$	$\bar{v}'^2_O$	$\bar{v}'^2_M$
San Nicolás (SN)	-2.4	-3.9	-1.3	-7.2	3.3	3.0	3.1	4.3
Puerto de Mogán (PM)	-0.3	0.2	0.8	-1.7	3.9	2.0	3.4	8.6
Aeropuerto de G.C. (TA)	-2.0	0.4	-8.8	-7.5	4.6	2.4	10.8	4.9
Las Palmas de G.C. (LP)	2.1	1.1	-3.7	-4.1	3.4	3.0	2.0	2.1
San Bartolomé de Tirajana (SB)	1.1	-2.3	0.3	-1.8	9.4	5.0	2.8	7.1

the 12- and 24-hour periodic components. The filtered wind speeds at TA are shown in Figure B.5, the site where the strongest winds are recorded in both observations and model. Figure B.5a shows observed and MM5 u-velocity components which lie within the range -4 to 4 m s^{-1}. The observations have a negative (onshore) tendency, which may be a result of the sea breeze phenomenon which is stronger in the observations (Figure B.4). The amplitudes of the southward-directed v-components at TA are large as expected, sometimes exceeding 10 m s^{-1} (Figure B.5b). There is good agreement between MM5 and the observations.

Table B.2 presents the means and variances for the unfiltered wind data at each station. The mean wind velocities at each station conform to the expected pattern over the island as outlined above. The flanks and upwind stations experience the strongest winds (i.e., SN, TA and LP). In the lee (PM) the averages are small, and the low observed variance confirms the sheltered status of this location.

Differences between the observed and simulated data may arise from errors in either or both datasets, and also from unresolved topographic features in the model domains. Observed winds contain systematic and random measurement error; in small samples the effects of random measurement errors are especially evident. Errors in the simulated winds may arise from biases in initial or boundary conditions, incorrect model physics, from fine-scale structures in the real wind that are not resolved at 6 km, or from processes absent from the simulation such as topographic shading (Hughes and Hall, 2009).

To objectively measure differences in the two wind datasets, Figure B.5c plots the Crosby et al. (1993) vector correlation coefficient, ρ^2. The filtered wind data are subsampled every 12 points so that they are approximately independent. As defined by Crosby et al. (1993), ρ^2, accounts for the contribution of each of the orthogonal wind components. A perfect correlation ($\rho^2 = 2$) means that two vector series may differ only by a constant offset in direction, and a multiplicative factor in magnitude. In this case, the covariance structure of both series is identical. ρ^2 was calculated for three sample sizes: 8, 16 and 24, which corresponds to periods of 4, 8 and 16 days. Figure B.5c shows the 4-day sampling, which resolves events of $\sim$2 - 4 days, and indicates that large variations occur in ρ^2. Relatively high values of ρ^2 ($\rho^2 > 1.5$) occur intermittently, but it is difficult to say what features of

Table B.3.: Mean of the Crosby vector correlation, ρ^2, at 4-, 8- and 16-day periods.

Station	ρ^2_4	ρ^2_8	ρ^2_{16}
San Nicolás (SN)	1.02	0.72	0.63
Puerto de Mogán (PM)	0.90	0.66	0.62
Aeropuerto de G.C. (TA)	1.09	0.93	0.91
Las Palmas de G.C. (LP)	1.20	1.03	0.97
San Bartolomé de Tirajana (SB)	0.86	0.66	0.54

the wind at these times cause the better correlation. Table B.3 summarises the results of the complete vector correlation analysis at each sampling period (4, 8 and 16 days). The best correlations are obtained for Las Palmas and the airport. Both of these sites are exposed to the persistent large-scale wind field. At periods greater than 4 days (i.e., larger sample sizes), ρ^2 drops off sharply at all stations. However, the drop is sharpest at the more sheltered stations, indicating that they are dominated by shorter-period (2 - 4 days) wind events.

The MM5 wind solution could be improved significantly with a higher resolution grid, and by using a high-frequency SST product, such as OSTIA (Stark et al., 2007), at the sea surface boundary. However, for the purposes of the ROMS simulations of Chapter 5 the MM5 data are shown to be more than adequate.

B.3. Choice of interpolation method

The MM5 wind stresses are interpolated onto the prospective ocean model grids. Care, however, should be taken with the choice of interpolation method. Figure B.6 compares monthly means of the v-component of the wind stress, and the wind stress curl, which have been interpolated onto the ROMS L2 grid using, respectively, a triangulation and a bi-cubic interpolation method. It is evident that while some differences are visible between the two v-component wind stresses, the fields are generally smooth. However, for the wind stress curl, interpolation artifacts as a consequence of using the triangulation method are readily apparent.

Figure B.6 demonstrates that, while different interpolation methods may appear to perform similarly for interpolating wind stress components from one grid to another, small errors associated with triangulation methods are amplified when considering the curl computed from these wind stress fields. Bi-cubic methods appear to perform better. The wind stress curl is a dynamic variable (Chelton et al., 2004), hence when evaluating wind stress interpolation methods, this is the critical variable to be examined, rather than the wind stress itself.

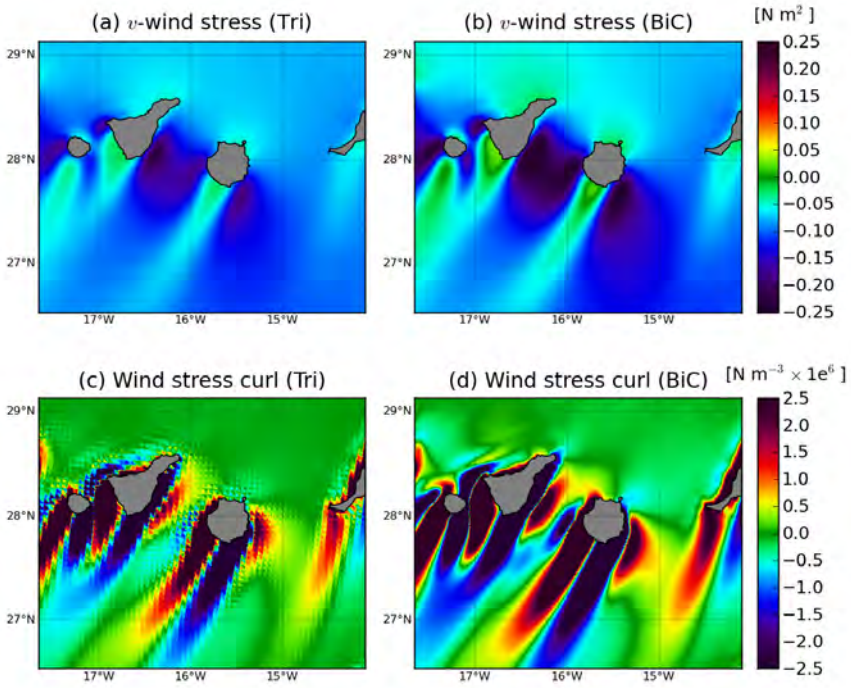

Figure B.6.: Effect of choice of interpolation method on the quality of the MM5 wind stress curl interpolated to the ocean model grid. The two methods used are triangulation (Tri) and bi-cubic (BiC). All fields are July 2006 averages. (a) and (b) show the v-component of the wind stress, (c) and (d) show the normalised wind stress curl.

C. Canary Island passage velocities

C.1. Vertical velocity sections

In Chapter 5, mean seasonal vertical sections of current velocity from the L1 (3-km) model solution were presented for three Canary Island passages:

- Fuerteventura - Africa (Figure 5.6 on page 124)
- Gran Canaria - Fuerteventura (Figure 5.7 on page 124)
- La Palma - Tenerife (Figure 5.8 on page 125)

In this section, figures showing seasonal velocity sections for the remaining island channels of the Canary Islands are included. The location of each passage and corresponding transports can be seen, respectively, in Figure 5.1 on page 115 and Table 5.3 on page 123.

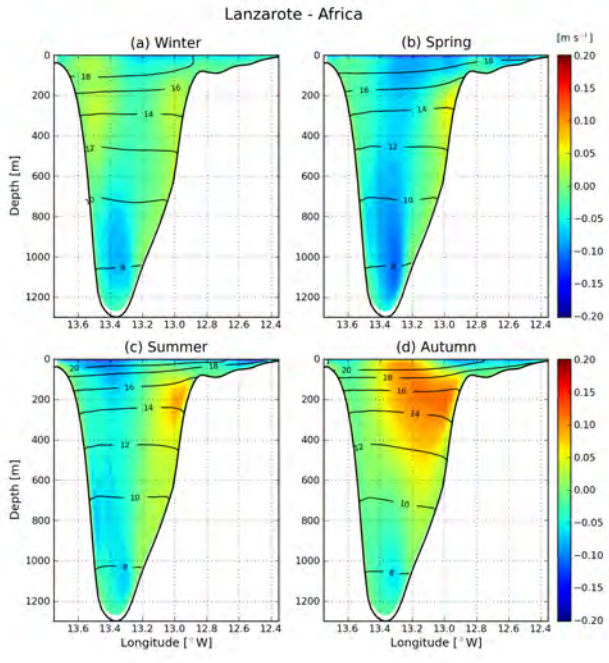

Figure C.1.: Seasonal velocity sections across the Lanzarote - Africa passage from L1. Contours in black show the vertical temperature structure.

- Lanzarote - Africa (Figure C.1): This is the northern section across the Lanzarote Passage and can be compared with the southern section in Figure 5.6 on page 124.

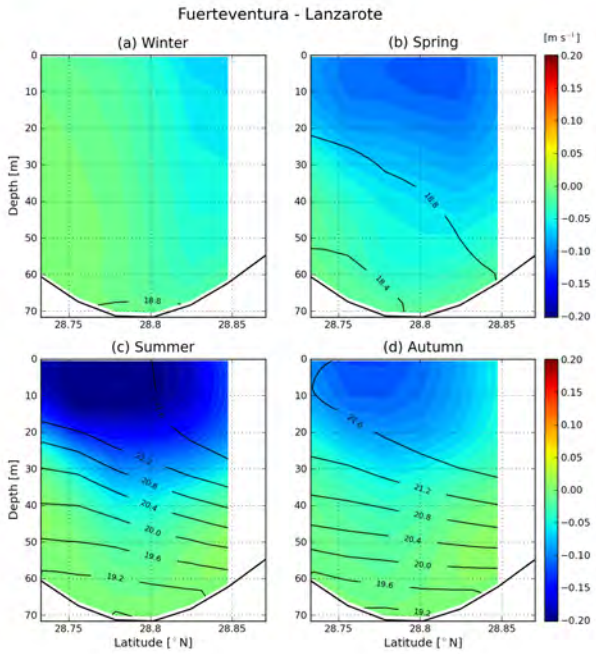

Figure C.2.: Seasonal velocity sections across the Fuerteventura - Lanzarote passage from L1. Contours in black show the vertical temperature structure.

The African shelf is notably wider in the north. In the surface layers the flow occupies the central part of the channel. It is is weak in winter, increases in spring and summer before reversing towards the north in autumn. In comparison with the southern section, the upwelling jet at the African coast is very weak; this may be related to the influence of the wide and shallow shelf north of Cape Juby (Marchesiello and Estrade, 2009). The depth of the autumn reversal is similar in the northern and southern sections (∼400 m) but, in the north, the flow is concentrated towards the eastern side of the passage. At depth there are no strong southward flows on the eastern flank of Lanzarote such as were seen for Fuerteventura. However, there is a deep southward jet at the bottom in the centre of the passage which is strongest in spring and weakest in autumn.

- Fuerteventura - Lanzarote (Figure C.2): Transport through this shallow passage (∼70 m) is westward all year. The flow is most intense in summer (>0.2 m s^{-1}), occupying the top 30 m of the stratified water column. The weakest flow is in winter.

- El Hierro - La Palma (Figure C.3): There is surprisingly little seasonal variability in this deep passage (∼3250 m). The most striking features are the deep flows on the flanks of the islands. On the northern side (La Palma) the westward flow between 2500 and 3000 m exceeds 0.2 m s^{-1} all year.

- Tenerife - Gran Canaria (Figure C.4): In the top 500 m there is considerable seasonal variability in the transport between Tenerife and Gran Canaria. The flow is generally weak, northward in winter, spring and autumn, and southward in summer. In the top

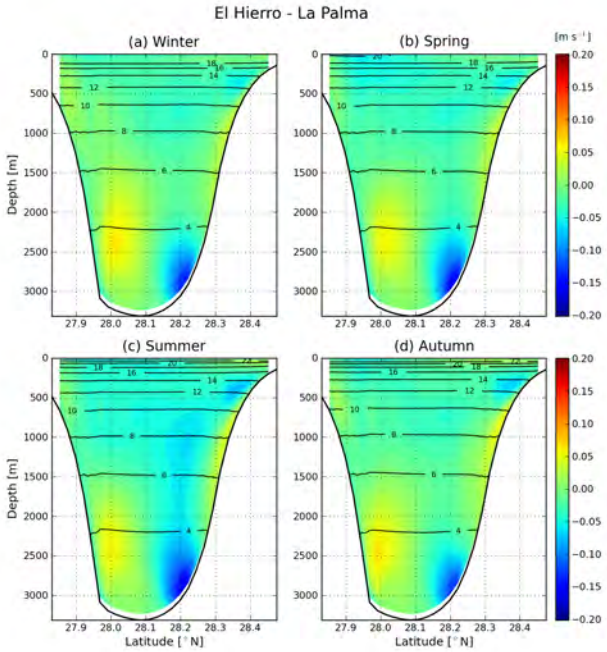

Figure C.3.: Seasonal velocity sections across the El Hierro - La Palma passage from L1. Contours in black show the vertical temperature structure.

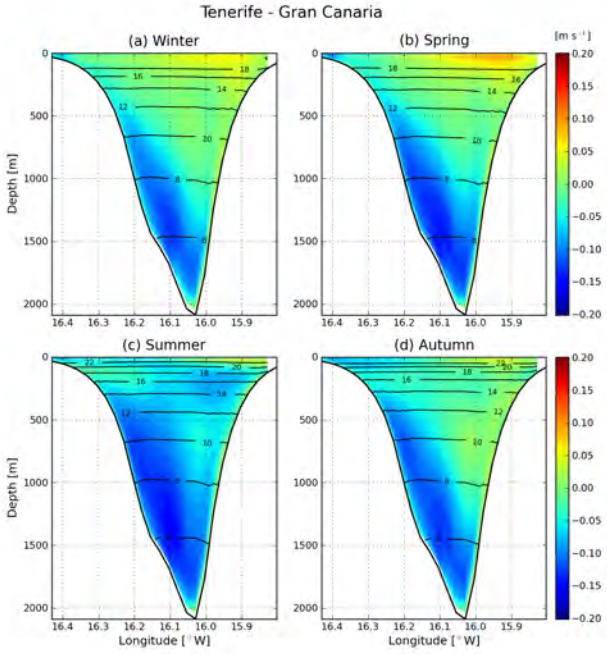

Figure C.4.: Seasonal velocity sections across the Tenerife - Gran Canaria passage from L1. Contours in black show the vertical temperature structure.

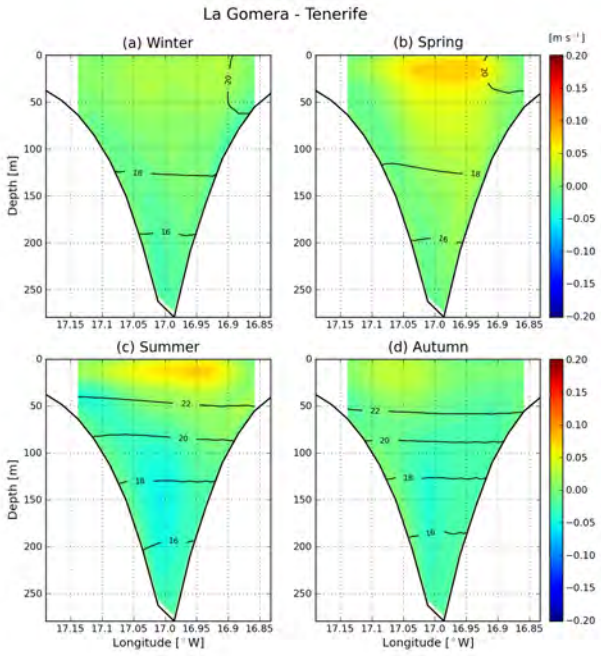

Figure C.5.: Seasonal velocity sections across the La Gomera - Tenerife passage from L1. Contours in black show the vertical temperature structure.

~100 m there is year-round northward flow at Gran Canaria which peaks in spring (>0.1 m s^{-1}). Between 500 and 2000 m there is strong southward flow (~0.2 m s^{-1}) at the Tenerife side of the passage.

- La Gomera - Tenerife (Figure C.5): The transport in this 250-m-deep passage is generally to the north. It is strongest in spring and summer (>0.1 m s^{-1}).
- La Palma - La Gomera (Figure C.6): Variability in this section is similar to the La Palma - Tenerife section (Figure 5.8 on page 125). However, at depth there is southward flow along the flank of La Palma which is not seen in the La Palma - Tenerife section despite their close proximity (Figure 5.1 on page 115; note that the angle between the sections could contribute to the apparent difference, as the velocities are plotted normal to each section).

C.2. Horizontal velocity fields

Magnitudes and direction of the horizontal velocity at the Canary Islands are shown at a selection of depths (50, 300, 600, 1300 m) in Figures C.7 to C.10 (pages 219 to 221). These are useful in relation to the vertical velocity sections presented in the previous section and in Section 5.3.3 on page 122.

- 50 m (Figure C.7): Patterns of surface velocities near to the base of the *Ekman* layer correspond closely with the vertically-integrated streamfunctions in Figure 5.5 on page

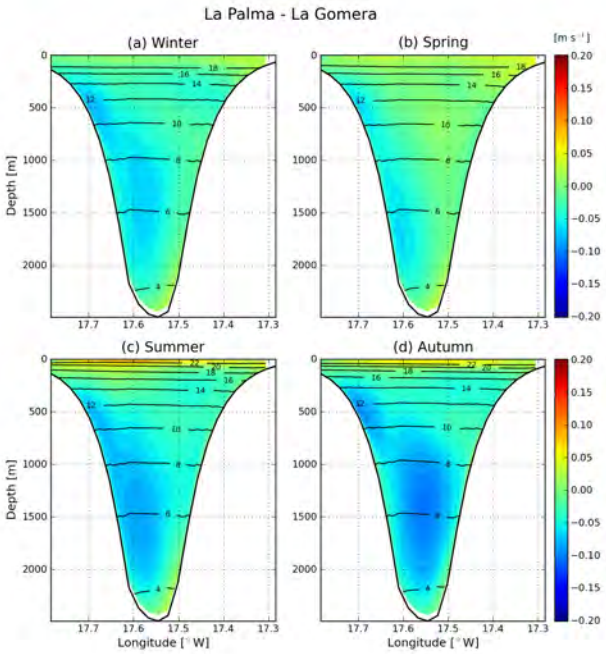

Figure C.6.: Seasonal velocity sections across the La Palma - La Gomera passage from L1. Contours in black show the vertical temperature structure.

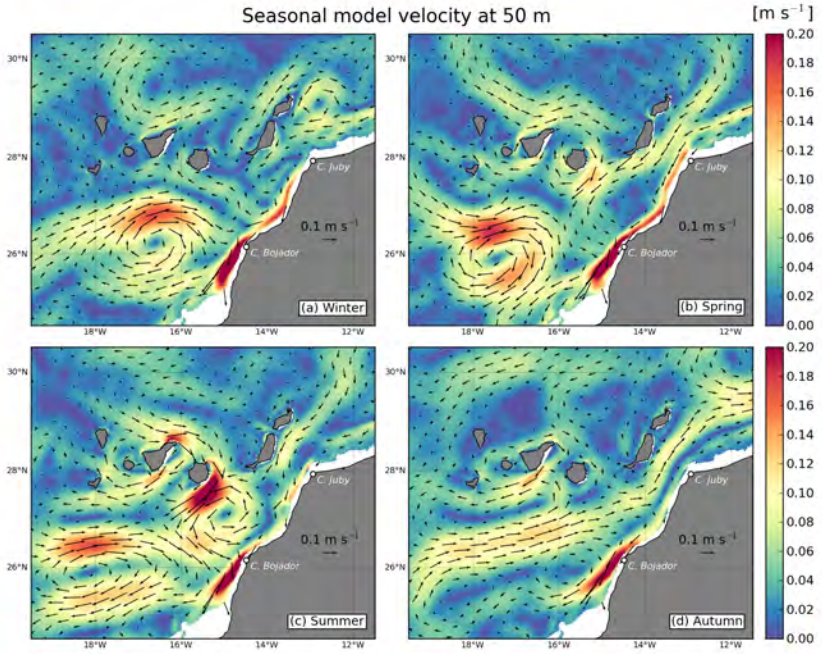

Figure C.7.: L1 seasonal velocity fields at 50 m. Arrows indicate the direction of the flow.

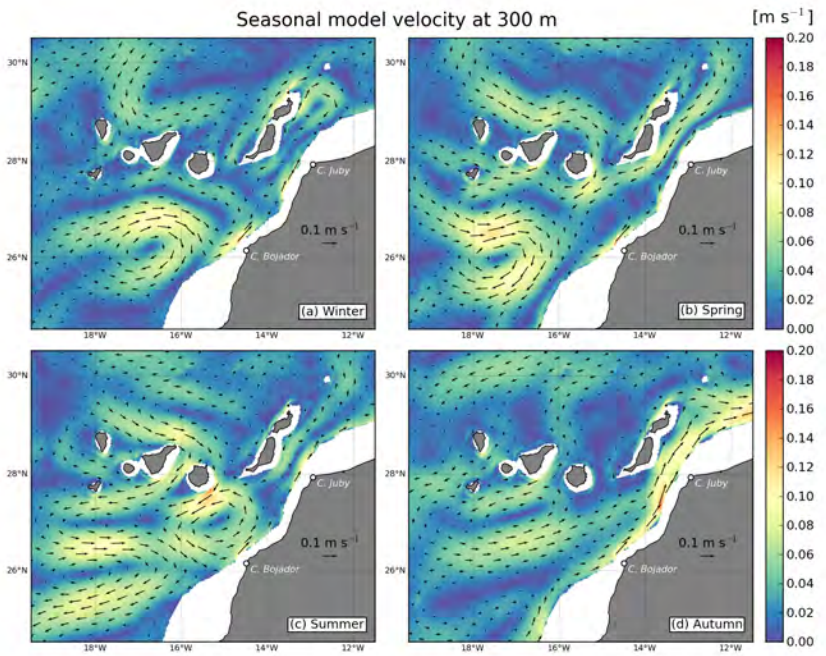

Figure C.8.: L1 seasonal velocity fields at 300 m. Arrows indicate the direction of the flow.

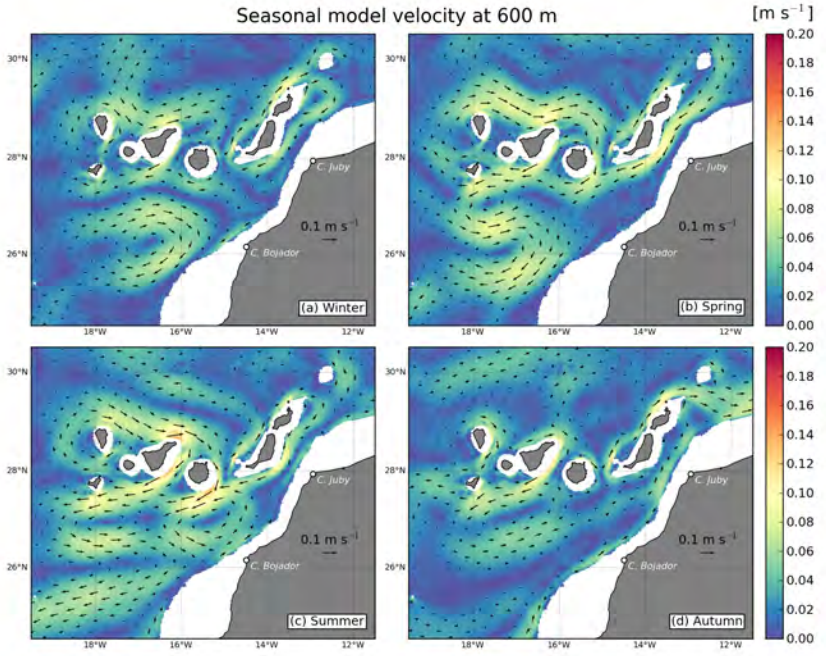

Figure C.9.: L1 seasonal velocity fields at 600 m. Arrows indicate the direction of the flow.

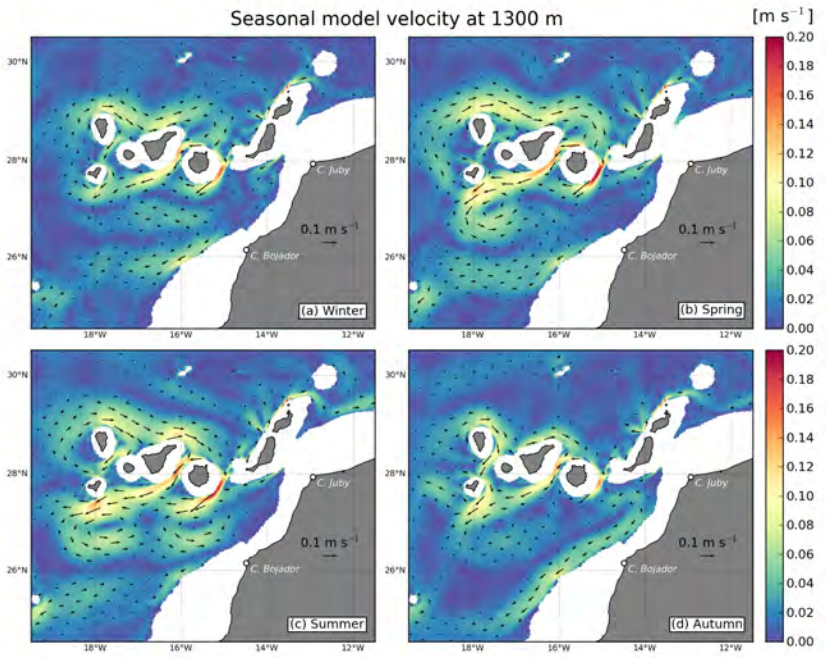

Figure C.10.: L1 seasonal velocity fields at 1300 m. Arrows indicate the direction of the flow.

121. Maximum velocities exceeding 0.2 m s^{-1} seen in all seasons along the African coast are associated with the coastal upwelling jet. North of Cape Bojador the jet appears to weaken in summer and autumn. In summer there is strong flow around the eastern part of Gran Canaria. This is linked to the large cyclonic cell described in Section 5.3 on page 120. In the Canary Island wake region the large anticyclonic cell of Section 5.3 is seen in all seasons. In autumn the cell is relatively weak, and flow towards the Lanzarote Passage is seen that appears to correspond to the seasonal autumn reversal that occurs within the passage.

- 300 m (Figure C.8): At 300-m depth the flow patterns are similar to those at 50 m, but the magnitudes of the velocities are greatly decreased. A poleward-flowing undercurrent is visible in all seasons along the African coast (Barton, 1989).

- 600 m (Figure C.9): The flow field related to the Canary Current becomes noticeably weaker at 600 m; compare the regions north of 29.5°N with the 300-m fields of Figure C.8. Around the islands and in the lee, however, significant flows persist. The strongest flows are in summer at the southeastern flanks of both Gran Canaria and Tenerife, and also at the northern tip of the latter island. There is a persistent northward flow along the western flanks of Fuerteventura and Lanzarote, which is perturbed by the Bajo de Amanay seamount located west of Fuerteventura (see Figure 2.15 on page 32). In the Lanzarote Passage the broad flow of the autumn reversal seen in the upper layers is reduced to just a narrow vein.

- 1300 m (Figure C.10): At 1300 m seasonal variability is minimal. The strongest flows are related to the island topography. Narrow jets of $\sim$0.18 m s^{-1} extend southward from the depths of the passages between Tenerife and Gran Canaria, and Gran Canaria and Fuerteventura. In spring and summer two cyclonic cells in the lee region appear to be associated with the two jets. Along the northern face of the archipelago there is persistent zonal eastward flow, that is at its broadest and strongest in spring. This appears to be part of a deep mean anticyclonic circulation that extends around the western part of the archipelago.

D. Sea surface height variance

In the comparison of sea surface height (SSH) variance from altimetry and from the L0 solution of Section 4.3.5 on page 88, we noted the model's inability to reproduce the high SSH variance observed in AVISO altimetry in the northwest corner of the domain. This result is repeated in Figure D.1a, which shows the annual model SSH variance (the seasonal variance was shown in Figure 4.9 on page 89) computed from 40 years of the L0 solution. In the boundary region between ~40° - 46°N, the expected high variability associated with the North Atlantic Current (NAC) is absent. We suggested that this was a consequence of the use of monthly climatological forcing at the model boundaries, so that both interannual (low frequency) and mesoscale (high frequency) signals are missing. Interannual effects are excluded *a priori* from climatological configurations.

To assess the impact of the loss of the high frequencies, we recalculated the AVISO SSH variance to reflect a monthly rather than a weekly deviation (Figure D.1). The SSH (η) at any given location in time and space can be seen as the sum of the long-term mean quantity and an instantaneous (or short-term average) deviation from that quantity: $\eta = \langle\eta\rangle + \eta'$. Here the value in angle brackets denotes the long-term mean, and the prime is the deviation (i.e., η - $\langle\eta\rangle$). AVISO provides 7-day averages of η, referred to hereinafter as η_7. Figure D.1b shows the SSH variance calculated using η_7. The SSH variance as the NAC enters the domain at the western boundary exceeds 400 cm^2, a clear contrast to the model result.

To obtain a monthly AVISO SSH variance ($\bar{\eta}'^2_{30}$), we used 30-day averages computed from the weekly AVISO product. Figure D.1c shows the $\bar{\eta}'^2_{30}$ SSH variance. Variability associated with the NAC is still visible, however it is much reduced in compare to $\bar{\eta}'^2_7$, particularly around the Flemish Cap. The model SSH variance remains significantly lower than both the AVISO results; this is not surprising because the model is constrained at all its forced

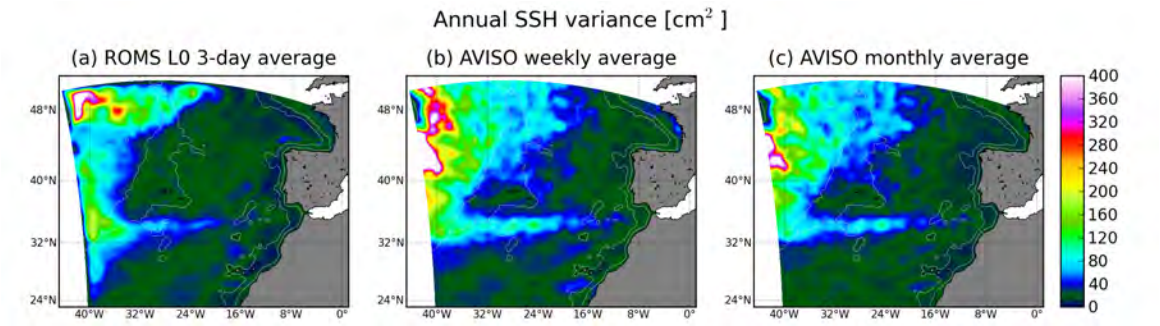

Figure D.1.: Annual mean SSH variance computed from (a) ROMS L0 using 3-day averages, (b) AVISO using 7-day averages, and (c) AVISO using 30-day averages.

surfaces (i.e., surface and lateral boundaries) by monthly values.

Figure D.1 demonstrates that the lack of high frequency forcing can be a clear shortcoming of the climatological forcing approach.

Nomenclature

AAIW Antarctic Intermediate Water

AzC Azores Current

AzCC Azores Counter-Current

AzFC Azores Front/Current system

AzH Azores High

CanC Canary Current

CanUC Canary Upwelling Current

CEC Canary Eddy Corridor

CUS Canary Upwelling System

CVFZ Cape Verde Frontal Zone

E-P Evaporation minus precipitation

EBUS Eastern Boundary Upwelling System

EKE Eddy Kinetic Energy

ENACW$_P$ Subpolar Eastern North Atlantic Central Water

ENACW$_T$ Subtropical Eastern North Atlantic Central Water

ESG Eastern Subtropical Gyre

GS Gulf Stream

IP Iberian Peninsula

ITCZ Inter-Tropical Convergence Zone

KPP K-profile planetary boundary layer vertical mixing scheme

MAP Madeira Abyssal Plain

MAR Mid-Atlantic Ridge

MC Mauritania Current

Meddy Mediterranean eddy

MO Mediterranean Outflow

MW Mediterranean Water

NAC North Atlantic Current

NACW North Atlantic Central Water

NADW North Atlantic Deep Water

NASG North Atlantic Subtropical Gyre

NEAClim Northeast Atlantic Climatology

NEC North Equatorial Current

NECC North Equatorial Counter-Current

NHF Net Heat Flux

OGCM Ocean General Circulation Model

SACW South Central Atlantic Water

SLA Sea Level Anomaly

SSH Sea Surface Height

SSS Sea Surface Salinity

SST Sea Surface Temperature

SubExp Subduction Experiment

Bibliography

Aiken, C. M., Moore, A. M., and Middleton, J. H. (2002). The nonnormality of coastal ocean flows around obstacles, and their response to stochastic forcing. *J. Phys. Oceanogr.*, 32(10):2955–2974.

Aiken, C. M., Moore, A. M., and Middleton, J. H. (2003). Non-normal perturbation growth in idealised island and headland wakes. *Dynam. Atmos. Oceans*, 37(3):171–195.

Álvarez-Salgado, X. A., Figueiras, F. G., Pérez, F. F., Groom, S., Nogueira, E., Borges, A. V., Choue, L., Castro, C. G., Moncoiffé, G., Ríosa, A. F., Miller, A. E. J., Frankignoulle, M., Savidge, G., and Wollast, R. (2003). The Portugal coastal counter current off NW Spain: new insights on its biogeochemical variability. *Prog. Oceanogr.*, 56(2):281–321.

Álvarez-Salgado, X. A., Rosón, G., Pérez, F. F., and Pazos, Y. (1993). Hydrographic Variability off the Rías Baixas (NW Spain) During the Upwelling Season. *J. Geophys. Res.*, 98(C8):14447–14455.

Alves, M. L. G. R. and Colin de Verdière, A. (1999). Instability dynamics of a subtropical jet and applications to the Azores Front Current System: Eddy-driven mean flow. *J. Phys. Oceanogr.*, 29(5):837–864.

Arakawa, A. (1966). Computational design for long-term numerical integration of the equations of fluid motion: Two-dimensional incompressible flow. Part I. *J. Comput. Phys.*, 1(1):119–143.

Arhan, M., Colin De Verdiére, A., and Mémery, L. (1994). The Eastern Boundary of the Subtropical North Atlantic. *J. Phys. Oceanogr.*, 24(6):1295–1316.

Arístegui, J., Álvarez-Salgado, X. A., Barton, E. D., Figueiras, F. G., Hernández-León, S., Roy, C., and Santos, A. M. P. (2006). *The Sea*, chapter Oceanography and fisheries of the Canary Current/Iberian region of the eastern North Atlantic, pages 878–931. Harvard College.

Arístegui, J., Barton, E. D., Álvarez-Salgado, X. A., Santos, A. M. P., Figueiras, F. G., Kifani, S., Hernández-León, S., Mason, E., and Machú, E. (2009). Sub-regional ecosystem variability in the Canary Current upwelling. *Prog. Oceanogr.*, In press.

Arístegui, J., Sangrà, P., Hernández-León, S., Cantón, M., Hernández-Guerra, A., and Kerling, J. L. (1994). Island-induced eddies in the Canary Islands. *Deep-Sea Res.*, 49(10):1087–1101.

Arístegui, J., Tett, P., Hernández-Guerra, A., Basterretxea, G., Montero, M. F., Wild, K., Sangrà, P., Hernández-León, S., Cantón, M., García-Braun, J. A., Pacheco, M., and Barton, E. D. (1997). The influence of island-generated eddies on chlorophyll distribution: A study of mesoscale variation around Gran Canaria. *Deep-Sea Res.*, 44(1):71–96.

Auclair, F., Estournel, C., Marsaleix, P., and Pairaud, I. (2006). On coastal ocean embedded modeling. *Geophys. Res. Lett.*, 33:L14602.

Bakun, A. and Nelson, C. S. (1991). The Seasonal Cycle of Wind-Stress Curl in Subtropical Eastern Boundary Current Regions. *J. Phys. Oceanogr.*, 21(12):1815–1834.

Baringer, M. and Price, J. (1997). Mixing and spreading of the Mediterranean Outflow. *J. Phys. Oceanogr.*, 27(8):1654–1677.

Barnier, B., Marchesiello, P., de Miranda, A. P., Molines, J.-M., and Coulibaly, M. (1998). A sigma-coordinate primitive equation model for studying the circulation in the South Atlantic. Part I: Model configuration with error estimates. *Deep-Sea Res.*, 45(4-5):543–572.

Barnier, B., Siefridt, L., and Marchesiello, P. (1995). Thermal forcing for a global ocean circulation model using a three-year climatology of ECMWF analyses. *J. Mar. Sys.*, 6(4):363–380.

Barton, E. D. (1987). Meanders, eddies and intrusions in the thermohaline front off Northwest Africa. *Oceanol. Acta*, 10(3):267–283.

Barton, E. D. (1989). *Poleward Flows Along Eastern Ocean Boundaries*, volume 34 of *Coastal and Estuarine Studies*, chapter The poleward undercurrent on the eastern boundary of the subtropical North Atlantic, pages 82–95. Springer, New York.

Barton, E. D. (1998). *The Sea. The Global Coastal Ocean: Regional Studies and Syntheses*, chapter Eastern boundary of the North Atlantic: Northwest Africa and Iberia coastal segment, pages 633–658. John Wiley & Sons, New York.

Barton, E. D. (2001). *Encyclopedia of Ocean Sciences*, volume 3, chapter Island wakes, pages 1397–1403. Academic Press, London.

Barton, E. D., Arístegui, J., Tett, P., Canton, M., Garcia-Braun, J., Hernández-León, S., Nykjaer, L., Almeida, C., Almunia, J., Ballesteros, S., Basterretxea, G., Escánez, J., García-Weill, L., Hernández-Guerra, A., López-Laatzen, F., Molina, R., Montero, M. F., Navarro-Pérez, E., Rodríguez, J. M., van Lenning, K., Vélez, H., and Wild, K. (1998). The transition zone of the Canary Current upwelling region. *Prog. Oceanogr.*, 41(4):455–504.

Barton, E. D., Arístegui, J., Tett, P., and Navarro-Pérez, E. (2004). Variability in the Canary Islands area of filament-eddy exchanges. *Prog. Oceanogr.*, 62(2-4):71–94.

Baschek, B., Send, U., Lafuente, J. G., and Candela, J. (2001). Transport estimates in the Strait of Gibraltar with a tidal inverse model. *J. Geophys. Res.*, 106(C12):31033–31044.

Bashmachnikov, I., Mohn, C., Pelegrí, J. L., Martins, A., Jose, F., Machín, F., and White, M. (2009). Interaction of Mediterranean water eddies with Sedlo and Seine Seamounts, Subtropical Northeast Atlantic. *Deep-Sea Res.*, In Press.

Basterretxea, G., Barton, E. D., Tett, P., Sangrà, P., Navarro-Pérez, E., and Arístegui, J. (2002). Eddy and deep chlorophyl maximum response to wind-shear in the lee of Gran Canaria. *Deep-Sea Res.*, 49(6):1087–1101.

Batteen, M. L. (1997). Wind-forced modeling studies of currents, meanders, and eddies in the California Current system. *J. Geophys. Res.*, 102(C1):985–1010.

Bécognee, P., Almeida, C., Barrera, A., Hernández-Guerra, A., and Hernández-León, S. (2006). Annual cycle of clupeiform larvae around Gran Canaria Island, Canary Islands. *Fish. Oceanogr.*, 15(4):293–300.

Biastoch, A., Lutjeharms, J. R. E., Böning, C. W., and Scheinert, M. (2008). Mesoscale perturbations control inter-ocean exchange south of Africa. *Geophys. Res. Lett.*, 35:L20602.

Blayo, E. and Debreu, L. (2005). Revisiting open boundary conditions from the point of view of characteristic variables. *Ocean Modell.*, 9(3):234–252.

Blevins, R. D. (1995). *Fluid Vortices (Fluid Mechanics and Its Applications)*, chapter Vortex-structure interaction, pages 533–574. Springer, 1 edition.

Bower, A. S., Armi, L., and Ambar, I. (1997). Lagrangian Observations of Meddy Formation during A Mediterranean Undercurrent Seeding Experiment. *J. Phys. Oceanogr.*, 27(12):2545–2575.

Bower, A. S., Le Cann, B., Rossby, T., Zenk, W., Gould, J., Speer, K., Richardson, P. L., Prater, M. D., and Zhang, H. M. (2002). Directly measured mid-depth circulation in the northeastern North Atlantic Ocean. *Nature*, 419:603–607.

Bower, A. S. and von Appen, W.-J. (2008). Interannual Variability in the Pathways of the North Atlantic Current over the Mid-Atlantic Ridge and the Impact of Topography. *J. Phys. Oceanogr.*, 38(1):104–120.

Brochier, T., Mason, E., Moyano, M., Colas, F., Sangrà, P., Hernández-Leon, S., and Lett, C. (2009). Ichthyoplankton transport from the African coast to the Canary Islands: A case study using a high-resolution hydrodynamic model. *Mar. Ecol. Progr.*, In preparation.

Brochier, T., Mason, E., Sangrà, P., and Lett, C. (2008). Ichthyoplankton transport from the African coast to the Canary Islands: A case study using a high-resolution hydrodynamic model. In *Eastern Boundary Upwelling Ecosystems*, Las Palmas, Spain. Poster.

Bryan, F. O. and Smith, R. D. (1998). Modelling the North Atlantic Circulation: From eddy-permitting to eddy-resolving. *International WOCE Newsletter*, 33:12–14.

Buffett, G. G., Biescas, B., Pelegrí, J. L., Machín, F., Sallarès, V., Carbonell, R., Klaeschen, D., and Hobbs, R. (2009). Seismic reflection along the path of the Mediterranean Undercurrent. *Cont. Shelf Res.*, 29(15):1848–1860.

Cailleau, S., Fedorenko, V., Barnier, B., Blayo, E., and Debreu, L. (2008). Comparison of different numerical methods used to handle the open boundary of a regional ocean circulation model of the Bay of Biscay. *Ocean Modell.*, 25(1-2):1–16.

Capet, X. J., Campos, E. J., and Paiva, A. M. (2008a). Submesoscale activity over the Argentinian shelf. *Geophys. Res. Lett.*, 35:L15605.

Capet, X. J., Colas, F., Penven, P., Marchesiello, P., and McWilliams, J. C. (2008b). *Eddy-Resolving Ocean Modeling*, volume Geophysical Monograph 177, chapter Eddies in eastern-boundary subtropical upwelling systems. AGU Monograph.

Capet, X. J., Marchesiello, P., and McWilliams, J. C. (2004). Upwelling response to coastal wind profiles. *Geophys. Res. Lett.*, 31(13):L13311.

Capet, X. J., McWilliams, J. C., Molemaker, M. J., and Shchepetkin, A. F. (2008c). Mesoscale to submesoscale transition in the California Current System. Part I: Flow structure, eddy flux, and observational tests. *J. Phys. Oceanogr.*, 38(1):29–43.

Carr, M.-E. (2002). Estimation of potential productivity in Eastern Boundary Currents using remote sensing. *Deep-Sea Res.*, 49(1-3):59–80.

Carr, M.-E. and Kearns, E. J. (2003). Production regimes in four Eastern Boundary Current systems. *Deep-Sea Res.*, 50(22-26):3199–3221.

Carr, M.-E., Kearns, E. J., and Rossby, H. T. (1997). Isopycnal RAFOS floats as roving hydrographers in the North Atlantic Current Region. *Geophys. Res. Lett.*, 24(5):551–554.

Carton, J. A. and Giese, B. S. (2008). A Reanalysis of Ocean Climate Using Simple Ocean Data Assimilation (SODA). *Mon. Weather Rev.*, 136(8):2999–3017.

Challenor, P. G., Cipollini, P., and Cromwell, D. (2001). Use of the 3D Radon Transform to Examine the Properties of Oceanic Rossby Waves. *J. Atmos. Ocean. Tech.*, 18(9):1558–1566.

Chapman, D. C. (1985). Numerical Treatment of Cross-Shelf Open Boundaries in a Barotropic Coastal Ocean Model. *J. Phys. Oceanogr.*, 15(8):1060–1075.

Chavanne, C., Flament, P., Lumpkin, R., Dousset, B., and Bentamy, A. (2002). Scatterometer observations of wind variations induced by oceanic islands: Implications for wind-driven ocean circulation. *Can. J. Rem. Sens.*, 28(3):466–474.

Chelton, D. B., deSzoeke, R. A., Schlax, M. A., El Naggar, K., and Siwertz, N. (1998). Geographical variability of the first-baroclinic Rossby radius of deformation. *J. Phys. Oceanogr.*, 28(3):433–460.

Chelton, D. B., Schlax, M. G., Freilich, M. H., and Milliff, R. F. (2004). Satellite measurements reveal persistent small-scale features in ocean winds. *Science*, 303(5660):978–983.

Chelton, D. B., Schlax, M. G., Samelson, R. M., and de Szoeke, R. A. (2007). Global observations of large oceanic eddies. *Geophys. Res. Lett.*, 34:L15606.

Chopra, K. P. (1973). Atmospheric and oceanic flow problems introduced by islands. *Adv. Geophys.*, 16:297–421.

Chopra, K. P. and Hubert, L. F. (1964). Karman vortex-streets in Earth's atmosphere. *Nature*, 203:1341–1343.

Chopra, K. P. and Hubert, L. F. (1965a). Karman vortex streets in wakes of islands. *AIAA Journal*, 3(10):1941–1943.

Chopra, K. P. and Hubert, L. F. (1965b). Mesoscale eddies in wake of islands. *J. Atmos. Sci.*, 22(6):652–657.

Colin De Verdière, A., Merchier, H., and Arhan, M. (1989). Mesoscale Variability Transition from the Western to the Eastern Atlantic along 48°N. *J. Phys. Oceanogr.*, 19(8):1149–1170.

Cromwell, D., Challenor, P. G., New, A. L., and Pingree, R. D. (1996). Persistent westward flow in the Azores Current as seen from altimetry and hydrography. *J. Geophys. Res.*, 101(C5):11923–11934.

Crosby, D. S., Breaker, L. C., and Gemmill, W. H. (1993). A Proposed Definition for Vector Correlation in Geophysics: Theory and Application. *J. Atmos. Ocean. Tech.*, 10(3):355–367.

Cushman-Roisin, B. (1994). *Introduction to Geophysical Fluid Dynamics*. Prentice-Hall, 1st edition. 320pp.

da Silva, A. M., Young, C. C., and Levitus, S. (1994). *Atlas of Surface Marine Data 1994*, volume 1-5. NOAA Atlas NESDIS 6-10, U.S. Government Printing Office.

de Boyer Montégut, C., Madec, G., Fischer, A. S., Lazar, A., and Iudicone, D. (2004). Mixed layer depth over the global ocean: An examination of profile data and a profile-based climatology. *J. Geophys. Res.*, 109(C12):C12003.

de Miranda, A. P., Barnier, B., and Dewar, W. K. (1999). Mode waters and subduction rates in a high-resolution South Atlantic simulation. *J. Mar. Res.*, 57(32):213–244.

Debreu, L. and Blayo, E. (2008). Two-way embedding algorithms: a review. *Ocean Dynam.*, pages 415–428. Special Issue on Multi-Scale Modelling: Nested Grid and Unstructured Mesh Approaches.

Debreu, L., Marchesiello, P., and Penven, P. (2009). Two-way embedding algorithms for a split-explicit free-surface ocean model. *Ocean Modell.*, In preparation.

Debreu, L., Vouland, C., and Blayo, E. (2008). AGRIF: Adaptive grid refinement in Fortran. *Computers and Geosciences*, 34(1):8–13.

Dong, C., Idica, E. Y., and McWilliams, J. C. (2009). Circulation and multiple-scale variability in the Southern California Bight. *Prog. Oceanogr.*, 82(3):168–190.

Dong, C. and McWilliams, J. C. (2007). A numerical study of island wakes in the Southern California Bight. *Cont. Shelf Res.*, 27(9):1233–1248.

Dong, C., McWilliams, J. C., and Shchepetkin, A. F. (2007). Island wakes in deep water. *J. Phys. Oceanogr.*, 37(4):962–981.

Ducet, N., Le Traon, P.-Y., and Reverdin, G. (2000). Global high-resolution mapping of ocean circulation from TOPEX/Poseidon and ERS-1 and -2. *J. Geophys. Res.*, 105(C8):19477–19498.

Durand, M.-H., Cury, P., Mendelssohn, R., Roy, C., Bakun, A., and Pauly, D., editors (1998). *Global Versus Local Changes in Upwelling Systems.* ORSTOM editions, Paris.

Echevin, V., Aumont, O., Ledesma, J., and Flores, G. (2008). The seasonal cycle of surface chlorophyll in the Peruvian upwelling system: A modelling study. *Prog. Oceanogr.*, 79(2-4):167–176.

Edwards, K. A., MacCready, P., Moum, J. N., Pawlak, G., Klymak, J. M., and Perlin, A. (2004). Form Drag and Mixing Due to Tidal Flow past a Sharp Point. *J. Phys. Oceanogr.*, 34(6):1297–1312.

Ekman, V. W. (1905). On the influence of the earth's rotation on ocean-currents. *Ark. Mat. Astron. Fys.*, 2:1–52.

Epp, D. and Smoot, N. C. (1989). Distribution of seamounts in the North Atlantic. *Nature*, 337:254–257.

Fennel, K., Wilkin, J., Levin, J., Moisan, J., O'Reilly, J., and Haidvogel, D. (2006). Nitrogen cycling in the Middle Atlantic Bight: Results from a three-dimensional model and implications for the North Atlantic nitrogen budget. *Global Biogeochem. Cy.*, 20:GB3007.

Fiekas, V., Elken, J., Muller, T. J., Aitsam, A., and Zenk, W. (1992). A view of the Canary Basin thermocline circulation in winter. *J. Geophys. Res.*, 97(C8):12495–12510.

Fiúza, A. F. G. (1984). *Hidrologia e dinâmica das aguas costeiras de Portugal.* PhD thesis, University of Lisbon. 294pp.

Fiúza, A. F. G. and Halpern, D. (1982). Hydrographic observations of the Canary Current between 21°N and 25.5°N in March/April 1974. *Rapp. p.-v. Reun. (ICES)*, 180:58–64.

Fiúza, A. F. G., Hamann, M., Ambar, I., Díaz del Río, G., González, N., and Cabanas, J. M. (1998). Water masses and their circulation off western Iberia during May 1993. *Deep-Sea Res.*, 45(7):1127–1160.

Flather, R. A. (1976). A tidal model of the north-west European continental shelf. *Memoires de la Societe Royale des Sciences de Liège*, 6(10):141–164.

Fraga, F., Mourino, C., and Manriquez, M. (1982). Las masas de agua en la costa de Galicia: junio-octubre. *Invest Pesq*, 10:51–77.

Gabric, A. J., Garcia, L., Van Camp, L., Nykjaer, L., Eifler, W., and Schrimpf, W. (1993). Offshore Export of Shelf Production in the Cape Blanc (Mauritania) Giant Filament as Derived From Coastal Zone Color Scanner Imagery. *J. Geophys. Res.*, 98(C3):4697–4712.

Gill, A. E. (1982). *Atmosphere-Ocean Dynamics.* Academic Press, New York. 662pp.

Goldner, D. R. and Chapman, D. C. (1997). Flow and particle motion induced above a tall seamount by steady and tidal background currents. *Deep-Sea Res.*, 44(5):719–744.

Gould, W. J. (1985). Physical Oceanography of the Azores Front. *Prog. Oceanogr.*, 14:167–190.

Grell, G. A., Dudhia, J., and Stauffer, D. R. (1995). A description of the fifth-generation Penn State/NCAR Mesoscale Model (MM5). Technical Report TN-398+STR, NCAR.

Gruber, N., Frenzel, H., Doney, S. C., Marchesiello, P., McWilliams, J. C., Moisan, J. R., Oram, J. J., Plattner, G.-K., and Stolzenbach, K. D. (2006). Eddy-resolving simulation of plankton ecosystem dynamics in the California Current System. *Deep-Sea Res.*, 53(9):1483–1516.

Hagen, E. (2005). Zonal Wavelengths of Planetary Rossby Waves Derived from Hydrographic Transects in the Northeast Atlantic Ocean. *J. Oceanogr.*, 61:1039–1046.

Hagen, E., Zuelicke, C., and Feistel, R. (1996). Near-surface structures in the Cape Ghir filament off Morocco. *Oceanol. Acta*, 19(6):577–598.

Haidvogel, D. B. and Beckmann, A. (1999). *Numerical Ocean Circulation Modeling.* Imperial College Press.

Harvey, J. (1982). θ-S relationships and water masses in the eastern North Atlantic. *Deep-Sea Res.*, 29(8):1021–1033.

Harvey, J. and Arhan, M. (1988). The Water Masses of the Central North Atlantic in 1983-84. *J. Phys. Oceanogr.*, 18:1855–1875.

Harzallah, A. (2009). Flow variability in the Strait of Gibraltar: The Mediterranean adjustment to tidal forcing. *Deep-Sea Res.*, 56(4):459–470.

Hecht, M. W. and Smith, R. D. (2008). Towards a Physical Understanding of the North Atlantic: A Review of Model Studies in an Eddying Regime. In Hecht, M. and Hasumi, H., editors, *Ocean Modeling in an Eddying Regime*, Geophysical Monograph Series. American Geophysical Union.

Hernández-Guerra, A., Arístegui, J., Canton, M., and Nykjaer, L. E. O. (1993). Phytoplankton pigment patterns in the Canary Islands area as determined using Coastal Zone Colour Scanner data. *Int. J. Rem. Sens.*, 14(7):1431–1437.

Hernández-Guerra, A., Fraile-Nuez, E., Borges, R., López-Laatzen, F., Vélez-Belchí, P., Parrilla, G., and Müller, T. J. (2003). Transport variability in the Lanzarote passage (eastern boundary current of the North Atlantic subtropical Gyre). *Deep-Sea Res.*, 50(2):189–200.

Hernández-Guerra, A., Fraile-Nuez, E., López-Laatzen, F., Martínez, A., Parrilla, G., and Vélez-Belchí, P. (2005). Canary Current and North Equatorial Current from an inverse box model. *J. Geophys. Res.*, 110:C12019.

Hernández-Guerra, A., Machín, F., Antoranz, A., Cisneros-Aguirre, J., Gordo, C., Marrero-Díaz, A., Martínez, A., Ratsimandresy, A. W., Rodríguez-Santana, A., Sangrá, P., López-Laatzen, F., Parrilla, P., and Pelegrí, J. L. (2002). Temporal variability of mass transport in the Canary Current. *Deep-Sea Res.*, 49(17):3415–3426.

Hernández-León, S. (1991). Accumulation of mesozooplankton in a wake area as a causative mechanism of the "island-mass effect". *Mar. Biol.*, 109(1):141–147.

Heywood, K. J., McDonagh, E. L., and White, M. A. (1994). Eddy kinetic energy of the North Atlantic subpolar gyre from satellite altimetry. *J. Geophys. Res.*, 99(C11):22525–22539.

Hirschi, J. M., Killworth, P. D., and Blundell, J. R. (2007). Subannual, Seasonal, and Interannual Variability of the North Atlantic Meridional Overturning Circulation. *J. Phys. Oceanogr.*, 37(5):1246–1265.

Hubert, L. F. and Krueger, A. F. (1962). Satellite pictures of mesoscale eddies. *Mon. Weather Rev.*, 90(11):457–463.

Hughes, M. and Hall, A. (2009). Local and synoptic mechanisms causing Southern California's Santa Ana winds. *Climate Dynamics*, Open Access.

Hunter, P. and Macnab, R. (2003). The GEBCO Digital Atlas published by the British Oceanographic Data Centre on behalf of IOC and IHO. North Atlantic region.

Huppert, H. E. and Bryan, K. (1976). Topographically generated eddies. *Deep-Sea Res.*, 23(8):655–679.

Jia, Y. (2000). Formation of an Azores Current due to Mediterranean overflow in a modeling study of the North Atlantic. *J. Phys. Oceanogr.*, 30(9):2342–2358.

Jiménez, B., Sangrà, P., and Mason, E. (2008). A numerical study of the relative importance of wind and topographic forcing on oceanic eddy shedding by tall deep water islands. *Ocean Modell.*, 22(3-4):146–157.

Johnson, J. and Stevens, I. (2000). A fine resolution model of the eastern North Atlantic between the Azores, the Canary Islands and the Gibraltar Strait. *Deep-Sea Res.*, 47(5):875–899.

Josey, S. A. (2001). A Comparison of ECMWF, NCEP-NCAR, and SOC Surface Heat Fluxes with Moored Buoy Measurements in the Subduction Region of the Northeast Atlantic. *J. Clim.*, 14(8):1780–1789.

Juliano, M. F. and Alves, M. L. G. (2007). The Atlantic Subtropical Front/Current Systems of Azores and St. Helena. *J. Phys. Oceanogr.*, 37(11):2573–2598.

Kalnay, E., Kanamitsu, M., Kistler, R., Collins, W., Deaven, D., Gandin, L., Iredell, M., Saha, S., White, G., Woollen, J., Zhu, Y., Leetmaa, A., Reynolds, R., Chelliah, M., Ebisuzaki, W., Higgins, W., Janowiak, J., Mo, K. C., Ropelewski, C., Wang, J., Jenne, R., and Joseph, D. (1996). The NCEP/NCAR 40-Year Reanalysis Project. *Bull. Amer. Meteor. Soc.*, 77:437–471.

Käse, R. and Krauss, W. (1996). *The Warmwatersphere of the North Atlantic Ocean*, chapter The Gulf Stream, the North Atlantic Current, and the Origin of the Azores Current in the Warm Watersphere of the North Atlantic Ocean, pages 291–337. Gebrüder Borntraeger.

Käse, R. H. and Seidler, G. (1982). Meandering of the subtropical front south-east of the Azores. *Nature*, 300:245–246.

Käse, R. H., Zenk, W., Sanford, T. B., and Hiller, W. (1985). Currents, fronts and eddy fluxes in the Canary Basin. *Prog. Oceanogr.*, 14:231–257.

Kearns, E. J. (1996). *A description of the North Atlantic current system from historical hydrography*. PhD thesis, ETD Collection for University of Rhode Island. Paper AAI9702086.

Kearns, E. J. and Paldor, N. (2000). Why are the meanders of the North Atlantic Current stable and stationary? *Geophys. Res. Lett.*, 27(7):1029–1032.

Kida, S., Price, J. F., and Yang, J. (2008). The upper oceanic response to overflows: A mechanism for the Azores Current. *J. Phys. Oceanogr.*, 38(4):880–895.

Kilpatrick, K., Podesta, G. P., and Evans, R. (2001). Overview of the NOAA/NASA Advanced Very High Resolution Radiometer Pathfinder algorithm for sea surface temperature and associated matchup database. *J. Geophys. Res.*, 106(C5):9179–9197.

Klaeschen, D., Hobbs, R. W., Krahmann, G., Papenberg, C., and Vsemirnova, E. (2009). Estimating movement of reflectors in the water column using seismic oceanography. *Geophys. Res. Lett.*, 36:L00D03.

Klein, B. and Seidler, G. (1989). On the origin of the Azores Current. *J. Geophys. Res.*, 94:6159–6168.

Klein, P. and Lapeyre, G. (2009). The Oceanic Vertical Pump Induced by Mesoscale and Submesoscale Turbulence. *Annual Review of Marine Science*, 1:351–375.

Knoll, M., Hernández-Guerra, A., Lenz, B., López-Laatzen, F., Machín, F., Müller, T. J., and Siedler, G. (2002). The Eastern Boundary Current system between the Canary Islands and the African Coast. *Deep-Sea Res.*, 49(17):3427–3440.

Krauss, W., Käse, R. H., and Heinrichsen, H. H. (1990). The branching of the Gulf Stream southeast of the Grand Banks. *J. Geophys. Res.*, 95:13089–13103.

La Violette, P. E. (1974). A Satellite-Aircraft Thermal Study of the Upwelled Waters off Spanish Sahara. *J. Phys. Oceanogr.*, 4(4):676–684.

Large, W. G., McWilliams, J. C., and Doney, S. C. (1994). Oceanic vertical mixing: A review and a model with a vertical K-profile boundary layer parameterization. *Rev. Geophys.*, 32(4):363–403.

Lázaro, C., Fernandes, M. J., Santos, A. M. P., and Oliveira, P. B. (2005). Seasonal and interannual variability of surface circulation in the Cape Verde region from 8 years of merged T/P and ERS-2 altimeter data. *Rem. Sens. Environ.*, 98(1):45–62.

Le Traon, P.-Y. and De Mey, P. (1994). The eddy field associated with the Azores Front east of the Mid-Atlantic ridge as observed by the Geosat altimeter. *J. Geophys. Res.*, 99(C5):9907–9924.

Lecointre, A., Penduff, T., Cipollini, P., Tailleux, R., and Barnier, B. (2008). Depth dependence of westward-propagating north atlantic features diagnosed from altimetry and a numerical 1/6° model. *Ocean Sci.*, 4:99–113.

Llinás, O., Rodríguez de Leon, A., Siedler, G., and Wefer, G. (1994). The ESTOC time series started operation. *International WOCE Newsletter*, 17:20.

Lorenz, E. (1963). Deterministic nonperiodic flow. *J. Atmos. Sci.*, 20(2):130–141.

Lozier, S. M., Owens, S. B., and Curry, R. G. (1995). The climatology of the North Atlantic. *Prog. Oceanogr.*, 36(1):1–44.

Lumpkin, R. and Garraffo, Z. (2005). Evaluating the decomposition of tropical Atlantic drifter observations. *J. Atmos. Ocean. Tech.*, 22(9):1403–1415.

Lumpkin, R. and Garzoli, S. L. (2005). Near-surface circulation in the tropical Atlantic Ocean. *Deep-Sea Res.*, 52(3):495–518.

Machín, F., Hernández-Guerra, A., and Pelegrí, J. L. (2006a). Mass fluxes in the Canary Basin. *Prog. Oceanogr.*, 70(2-4):416–447.

Machín, F. and Pelegrí, J. L. (2009). Northward Penetration of Antarctic Intermediate Water off Northwest Africa. *J. Phys. Oceanogr.*, 39(3):512–535.

Machín, F., Pelegrí, J. L., Marrero-Díaz, A., Laiz, I., and Ratsimandresy, A. W. (2006b). Near-surface circulation in the southern Gulf of Cádiz. *Deep-Sea Res.*, 53(11-13):1161–1181.

Madec, G. (2008). NEMO Ocean Engine (Note du Pole de Modélisation). Technical Report 27, Institut Pierre-Simon Laplace (IPSL), France. ISSN 1288-1619.

Madec, G., Delecluse, P., Imbard, M., and Lévy, C. (1998). OPA 8, Ocean General Circulation Model Reference Manual. Internal Report. Technical report, LODYC/IPSL, Paris.

Mahowald, N. M., Baker, A. R., Bergametti, G., Brooks, N., Duce, R. A., Jickells, T. D., Kubilay, N., Prospero, J. M., and Tegen, I. (2005). Atmospheric global dust cycle and iron inputs to the ocean. *Global Biogeochem. Cy.*, 19:GB4025.

Marchesiello, P., Barnier, B., and de Miranda, A. P. (1998). A sigma-coordinate primitive equation model for studying the circulation in the South Atlantic Part II: Meridional transports and seasonal variability. *Deep-Sea Res.*, 45(4-5):573–608.

Marchesiello, P., Debreu, L., and Couvelard, X. (2009). Spurious diapycnal mixing in terrain-following coordinate models: The problem and a solution. *Ocean Modell.*, 26(3-4):156–169.

Marchesiello, P. and Estrade, P. (2009). Eddy activity and mixing in upwelling systems: a comparative study of Northwest Africa and California regions. *Int. J. Earth Sci.*, 98(2):1437–3254.

Marchesiello, P., Herbette, S., Nykjaer, L., and Roy, C. (2004). Eddy-driven dispersion processes in the Canary Current upwelling system: comparison with the California system. *GLOBEC International Newsletter*, 10(1):5–7.

Marchesiello, P., McWilliams, J. C., and Shchepetkin, A. (2001). Open boundary conditions for long-term integration of regional oceanic models. *Ocean Modell.*, 3(1-2):1–20.

Marchesiello, P., McWilliams, J. C., and Shchepetkin, A. (2003). Equilibrium structure and dynamics of the California Current System. *J. Phys. Oceanogr.*, 33(4):753–783.

McCabe, R. M., MacCready, P., and Pawlak, G. (2006). Form Drag due to Flow Separation at a Headland. *J. Phys. Oceanogr.*, 36(11):2136–2152.

McCartney, M. (1992). Recirculating components to the deep boundary current of the northern North Atlantic. *Prog. Oceanogr.*, 29(4):283–383.

McClain, C. R., Cleave, M. L., Feldman, G. C., Gregg, W. W., Hooker, S. B., and Kuring, N. (1998). Science quality SeaWiFS data for global biosphere research. *Sea Tech.*, 39:10–16.

McWilliams, J. C., Colas, F., and Molemaker, M. J. (2009). Cold filamentary intensification and oceanic surface convergence lines. *Geophys. Res. Lett.*, 36(18):L18602.

Mittelstaedt, E. (1991). The ocean boundary along the northwest African coast: Circulation and oceanographic properties at the sea surface. *Prog. Oceanogr.*, 26(4):307–355.

Mohn, C., White, M., Bashmachnikov, I., Jose, F., and Pelegrí, J. L. (2009). Dynamics at an elongated, intermediate depth seamount in the North Atlantic (Sedlo Seamount, 40°20′N, 26°40′W). *Deep-Sea Res.*, In Press.

Molina, R., Cabanas, J. M., and López-Laatzen, F. (1996). Corrientes e hidrografía en la región Canaria. Campaña Canarias 9205. *Boletín del Instituto Español de Oceanografía*, 12(1):43–51.

Molinari, R. L., Garzoli, S. L., Katz, E. J., Harrison, D. E., Richardson, P. L., and Reverdin, G. (1986). A synthesis of the First GARP Global Experiment (FGGE) in the equatorial Atlantic Ocean. *Prog. Oceanogr.*, 16:91–112.

Moyano, M., Rodríguez, J. M., and Hernández-León, S. (2009). Larval fish abundance and distribution during the late winter bloom off Gran Canaria Island, Canary Islands. *Fish. Oceanogr.*, 18(1):51–61.

Müller, T. J. and Siedler, G. (1992). Multi-year current time series in the eastern North Atlantic Ocean. *J. Mar. Res.*, 50(1):63–98.

Navarro-Pérez, E. and Barton, E. D. (1998). The physical structure of an upwelling filament off the north-west African coast during August 1993. *South African Journal of Marine Science*, 19:61–73.

Navarro-Pérez, E. and Barton, E. D. (2001). Seasonal and interannual variability of the Canary Current. *Sci. Mar.*, 65:205–213. Supplement 1.

Naya, A. (1984). *Meteorología superior*. Espasa-Calpe SA, Madrid. 546pp.

Nykjær, L. and Van Camp, L. (1994). Seasonal and interannual variability of coastal upwelling along northwest Africa and Portugal from 1981 to 1991. *J. Geophys. Res.*, 99(C7):14197–14207.

Onken, R. (1993). The Azores Countercurrent. *J. Phys. Oceanogr.*, 23(8):1638–1646.

Orlanski, I. (1976). A simple boundary condition for unbounded hyperbolic flows. *J. Comput. Phys.*, 21:251–269.

Osychny, V. and Cornillon, P. (2004). Properties of Rossby Waves in the North Atlantic Estimated from Satellite Data. *J. Phys. Oceanogr.*, 34(1):61–76.

Özgökmen, T. M., Chassignet, E. P., and Rooth, C. G. H. (2001). On the Connection between the Mediterranean Outflow and the Azores Current. *J. Phys. Oceanogr.*, 31(2):461–480.

Paillet, J. and Mercier, H. (1997). An inverse model of the eastern North Atlantic general circulation and thermocline ventilation. *Deep-Sea Res.*, 44(8):1293–1328.

Pascual, A., Faugère, Y., Larnicol, G., and Le Traon, P.-Y. (2006). Improved description of the ocean mesoscale variability by combining four satellite altimeters. *Geophys. Res. Lett.*, 33:L02611.

Pastor, M. V., Pelegrí, J. L., Hernández-Guerra, A., Font, J., Salat, J., and Emelianov, M. (2008). Water and nutrient fluxes off Northwest Africa. *Cont. Shelf Res.*, 28(7):915–936.

Pedlosky, J. (1996). *Ocean Circulation Theory*. Springer-Verlag, New York. 453pp.

Pelegrí, J. L., Arístegui, J., Cana, L., González-Dávila, M., Hernández-Guerra, A., Hernández-León, S., Marrero-Díaz, A., Montero, M. F., Sangrà, P., and Santana-Casiano, M. (2005a). Coupling between the open ocean and the coastal upwelling region off northwest Africa: water recirculation and offshore pumping of organic matter. *J. Mar. Sys.*, 54(1-4):3–37.

Pelegrí, J. L., Marrero-Díaz, A., Ratsimandresy, A., Antoranz, A., Cisneros-Aguirre, J., Gordo, C., Grisolía, D., Hernández-Guerra, A., Láiz, I., Martínez, A., Parrilla, G., Pérez-Rodríguez, P., Rodríguez-Santana, A., and Sangrà, P. (2005b). Hydrographic cruises off northwest Africa: The Canary Current and the Cape Ghir region. *J. Mar. Sys.*, 54(1-4):39–63.

Pelegrí, J. L., Marrero-Díaz, A., and Ratsimandresy, A. W. (2006). Nutrient irrigation of the North Atlantic. *Prog. Oceanogr.*, 70(2-4):366–406.

Peliz, Á. J., Dubert, J., Marchesiello, P., and Teles-Machado, A. (2007). Circulation in the Gulf of Cadiz: Part I Model and mean flow structure. *J. Geophys. Res.*, 112:C11015.

Peliz, Á. J., Dubert, J., Santos, A. M. P., Oliveira, P. B., and Le Cann, B. (2005). Winter upper ocean circulation in the Western Iberian Basin-Fronts, Eddies and Poleward Flows: an overview. *Deep-Sea Res.*, 52(4):621–646.

Peliz, Á. J. and Fiúza, A. (1999). Temporal and spatial variability of CZCS-derived phytoplankton pigment concentrations off the western Iberian Peninsula. *Int. J. Rem. Sens.*, 20:1363–1403.

Peliz, Á. J., Rosa, T. L., Santos, A. M. P., and Pissarra, J. L. (2002). Fronts, jets, and counter-flows in the Western Iberian upwelling system. *J. Mar. Sys.*, 35(1-2):61–77.

Penven, P., Debreu, L., Marchesiello, P., and McWilliams, J. C. (2006). Evaluation and application of the ROMS 1-way embedding procedure to the central California upwelling system. *Ocean Modell.*, 12(1-2):157–187.

Penven, P., Echevin, V., Pasapera, J., Colas, F., and Tam, J. (2005). Average circulation, seasonal cycle, and mesoscale dynamics of the Peru Current System: A modeling approach. *J. Geophys. Res.*, 110:C10021.

Penven, P., Marchesiello, P., Debreu, L., and Lefevre, J. (2008). Software tools for pre- and post-processing of oceanic regional simulations. *Environ. Model. Software.*, 23:660–662.

Perkins, A. L., Smedstad, L. F., Blake, D. W., Heburn, G. W., and Wallcraft, A. J. (1997). A new nested boundary condition for a primitive equation ocean model. *J. Geophys. Res.*, 102(C2):3483–3500.

Peterson, R. G., Stramma, L., and Kortum, G. (1996). Early concepts and charts of ocean circulation. *Prog. Oceanogr.*, 37:1–115.

Piedeleu, M., Sangrà, P., Sánchez-Vidal, A., Fabrés, J., Gordo, C., and Calafat, A. (2009). An observational study of oceanic eddy generation mechanisms by tall deep-water islands (Gran Canaria). *Geophys. Res. Lett.*, 36:L14605.

Pingree, R. D. and Le Cann, B. (1992). Three anticyclonic slope water oceanic eddies (swoddies) in the southern bay of biscay in 1990. *Deep-Sea Res.*, 39(7-8):1147–1175.

Pollard, R. T., Grifftths, M. J., Cunningham, S. A., Read, J. F., Pérez, F. F., and Ríos, A. F. (1996). Vivaldi 1991 - A study of the formation, circulation and ventilation of Eastern North Atlantic Central Water. *Prog. Oceanogr.*, 37(2):167–172.

Reverdin, G., Niiler, P. P., and Valdimarsson, H. (2003). North Atlantic Ocean surface currents. *J. Geophys. Res.*, 108(C1):3002.

Richardson, P. L., Bower, A. S., and Zenk, W. (2000). A census of Meddies tracked by floats. *Prog. Oceanogr.*, 45(2):209–250.

Richardson, P. L., Price, J. F., Walsh, D., Armi, L., and Schröder, M. (1989). Tracking three meddies with SOFAR Floats. *J. Phys. Oceanogr.*, 19(3):371–383.

Rio, M.-H. and Hernandez, F. (2004). A mean dynamic topography computed over the world ocean from altimetry, in situ measurements and a geoid model. *J. Geophys. Res.*, C109:C12032.

Ríos, A. (1992). Water masses in the upper and middle North Atlantic Ocean east of the Azores. *Deep-Sea Res.*, 39(3-4):645–658.

Risien, C. M. and Chelton, D. B. (2008). A Global Climatology of Surface Wind and Wind Stress Fields from Eight Years of QuikSCAT Scatterometer Data. *J. Phys. Oceanogr.*, 38(11):2379–2413.

Roest, W. R., Dañobeitia, J. J., Verhoef, J., and Collette, B. J. (1992). Magnetic anomalies in the Canary Basin and the Mesozoic evolution of the Central North Atlantic. *Mar. Geophys. Res.*, 14(1):1–24.

Rossby, T. (1996). The North Atlantic Current and surrounding waters: At the crossroads. *Rev. Geophys.*, 34(4):463–481.

Sandulescu, M., Hernández-Garcia, E., López, C., and Feudel, U. (2006). Kinematic studies of transport across an island wake, with application to the Canary islands. *Tellus*, 58(5):605–615.

Sangrà, P. (1995). *Perturbación de un flujo geofísico por un obstáculo: Aplicación a la isla de Gran Canaria.* PhD thesis, Universidad de Las Palmas de Gran Canaria. 201pp.

Sangrà, P., Auladell, M., Marrero-Díaz, A., Pelegrí, J. L., Fraile-Nuez, E., Rodríguez-Santana, A., Martín, J. M., Mason, E., and Hernández-Guerra, A. (2007). On the nature of oceanic eddies shed by the island of Gran Canaria. *Deep-Sea Res.*, 54(5):687–709.

Sangrà, P., Basterretxea, G., Pelegrí, J. L., and Arístegui, J. (2001). Chlorophyll increase due to internal waves in the shelf-break of Gran Canaria Island (Canary Islands). *Sci. Mar.*, 65(1):89–97.

Sangrà, P., Pascual, A., Rodríguez-Santana, Á., Machín, F., Mason, E., McWilliams, J. C., Pelegrí, J. L., Dong, C., Rubio, A., Arístegui, J., Marrero-Díaz, Á., Hernández-Guerra, A., Martínez-Marrero, A., and Auladell, M. (2009). The Canary Eddy Corridor: a major pathway for long-lived eddies in the subtropical North Atlantic. *Deep-Sea Res.*, In Press.

Sangrà, P., Pelegrí, J. L., Hernández-Guerra, A., Arregui, I., Martín, J. M., Marrero-Díaz, A., Martínez, A., Ratsimandresy, A. W., and Rodríguez-Santana, A. (2005). Life history of an anti-cyclonic eddy. *J. Geophys. Res.*, 110:C03021.

Schmitt, R. W., S., B. P., and Dorman, C. E. (1989). Evaporation Minus Precipitation and Density Fluxes for the North Atlantic. *J. Phys. Oceanogr.*, 19(9):1208–1221.

Schmitz, W. J. and McCartney, M. S. (1993). On the North Atlantic Circulation. *Rev. Geophys.*, 31(1):29–49.

Sena Martins, C., Hamann, M., and Fiúza, A. F. G. (2002). Surface circulation in the eastern North Atlantic, from drifters and altimetry. *J. Geophys. Res.*, 107(C12):3217.

Serra, N. and Ambar, I. (2002). Eddy generation in the Mediterranean undercurrent. *Deep-Sea Res.*, 49(19):4225–4243.

Serra, N., Ambar, I., and Käse, R. H. (2005). Observations and numerical modelling of the Mediterranean outflow splitting and eddy generation. *Deep-Sea Res.*, 52(3-4):383–408.

Shchepetkin, A. F. and McWilliams, J. C. (2005). The regional oceanic modeling system (ROMS): a split-explicit, free-surface, topography-following-coordinate oceanic model. *Ocean Modell.*, 9(4):347–404.

Shchepetkin, A. F. and McWilliams, J. C. (2009a). An Accurate Boussinesq Oceanic Model with a Practical, "Stiffened"' Equation of State. *Ocean Modell.*, Submitted.

Shchepetkin, A. F. and McWilliams, J. C. (2009b). Correction and Commentary for "Ocean Forecasting in Terrain-Following Coordinates: Formulation and Skill Assessment of the Regional Ocean Modeling System" by Haidvogel et al., J. Comp. Phys. 227, pp. 3595-3624. *J. Comput. Phys.*, In press.

Siedler, G. and Onken, R. (1996). *The Warmwatersphere of the North Atlantic Ocean*, chapter Eastern Recirculation, pages 339–364. Gebrüder Borntraeger.

Siedler, G., Zenk, W., and Emery, W. J. (1985). Strong Current Events Related to a Subtropical Front in the Northeast Atlantic. *J. Phys. Oceanogr.*, 15(7):885–897.

Signell, R. P. and Geyer, W. R. (1991). Transient Eddy Formation Around Headlands. *J. Geophys. Res.*, 96(C2):2561–2575.

Simpson, J. E. (1994). *Sea Breeze and Local Winds*. Cambridge University Press. 248pp.

Skamarock, W. C., Klemp, J. B., Dudhia, J., Gill, D. O., Barker, D. M., Duda, M. G., Xiang-Yu, H., Wang, W., and Powers, J. G. (2008). A Description of the Advanced Research WRF Version 3. Technical report, NCAR, Boulder, Colorado, USA.

Smith, R. D., Maltrud, M. E., Bryan, F. O., and Hecht, M. W. (2000). Numerical simulation of the North Atlantic Ocean at 1/10°. *J. Phys. Oceanogr.*, 30(7):1532–1561.

Smith, W. H. F. and Sandwell, D. T. (1997). Global sea floor topography from satellite altimetry and ship depth soundings. *Science*, 277(5334):1956 – 1962.

Søiland, H., Budgell, W. P., and Knutsen, Ø. (2008). The physical oceanographic conditions along the Mid-Atlantic Ridge north of the Azores in June-July 2004. *Deep-Sea Res.*, 55(1-2):29–44.

Spall, M. A. (1990). Circulation in the Canary Basin: A model/data analysis. *J. Geophys. Res.*, 95(C6):9611–9628.

Stammer, D. and Böning, C. W. (1996). *The Warmwatersphere of the North Atlantic Ocean*, chapter Generation and distribution of mesoscale eddies in the North Atlantic Ocean, pages 159–193. Gebrüder Borntraeger.

Stark, J. D., Donlon, C. J., Martin, M. J., and McCulloch, M. E. (2007). OSTIA: An operational, high resolution, real time, global sea surface temperature analysis system. *OCEANS 2007 - Europe*, pages 1–4.

Stevens, I. G. and Johnson, J. A. (2003). A numerical modelling study of upwelling filaments off the NW African coast. *Oceanol. Acta*, 26(5):549–564.

Stommel, H. (1982). Is the South Pacific helium-3 plume dynamically active? *Earth. Planet. Sci. Lett.*, 61(1):63–67.

Stramma, L. (1984). Geostrophic transport in the warm water sphere of the eastern subtropical North Atlantic. *J. Mar. Res.*, 42:537–558.

Stramma, L., Fischer, J., Brandt, P., and Schott, F. (2003). *Interhemispheric water exchange in the Atlantic Ocean*, chapter Circulation, variability and near-equatorial meridional flow in the central tropical Atlantic, pages 1–22. Elsevier Oceanography Series. Elsevier.

Stramma, L., Hüttl, S., and Schafstall, J. (2005). Water masses and currents in the upper tropical northeast Atlantic off northwest Africa. *J. Geophys. Res.*, 110:C12006.

Stramma, L. and Muller, T. J. (1989). Some observations of the Azores Current and the North Equatorial Current. *J. Geophys. Res.*, 94(C3):3181–3186.

Stramma, L. and Schott, F. (1999). The mean flow field of the tropical Atlantic Ocean. *Deep-Sea Res.*, 46(1-2):279–303.

Stramma, L. and Siedler, G. (1988). Seasonal changes in the North Atlantic subtropical Gyre. *J. Geophys. Res.*, 93(C7):8111–8118.

Sturges, W. and Hong, B. G. (1995). Wind Forcing of the Atlantic Thermocline along 32°N at Low Frequencies. *J. Phys. Oceanogr.*, 25(7):1706–1715.

Suga, T. and Talley, L. D. (1995). Antarctic Intermediate Water circulation in the tropical and subtropical South Atlantic. *J. Geophys. Res.*, 100(C7):13441–13453.

Sverdrup, H. U. (1942). Wind-driven currents in a baroclinic ocean; with application to the equatorial currents of the eastern Pacific. *Proceedings of the National Academy of Sciences*, 33:318–326. USA.

Tejera, A., García-Weil, L., Heywood, K., and Cantón-Garbín, M. (2002). Observations of oceanic mesoscale features and variability in the Canary Islands area from ERS-1 altimeter data, satellite infrared imagery and hydrographic measurements. *Int. J. Rem. Sens.*, 23(22):4897–4916.

Thomas, L. and Ferrari, R. (2008). Friction, frontogenesis, frontal instabilities and the stratification of the ocean surface mixed layer. *J. Phys. Oceanogr.*, 38(11):2501–2518.

Thomas, L., Tandon, A., and Mahadevan, A. (2008). *Eddy-Resolving Ocean Modeling*, volume Geophysical Monograph 177, chapter Submesoscale processes and dynamics, pages 17–38. AGU Monograph.

Tokmakian, R. T. and Challenor, P. G. (1993). Observations in the Canary Basin and the Azores Frontal Region Using Geosat Data. *J. Geophys. Res.*, 98(C3):4761–4773.

Tomczak, M. and Godfrey, J. S. (1994). *Regional Oceanography: An Introduction*. Pergamon, New York. 424pp.

Tomczak, M. and Godfrey, J. S. (2003). *Regional Oceanography: An Introduction*. Daya Publishing House, Delhi, India, 2 edition. 390pp.

Tomczak, M. and Hughes, P. (1980). Three dimensional variability of water masses and currents in the Canary Current upwelling region. *Meteor Forschungs-Ergebnisse*, A21:1–24.

Townsend, T. L., Hurlburt, H. E., and Hogan, P. J. (2000). Modeled Sverdrup flow in the North Atlantic from 11 different wind stress climatologies. *Dynam. Atmos. Oceans*, 32(3-4):373–417.

Troupin, C., Machín, F., Sirjacobs, D., Ouberdous, M., and Beckers, J.-M. (2009a). High-resolution climatology of the North-East Atlantic using Data-Interpolating Variational Analysis (DIVA). *J. Geophys. Res.*, In revision.

Troupin, C., Mason, E., Beckers, J.-M., and Sangrà, P. (2009b). A new mechanism of upwelling generated filaments based on potential vorticity balance. In *II Simposio Internacional de Ciencias del Mar*, Vigo, Spain. Presentation.

Tsimplis, M. N. and Bryden, H. L. (2000). Estimation of the transports through the Strait of Gibraltar. *Deep-Sea Res.*, 47(12):2219–2242.

van Aken, H. M. (2000). The hydrography of the mid-latitude northeast Atlantic Ocean: I: The deep water masses. *Deep-Sea Res.*, 47(5):757–788.

Van Camp, L., Nykjaer, L., Mittelstaedt, E., and Schlittenhardt, P. (1991). Upwelling and boundary circulation off northwest Africa as depicted by infrared and visible satellite observations. *Prog. Oceanogr.*, 26(4):357–402.

Waliser, D. E. and Gautier, C. (1993). A satellite-derived climatology of the ITCZ. *J. Clim.*, 6(11):2162–2174.

Wang, G. and Dewar, W. K. (2003). Meddy-Seamount Interactions: Implications for the Mediterranean Salt Tongue. *J. Phys. Oceanogr.*, 33(11):2446–2461.

Warrick, J. A. and Fong, D. A. (2004). Dispersal Scaling from the World's Rivers. *Geophys. Res. Lett.*, 31:L04301.

Weller, R. A., Furey, P. W. Spall, M. A., and Davis, R. E. (2004). The large-scale context for oceanic subduction in the Northeast Atlantic. *Deep-Sea Res.*, 51(5):665–699.

Wilkins, E. M. (1968). Energy dissipated by atmospheric eddies in the wake of islands. *J. Geophys. Res.*, 73(6):1877–1881.

Woodruff, S. D., Diaz, H. F., Elms, J. D., and Worley, S. J. (1998). COADS Release 2 Data and metadata enhancements for improvements of marine surface flux fields. *Phys. Chem. Earth*, 23(5):517–526.

Wooster, W. S., Bakun, A., and McLain, D. R. (1976). The seasonal upwelling cycle along the eastern boundary of the North Atlantic. *J. Mar. Res.*, 34:131–140.

Worley, S. J., Woodruff, S. D., Reynolds, R. W., Lubker, S. J., and Lott, N. (2005). ICOADS release 2.1 data and products. *Int. J. Climatol.*, 25(7):823 – 842.

Ye, S., Canales, J. P., Rihm, R., Dañobeitia, J. J., and Gallart, J. (1999). A crustal transect through the northern and northeastern part of the volcanic edifice of Gran Canaria, Canary Islands. *J. Geodyn.*, 28(1):3–26.

Yelland, M. and Taylor, P. K. (1996). Wind stress measurements from the open ocean. *J. Phys. Oceanogr.*, 26(4):541–558.

Yelland, M. J., Moat, B. I., Taylor, P. K., Pascal, R. W., Hutchings, J., and Cornell, V. C. (1998). Wind Stress Measurements from the Open Ocean Corrected for Airflow Distortion by the Ship. *J. Phys. Oceanogr.*, 28(7):1511–1526.

Zenk, W., Klein, B., and Schröder, M. (1991). Cape Verde Frontal Zone. *Deep-Sea Res.*, 38(S1):505–530.

Zhou, M., Paduan, J. D., and Niiler, P. P. (2000). Surface currents in the Canary Basin from drifter observations. *J. Geophys. Res.*, 105(C9):21893–21911.

Zimmerman, L. I. (1969). Atmospheric wake phenomena near the Canary Islands. *J. Appl. Meteorol.*, 8(6):896–907.